Imperial College London

QUANTIFICATION OF GLIAL ACTIVATION USING POSITRON EMISSION TOMOGRAPHY IN NEURODEGENERATIVE DISEASE

Zhen Fan

Department of Medicine

Imperial College London, UK

A thesis submitted to Imperial College London for the degree of Doctor of Philosophy October 2018

ABSTRACT

Background: There is considerable evidence that neuroinflammation plays a significant role in neurodegenerative diseases, hence there is a need for glial activation measurements in Alzheimer's disease (AD) with positron-emission tomography (PET). This thesis aims to 1) explore the quantification approach for novel glial activation tracers, 2) and develop new imaging techniques to evaluate biomarker interactions.

Methods: [^{18}F]GE180 and [^{11}C]PBR28 for microglial activation were evaluated in 13 participants with AD and 13 with Mild Cognitive Impairment (MCI). [^{11}C]BU99008 for astroglial activation was studied in 11 AD and MCI. Arterial input functions were acquired and full compartmental modelling, spectral analysis, graphic analysis, cluster analysis and standardized uptake value were evaluated. The VOI (Volume of interest) Prediction Tool (biomarker co-localization) and Individual Correlation Mapping (ICM) (biomarker correlation) were developed to assess biomarker interactions.

Results: Based on Akaike Information Criterion, a two-tissue compartmental model demonstrated the best fit for [^{18}F]GE180 and [^{11}C]BU99008, while [^{11}C]PBR28 fitted the two-tissue model with a vascular component. Impulse response function (IRF) generated by spectral analysis, have shown good consistency with compartmental modelling (R^2>0.8, p<0.0001). [^{18}F]GE180 revealed high plasma binding and low V_T (AD=0.21 ±0.06 mL·cm^{-3}, HC=0.17 ±0.05 mL·cm^{-3}) in the brain. For amyloid-positive patients, I discovered 25% (p<0.01) and 19% (p<0.03) group-level increase in [^{11}C]PBR28 and [^{11}C]BU99008 V_T, respectively. The interactive VOI of microglial activation, amyloid and tau has demonstrated a linear prediction model of individual annual cognitive decline (R^2=0.86, p<0.0001). ICM demonstrated a positive correlation (R^2=0.7, p<0.03) between the volume of biomarker interaction and the severity of the cognitive impairment on individual basis.

Conclusion: This work explores the best quantification method for three new tracers and demonstrates elevation of glial activation in patients with neurodegenerative disease. The novel imaging techniques demonstrate an individualized association between biomarker interaction and cognitive performance, indicating the importance of biomarker interactions in AD.

COPYRIGHT DECLARATION

The copyright of this thesis rests with the author and is made available under a Creative Commons Attribution Non-Commercial No Derivatives licence. Researchers are free to copy, distribute or transmit the thesis on the condition that they attribute it, that they do not use it for commercial purposes and that they do not alter, transform or build upon it. For any reuse or redistribution, researchers must make clear to others the licence terms of this work. For the avoidance of doubt, Imperial College reserves all rights in the content and subject matter of this thesis.

Zhen Fan
Oct 2018

DECLARATION OF ORIGINALITY

I declare that the work described in this thesis is that of the author and that all work by others is appropriately referenced. None of this work has been submitted for any other qualification at this or any other university.

Zhen Fan
Oct 2018

ACKNOWLEDGEMENTS

I would like to express my deepest gratitude to my supervisors, Prof Steve Gentleman and Dr Rainer Hinz, for their supervision and generous support during my time of PhD study at Imperial College London. Without their guidance and encouragement, this thesis would not have been possible. Dr Paul Edison was also a supervisor to the research project (Sep 2014 – Jun 2018). Special thanks to Dr Mattia Veronese for the guidance in mathematical imaging modelling and programing. I would like to send my sincere appreciation to Dr Melanie Dani, Dr Adam Connolly, Dr Yixing Wu, and Mr Tony Thayanandan who proofread the thesis and offered me enormous insightful suggestions and comments. My earnest thanks to my fellow colleagues, Dr Valeria Calsolaro, and Dr Grazia D. Femminella, Dr Melanie Dani, and Miss Rebecca A. Atkinson for recruiting and clinical assessing for patients throughout my research tenure. I am thankful to GE Healthcare for provision of radiotracers, Imperial College Clinical Imaging Facility and Invicro, London (Centre for Imaging Science) for providing MRI and PET scanning. Thanks to all the patients who kindly take part in this work.

Finally, I wish to dedicate this thesis to my beloved parents, Mr Xiannian Fan and Mrs Ying Zhen who always show faith in me and be there for me as my closest friends. My husband, Mr Kai Liang, who gives me unconditional love, encouragement and support during the pursuit of my PhD degree. My maternal grandmother, Mrs Linghua Lv, who raised me with love and shaped who I am today, has suffered from AD for two decades, which was the root of my motivation and determination in devoting my life in the research to fight against this devastating disease. I am ever grateful for my paternal grandfather, Mr Hengli Fan and grandmother, Mrs Daopei Hu's selfless love, and wish they could have seen me graduating, but their love and my memory of them will always be with me.

PUBLICATIONS, CONFERENCES AND AWARDS

PUBLICATIONS DERIVED AND RELATED TO THIS THESIS

1. **Fan Z**, Dani M, Femminella GD, Wood M, Calsolaro V, Veronese M, et al., Parametric mapping using spectral analysis for (11)C-PBR28 PET reveals neuroinflammation in mild cognitive impairment subjects. *Eur J Nucl Med Mol Imaging*. 2018.
2. **Fan Z**, Brooks DJ, Okello A, Edison P. An early and late peak in microglial activation in AD trajectory. *Brain*. 2017 Jan 24;140(3):792-803.
3. **Fan Z**.*, Calsolaro V.*, Atkinson R. A., Femminella G. D., Waldman A., Buckley C., et al., Flutriciclamide (^{18}F-GE180) PET: First-in-Human PET Study of Novel Third-Generation in Vivo Marker of Human Translocator Protein. *J Nucl Med*. 2016; 57:11, 1753-1759.
4. **Fan Z**, Okello AA, Brooks DJ, Edison P. Longitudinal influence of microglial activation and amyloid on neuronal function in Alzheimer's disease. *Brain* 2015;138;3685-98.
5. **Fan Z**, Harold D, Pasqualetti G, Williams J, Brooks DJ, Edison P. Can studies of neuroinflammation in a TSPO genetic subgroup (HAB or MAB) be applied to the entire AD cohort? *J Nucl Med* 2015;56;707-13.
6. **Fan Z**, Aman Y, Ahmed I, Chetelat G, Landeau B, Ray Chaudhuri K et al. Influence of microglial activation on neuronal function in Alzheimer's and Parkinson's disease dementia. *Alzheimers Dement* 2015;11;608-21 e7.
7. Femminella GD, Dani M, Wood M, **Fan Z**, Calsolaro V, Atkinson R, et al. Microglial activation in early Alzheimer trajectory is associated with higher gray matter volume. Neurology. 2019 Mar 19;92(12):e1331–43.
8. Dani, M., Wood, M., Mizoguchi, R., **Fan, Z**., Walker Z., Morgan, R., Hinz, R., et al. 2018. Microglial Activation Correlates in Vivo with Both Tau and Amyloid in Alzheimer's Disease." *Brain*, 2018 July 20.

Under Review:

9. Calsolaro V*, **Fan Z*,** Veronese M, Femminella G, Pasqualetti G, Trigg W, et al. Third generation microglial tracer flutriciclamide ([^{18}F]GE180) in Alzheimer disease.

10. **Fan Z**, Calsolaro V, Myers J, Tyacke RJ, Venkataraman A, Femminella GD, Perneczky R, Gunn R, Rabiner I, Matthews PM, Nutt D, Edison P. Relationship between astrocytes activation using [^{11}C]BU99008 PET, glucose metabolism and amyloid in Alzheimer's disease: A Dementia Platform UK experimental medicine study. (Ready for submission)

(*Contributed equally)

CONFERENCE ABSTRACTS ARISING FROM THIS THESIS

Alzheimer's Association International Conference 2018 (AAIC18), Chicago, U.S.

- Oral presentation: The individual voxel-level correlation between tau (NFT) and amyloid predicts the rate of cognitive decline in MCIs, using a novel imaging correlation method: ICM (Individual Correlation Mapping)

Mapping Neuroreceptors at Work 2018 (NRM18), London UK.

- Oral presentation: Neuroimaging strategies for novel TSPO Flutriciclamide PET to evaluate the neuroinflammation in patients with Alzheimer's disease
- Single-subject correlation map: a novel approach to evaluate the pathological interaction in single subject

Alzheimer's Association International Conference 2017 (AAIC17), London UK.

- Strategies to Develop Parametric Maps for TSPO PET Tracer [^{11}C]PBR28 in Patients with Mild Cognitive Impairment.
- Regional Kinetic Modelling Application for TSPO PET Tracer [^{11}C]PBR28

Dementia symposium 2017 (Alzheimer's Research UK Network Centre), London, UK.

- Oral presentation: An early and late peak in microglial activation in AD trajectory: a longitudinal PET study.

Alzheimer's Association International Conference 2016 (AAIC16), Toronto, Canada.

- Flutriciclamide (^{18}F-GE180) PET: first in human PET study of novel *in vivo* marker of human translator protein (TSPO).
- An early and late peak in microglial activation in AD trajectory: a longitudinal PET study.

Alzheimer's & Parkinson's Diseases 2015 (AD/PD2015), Nice, France.

- Can studies of neuroinflammation in a TSPO genetic subgroup (HAB or MAB) be applied to the entire AD cohort?

INTERNATIONAL AWARDS

- **Alavi–Mandell Publication Award (July 2017)**

Honour issuer: Society of Nuclear Medicine and Molecular Imaging (SNMMI); The Education and Research Foundation for Nuclear Medicine and Molecular Imaging (ERF).

- **AAIC The Best Student Poster Presenter Competition (July 2016)** - The winner of Basic and Translational Science Theme

Honour issuer: Alzheimer's & Association; Alzheimer' Association International Conference (AAIC).

TABLE OF CONTENTS

ABSTRACT **2**
COPYRIGHT DECLARATION **3**
DECLARATION OF ORIGINALITY **4**
ACKNOWLEDGEMENTS **5**
PUBLICATIONS, CONFERENCES AND AWARDS **6**
Publications derived and related to this thesis *6*
Conference abstracts arising from this thesis *7*
International awards *8*
TABLE OF CONTENTS **9**
CONTRIBUTION AND FUNDING SOURCES **14**
LIST OF FIGURES **16**
LIST OF TABLES **19**
LIST OF EQUATIONS **20**
ABBREVIATIONS **21**
CHAPTER I. BACKGROUND **23**
I-1. ALZHEIMER'S DISEASE *23*
1.1. Overview of Alzheimer's disease 23
1.2. Pathophysiology 24
I-2. GLIAL ACTIVATION *26*
2.1. Microglia 26
2.2. Plasticity of Microglial Activation 28
2.3. Microglia in Neurodegenerative Disease 30
2.4. Astrocyte 31
2.5. Inflammatory Mediators 31
I-3. MAGNETIC RESONANCE IMAGING *35*
I-4. POSITRON EMISSION TOMOGRAPHY *38*
4.1. PET Basis 38
4.2. PET Corrections 39
4.3. Principle of PET Tracers 41
4.4. Tracers for Glial Activation 41
I-5. THESIS OBJECTIVES AND CHAPTERS *43*
CHAPTER II. METHODS FOR BRAIN PET QUANTIFICATION **45**
II-1. COMPARTMENTAL MODELLING *46*
1.1. Kinetic Models 46
1.2. Model Selection 48
II-2. PARAMETRIC MAPPING *49*
2.1. Spectral Analysis 49
2.2. Graphic Analysis 52
2.3. Reference Model 53

2.3.1 Reference input model 53
2.3.2 Supervised Cluster Analysis 54
2.3.3 Ratio imaging of amyloid, tau and glucose metabolism 54
2.4. Standardized Uptake Value 55
II-3. IMAGE ANALYSIS *56*
3.1. ROI Analysis 56
3.2. SPM Analysis 58
3.3. BPM Correlation 59
II-4. STATISTICAL ANALYSIS *60*
CHAPTER III. QUANTIFICATION OF MICROGLIAL ACTIVATION USING [^{18}F]GE180 PET 61
III-1. INTRODUCTION *61*
1.1. Objectives 62
III-2. METHODS *62*
2.1. Subjects 62
2.2. Data Acquisition 63
2.2.1 MRI 63
2.2.2 [^{18}F]GE180 PET 63
2.2.3 Blood acquisition 64
2.3. Kinetic Modelling 64
2.3.1 Time activity curve 64
2.3.2 Compartment modelling 65
2.3.3 Scan length 65
2.4. Parametric Mapping 66
2.4.1 Spectral analysis 66
2.4.2 Graphic analysis 66
2.4.3 SUV and SUVR 67
2.4.4 Supervised cluster analysis 67
2.5. Extraction of Vascular Signal from Brain Tissue 68
III-3. RESULTS *69*
3.1. Study 1: Quantification of [^{18}F]GE180 PET in Healthy Control 69
3.1.1 Blood modelling 69
3.1.2 Time activity curve 70
3.1.3 Model selection 70
3.1.4 HAB vs. MAB 71
3.1.5 Scan length 72
3.2. Study 2. Quantification of [^{18}F]GE180 in Neurodegenerative Disease 72
3.2.1 Compartmental modelling 72
3.2.2 Spectral analysis 74
3.2.3 Graphic analysis 77
3.2.4 SUV and SUVR 78
3.2.5 Cluster analysis 79
III-4. DISCUSSION *80*

4.1. Consensus in [18F]GE180 studies 80
4.2. Kinetic Modelling 81
4.3. HAB vs. MAB 82
4.4. [18F]GE180 in Disease 83
4.4.1 Volume of distribution in AD 83
4.4.2 Parametric mapping 84
4.4.3 Reference region 85
4.4.4 Cluster analysis 85
4.5. Blood-Brain Barrier 86
4.6. Conclusion 87
CHAPTER IV. QUANTIFICATION OF MICROGLIAL ATIVATION USING [11C]PBR28 PET 89
IV-1. INTRODUCTION 89
1.1. Objective 89
IV-2. METHODS 90
2.1. Demographics 90
2.2. Data Acquisition 90
2.2.1 MRI acquisition 90
2.2.2 [11C]PBR28 PET Acquisition 91
2.2.3 Blood acquisition 91
2.3. Spectral Analysis of [11C]PBR28 91
2.4. Compartmental Modelling of [11C]PBR28 92
2.5. Graphic Analysis of [11C]PBR28 92
2.6. SUVR of [11C]PBR28 92
2.7. Amyloid Deposition 92
2.8. Imaging Analysis 93
IV-3. RESULTS 94
3.1. Demographics and Amyloid Status 94
3.2. Spectral Analysis 94
3.3. Compartmental Modelling 97
3.4. Logan Graphic Analysis 99
3.5. SUVR 100
IV-4. DISCUSSION 101
4.1. Quantification of [11C]PBR28 PET 101
4.2. IRF-90 [11C]PBR28 PET 101
4.3. IRF-90 [11C]PBR28 vs. Other Methods 102
4.4. IRF-90 [11C]PBR28 Reveals Neuroinflammation In MCI Subjects 104
4.5. Conclusion 105
CHAPTER V. QUANTIFICATION OF [11C]BU99008 PET IN PATIENTS WITH ALZHEIMER'S DISEASE 106
V-1. INTRODUCTION 106
1.1. Objectives 107
V-2. METHODS 108

2.1. Demographics 108
2.2. Blood Data Analysis of [11C]BU99008 PET 108
2.3. Acquisition of [11C]BU99008 PET 109
2.4. Quantification of [11C]BU99008 PET 110
2.4.1 Quantification of [11C]BU99008 PET using compartmental modelling 110
2.4.2 Quantification of [11C]BU99008 PET using spectral analysis 111
2.4.3 Quantification of [11C]BU99008 PET using graphic analysis 111
2.4.4 Quantification of [11C]BU99008 PET using SUV 111
2.5. Quantification of [18F]Florbetaben PET Using Reference Input Approach 112
2.6. Quantification of [18F]FDG PET Using Reference Input Approach 112
2.7. Imaging Processing 112
2.7.1 Region of Interest (ROI) analysis 112
2.7.2 SPM voxel-wise image analysis 112
2.7.3 BPM voxel-wise correlation analysis 113
V-3. RESULTS 113
3.1. Brain Amyloid Status 113
3.2. Results of [11C]BU99008 Quantification 115
3.2.1 Results of [11C]BU99008 PET using compartmental modelling 115
3.2.2 Results of [11C]BU99008 PET using spectral analysis 118
3.2.3 Results of [11C]BU99008 PET using Logan graphic analysis 121
3.2.4 Results of [11C]BU99008 PET using SUV 123
3.3. Astrocyte Reactivity in Patients 123
3.4. Glucose Metabolism in Patients 125
3.5. Correlation between Astrocyte Reactivity, Glucose Metabolism and Amyloid Deposition 126
V-4. DISCUSSION 127
4.1. Quantification of [11C]BU99008 PET 127
4.2. Astrocyte Reactivity in AD Subjects and age-matched Controls 129
4.3. Relationship between Astrocyte Reactivity and Amyloid in AD 130
4.4. Relationship between Astrocyte Reactivity and Glucose Metabolism in AD 131
4.5. [11C]BU99008 vs. other astrocyte PET tracers 133
4.6. Conclusion 134
CHAPTER VI. NOVEL TECHNIQUES: INTERACTIVE vOLUME OF INTEREST (VOI) PREDICTION TOOL, INDIVIDUAL CORRELATION MAP (ICM), AND AUTOMATED QUALITY CONTROL 135
VI-1. BACKGROUND 135
1.1. Objectives 138
VI-2. TECHNIQUE I. VOI PREDICTION TOOL 140
2.1. Principle of VPT 140
2.2. Clinical Application of VPT 143
2.2.1 VPT methods 143
2.2.2 VPT results and discussion 144
2.3. Possible Usage in VPT 147

VI-3. TECHNIQUE II. INDIVIDUAL CORRELATION MAPPING (ICM) *147*
3.1. Principle of ICM 147
3.1.1 General concept of ROI-Correlation 147
3.1.2 Correlation framework 148
3.2. Clinical Application of ICM 150
3.2.1 ICM method 150
3.2.2 ICM results of tau and microglial activation 152
3.2.3 ICM results of amyloid and microglial activation 154
3.2.4 ICM revealed correlation patterns in microglial activation with tau and amyloid in AD 156
3.2.5 ICM signal validation 158
3.3. Possible Use of ICM 160
VI-4. TECHNIQUE III. AUTOMATED SPATIAL TRANSFORMATION QC *161*
4.1. Principle of Automated Spatial Transformation QC 161
4.2. Clinical application of Auto Spatial Transformation QC 162
4.3. Possible Usage of Auto Spatial Transformation QC 164
CHAPTER VII. SUMMARY AND CONCLUSIONS 165
VII-1. SUMMARY OF THIS WORK *165*
1.1. GLIAL ACTIVATION IN PET 165
1.2. IMAGING BIOMARKER CORRELATION 166
VII-2. LIMITATIONS AND FUTURE DIRECTION *167*
VII-3. CONLCUSION *168*
REFERENCES 170
APPENDIX 194

CONTRIBUTION AND FUNDING SOURCES

Contribution: This work was focused on the mathematical modelling of novel PET tracers and development of novel imaging techniques. The academic guidance in PET modelling was mainly provided by my supervisor Dr Rainer Hinz; additional professional feedbacks were received from Dr Mattia Veronese and Prof Federico Turkheimer. Regarding blood analysis, I assisted in the data acquisition, and I investigated and implanted new modelling strategies for the optimal fitting of the parent fraction, plasma over blood, and arterial input function for three novel PET tracers ([^{18}F]GE180, [^{11}C]PBR28 and [^{11}F]BU99008). For data quantification, I conducted different kinetic compartmental modelling (e.g. 2TCM4k and 2TCM4k-1K), spectral analysis, graphic analysis, cluster analysis, reference model analysis, and standardized uptake value (SUV) parametric methods for all novel PET tracers. I compared and verified different quantification methods and improved the data quantification by developing new techniques (e.g. automated vascular signal extraction and automated spatial transformation quality control pipeline). Last but not least, I developed two novel imaging techniques for 3-dimensional biomarker correlation at individual basis: 1) the multilinear VOI (Volume of interest) Prediction Tool (biomarker co-localization) and 2) voxel-level Individual Correlation Mapping (ICM) (biomarker correlation). In summary, I evaluated all potential models for three novel glial activation PET tracers, carried out analysis to compare and determine the optimal quantification model, developed new imaging techniques to improve data quantification, developed novel techniques for biomarker correlation analysis, wrote all my scripts/codes for my work, performed all the data analysis, generated figures/tables for all the results and wrote my PhD thesis independently.

Dr Valeria Calsolaro carried out the MRI and PET scan acquisition for participants recruited for [^{18}F]GE180 and [^{18}F]BU99008 studies, with help from Dr Grazia D. Femminella and Dr Melanie Dani. Miss Rebecca A. Atkinson and Mr Tony Thayanandan performed clinical assessments for those patients. Dr Melanie Dani carried out the MRI/PET scans and psychological assessments for [^{11}C]PBR28 study. The presented independent researches were carried out at Imperial College London, Neuroimaging Unit. Clinical commentaries were received from Dr Melanie Dani, Dr

Grazia D. Femminella, Dr Valeria Calsolaro, Dr Paul Edison, and Professor Steve Gentleman.

Funding sources: The data used in CHAPTER III ([^{18}F]GE180) were funded by Alzheimer's Research, UK and GE Healthcare, and supported by the NIHR (National Institute for Health Research) CRF and BRC at Imperial College London and Imperial College Healthcare NHS Trust to Dr Paul Edison. The data presented in CHAPTER IV ([^{11}C]PBR28) and data used as clinical application for novel techniques in CHAPTER VI (VI-1 to VI-3) ([^{11}C]PBR28, [^{18}F]AV1451 and [^{18}F]Flutemetamol) were funded by Medical Research Council (MRC) and supported by the NIHR CRF and BRC at Imperial College Healthcare NHS Trust to Prof David Brooks and Dr Paul Edison. The [^{11}C]BU99008 project was originally funded by Medical Research Council to Prof David Nutt, and the [^{11}C]BU99008 data in AD were funded by Dementia Platforms UK (DPUK) to Prof Paul Matthews (CHAPTER V). The data used in the CHAPTER VI (VI-4) were from the Alzheimer's Disease Neuroimaging Initiative (ADNI http://adni.loni.usc.edu/), which were mainly funded by National Institutes of Health Grant, National Institute on Aging (NIA), and American Recovery Act funds. The views expressed in the publications and this thesis are those of the author(s) and not necessarily those of the funders, the NHS, the NIHR, the MRC, the DPUK and the Department of Health.

LIST OF FIGURES

FIGURE I-1. NEUROIMAGING IN ALZHEIMER'S DISEASE....23
FIGURE I-2. MOLECULAR AND CELLULAR PROCESSES PRESUMED TO PARTICIPATE IN AD PATHOGENESIS....25
FIGURE I-3. MICROGLIA ARE RAPIDLY ACTIVATED AFTER LOCAL BBB (BLOOD BRAIN BARRIER) DISRUPTION....27
FIGURE I-4. RELATIONSHIP BETWEEN MICROGLIAL ACTIVATION AND NEUROFIBRILLARY TANGLE FORMATION IN ALZHEIMER'S DISEASE....29
FIGURE I-5. CHANGES IN MICROGLIA AND ASTROCYTE IN ALZHEIMER'S DISEASE....30
FIGURE I-6. NLRP3 GENE DEFICIENCY INCREASES MICROGLIAL AB PHAGOCYTOSIS AND SHOWS PROTECTIVE EFFECTS IN APP/PS1 MICE ON MEMORY AND BEHAVIOURS....34
FIGURE I-7. MRI IMAGES IN HEALTHY CONTROL, AND TWO AD PATIENTS WITH SEVERE BRAIN ATROPHY (YELLOW ARROWS)....35
FIGURE I-8. T1 AND T2 MRI....37
FIGURE I-9. SCHEMATIC DIAGRAM OF PET IMAGING....39
FIGURE I-10. PET COINCIDENCE....40
FIGURE II-1. KINETIC COMPARTMENTAL MODELS....46
FIGURE II-2. ILLUSTRATION OF IRF(T) IMAGES GENERATED VIA SPECTRAL ANALYSIS....50
FIGURE II-3. SCHEMATIC REPRESENTATION OF THE ROI ANALYSIS USING SPM....56
FIGURE II-4. SCHEMATIC REPRESENTATION OF THE SPM ANALYSIS AT VOXEL-LEVEL....58
FIGURE III-1. EXTRACTION OF VASCULAR SIGNAL AND SIGNAL DISPERSION FROM BRAIN TISSUE....68
FIGURE III-2. [^{18}F]GE180 BLOOD MODELLING FOR PARENT FRACTION AND POB (PLASMA OVER BLOOD) RATIO....69
FIGURE III-3. RESULTS OF MEAN AIC AND AIC FRACTION....70
FIGURE III-4. HETEROGENEITY OF [^{18}F]GE180 VOLUME OF DISTRIBUTION (ML·CM^{-3}) IN AD (N=13) AND HC (N=8) THROUGHOUT THE BRAIN. THE V_T ESTIMATIONS WERE DERIVED FROM A REVERSIBLE TWO-TISSUE COMPARTMENTAL MODEL WITH ARTERIAL INPUT FUNCTION....73
FIGURE III-5 VOLUME OF DISTRIBUTION IN AD AND HEALTHY CONTROLS IN WHOLE BRAIN (LEFT) AND CORTICAL REGIONS (RIGHT TOP) AND SUBCORTICAL REGIONS (RIGHT BOTTOM)....74
FIGURE III-6. ILLUSTRATION OF IRF PARAMETRIC IMAGES FOR [^{18}F]GE180....74
FIGURE III-7. PEARSON CORRELATION BETWEEN 2TCM4K AND IRF-90 IN FRONTAL LOBE, TEMPORAL LOBE, PARIETAL LOBE AND OCCIPITAL LOBE. THE [^{18}F]GE180 V_T DERIVED FROM THE 2TCM4K WERE SIGNIFICANTLY CORRELATED WITH THE TISSUE RESPONSE FUNCTION DERIVED FROM IRF-90 IN ALL FOUR REGIONS....75
FIGURE III-8. ROI REGIONAL RESULTS OF [^{18}F]GE180 IRF-90 PARAMETRIC MAPS IN 13 AD AND 8 HC SUBJECTS. SIGNIFICANTLY INCREASED [^{18}F]GE180 IRF WERE FOUND IN AD PATIENTS COMPARED WITH HEALTHY CONTROLS IN FRONTAL LOBE, TEMPORAL LOBE, PARIETAL LOBE, OCCIPITAL LOBE, ANTERIOR CINGULATE, POSTERIOR CINGULATE, AMYGDALA AND FUSIFORM....76
FIGURE III-9. SINGLE SUBJECT SPM ANALYSIS OF [^{18}F]GE180 IRF-90 WHEN COMPARED EACH PATIENT TO THE HEALTHY CONTROLS....77

FIGURE III-10. GOOD CORRELATION WERE FOUND BETWEEN LOGAN V_T AND 2TCM4K V_T IN FRONTAL LOBE, TEMPORAL LOBE, PARIETAL LOBE AND OCCIPITAL LOBE. 78
FIGURE III-11. MRI T1, MRI T2 AND [^{18}F]GE180 PET OF AN ISCHEMIC STROKE PATIENT. 79
FIGURE III-12. TIME ACTIVITY CURVE FOR STROKE (ORANGE), OPPOSITE-STROKE (BLUE) AND WHITE MATTER (GREY) 80
FIGURE IV-1. KINETIC SPECTRUM AND DYNAMIC IRF CURVE OF [^{11}C]PBR28 PET. 94
FIGURE IV-2. VOXEL-WISE INDIVIDUAL SPM ANALYSIS OF IRF-90 OF [11C]PBR28. 96
FIGURE IV-3. AIC (AKAIKE INFORMATION CRITERIA) VALUES WERE ESTIMATED FOR [^{11}C]PBR28 PET USING 1TCM4K (RED), 2TCM3K (GREY), 2TCM4K (BLUE), 1TCM2K-1K (GREEN) AND 2TCM4K-1K (YELLOW) COMPARTMENTAL MODEL. THE BAR CHART SHOWED THAT THE LOWER AIC VALUES WERE FOUND IN BOTH 2TCM4K AND 2TCM4K-1K MODELS IN FRONTAL LOBE, TEMPORAL LOBE, OCCIPITAL LOBE AND WHOLE BRAIN. 98
FIGURE IV-4. THE PEARSON CORRELATION BETWEEN [^{11}C]PBR28 BINDING POTENTIALS DERIVED FROM DIFFERENT MODELLING METHODS IN FRONTAL LOBE AND TEMPORAL LOBE. 99
FIGURE V-1. PARENT FRACTION WAS FITTED WITH A (DECREASING) SIGMOID MODEL AND PLASMA OVER BLOOD RATIO WAS FITTED WITH AN (INCREASING) SIGMOID MODEL IN AN AD PATIENT. 110
FIGURE V-2. KINETIC MODEL SELECTION OF [^{11}C]BU99008 PET IN HEALTHY CONTROLS AND PATIENTS WITH AD AND MCI 115
FIGURE V-3. BAR CHART REVEALING REGIONAL [^{11}C]BU99008 DISTRIBUTION (V_T) IN 11 PATIENTS (RED) AND 10 HEALTHY CONTROLS (CLEAR). 116
FIGURE V-4. SCATTER PLOT DEMONSTRATING THE REGIONAL [^{11}C]BU99008 V_T USING 2TCM4K MODEL 117
FIGURE V-5. KINETIC SPECTRUM AND IRF PLOTS OF [^{11}C]BU99008 PET OF WHOLE BRAIN. 118
FIGURE V-6. IMPULSE RESPONSE FUNCTION (IRF) PARAMETRIC MAPS GENERATED FOR [^{11}C]BU99008 PET. 119
FIGURE V-7. [^{11}C]BU99008 IRF (S^{-1}) IN AMYLOID POSITIVE PATIENTS, AMYLOID NEGATIVE PATIENTS AND HEALTHY CONTROLS AT TEMPORAL LOBE (LEFT) AND HIPPOCAMPUS (RIGHT) USING 8 DIFFERENT IRF PARAMETRIC IMAGES. 120
FIGURE V-8. CORRELATION BETWEEN [^{11}C]BU99008 SPECTRAL IRF-120 PARAMETRIC MAPS AND 2TCM4K V_T IN FRONTAL LOBE (FL), TEMPORAL LOBE (TL), PARIETAL LOBE (PARIETAL LOBE) AND OCCIPITAL LOBE (OL). BLUE CIRCLE=HEALTHY CONTROL; GREEN CIRCLE= PATIENT. 120
FIGURE V-9. SCATTER PLOT DEMONSTRATING THE REGIONAL [^{11}C]BU99008 IRF-120 (S^{-1}) IN AMYLOID POSITIVE PATIENTS (RED FILLED CIRCLE), AMYLOID NEGATIVE PATIENTS (RED UNFILLED CIRCLE) AND HEALTHY CONTROLS (GREEN SQUARE) 121
FIGURE V-10. SCATTER PLOT DEMONSTRATING THE REGIONAL [^{11}C]BU99008 LOGAN V_T IN AMYLOID POSITIVE PATIENTS (RED FILLED CIRCLE), AMYLOID NEGATIVE PATIENTS (RED UNFILLED CIRCLE) AND HEALTHY CONTROLS (GREEN SQUARE). 122
FIGURE V-11. PEARSON CORRELATION BETWEEN [^{11}C]BU99008 LOGAN V_T PARAMETRIC MAPS AND 2TCM4K V_T IN FRONTAL LOBE (FL), TEMPORAL LOBE (TL), PARIETAL LOBE (PARIETAL LOBE) AND OCCIPITAL LOBE

(OL). THE BLUE CIRCLES REPRESENT THE HEALTHY CONTROLS (HC) AND THE GREEN CIRCLES REPRESENT THE PATIENTS. THE R SQUARE FOR EACH ROI REGION WAS ESTIMATED. 123
FIGURE V-12. SPM GROUP ANALYSIS OF ASTROCYTE REACTIVITY, GLUCOSE METABOLISM AND AMYLOID DEPOSITION. 124
FIGURE V-13. BIOLOGICAL PARAMETRIC MAPPING CORRELATION BETWEEN LEVELS OF ASTROCYTE REACTIVITY, AMYLOID AND GLUCOSE METABOLISM. 126
FIGURE VI-1. STEREOTYPICAL PATTERNS OF TAU (A-B) AND AMYLOID (C-D) IN ALZHEIMER'S DISEASE. THE SEQUENTIAL PATTERN OF AMYLOID DEPOSITION FOLLOWS AN OPPOSITE DIRECTION IN CONTRAST TO THE NEUROFIBRILLARY TANGLES IN AD 137
FIGURE VI-2. A PARTITION VOI MAP GENERATED FOR AN AD PATIENT. 140
FIGURE VI-3. THE ALGORITHM OF GENERATING INTERACTIVE VOI PARTITION MAP. 141
FIGURE VI-4. DEMONSTRATION OF VOI PARTITION MAP WITH DIFFERENT COLOUR LUMPS, WHICH REPRESENTED DIFFERENT VOI CATEGORIES. 142
FIGURE VI-5. AN ILLUSTRATION OF VOLUMES OF VOI PARTITIONS IN AN AD PATIENT USING THREE SPM-T IMAGING MODALITIES: TAU PET (M1), AMYLOID PET (M2) AND TSPO PET (M3). EACH MODALITY REPRESENTS THE SIGNIFICANT INCREASED BIOMARKERS IN AN INDIVIDUAL COMPARED WITH CONTROLS USING ONE-WAY ANOVA. 144
FIGURE VI-6. MULTILINEAR REGRESSION MODEL BETWEEN DIFFERENT SETS OF VOI VARIABLES (AMYLOID, TAU AND MICROGLIAL ACTIVATION) AND THE ANNUAL COGNITIVE DECLINE RATE (MMSE). 146
FIGURE VI-7. THE PROCEDURE OF ICM AND GENERATION OF ROI-CORR MAP. 149
FIGURE VI-8. ICM ROI-CORR MAPS DEMONSTRATED THE POSITIVE CORRELATED CLUSTERS IN THREE DIMENSIONAL BETWEEN TAU AND REACTIVE MICROGLIA IN AN AD PATIENT AND AN MCI PATIENT 153
FIGURE VI-9. ROI-CORR MAPS DEMONSTRATED THE POSITIVE CORRELATED CLUSTERS BETWEEN AMYLOID AND MICROGLIAL ACTIVATION IN AN AD PATIENT AND AN MCI PATIENT. 155
FIGURE VI-10. ICM PLOT SHOWS THE CORRELATION PATTERN BETWEEN TAU AND MICROGLIAL ACTIVATION (UPPER PANEL) AND CORRELATION PATTERN BETWEEN AMYLOID AND MICROGLIAL ACTIVATION (LOWER PANEL) IN FOUR AD SUBJECTS. 157
FIGURE VI-11. SPM GROUP ANALYSIS FOR ICM POSITIVE SUBJECTS. 158
FIGURE VI-12. SPATIAL PATTERN BETWEEN INDIVIDUAL CORRELATION MAPS (ICM) AND INDIVIDUAL SPM-T MAPS WHICH SHOWED THE DISTRIBUTION OF [^{11}C]PBR28 AND [^{18}F]AV1451. TWO AD SUBJECTS (1ST AND 2ND PANEL) AND ONE MCI SUBJECT (3RD PANEL) WERE PRESENTED 159
FIGURE VI-13. AUTOMATED SPATIAL TRANSFORMATION QC RESULTS SUMMARY. 163

LIST OF TABLES

TABLE III-1. REGIONAL V_T (mL·cm^{-3}) FOR [^{18}F]GE180 APPLIED 2TCM4K MODEL IN ALL HEALTHY CONTROLS, HABS AND MABS. 71
TABLE IV-1. DEMOGRAPHICS FOR [^{11}C]PBR28 STUDY 94
TABLE IV-2. THE TOTAL VOLUME OF SIGNIFICANTLY INCREASED BINDING IN INDIVIDUAL MCIS COMPARED TO HEALTHY CONTROLS AT VOXEL-LEVEL, USING [^{11}C]PBR28 PARAMETRIC MAPPING OF IRF-90 AND LOGAN V_T 96
TABLE IV-3. ROI ANALYSIS OF IRF-90 MEAN (s^{-1}) AND SD (STANDARD DEVIATION) IN AMYLOID-POSITIVE MCI AND HEALTHY CONTROLS. THE PERCENTAGE CHANGES OF THE MEANS AND P VALUES (PARAMETRIC TEST) WERE REPORTED FOR THE GROUP-LEVEL COMPARISON. 97
TABLE IV-4. COEFFICIENT OF VARIATION (CV) FOR IRF-90 AND LOGAN PARAMETRIC MAPS OF [^{11}C]PBR28 ACROSS ALL SUBJECTS. THE MEAN AND STANDARD DEVIATION (SD) OF CV WERE REPORTED FOR BOTH IRF-90 AND LOGAN ANALYSIS. 100
TABLE V-1. DEMOGRAPHICS OF PATIENTS AND CONTROL SUBJECTS 108
TABLE V-2. ROI (GREY MATTER) RESULTS FOR AMYLOID DEPOSITION IN PATIENTS AND HEALTHY CONTROLS USING [^{18}F]FLORBETABEN RATIO PET. 114
TABLE VI-1. ICM INDIVIDUAL RESULTS BETWEEN TAU AND MICROGLIAL ACTIVATION. 152
TABLE VI-2. ICM INDIVIDUAL RESULTS BETWEEN AMYLOID AND MICROGLIAL ACTIVATION 154

LIST OF EQUATIONS

EQUATION 1. MULTILINEAR ANALYSIS 1 47
EQUATION 2. AKAIKE INFORMATION CRITERION 48
EQUATION 3. VOLUME OF DISTRIBUTION 48
EQUATION 4. BINDING POTENTIAL (BP_{ND}) 48
EQUATION 5. SPECTRAL ANALYSIS 49
EQUATION 6. IMPULSE RESPONSE FUNCTION 51
EQUATION 7. COEFFICIENT OF VARIATION 51
EQUATION 8. F-RATIO 52
EQUATION 9 LOGAN ANALYSIS 52
EQUATION 10. STANDARDIZED UPTAKE VALUE 55
EQUATION 11. INDIVIDUAL Z-SCORE MAP 59
EQUATION 12. MMSE ANNUAL DECLINE RATE 143
EQUATION 13. MULTILINEAR REGRESSION OF THREE VARIABLES 144
EQUATION 14. THE MULTILINEAR MODEL OF VOI PREDICTION TOOL 145

ABBREVIATIONS

AD	Alzheimer's Disease
1TCM2k	One-Tissue Reversible Model
1TCM2k-1K	One-Tissue Reversible Model With A Vascular Component
2TCM3k	Two-Tissue Irreversible Model
2TCM4k	Two-Tissue Reversible Model
2TCM4k-1K	Two-Tissue Reversible Model With A Vascular Component
AIC	Akaike Information Criterion
APP	Amyloid Precursor Protein
ARSAC	Administration Of Radioactive Substances Advisory Committee
Aβ-40	Amyloid Peptide Isoforms 40
Aβ-42	Amyloid Peptide Isoforms 42
BBB	Blood-Brain Barrier
BPM	Biological Parametric Mapping
BPND	Non-Displaceable Binding Potential
CNS	Central Nervous System
CSF	Cerebrospinal Fluid
CSF	Cerebrospinal Fluid Levels
CSF	Cerebrospinal Fluid
CV	Coefficient Of Variation
df	Degree Of Freedom
FEW	Family-Wise Error
FOV	Field Of View
f_p	Free Fraction
GFAP	Glial Fibrillary Acidic Protein
HAB	High Affinity Binders
HPLC	High-Performance Liquid Chromatography
I2BS	I2-Imidazoline Binding Site
I_2BS	Imidazoline-2 Binding Site
ICM	Individual Correlation Mapping
IL	Interleukin
IRF	Impulse Response Function

k	Rate Constant
Ki	Net Influx
LAB	Low Affinity Binders
LC	Locus Coeruleus
LOR	Line Of Response
MA	Multilinear Analysis
MAB	Mixed Affinity Binders
MAP	Microtubule-Associated Protein
MAPT	Microtubule-Associated Protein Tau
MCI	Mild Cognitive Impairment
M-CSF	Macrophage Colony-Stimulating Factor
MMSE	Mini-Mental State Examination
MRI	Magnetic Resonance Imaging
MT	Microtubules
NFT	Neurofibrillary Tangles
NIA-AA	National Institute On Aging And Alzheimer's Association
PET	Positron Emission Tomography
PHF	Paired Helical Filament
POB	Plasma Over Blood
QC	Quality Control
ROI	Region Of Interest
SPM	Statistical Parametric Mapping
SS	Sum Of Squares
SUV	Standardized Uptake Value
SUVR	Standardized Uptake Value Ratio
TAC	Time Activity Curve
TNF	Tumor Necrosis Factor
TSPO	Translocator Protein
VOI	Volume Of Interest
VPT	VOI Prediction Tool
V_T	Volume Of Distribution
WRSS	Weighted Residual Sum Of Squares

CHAPTER I. BACKGROUND

I-1. ALZHEIMER'S DISEASE

1.1. Overview of Alzheimer's disease

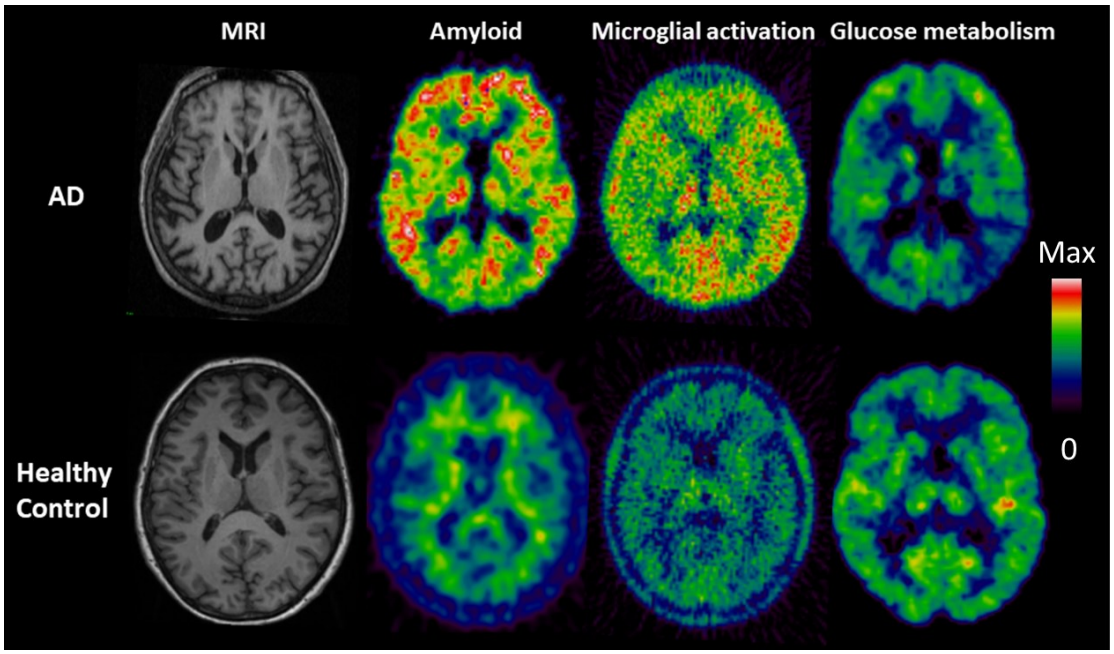


Figure I-1. Neuroimaging in Alzheimer's disease.

Upper panel shows an AD patient and lower panel shows an age-matched healthy control. MRI T1 image shows the brain structure and atrophy. Amyloid deposition was quantified by [^{11}C]PIB Ratio image (60-90 min) using the cerebellum as the reference region (colour bar max=3); microglial activation was quantified by [^{11}C]PK11195 BP image which generated by supervised cluster analysis (colour bar max=1); and glucose metabolism was quantified by [^{18}F]FDG ratio image (reference to pons). Colour bar max=1.

Alzheimer's disease (AD) is the most common form of dementia affecting people over 65 years old. It is characterised by progressive symptoms associated with the deterioration of memory, speech, thinking and cognitive function (Association, 2017; Castillo-Carranza, Guerrero-Muñoz & Kayed, 2014; Nelson, Gard & Tabet, 2014). To date, around 850,000 people in the UK suffer from dementia, and the number is expected to soar to 1 million by 2025 (www.alzheimers.org.uk). AD was firstly described in 1906 by Dr Alois Alzheimer, but little is known about the exact etiological mechanism of the disease, the reason for the heterogeneous progression profiles in individuals, and how to prevent, slow down or stop such progression. Mild Cognitive

Impairment (MCI) is an intermediate phase between healthy brains and Alzheimer's disease. Patients with MCI often have noticeable memory impairment and cognitive deficit, but are still able to carry on a normal life. Meta-analysis of studies in MCI and AD suggest that 38% of individuals with MCI develop AD dementia in 5 years, indicating MCI is a potential precursor to Alzheimer's dementia (Hatashita & Yamasaki, 2013; Alzheimer & Association, 2018). Thus, there is an increasing interest in MCI as an important focus for development of preventative or disease modifying treatments (Portet *et al.*, 2006). Emerging evidence shows that pathological changes in the brain precede the symptoms by many years, thereby pointing to the critical need for *in vivo* biomarker imaging in AD research (Jack *et al.*, 2018a; Alzheimer & Association, 2018). (Figure I-1)

1.2. Pathophysiology

As mentioned, the symptoms of memory impairment, confusion and cognitive impairment may appear 15-20 years after the pathological changes start to appear in the brain (Jack *et al.*, 2018a). Thus, it is crucial to develop novel biomarkers for AD pathology to allow early diagnosis. Compared with a healthy brain, the AD brain is characterised by the accumulation of extracellular amyloid plaques composed of β-amyloid (Aβ) protein and intracellular neurofibrillary tangles (NFTs) composed of tau protein (Castillo-Carranza, Guerrero-Muñoz & Kayed, 2014; Ittner & Götz, 2011) (Figure I-2). In 2018, the National Institute on Aging and Alzheimer's Association (NIA-AA) Research Framework changed the definition of AD from individuals' clinical symptoms to a biological based construct in the brain, where AD brain in observational and intervention research studies has to present with amyloid deposition, tau pathology, and neurodegeneration in post-mortem examination or *in vivo* biomarkers (cerebrospinal fluid makers or molecular imaging) (Jack *et al.*, 2018a). These amendments of AD definition were initially raised due to the fact that dementia have shown a considerable heterogeneous neuropathology in post-mortem brains (Boyle *et al.*, 2017). Therefore, there is an urgent need to investigate biomarkers for the multiple neuropathology *in vivo* and their relationship to the diverse cognitive presentation during disease progression.

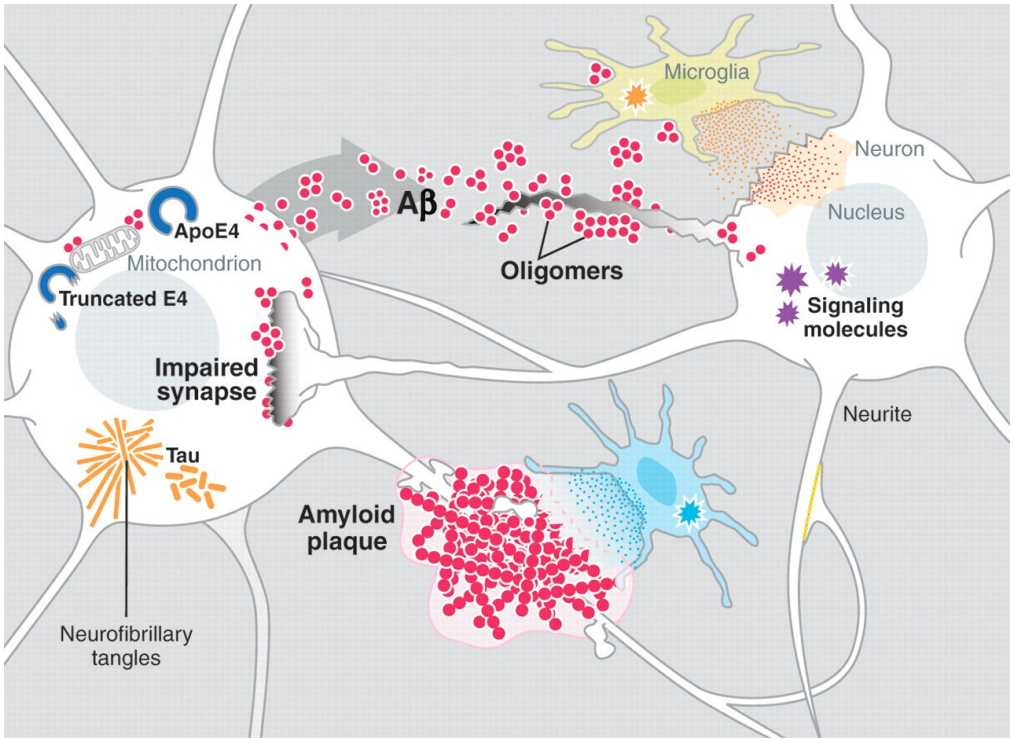


Figure I-2. Molecular and cellular processes presumed to participate in AD pathogenesis.

In AD brain, the accumulation of insoluble Aβ assemblies and deficiency of the clearance mechanism (e.g. microglia) could lead to further increase of amyloid plaques. Figure from Erik D. Roberson, and Lennart Mucke Science 2007 (Roberson et al., 2007) (Appendix 1. Permission Table)

Amyloid peptide is a downstream product derived from the Amyloid Precursor Protein (APP). The precise effects of amyloid in normal brain is not fully understood; however, animal studies have demonstrated that amyloid function may be related to the activation of kinase enzymes (Tabaton *et al.*, 2010), regulation of cholesterol transportation (Bailey *et al.*, 2011; Di Scala *et al.*, 2014; Maloney & Lahiri, 2011) and induction of pro-inflammatory activity (Chakravarthy *et al.*, 2008; Soscia *et al.*, 2010). In a diseased brain, the toxic hydrophobic Aβ-42 oligomers are abundant in the extracellular space of the central nervous system (CNS). The imbalanced production of downstream amyloid peptide isoforms (Aβ-42 and Aβ-40) could be due to the mutation in APP cleavage proteolytic enzymes (e.g. γ-secretase) (Selkoe & Hardy, 2016). As a result, Aβ aggregates into soluble oligomers, then forms fibrils of insoluble ß-pleated sheet, which subsequently builds up in toxic senile plaques (Kumar, Singh & Ekavali, 2015). Recent studies have shown that amyloid plaques devastate brain function by interfering with the neural synaptic function by lowering density of synapses and altering synaptic

structure, thereby cause the impairment of communication between neurons (Borlikova *et al.*, 2013). Aß is also found to induce oxidative damage which causes neuronal degeneration (Nunomura *et al.*, 2010). Other studies indicated that Aß promotes tau hyperphosphorylation (Kumar, Singh & Ekavali, 2015; Kurz & Perneczky, 2011) and accelerates the proinflammatory stress with excessive activation of the microglia cells. (Selkoe & Hardy, 2016)

Tau protein is a microtubule-associated protein (MAP) and is found in abundance in axons of the neurons (Figure I-2). With different numbers of tubulin-binding repeats (e.g. 3R tau or 4R tau), six major isoforms of tau protein in the human brain are observed, all of which are the products of alternative splicing from a single gene MAPT (microtubule-associated protein tau) that are found on chromosome 17. In general, all tau isoforms seem to play a similar role in interacting with microtubules (MTs) and modulating the stability of axonal microtubules in CNS. However, various expression of tau isoforms are observed during the development, suggesting different isoforms may adopt distinctive functions in axonal development and neural plasticity (Takuma, Arawaka & Mori, 2003). Under pathological conditions, excessive phosphorylation of tau leads to the production of paired helical filament (PHF) tau and NFT. In contrast to the normal tau protein which interacts with microtubules in the neurons, the hyperphosphorylated tau can form highly insoluble aggregates (e.g. NFT) which compromise microtubule stabilization the axonal transport, which in turn causes disruption of synaptic function and promotes neurodegeneration.

I-2. GLIAL ACTIVATION

2.1. Microglia

Microglia are resident macrophages in the central nervous system. They distribute ubiquitously in the brain and are the most abundant type of glial cells, accounting for 10-15% of all cells within the brain (Lawson, Perry & Gordon, 1992). Microglia cells act as the main endogenous immune system in the CNS and provide the primary brain defence against external insults. It has been shown that microglia provide support to normal memory formation by stimulating neurotrophic factors (Parkhurst *et al.*, 2013). Microglia act as a constant surveillance system using their long branching motile processes to chemically survey the local environment and provide neurotrophic factors

for supporting tissue maintenance. When there is a presence of pathogens or cellular debris (Figure I-3), microglia quickly identify foreign bodies, migrate to the lesion and become activated. In order to remove those immune threats, activated microglia cells are morphologically changed into an amoeboid form, where their processes are retracted and cell bodies are enlarged. Activated microglia accumulate around the site of lesion and start to proliferate around the lesion with increased expression of inflammatory mediators and receptors. An innate immune response can then be initiated by inflammatory mediators, such as cytokines, chemokines and caspases. Subsequently, microglial cells mediate the immune response by acting as the antigen-presenting cells to T lymphocytes. If the damage is persistent in the brain, some of the microglia undergo further transformation into macrophages, which eventually remove the cellular debris at the injury site by phagocytosis (Heneka *et al.*, 2015; Stefaniak & O'Brien, 2015; Tremblay, 2011).

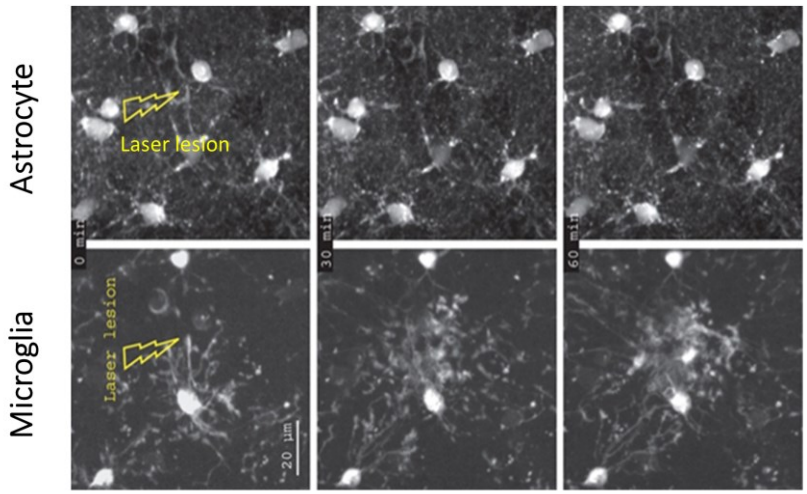


Figure I-3. Microglia are rapidly activated after local BBB (blood brain barrier) disruption.

Fluorescence images of astrocytes (SR101 constrained astrocytes) were shown on the upper panel, and EGFP-expressing microglial cells were shown on the lower panel. A targeted laser-induced microlesion were performed (yellow flashes indicate the site of injury) to cause a disruption of blood vessel. The 2 panels of three Fluorescence images (horizontal) were taken at baseline (0 min), 30 min, and 60 min after the lesion for astrocyte and microglia at the site of blood vessel disruption, where microglia were rapidly activated at the lesion site. Bar=20 µm. From Axel Nimmerjahn et al. Science 2005; 308:1314-1318 (Appendix 1. Permission Table)

2.2. Plasticity of Microglial Activation

Microglial activation is a complex process. It involves physical morphology changes, secretion of different inflammatory cytokines, and possible changes in activation phenotype based on the factors that are presented in the brain. The concept of a spectrum in microglial activation phenotypes arises from *in vitro* studies. Previously, it was suggested that there are two major forms of microglial activation (Figure I-4), the toxic classical activation (M1) that is induced by interferon-γ and the protective alternative activation (M2) that is induced by IL-4 (Martinez & Gordon, 2014; Stein *et al.*, 1992). The microglial classical activation (M1) was characterised by impairment of phagocytosis capability and increased secretion of pro-inflammatory cytokines, such as interleukin 1 (IL-1), IL-6, IL-12, IL-18 and TNFα. The alternative activation (M2) of microglia cells increased the phagocytosis without generating toxic nitric oxide, and elevated the expression in a series of anti-inflammatory cytokines, such as IL-4, IL-10, IL-13, and TGF-β (Goerdt & Orfanos, 1999; Koenigsknecht-Talboo & Landreth, 2005; Mantovani *et al.*, 2002; Zelcer *et al.*, 2007). However, recent studies have come up with a different view based on studies of peripheral monocytes (Chiu *et al.*, 2013; Xue *et al.*, 2014). Rather than two stable subsets (M1 or M2), with various stimuli in the tissue, microglia seem to have a near-infinite plasticity in activated phenotypes, which allows them to specifically respond to enormous environmental alterations (Martinez & Gordon, 2014). Thus, the microglial activation phenotypes could be a spectrum of functionality: from the anti-inflammatory dominated to pro-inflammatory dominated activation depending on specific environmental triggers.

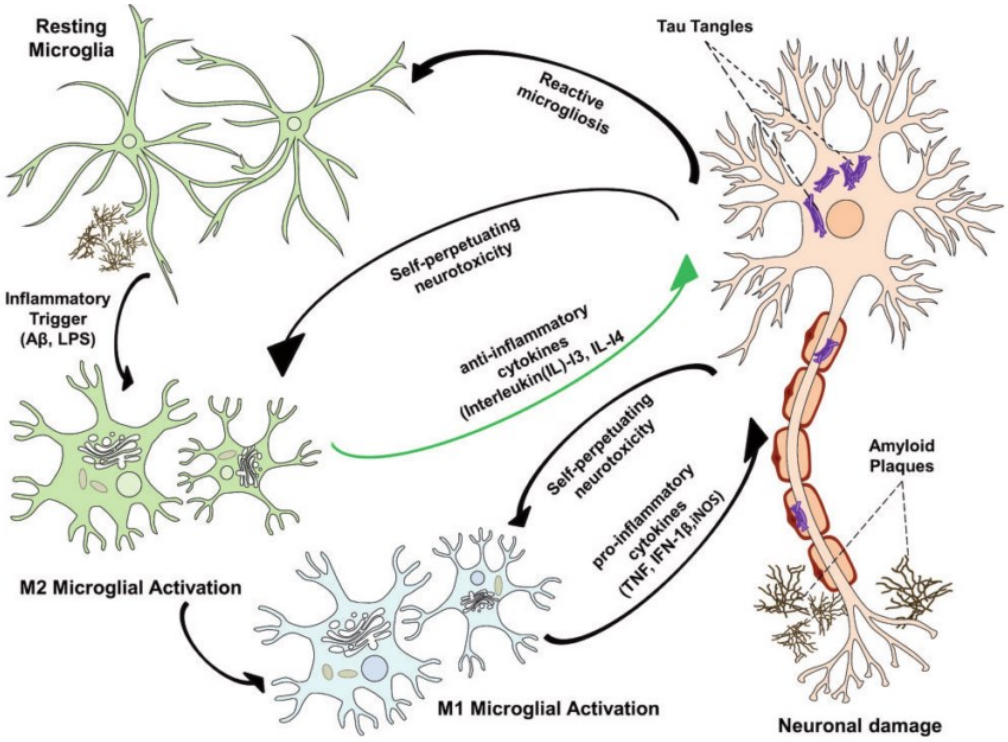


Figure I-4. Relationship between microglial activation and neurofibrillary tangle formation in Alzheimer's disease.

The microglial classical activation (M1) was characterised by impairment of phagocytosis capability and increased secretion of pro-inflammatory cytokines, such as interleukin 1 (IL-1), IL-6, IL-12, IL-18 and TNFα. The alternative activation (M2) of microglia cells increased the phagocytosis without generating toxic nitric oxide, and elevated the expression in a series of anti-inflammatory cytokines, such as IL-4, IL-10, IL-13, and TGF-β. IL = interleukin; TNF = tumour necrosis factor; IFN = interferon; iNOS = inducible nitric oxide synthase; Ab = amyloid-b; LPS = lipopolysaccharide. (Z Fan, 2015, Brain) (Appendix 1. Permission Table)

In ageing CNS and brains with on-going degeneration of neurons, the phenomenon of microglia priming is observed, where the sensitivity of microglia to the local inflammatory stimuli is enhanced. In a study of ageing mice, profound age-related microglial priming was presented in aged mice brain with enhanced phagocytic capacity, increased secretion of cytokines and stimulation of reactive oxygen mediators (Haley *et al.*, 2018; Niraula, Sheridan & Godbout, 2017). Those findings suggested that microglial priming can be initialized by environmental effects, such as oxidative aging or persistent aberrant degeneration of the neurons.

2.3. Microglia in Neurodegenerative Disease

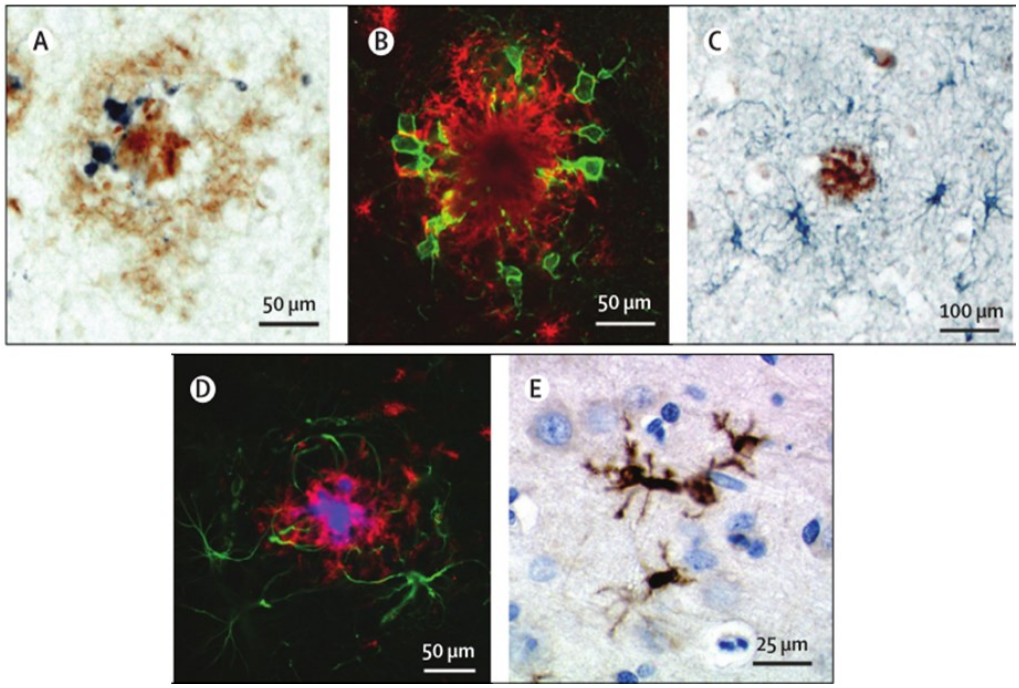


Figure I-5. Changes in microglia and astrocyte in Alzheimer's disease.

(A) CD11b-positive microglia (blue) within an amyloid β (Aβ) deposit (brown) in Alzheimer's disease. (B) Activated, IBA1-positive microglia (green) at an Aβ plaque site (red) in an APP/PS1 transgenic mouse. (C) GFAP-positive astrocytes (blue) surround the site of Aβ deposition (brown) in Alzheimer's disease. (D) GFAP-positive astrocytes (green) at an Aβ plaque site (red) in an APP/PS1 transgenic mouse. (E) Interleukin-1β-positive microglia (brown) from a patient with Alzheimer's disease. (M. Heneka, 2015, The Lancet Neurology) (Appendix 1. Permission Table)

In neurodegenerative disease, there is considerable evidence that neuroinflammation plays a significant role (Figure I-5). Inflammation, particularly microglial activation, is a common feature of many neurodegenerative disorders (Amor *et al.*, 2010; Cappellano *et al.*, 2013). However, the exact role of microglia is still under debate. As mentioned above, microglia activation may have a spectrum of phenotypes, and can be both beneficial and detrimental to the brain. In a normal brain, when there is a pathogenic stimulus, microglial cells respond effectively to remove the dangerous signal and restore normal brain function. On the contrary, in the AD brain and AD transgenic mouse models, activated microglia are observed in the vicinity of amyloid plaques, but they do not effectively phagocytose the Aβ protein. Moreover, activated microglia may further accelerate neuronal loss by stimulating pro-inflammatory pathways. (Joshi *et*

al., 2014) Sustained exposure to the intractable amyloid and inflammatory mediators leads to dysfunctional microglia with persistent production of pro-inflammatory cytokines, and thus damage to surrounding cells. Beclin-1, an autophagy protein, regulates the microglial function by sorting cellular components, such as TREM2, APP, BACE1 and CD36, via the endolysosomal pathway. However, expression of Beclin-1 is suppressed in AD patients, therefore impairs the microglial phagocytosis function and reduces in CD36 and TREM2 (Lucin *et al.*, 2013). Previous PET imaging studies have suggested that microglial activation, rather than amyloid plaques, correlates more closely with the severity of dementia (Edison *et al.*, 2013).

2.4. Astrocyte

The star-shaped astrocyte cell is another sub-type of glial cells in the CNS, which bears many similarities to microglial cells. Astrocytes monitors the synaptic activity and balances the brain homeostasis by constantly conducting metabolic coupling and reducing excessive potassium or glutamate (Benjamin & Quastel, 1972; Pellerin & Magistretti, 1994). When there is a molecular trigger which alters the brain homeostasis, astrocytes respond rapidly and get activated with multiple expressions of receptors and intracellular signalling cascades on the synapses (Buffo, Rolando & Ceruti, 2010; Burda & Sofroniew, 2014). Astrocyte reactivity has been found around senile plaques in animal model of AD and post-mortem AD brain. It may also appear prior to the presence of Aβ deposition in the course of AD (Kummer *et al.*, 2014; Medeiros & LaFerla, 2013; Olabarria *et al.*, 2010) (Figure I-5). Reduction of astroglial cells were observed in animal models of AD, indicating an early phase of impaired astrocyte function in maintenance of synaptic transmission and connectivity, which resulted in cognitive deficits (Beauquis *et al.*, 2013; Kulijewicz-Nawrot *et al.*, 2012; Olabarria *et al.*, 2011; Yeh *et al.*, 2011).

2.5. Inflammatory Mediators

Microglia and astrocytes orchestrate the process of pro-inflammatory, anti-inflammatory, and apoptosis by releasing different inflammatory mediators. At the same time, microglial and astroglial reactivity can be induced and driven by inflammatory mediators.

In Alzheimer's disease, significant elevation of pro-inflammatory cytokines, including interleukin 6 (IL6), interleukin 1α and TNFα (Tumour necrosis factor), was observed with increased Aβ in ageing TgAPPsw and PSAPP transgenic mice, suggesting Aβ accumulation may induce the neuroinflammatory response in AD (Patel *et al.*, 2005). This is consistent with *in vitro* findings. When applying a pre-aggregated Aβ simulation in the microglial cell culture, increased production of pro-inflammatory cytokines (IL1β, IL6 and TNFα), MIP-1α and M-CSF (Macrophage colony-stimulating factor) was found (Lue *et al.*, 2001). The caspase-1 is fundamental for interleukin-1β mutation in AD. In human MCI and AD brain tissue, the active caspase-1 expression is upregulated significantly *in vitro*. Additionally, in close vicinity to Aβ plaques, interleukin-1β was found to be the most pronounced pro-inflammatory cytokine secreted by microglial cells in disease tissue. (Akama & Van Eldik, 2000; Heneka, Kummer & Latz, 2014) *In vivo*, the APP/PS1 Alzheimer's transgenic mice with NLRP3 and caspase-1 deficiency, have revealed a reduction in Aβ accumulation by inducing the microglial activation to an anti-inflammatory state. Moreover, those transgenic mice were found to be protected from the impairment of spatial memory (Heneka *et al.*, 2012). With the *in vivo* findings, NLRP3 and caspase-1 were proven to play a significant role in the course of Alzheimer's disease, and NLRP3 inflammasome could be therefore a possible therapeutic intervention target. M-CSF, a hematopoietic growth factor, activates the microglial cells and contributes to phagocytosis of Aβ. It has been shown that M-CSF levels in plasma were found substantially increased in dementia AD patients compared to MCI cohort or age-matched healthy controls, while the M-CSF level in cerebrospinal fluid (CSF) was significantly reduced in MCI patients compared to AD patients and patients with other non-inflammatory neurological disease (Laske *et al.*, 2010). This clinical trial suggested M-CSF plays a major role in distinguishing various forms of neurodegenerative disease, which can be used as a putative biomarker for MCI patients.

In patients with Alzheimer's disease, the pro-inflammatory environment in the CSF which is characterized by increased pro-inflammatory mediators (cytokine TNFα) and reduced anti-inflammatory mediators (TGF-β), was found to raise the risk of conversion from MCI to AD (Tarkowski *et al.*, 2003). Conversely, studies in mouse models of AD demonstrated that some pro-inflammatory mediators may be beneficial in the disease (Shaftel *et al.*, 2007). When induced a blood-brain barrier leakage in a mouse brain, the

chronic interleukin-1β expression in unilateral hippocampus enhanced the leukocyte recruitment dramatically to the CNS, which comprised of neutrophils, macrophages and T cells, with no evidence of neuronal degeneration in the hippocampus (Shaftel *et al.*, 2007). When overexpressing interleukin-1β in a triple transgenic mouse model of AD, Ghosh et al. (Ghosh *et al.*, 2013) found 4-6 fold increase in microglia surrounding the Aβ plaques and robust reduction in amyloid load. Moreover, they observed greater microglial activation and tau phosphorylation as well at the site of inflammation. Those results suggested that the pro-inflammatory interleukin 1β expression is capable of inducing a beneficial form of neuroinflammation and potentially assisted in reducing the pathology in transgenic mouse models by recruiting protective neutrophils and scavenging the misfolded protein in APP/PS1 mice.

In Alzheimer's disease, most chemokines (e.g. CCL2, CCR3 and CCR5) are reported to be upregulated in reactive microglia, while CCL4 are found in reactive astrocytes that surrounding the amyloid deposition (Ishizuka *et al.*, 1997; Xia *et al.*, 1998). In response to Aß simulation, overexpression of CCL2, CCL3, CCL4 and CXCL8 (i.e. interleukin 8) were observed in human macrophages and reactive astrocytes *in vitro* (Smits *et al.*, 2002). In the post-mortem microglia culture from AD brains, a range of chemokines were generated by post-mortem microglia after exposure to Aβ, including CXCL8, CCL2 and CCL3 (Fiala *et al.*, 1998; Lue, Walker & Rogers, 2001). *In vivo*, CX3CR1 knockout mice were protected from neurodegeneration (Fuhrmann *et al.*, 2010), suggesting that the CX3CR1 signal deficiency modulates the capacity of phagocytosis in reactive microglia and enhances the clearance of Aβ deposition in AD (Lee *et al.*, 2010b). In contrast, the CCR5 knockout mice showed impairment of long-term memory and spatial memory. Compared with wild type mice, CCR5 -/- mice demonstrated significantly higher expression of GFAP and CCR2, indicating the deficiency of CCR5 may lead to astrocyte activation and CCR2 expression, which results in amyloid accumulation and memory deficiency (Hwang *et al.*, 2016; Lee *et al.*, 2009). Additionally, over-expression of CCL2 in cell culture or transgenic mice model demonstrated modulation of toxic cytokine production in activated astrocyte (Semple, Frugier & Morganti-Kossmann, 2010). In microglial cells, the over-expressed CCL2 was found to accelerate the amyloid oligomers generation by facilitating Aβ uptake, intracellular oligomerization and protein secretion, and eventually led to deficits in spatial and working memory (Kiyota *et al.*, 2009). Those findings proved

that inflammatory mediators are capable of altering the course of disease by interacting with reactive microglia and astrocytes.

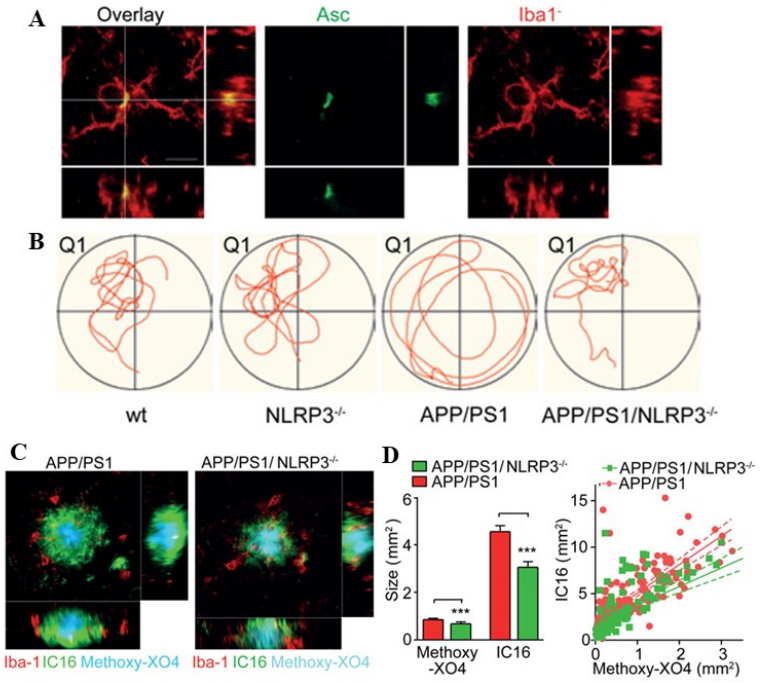


Figure I-6. NLRP3 gene deficiency increases microglial Aβ phagocytosis and shows protective effects in APP/PS1 mice on memory and behaviours.

*A) Immunohistochemistry of microglia from APP/PS1 mice for Iba1 (red) and Asc (green), which is an apoptosis-associated inflammasome component. Bar= 10 µm. B) Representative runs. C) Representative micrographs from methoxy-X04-treated APP/PS1 and APP/PS1/NLRP3−/− mice stained for Iba-1 and Aβ. D) Average IC16-positive Aβ plaque size, determined by co labelling with methoxy-X04, was markedly reduced in APP/PS1/NLRP3−/− mice (n=150, *** p<0.001). A scatter blot of all plaques that was analysed by linear regression (R^2=0.5588 for APP/PS1 and R^2=0.4431 for APP/PS1/NLRP3−/− mice). (M. Heneka Nature. 2013 Jan 31; 493(7434): 674–678.) (Appendix 1. Permission Table)*

Caspases are intracellular proteases that modulate apoptosis and inflammation. When infection occurs, Caspase-1 is activated by inflammasomes (e.g. NRLP3) autocatalytically, which subsequently leads to activation of interleukin 1β and interleukin 18 by cleaving the inactive precursors (van de Veerdonk *et al.*, 2011). In patients with AD and APP/PS1 mice model, active caspase-1 was found significantly elevated compared with healthy brains. The NRLP3 inflammasome was found to be associated with tissue damage and innate immune response to Aβ accumulation via lysosomal damage. NRLP3 inflammasome was also essential for recruiting microglia to the site of Aβ plaques. (Halle *et al.*, 2008) Deficiency of NLRP3 or caspase in

APP/PS1 AD mice demonstrated reduction of brain caspase-1, interleukin-1β and Aβ; and were found mostly spared from impairment of memory function and hippocampal synaptic plasticity. It suggested that NLRP3 deficiency may shift the activation phenotype of microglia from pro-inflammatory to anti-inflammatory. In mouse models of AD, the utilizing of activated caspases inhibitors were reported successfully protecting the hippocampus from neurodegeneration and improved cognitive function (Biscaro *et al.*, 2012; Rohn *et al.*, 2009). (Figure I-6)

In summary, mounting evidences in pathological, epidemiological, *in vivo* animal and human imaging studies have demonstrated the relevance of neuroinflammation in neurodegenerative disease pathogenesis. It has demonstrated that activated microglia were found clustering around amyloid deposition, which disrupts the microglial function by impairing phagocytosis mechanism and over-expressing pro-inflammatory mediators. The heterogeneity of glial cell behaviour in neurodegenerative disease need to be explored *in vivo*. Therefore, in neuroimaging field, there is an unmet need for detecting brain glial activation *in vivo* in human brains.

I-3. MAGNETIC RESONANCE IMAGING

Magnetic Resonance Imaging (MRI) is a non-invasive medical imaging technique, which uses the spin properties of the nuclei and protons, hydrogen nuclei in particular, to generate a high-resolution structural imaging of the brain's anatomy. (Figure I-7)

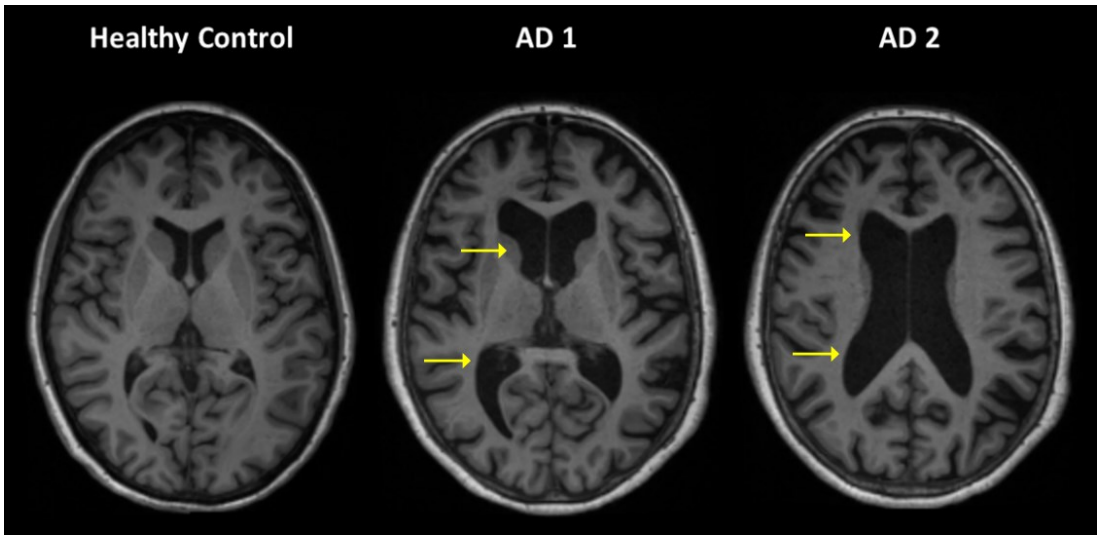


Figure I-7. MRI images in healthy control, and two AD patients with severe brain atrophy (yellow arrows).

Up to 70% of the human brain is composed of water (Forbes, COOPER & MITCHELL, 1953), which allows MRI to map the water and fat distribution. An MRI scanner contains a magnet, which provides strong external magnetic fields that force the spin hydrogen nuclei in water to align in the same direction with the natural precession frequency of a spin, called Larmor frequency. Larmor frequency is determined by the gyromagnetic ratio (i.e. mechanic and magnetic properties of the nucleus) and strength of the magnetic field in Tesla (T). Then a short burst of radiofrequency (RF) pulse is sent to the scanning field. Those radio waves disrupt the equilibrium and cause the hydrogen proton to jump to the high energy level. This is known as excitation. For a given RF intensity, the spins are no longer aligned, and instead they shift the magnetic moments away from for a pulse angle (e.g. 90 degree), which is based on the duration of the RF pulse. When the external radio waves are switched off, the spins start to realign and return to their equilibrium phase at the Larmor frequency. This process of transition back to the equilibrium is called relaxation. During the relaxation, the same amount of spins jumps back to low energy level and emit certain amount of energy which can be picked up by MRI energy receivers. Since these relaxations are distinct across various types of tissues, the retrieval of signals provides not only the location information of the protons in the brain, but also indicates different types of tissue in the brain due to various magnetic gradients. (Dale, Brown & Semelka, 2015)

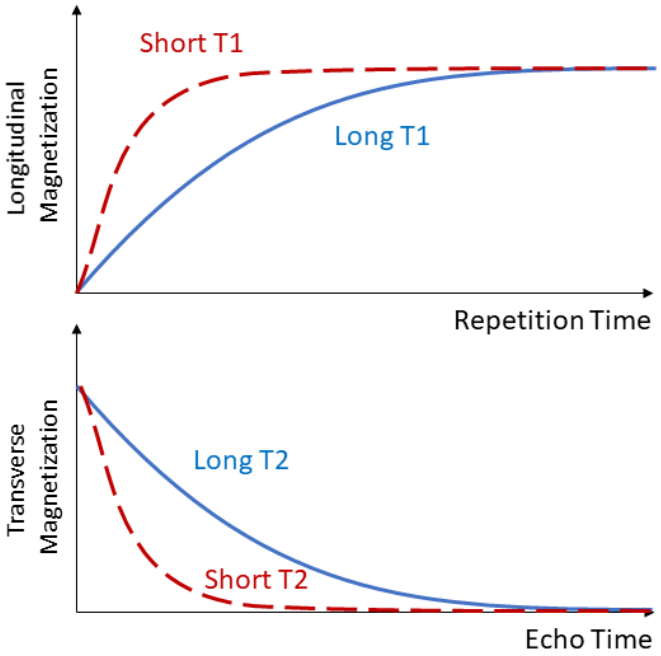


Figure I-8. T1 and T2 MRI.

In T1-weighted MRI (upper panel), tissues with short T1 recover more quickly than those with long T1's, thus they show higher signal intensity and appear brighter than long T1's. In T2-weighted MRI (lower panel), substances with short T2 decay very rapidly, thus they have lower signal intensity and appear darker than the long T2's.

The relaxation does not occur immediately after the cease of the excitation pulse, instead, the length of the relaxation time depends on the local conditions of the excited protons. In MRI, both the spin-lattice T1 (longitudinal) and spin-spin T2 (transverse) magnetic field relaxation time are measured when the spins return to the equilibrium state. T1-weighted images reflect the relaxation time for protons' spins realigning with the main magnetic field longitudinally, which tend to have short echo time (ET) and repetition time (TR) (Figure I-8). In this case, fatty tissue realigns with the magnetic field quickly, therefore demonstrates high signal and appears bright in T1-weighted image, while water reaches the realignment state much slower, which leads to low signal and dark appearance. Thus, T1-weighted MRI provides good contrast imaging for cerebral cortex and general brain anatomy information. On the contrary, T2-weighted images refer to the difference of the protons' spins decaying from their aligned precession in the transverse plane, which tends to have long ET and TR. The T2 relaxation time depends on the pure inherited tissue molecular interactions and the external variations, such as magnetic field inhomogeneity. Fluids with few

macromolecules have a long T2 time that appear bright on T2-weighted images, whereas the relaxation rate of the tissue are much faster, which leads to a short T2 time which appears less bright. Therefore, T2-weighted images are generally used to visualize the atrophy and white matter lesions in the brain. Combining the use of T1 and T2 weighted MRI images, MRI technique provides a high-resolution structural imaging of the brain. (Dale, Brown & Semelka, 2015; Tofts & John Wiley & Sons, 2003)

Diffusion tensor imaging (DTI) is another popular MRI technique applied in brain imaging research, which provides visualization and quantification of white matter tracks in three dimensions. It estimates the fractional anisotropy (FA) index of water motions in each voxel by measuring diffusion in multiple directions, and using tensor decomposition to extract the motions of parallel or perpendicular to the fibres. The FA values demonstrates the intensity between zero and one, where high FA represents that diffusion occurs highly restricted along one direction (e.g. corpus callosum), whereas zero FA means the diffusion is isotropic and equally restricted in all directions (e.g. grey matter). While DTI provides an efficient technique to detect white matter lesions, inherent limitations of partial volume effect and questions with non-Gaussian diffusion in white matter are constantly debated. However, DTI indeed provides comprehensive *in vivo* white matter mapping, and widely used along with functional brain imaging in neurodegenerative diseases. (Assaf & Pasternak, 2008)

I-4. POSITRON EMISSION TOMOGRAPHY

4.1. PET Basis

Positron Emission Tomography (PET) is a nuclear imaging technique that allows visualisation and quantification of functional changes *in vivo* in the body by a positron labelled radioactive tracer (Rahmim, Qi & Sossi, 2013). The positron emission detection system was first introduced in the 1950s. It evolved continuously for a half century in improving its configurations in acquisition mode capability and producing a wide variety of transmission scanning arrangements with different radioactive sources. For instance, the transmission scans (e.g. CT scan) can be acquired before, during or after a PET scan, which contribute in the data reconstruction (e.g. attenuation correction) by providing the anatomical localization of the brain (Bailey, 1998). The PET imaging

system has now been substantially enhanced with sensitivity and resolution for the image quality. The PET technology has been widely applied in both academia and industry for clinical diagnostic imaging, clinical trial research and drug development.

In a modern clinical imaging PET scanner, a PET scan is normally combined with a CT scan. After the acquisition of a CT scan, PET emission acquisition starts with the intravenously injection of radioactive PET tracer, which travels across the BBB into the brain. Positron is emitted from the tracer, and travels a short distance. When it meets an electron, annihilation occurs and usually generates two gamma rays, each of 511 KeV energy, at an almost perfect 180-degree angle. This is known as the line of response (LOR). The ring of detectors in PET scanner captures the gamma rays and estimates the LOR within a very narrow time-window (in nanoseconds), which determines the location of the annihilation event, and hence monitors the distribution of the radioactive tracer in the field of view (FOV) during the PET scanning. (Figure I-9)

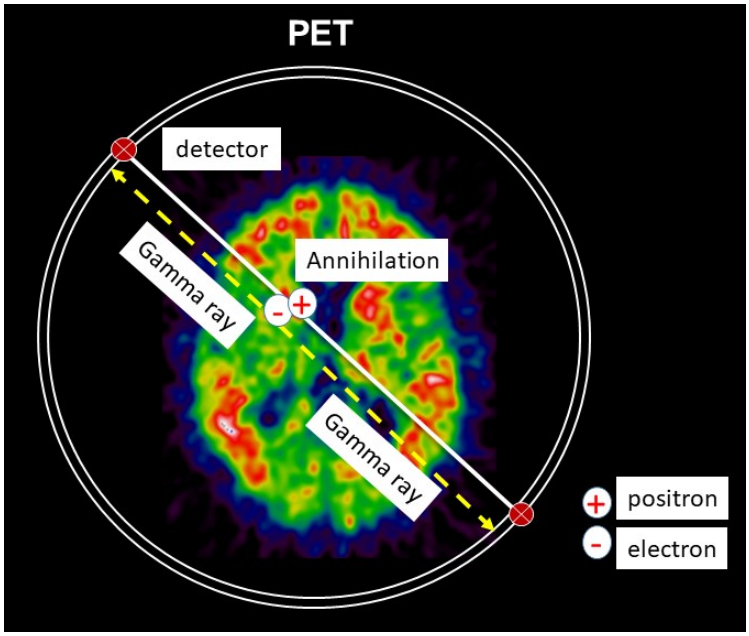


Figure I-9. Schematic diagram of PET imaging.

Annihilation occurs when a positron meets an electron, and usually generates two gamma rays (each of 511 KeV energy) at 180-degree angle. Then the ring of detectors in PET scanner captures the two gamma rays to estimate the location of annihilation.

4.2. PET Corrections

A valid coincident event, known as prompt event, requires 1) two photos to be detected within a predefined electronic coincidence time window, 2) the line-of-response to be

formed within a valid acceptance angle, and 3) the energy deposited is within a selected energy window. Among all prompt events that satisfy the above criteria, there are true coincidences, but there are also some unwanted coincidences. Those accidental events could be due to various reasons: 1) scattered events, where the photon undergoes a Compton scattering, which causes loss of energy in the photon and changes the direction; 2) random coincidence, where unrelated random photons from different annihilations are detected; 3) multiple events, where three photons from two separated annihilations are detected within the time window. With appropriate corrections applied, the prompt count rate can be calculated by the sum of true event rate plus the corrected scatter and random event rates. Eventually, the corrected signals (true coincidences) generate a PET image, which demonstrates the distribution and concentration of radiotracers in the brain *in vivo*. (Bailey, 2005)

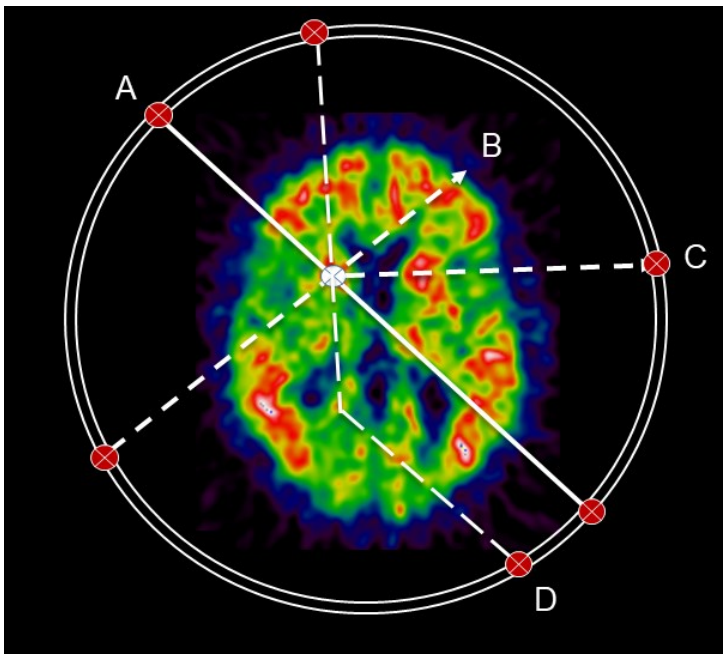


Figure I-10. PET coincidence.

A) True coincidence B) Attenuation C) Random coincidence and D) Scattered coincidence.

Physical corrections are necessary to calibrate the PET data and allow the absolute quantification of the accurate coincidence within the FOV. Four main types of corrections are involved, attenuation, dead-time, randoms and scatter correction (Figure I-10). Attenuation correction corrects the attenuation of the signal when gamma rays are scattered outside the angle of detective FOV before being received by the PET

detector. Signal attenuations in humans can significantly reduce the gamma ray detection by 50-75%. Therefore, without such corrections, there is a significant amount of signal variation across the FOV, typically in the centre where the lowest signal intensity is revealed. A CT scan is therefore used for the attenuation correction. It provides a contrast image of the body and compensates the loss of activity in the PET image, especially in the centre where attenuation is more likely to take place.

4.3. Principle of PET Tracers

In clinical research and clinical practice, biomarkers are widely used to reveal the disease progression and treatment response. PET tracer is an imaging biomarker, which designed for specific functional processes, where a chemical compound of interest is labelled with positron emitters, such as ^{18}F, ^{11}C and ^{15}O. In PET instrumentation (Bailey, 2005), all three principles of radiotracer are perfectly met:

1. The PET tracer is in trace quantities and will not alter or perturb the system.
2. The interaction between the PET tracer and the system is predictable, informative and reproducible.
3. The PET tracer concentration allows absolute quantification.

The radioisotope is generated by a particle accelerator called a cyclotron, which accelerates the charged particle to a high velocity. Depending on what positron emitting isotope is needed, different target gas mixture is placed in the reaction vessel (e.g. Nitrogen+0.1% Oxygen), which reacts with the accelerated particle. The most common isotopes used in PET tracer labelling are ^{11}C, ^{18}F or ^{15}O, which substitutes the carbon, fluorine or oxygen in the chemical substrate of interest. Considering the isotope decays, the chemical reactions of attaching the isotope onto the substrate should be performed in a timely manner, especially for those labels with a very short half-life (e.g. ^{15}O= 2.03 min half-life and ^{11}C = 20.38 min half-life).

4.4. Tracers for Glial Activation

The 18-kDa translocator protein (TSPO) is a cholesterol-transporter protein expresses in the outer membrane of mitochondria on microglial cells and astrocytes in the brain (Gatliff & Campanella, 2016). Translocator protein expression in normal brain is very low but it increases dramatically during glial activation after brain injury and

inflammation (Dickens *et al.*, 2014; Su *et al.*, 2013). Therefore, TSPO PET tracers were generated for detecting microglial activation *in vivo*.

The first generation TSPO PET tracer [^{11}C](R)PK11195 has been used for over 30 years to assess the level of microglial activation *in vivo* (Charbonneau *et al.*, 1986). However, [^{11}C](R)PK11195 was found not only binds to TSPO, but also binds to other structures within the brain, such as endothelial tissue and smooth muscle (Turkheimer *et al.*, 2007). Due to the poor signal-to-noise ratio (Dickens *et al.*, 2014), there is a urgent need for developing new TSPO tracers with minimal non-specific binding. More selective radioligands were developed as second generation of TSPO tracers, such as [^{11}C]PBR28, [^{11}C]vinpocetine, [^{11}C]DAC, [^{11}C]DAA1106, [^{11}C]N1-methyl-2-phenylindol-3-ylglyoxylamide and [^{11}C]CLINME (Chauveau *et al.*, 2008; Vivash & OBrien, 2016). Since carbon 11 has a short radioactive half-life of 20 min, the need for an on-site cyclotron limits the use of these tracers. Therefore, fluorine 18 labelled TSPO makers have been developed, such as [^{18}F]GE180, [^{18}F]FEPPA, [^{18}F]FEDAA1106, [^{18}F]DPA-713, [^{18}F]DPA-714 and [^{18}F]PBR06 (Dickens *et al.*, 2014).

New generation of TSPO tracers have demonstrated promising results in preclinical studies (Wadsworth *et al.*, 2012; Dickens *et al.*, 2014); however, most of those tracers failed to reproduce similar results in human trails. This may be due to three confounding factors which human brain suffers when applying second-generation TSPO tracers. Firstly, binding affinity of the most newly developed TSPO tracers in human brain are affected by the TSPO genetic variability (Owen *et al.*, 2011b). The genetic variability of TSPO binding site associates with the single-nucleotide polymorphism (SNP) rs6971 (Owen *et al.*, 2011b). In preclinical models, the high-affinity binders (HAB) have 40-50% increase in binding affinity compared to mixed affinity binders (MAB), while low affinity binders (LAB) are unsuitable for evaluation (Owen *et al.*, 2011a, 2014), which is also true in humans. Secondly, like many other neuroreceptor ligands used in PET, the high variability in the subject's plasma free fraction leads to difficulty in providing an accurate and reliable f_p (plasma free fraction) measurement for TSPO tracer (Fan *et al.*, 2016). Lastly, TSPO signals in human brain are found in the venous sinuses, endothelial cells of the blood brain barrier, and the brain tissue; therefore, apart from developing more selective tracers, it is also critical to account for the signal dispersion if high signal contamination is observed from the peripheral area of blood vessels.

Similar to microglial activation, researchers found that I2-imidazoline binding site (I_2BS) is significantly upregulated on the mitochondrial membrane in activated astrocytes (Tyacke *et al.*, 2012). In recent years, novel PET tracers were developed to target I_2BS expression in the brain for distribution of astrocyte reactivity. *In vitro*, [^{11}C]BU99008 tracer demonstrated a good penetration of the blood-brain barrier and showed a high binding affinity for the I_2BS expression (Tyacke *et al.*, 2012). By applying [^{11}C]BU99008 PET *in vivo*, a good contrast was found between region with known expression of I_2BS versus the reference area (Kealey *et al.*, 2013; Parker *et al.*, 2014). Additionally, no genetic variability influence was reported in [^{11}C]BU99008 PET tracer binding.

I-5.THESIS OBJECTIVES AND CHAPTERS

In this work, PET methods were developed and evaluated for two novel TSPO tracers ([^{11}C]PBR28 and [^{18}F]GE180) for microglial activation and one novel I_2BS tracer ([^{11}C]BU99008) for astrocyte reactivity in healthy controls and neurodegenerative disease patients. The pathological influence of glial activation on other biomarkers was evaluated in AD and MCI patients, and the relationship between biomarker interaction and clinical performance was interoperated using novel voxel-level imaging techniques which I have developed as part of my PhD.

There are two major research objectives of this thesis:

1) To determine the optimal modelling approach for novel PET tracers targeting glial activation in human brain in neurodegeneration
2) To develop novel multimodal imaging techniques to account for the complex pathological interactions occurring in AD

In order to achieve these objectives in a logical fashion, the thesis is structured into seven chapters. The thesis starts with the background chapter (CHAPTER I) that aims to provide a general overview of Alzheimer's disease, neuroinflammation, theories of MRI and PET imaging, PET radioligands, and the structure of the this work. This is followed by the methodology chapter (CHAPTER II), which details the basis in imaging acquisition, dynamic quantitative modelling approaches, parametric mapping, neuroimaging analysis, and statistical analysis. After that, three independent PET studies with novel PET tracers targeting microglial and astroglial activation are presented to address the first research goal. Those three pilot studies in AD are set to

explore and evaluate the kinetic modelling and feasibility of parametric mapping of TSPO tracer [^{18}F]GE180 (CHAPTER III), TSPO tracer [^{11}C]PBR28 (CHAPTER IV) for microglial activation and I_2BS tracer [^{11}C]BU99008 PET (CHAPTER V) for astroglial activation in human brain. The second goal of this thesis is to develop novel PET imaging techniques to reveal the biomarker interactions. In CHAPTER VI, the VOI Prediction Tool and Individual Correlation Mapping (ICM) are developed to reveal the biomarker interactions, while Automated Spatial Transformation QC is designed to provide support in imaging analysis using large datasets. The final chapter (CHAPTER VII) summaries the thesis, addresses the limitations, discusses the future directions, and draws the conclusion for the present work.

CHAPTER II. METHODS FOR BRAIN PET QUANTIFICATION

In this chapter, the background of the main method approaches applied in the current thesis are discussed and summarized. This chapter starts with the introduction of compartmental modelling approaches that I evaluated for the novel TSPO and I_2BS PET radioligand. Then four major method approaches in generating the parametric maps for each glial tracer are introduced. After that, the general imaging analysis pipeline, including Region of Interest (ROI) analysis, Statistical Parametric Mapping (SPM) voxel-level analysis and Biological Parametric Mapping (BPM) correlation analysis are discussed. Lastly, the statistical analysis details for this work were illustrated.

II-1. COMPARTMENTAL MODELLING

1.1. Kinetic Models

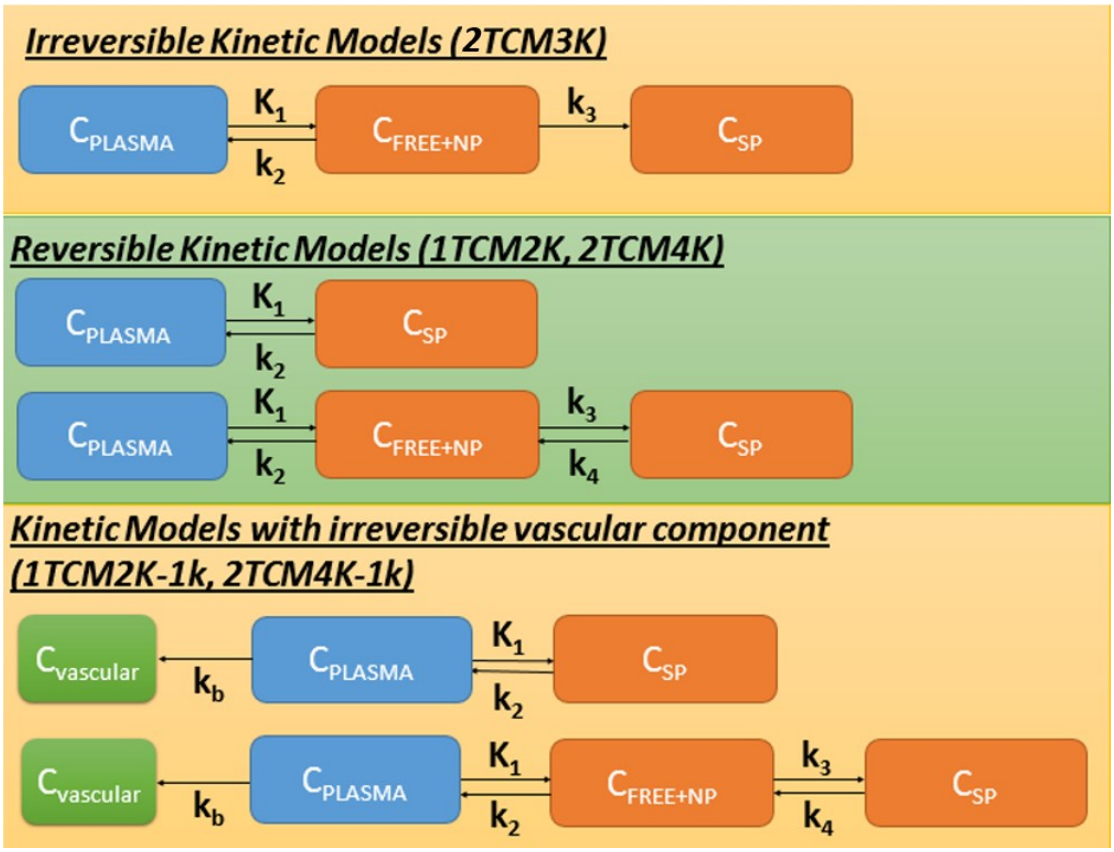


Figure II-1. Kinetic compartmental models

C_{PLASMA} represents the parent tracer concentration in plasma, $C_{FREE+NP}$ represents the concentration of free and non-specifically bound tracer, C_{SP} represents the specifically bound tracer, and $C_{VASCULAR}$ indicates the tracer trapped inside the vascular component. K denotes the rate constant for tracer that travels between different compartments represents the rate constant. For instance, K_1 (mL min^{-1} mL^{-1}) indicates the amount of tracer that travels from the plasma into the first tissue compartment per minute per tissue, while k_2, k_3, and k_4 indicate the fraction of the tracer that travels in-between different compartments, The two-tissue irreversible model (2TCM3k) is displayed on the top panel, one-tissue (1TCM2k) and two-tissue reversible model (2TCM4k) are displayed in the middle, and one-tissue (1TCM2k-1K) and two-tissue reversible model with an extra irreversible vascular component (2TCM4k-1K) are shown on the bottom.

In PET, the mathematical models of the tracer uptake are convolved by input function and output dynamic tissue activity in the PET scan (i.e. time activity curve). Depending on the types of input, either 1) a plasma input model or 2) a reference tissue input model can be used. The plasma input model is often regarded as a quantification golden

standard method. It estimates the tracer activity concentration in plasma due to un-metabolised parent compound by monitoring the radioactivity in the arterial blood during the scan. Whereas the reference tissue input model requires a proper reference region that is free of specifically bound tracer. An ideal reference tissue is a region 1) with no specific uptake of the radioligand; 2) or the radioligand uptake is independent of the disease progression or treatment, 3) or the non-specific binding in that region is similar to the target region (region of interest). To explore the optimal quantification method for the novel PET tracer kinetics, mainly five compartmental models with plasma input model were investigated in this thesis (Figure II-1). The one-tissue reversible model (1TCM2k), two-tissue reversible model (2TCM4k), and two-tissue irreversible model (2TCM3k) were evaluated, where k denotes the rate constant for tracer that travels between different compartments. Due to the fact that TPSO tracers also bound to BBB endothelial cells, the kinetic modelling can be significantly influenced by the endothelia binding. Thus, I have also considered the one-tissue and two-tissue compartmental models with extra vascular component (1TCM2k-1K and 2TCM4k-1K) for TSPO tracers ([^{18}F]GE180 and [^{11}C]PBR28). The extra component represents the tracer that is trapped by the endothelial cells of blood vessels.

Additionally, Multilinear Analysis 1 (MA1) component model was tested for the [^{11}C]BU99008 PET tracer (Parker *et al.*, 2014; Ichise *et al.*, 2002) for astrocyte reactivity, which often regards as an intermediate model between standard one-tissue and two-tissue kinetic model. The MA1 approach is developed as an alternative linear method to Logan graphic analysis (Equation 1), which aims to reduce the noise-induced graphic analysis bias.

Equation 1. Multilinear Analysis 1

$$C(t) = -\frac{V_T}{b}\int_0^t C_p(\tau)d\tau + \frac{1}{b}\int_0^t C(\tau)d\tau$$

Where C(t) denotes the tissue time activity curve, Cp(t) denotes the tracer activity in plasma, V_T is the total volume of distribution and b represents the intercept of the Logan plot which becomes constant after an equilibration time (t*). The t* demonstrates the beginning of the data used in the linear regression analysis. MA1 demonstrated the most pronounced bias improvement when the portion (t*) of the tracer kinetics can be accurately identified within the scan duration.

1.2. Model Selection

The quality of the potential kinetic model fitting is assessed by the Akaike Information Criterion (AIC) for each model (Akaike, 1973; Turkheimer, Hinz & Cunningham, 2003). The AIC statistical quantifies the distance between the candidate model fitting against the real data point by calculating the weighted Residual Sum of Squares (WRSS) for each data point. In simple terms, AIC of each candidate model indicates the information lost from the real data when a candidate model is applied; therefore, the model with the smallest AIC indicates the best data estimation with the minimal information lost, and can be selected as the preferred model to describe the tracer kinetics (Akaike, 1973; Turkheimer, Hinz & Cunningham, 2003). AIC is calculated using the formula below:

Equation 2. Akaike Information Criterion

$$AIC = 2k + n * LN(WRSS)$$

k denotes number of parameters, n equals the sum of degrees of freedom and number of parameters, WRSS denotes weighted residual sum of squares and LN is the natural logarithm ($\log_e$). The AIC fraction was also calculated to measure the frequency of the model preference across all subjects. Wald-Wolfowitz runs test is a non-parametric statistical test that measure the number of residuals that distributed around the model fitting, in order to assess the randomness of data distribution for each candidate model. In the end, the preferable kinetic compartment model with the best fit was used to describe the new tracer binding properties. Total volume of distribution (V_T) and non-displaceable binding potential (BP_{ND}) were estimated by the parameters derived from the kinetic models in MATLAB 2014a using (Innis *et al.*, 2007):

Equation 3. Volume of Distribution

$$V_T = \frac{K_1}{k_2} \times (1 + \frac{k_3}{k_4})$$

Equation 4. Binding Potential (BP_{ND})

$$BP_{ND} = \frac{V_T - V_{ND}}{V_{ND}} = k3/k4$$

In formulae above, k represents the rate constants, which describes the rate of the tracer travels between different kinetic compartments. For instance, in a 2TCM4k model, K_1 (mL min^{-1} mL^{-1}) indicates the amount of tracer that travels from plasma into the first tissue compartment per minute per tissue, while k_2, k_3, k_4 indicate the fraction of the tracer that travels in-between different compartments (Figure II-1). V_T refers to the ratio

between total concentration of tracer in tissue and plasma, while V_{ND} presents the tracer concentration of non-displaceable compartment over plasma. BP_{ND} indicates the ratio of specifically bound tracer to that of non-displaceable tracer in tissue at equilibrium.

II-2. PARAMETRIC MAPPING

The parametric maps are 3-D image generated from dynamic data through different quantification approaches, which allow us to evaluate the imaging data at voxel level. As part of my PhD, based on the tracer properties, I have applied different parametric mapping approaches to the novel TSPO and I_2BS tracers to quantify the reactivity of microglia and astrocytes in neurodegenerative disease.

2.1. Spectral Analysis

Spectral analysis (SA) quantifies the volume of distribution of the reversibly binding ligand using the dynamic tracer concentration in the brain tissue and in plasma. It generates the IRF (Impulse Response Function) parametric maps based on different observation time. Spectral analysis makes no assumptions about tracer kinetics. Instead, it identifies heterogeneous kinetic components based on the spectral peaks that represent tracer delivery, vascular binding, and later parenchymal tracer binding (Cunningham & Jones, 1993; Veronese *et al.*, 2016). In addition, the fact that SA give considerations for all tissue components, including the tracer presents in vascular blood (e.g. signal generated by the tracer activity in blood cells or by tracer bound to the vascular walls) makes the SA an excellent candidate approach to quantify the TSPO tracer distribution (Veronese *et al.*, 2016).

In mathematical details, spectral analysis applies a positively constrained general linear model to fit the tissue kinetics through a large matrix of exponential functions and a range of decaying factors that convoluted with the plasma input function (Veronese *et al.*, 2016).

Equation 5. Spectral analysis

$$C_{tissue}(t) = \sum_{i=0}^{M} \alpha_i * e^{-\beta_i t} \otimes C_{plasma}(t)$$

$C_{tissue}(t)$ and $C_{plasma}(t)$ denote the tracer concentration time course in tissue and parent plasma, respectively. The impulse response function is assumed to be the sum of M+1 exponential functions ($\sum_{i=0}^{M} \alpha_i * e^{-\beta_i t}$). The solution to each fit is a vector of linear

coefficients α_i (peak height), which corresponds to a decay β_i (peak position). Those estimations are obtained via non-negative least squares (NNLS) (Cunningham & Jones, 1993; Turkheimer *et al.*, 1994). Among solution vectors, the non-zero coefficient for the high frequency components (e.g. large β_i) usually reflect the dynamics of the tracer in the blood, the one with slower β_i reflects the kinetics of reversible parenchymal perfusion between plasma or tissue compartments, while the slowest component represents irreversible trapping (Figure IV-1).

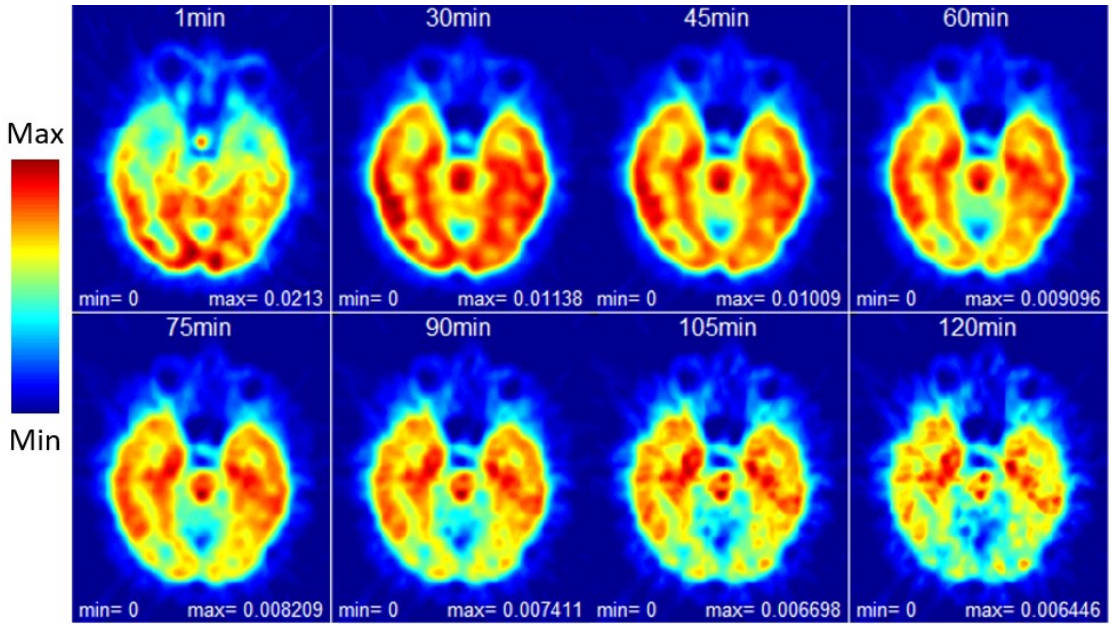


Figure II-2. Illustration of IRF(t) images generated via spectral analysis.

IRF(t) parametric maps were generated for [^{11}C]BU99008 PET at 1 min, 30 min, 45 min, 60 min, 75 min, 90 min and 120 min.

With those substantial advantages, spectral analysis was applied to the [^{18}F]GE180, [^{11}C]PBR28 and [^{11}C]BU99008 PET images to separate the tracer activity into heterogeneous spectral peaks of tracer delivery, vascular binding, and later tissue binding component (Cunningham & Jones, 1993; Veronese *et al.*, 2016). The tracer binding response in tissue can be measured as a portion of impulse response function (IRF), which reflects by the sum of the intermediate and low frequency components of the spectrum (Figure II-2). The IRF(t) parametric maps can be generated with different epochs of observation-time using the formula:

Equation 6. Impulse Response Function

$$IRF(t) = \sum_{i=1}^{n} \alpha_i * e^{-(\beta_i - \lambda)*t}$$

where t represents the selected observation time, n denotes number of PET time frames, α_i and β_i are the peak height and peak position for time frame i. Decay constant λ of 0.00056629 s^{-1} was used for Carbon 11 labelled tracers (e.g. [^{11}C]PBR28 and [^{11}C]BU9908) and 0.00010532 s^{-1} for Fluorine 18 labelled tracer (e.g. [^{18}F]GE180). Spectral analysis is a powerful approach, therefore its solution to each component fit is highly sensitive to the pre-defined parameters, such as beta minimal, beta maximal, and number of the basis function. In this work, the initial set of parameters tested for the novel tracers were βmin=decay constant λ, βmax=0.1 and 100 basis functions. Numbers of exponential curves were predefined and implanted as the candidate interpolating curves which presented within the λ and 0.1 (see above equation). Those candidate models were then tested against the real data points and solved by the non-negative least-squares (NNLS) curve fitting. Subsequently, only a few components with non-negative α are selected by NNLS, which composites the kinetic spectrum of the tracer. Visual assessment was necessary for model fitting evaluation between different sets of parameters, as higher number candidate models normally ends up with a better fit (e.g. NNLS), but it may over fit the model (e.g. noise). Therefore, the adjustment of parameters in spectral analysis was required for quantifying novel tracers (e.g. 100-1000 basis function) (Veronese *et al.*, 2016).

The IRF(t) parametric maps generated with different observation time was compared according to the coefficient of variation (CV) of tracer binding in major cortices (frontal, temporal, parietal and occipital lobe) and subcortical regions.

Equation 7. Coefficient of variation

$$\boldsymbol{CV}\ (\%) = \frac{\boldsymbol{Standard\ Deviation}}{\boldsymbol{Mean}} \times \mathbf{100\%}$$

The lower CV indicates a higher precision and lower noise level for that IRF(t) parametric map (Fan *et al.*, 2018). Repeated ANOVA was performed on different IRF parametric maps to assess the within-participant variation (SS_W), which can be further divided to variance explained by the observation time (SS_M) and variation due to extraneous factor (SS_R). Then F-ratio was estimated to present the ratio of variances for a repeated-measures and determine whether means are equal:

Equation 8. F-ratio

$$F = \frac{SS_M/df_M}{SS_R/df_R}$$

df_M and df_R denote the degree of freedom of those two variances. The sensitivity of differentiating tracer distribution in patients compared to healthy controls was evaluated and taken into account for selecting the most appropriate IRF parametric maps.

2.2. Graphic Analysis

Graphical analysis is a popular approach to generate parametric maps for dynamic PET images with either reference input function or arterial blood input function. Based on the nature of the tracer, Logan or Patlak plot can be applied for reversible or irreversible tracer, respectively. In Logan plot, where ligands travel reversibly from the specific component, the graphical quantification approach linearizes PET uptake data using the plasma input or non-specific tissue reference input, and produces the tracer V_T. For irreversible tracer, Patlak plot is used to describe the tracers that are irreversibly trapped in the tissue compartment and produce the net influx (Ki). The slope of the linear section of the graphic plot that represents V_T or Ki, can be used to generate the parametric maps at a voxel level (Logan, 2000). In theory, graphic analysis is independent of the number of compartments as long as they are all in equilibrium after a time t*, which is the optimal threshold time (Equation 9).

Equation 9 Logan analysis

$$\frac{\int_0^t ROI(t')dt'}{ROI(t)} = (V_T + V_p)\frac{\int_0^t C_p(t')dt'}{ROI(t)} + int$$

Where V_p denotes the regional blood volume, ROI(t) represents the tissue activity, and Cp(t) represents the plasma activity. The slope of the linear plot after an equilibration between $\frac{\int_0^t ROI(\tau')d\tau'}{ROI(\tau)}$ and $\frac{\int_0^t C_p(\tau')d\tau}{ROI(\tau)}$ demonstrates the sum of volume of distribution and regional blood volume. The *int* presents the intercept for the linear part of the Logan plot after t*.

As a popular and simple linear quantification method, graphic analysis has been applied to generate Logan V_T parametric maps in this thesis. The graphical analysis was performed using MIAKAT software developed by Invicro (used to be Imanova) based on MATLAB (MathWorks, USA). The regional V_T and coefficient of variation were

measured in major cortices and thalamus to assess the signal variation for the Logan V_T maps with different t*. The MIAKAT produces dynamic linear plot for different time t*, therefore, a visual assessment was performed to assist the selection of the t* for Logan V_T.

2.3. Reference Model

2.3.1 Reference input model

An alternative approach to the arterial input function is to propose a reference region with non-specific tracer binding, which is called the reference tissue input model (Gunn *et al.*, 1997; Schuitemaker *et al.*, 2007; Tomasi *et al.*, 2008; Blomqvist, 1984; Lammertsma & Hume, 1996). The simplified reference tissue model (SRTM) assumes K_1/k_2 is the same for the target tissue and reference tissue, and follows the equation below:

$$C(t) = R_1 C_R(t) + \left[k_2 - \frac{R_1 k_2}{1 + BP_{ND}}\right] C_R(t) \otimes e^{-\frac{k_2}{1+BP_{ND}}t}$$

Where Ct represents the tissue activity, R_1 denotes the ratio of tracer delivery (K_1/K_1'), k_2 represents the transfer of tracer from tissue back to the plasma, BP_{ND} presents the binding potential quantifies the equilibrium concentration of specifically bound radioligand to that of non-displaceable radioligand in tissue.

Compared with arterial input function, reference input model is much less invasive and provides a simple measurement of tracer binding ratio in relative to the non-specific reference region. For a novel PET tracer quantification, reference input model is always worth to investigate as it massively reduces the cost and invasiveness of the scan (e.g. Standardized Uptake Value Ratio), which benefits both the sponsors and patients. The reference model requires a reference region which is ideally free of specific binding. For instance, the cerebellum is used as the reference region for amyloid deposition and tau pathology. In order to seek a possible reference region, the time activity curve and volume of distribution in patients and healthy controls are compared to investigate possible candidate reference regions, which should contain relatively low level of tracer activity and free of pathological binding, namely no biological difference between patients and healthy controls.

2.3.2 Supervised Cluster Analysis

Apart from anatomical reference region, the reference tissue kinetics from dynamic PET scans can be extracted by the data driven methods, cluster analysis. In general, the clustering method uses centroid-based analysis to define a cluster according to the closest mean and the minimal within-cluster sum of square (WCSS) algorithm. The supervised clustering method to extract the reference region was firstly introduced in 2000 by Chen et al. (Chen J, Gunn S, Nixon M, Myers R, 2000), and was used in [11C](R)PK11195 quantification. Instead of clustering the data in a data-dependent manor (generalised), supervised cluster analysis segments the dynamic data according to a set of six physiological related predefined kinetic classes (SVCA6), including pathological binding, non-specific binding in grey matter, non-specific binding in white matter, blood pool, skull and muscle. Those predefined classes are normally derived from a historical database of healthy controls and disease condition. Boellaard et al. modified the method (SVCA4) by reducing six kinetic classes to four: grey matter with specific binding, grey matter without specific binding, white matter and blood by removing bones and soft tissue with a prior mask (Boellaard *et al.*, 2008). Normalization for each time frame in the dynamic sequence is estimated by subtracting the mean and then dividing by the standard deviation. The total TAC equals to the sum of all scaled kinetic classes. The non-negative least squares interpolation is applied to estimate the scaling coefficient for each class. The fitting with the least residual square between interpolated value and actual measurement is selected as the optimal.

2.3.3 Ratio imaging of amyloid, tau and glucose metabolism

As mentioned above, the reference input model is used to quantify the amyloid and tau uptake. In this work, the amyloid status was assessed using cerebellum (grey matter) RATIO image of [^{18}F]Florbetaben or [^{18}F]Flumetamol PET. In detail, the 60-90 min PET frames were firstly summed to generate a summed image. The RATIO image was generated by divide the summed image to the regional tracer uptake in cerebellum, which can be calculated in Analyze 11.0 (Bullich *et al.*, 2017; Catafau *et al.*, 2015; Lowe *et al.*, 2017). Currently, the definition of amyloid positivity was normally based on visual reading of the amyloid image, but it may cause variation due to the experience of the reader (Selkoe & Hardy, 2016; Fagan, 2015; O'Sullivan & Vann, 2016; Ossenkoppele *et al.*, 2015). In order to ensure the consistency across different

independent studies in my PhD, along with visual assessments, extra criterion are accounted to qualify an amyloid-positive subject in my work: 1) having uptake in at least one of the large cortices or two separate cortical regions higher than the mean+2SD of healthy controls at regional level (CHAPTER II.3.1); and 2) showing clusters with significant uptake at voxel-level (CHAPTER II.3.2) (Johnson *et al.*, 2013; Ossenkoppele *et al.*, 2015).

In astrocyte study (CHAPTER V), the RATIO image of [^{18}F]FDG was created using the pons as the reference region for glucose metabolism. The RATIO images were generated in Analyze 11.0 by dividing the original static [^{18}F]FDG PET images by the mean tracer activity in pons (Singh *et al.*, 2015; Lowe *et al.*, 2009). In the clinical application for the novel techniques (CHAPTER VI), [^{18}F]AV1451 PET was applied to assess the tau deposition in the MCI and AD patients. Similar to amyloid deposition, the 80-120 min time frames were summed and cerebellum grey matter was used as the reference region for the [^{18}F]AV1451 RATIO image (Firouzian *et al.*, 2018).

2.4. Standardized Uptake Value

Last but not least, to investigate whether a simplified quantification method is capable to perform as well as arterial input for the novel TSPO and I_2BS tracers, Standardized Uptake Value (SUV) was performed (Fletcher & Kinahan, 2010; Yoder *et al.*, 2015). SUV images demonstrated the tracer distribution throughout the body for each individual, by normalizing the total amount of tracer administration and individual's body weight. Therefore, SUV image can be generated by PET summed image without the arterial input, using the following formula:

Equation 10. Standardized Uptake Value

$$SUV = \frac{PET\ summed\ Image\ (kBq/ml)}{Tracer\ injected\ dose\ (MBq) \Big/ Body\ Weight\ (kg)}$$

II-3. IMAGE ANALYSIS

3.1. ROI Analysis

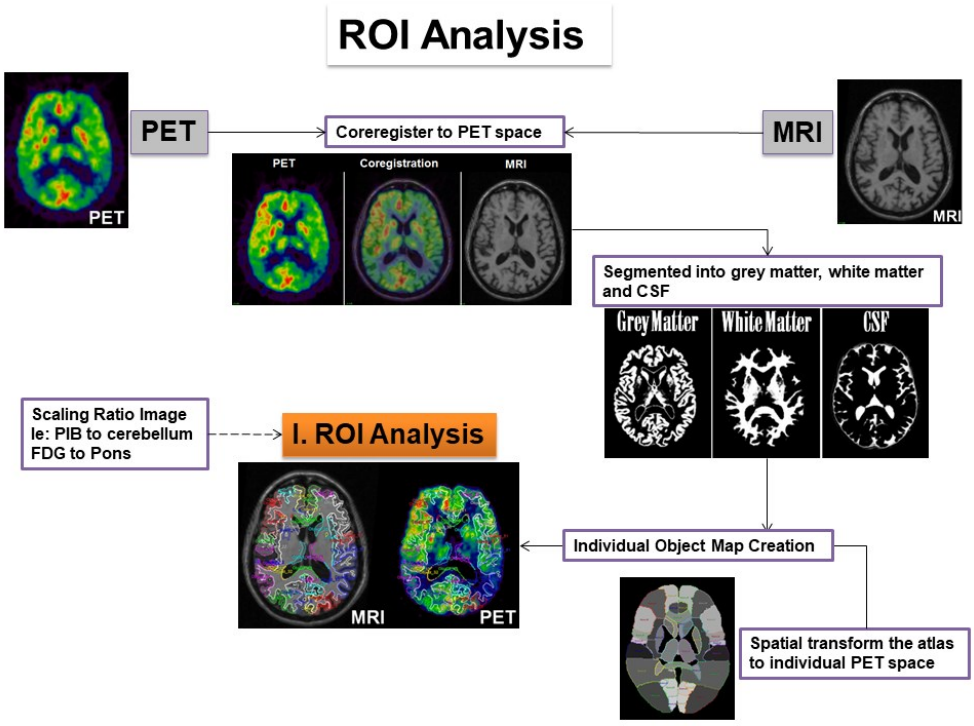


Figure II-3. Schematic representation of the ROI analysis using SPM

The MRI is firstly co-registered to the static PET static image. The co-registered MRI is segmented into grey matter, white matter and CSF. The probabilistic ROI atlas in MNI (Montreal Neurological Institute) space is transformed into native PET space. The grey matter MRI is multiplied by ROI atlas to generate an individual grey matter masked atlas. Lastly, the regional mean activity is estimated by applying individual atlas to the PET data (ROI analysis).

Region of interest (ROI) quantifies the average tracer binding in specific regions. It was estimated for compartmental model V_T, SA parametric map (IRF), Logan V_T map, RATIO images and SUV images for regional activity. To evaluate the regional binding, MRI and brain atlas (83-reigon Hammersmith atlas) were spatially transformed into native PET space using Statistical Parametric Mapping version 2008 (SPM8); and subsequently Analyze 11.0 (AnalyzeDirect, Inc) was used to sample the regional mean activity in predefined ROI regions as described in our previous studies (Fan *et al.*, 2015b, 2014, 2017) (Figure II-3). In this work, an individualized brain atlas (object map) in PET space was generated using the following procedure: 1) MRI was co-registered to the static PET static image (e.g. parametric map); 2) The co-registered

MRI was then segmented into grey matter, white matter and CSF; 3) the probabilistic ROI atlas in MNI (Montreal Neurological Institute) space was transformed into native PET space; 4) lastly, the grey matter MRI was multiplied by ROI atlas to generate an individual grey matter atlas.

In dynamic PET images, head motion was firstly corrected using the frame-by-frame realignment tool in SPM8. Based on the tracer distribution, one frame from the dynamic PET data was selected as the reference frame, and all other frames were realigned to the reference frame. In particular, if there were two separate scans, such as [^{18}F]GE180 PET study, the realignment also re-aligned the second scan to the first scan. With the individual ROI atlas, the ROI time activity curves (TACs) were generated by sampling the regional mean in each frame of the dynamic PET image. In general, the merging regions (grey matter): frontal, temporal, parietal, occipital lobes and whole brain and smaller brain structures: posterior cingulate, thalamus, brainstem, whole medial temporal lobe, hippocampus, and cerebellum were sampled.

3.2. SPM Analysis

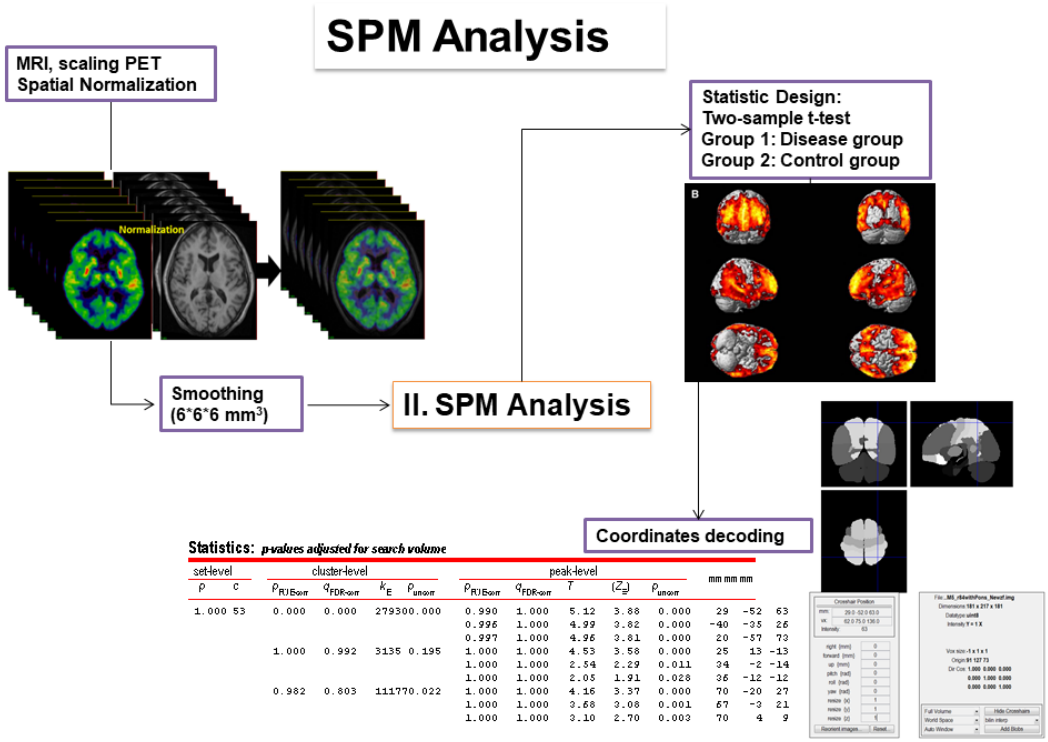


Figure II-4. Schematic representation of the SPM analysis at voxel-level

The 3D parametric maps or static PET images are firstly co-registered to their corresponding MRIs, and then normalized and smoothed in MNI space. A voxel-level comparison between disease and control groups can be performed using two-sample t-test (e.g. Group 1. Disease and Group 2 Control group) using SPM8. After setting up the threshold for the significance (e.g. threshold of p<0.05 with an extend threshold of 50 voxels), SPM8 generate a statistic table to present all clusters with significant changes (e.g. p values, Z-score, and coordinates), and a colour-coded render image to show the significant clusters.

Parametric maps generated by different quantification methods allowed to perform voxel-wise image statistical comparisons between patients and healthy controls (Figure II-4). In SPM8, parametric maps were firstly co-registered to their corresponding MRIs, and then normalized and smoothed (6mm x 6mm x 6mm) in MNI space. As a result, the voxel-level group comparison between patients and healthy controls were performed using group t-test in SPM8. On the individual basis, each patient's normalized PET image was compared against a group of healthy controls to generate a single subject SPM T-map using one-way ANOVA, which presents the significant pathological changes for each patient at voxel basis. Based on different tracer distributions, different thresholds were selected for cluster significance with the lowest

acceptable threshold of $p<0.05$ with an extend threshold of 50 voxels. In general, I started with a cluster threshold at $p<0.01$ with an extent threshold of 200 voxels, and adjusted the threshold accordingly due to the specific tracer distribution. Individually, when there were clusters with significant pathological changes in patient brain compared with the healthy controls, those significant VOI clusters (volume of interest) were extracted and calculated for the total volume in mm3 using Analyze 11.0 (AnalyzeDirect, Inc.).

3.3. BPM Correlation

Neurodegenerative diseases are characterised by multiple pathologies. In order to evaluate the relationship between different pathologies at voxel-level, the Z-score map (Zmap) of different PET modalities were generated to present the individual level of microglial activation, astrocyte reactivity, glucose metabolism and amyloid deposition in relation to the healthy controls' mean and variance (standard deviation). The individual Z-score map (Zmap) of each PET tracer (x) were generated using following formulae:

Equation 11. Individual Z-score Map

$$Individual\ Zmap\ \text{of}\ x = \frac{Patient\ of\ x - mean\ (healthy\ controls\ of\ x)}{SD\ (healthy\ controls\ of\ x)}$$

By applying individual Z-score maps for each biomarker, the voxel-level correlation between microglial activation, astrocyte reactivity, glucose metabolism and amyloid deposition can be estimated via BPM toolbox developed in MATLAB (Casanova *et al.*, 2007). BPM toolbox uses the general linear model (GLM), which has been widely used in SPM framework, to perform voxel-wise regressions on different image modalities. BPM provides different statistical imaging analysis approaches, including correlation, ANOVA, ANCOVA and multiple regression. Regarding the correlation analysis, BPM applies the random field results for a homologous correlation field, which is updated from the random field theory (Worsley *et al.*, 1996) for statistical inference. Rather than T-scored maps, I implemented Z-score maps in the correlation analysis, which offers a more accurate statistical inference for a correlation field. (Casanova *et al.*, 2007)

II-4. STATISTICAL ANALYSIS

Statistical estimation of group-wise mean, standard deviation and differences in ROI analysis was calculated in SPSS for Windows version 22 (SPSS, Chicago, Illinois, USA). The Shapiro-Wilk test was applied to assess the normality of the data distribution, where significant results (e.g. $p<0.05$) suggest a deviation from normality. In general, a p value of <0.05 was regarded as a group-level statistical significance in two sample test. Individually, the patient who had ROI average signal higher than that of the healthy control mean plus two-times standard deviations (mean+2SD), was considered as significantly increased signal in that region. The Pearson correlation was applied to measure the R squares (R^2) and p values for the linear correlation between two groups of variables using SPSS22. Repeated measures ANOVA was applied to detect any overall differences between repeated measurements.

CHAPTER III. QUANTIFICATION OF MICROGLIAL ACTIVATION USING [^{18}F]GE180 PET

III-1. INTRODUCTION

As discussed in Chapter One, AD is a neurodegenerative disorder that is characterised by worsening of memory and cognition. There is considerable evidence that neuroinflammation plays a significant role in neurodegenerative diseases (Calsolaro & Edison, 2016; Heneka *et al.*, 2015; Cherry *et al.*, 2016; Latta, Brothers & Wilcock, 2015). Microglia are the resident macrophage in the central nervous system (CNS). Inflammation, activation of microglia in particular, is a common feature of many neurodegenerative disorders (I-2). However, the exact role and the course of microglial activation in neurodegenerative disease are still poorly understood.

In brain, 18-kDa translocator protein (TSPO) is a cholesterol-transporter protein expressed in the outer mitochondrial membrane of microglial cells and astrocytes (Alam, Lee & Lee, 2017). Under normal condition, the TSPO expression in brain is very low. However, during injury or neurodegenerative process, overexpression of TSPO is found in activated microglial cells. Therefore, PET tracers are designed to target TSPO to provide an *in vivo* detection of microglial activation. [^{11}C](R)PK11195 has been used for TSPO PET imaging over 20 years, but due to the low signal-to-noise ratio and short half-life with 11C labelling, a series of new TSPO tracers have been developed (CHAPTER I.4.4). [^{18}F]GE180 is a novel TSPO tracer with 18F labelling (longer half-life), which showed promising results in preclinical models of Alzheimer's disease, stroke and CNS inflammation (Sridharan *et al.*, 2016; Deussing *et al.*, 2018; Boutin *et al.*, 2014; James *et al.*, 2017). In fact, the quantification of TSPO is challenging (Hinz & Boellaard, 2015) since the tracer binds not only to microglia (and to a lesser extent to astrocytes) in the parenchyma but also to the endothelium and smooth muscle cells (Turkheimer *et al.*, 2007, 2015; Alam, Lee & Lee, 2017). Because endothelial TSPO is physically in contact with plasma, its apparent affinity for the radioligand is higher than parenchymal TSPO. The new generation TSPO tracers are affected by genetic variability of TSPO binding site induced by the rs6971 single-nucleotide polymorphism (Owen *et al.*, 2011b). Recent studies have demonstrated that

tracer signal in the high-affinity binders (HAB) is 25-35% higher compared with the mixed affinity binders (MAB) (Yoder *et al.*, 2013; Park *et al.*, 2015).

1.1. Objectives

- Firstly, to establish the novel [^{18}F]GE180 scan protocol and quantification methods in healthy human controls (Study 1)
- Secondly, to evaluate the [^{18}F]GE180 performance in AD and find the optimal PET method for quantifying pathological microglial activation in AD patients using [^{18}F]GE180 (Study 2)

In this chapter, two consecutive studies were designed to evaluate the novel [^{18}F]GE180 radioligand for the first time in human trial, and to address the question whether this novel TSPO tracer can be useful in detecting microglial activation. Study 1 aimed to assess the [^{18}F]GE180 basic kinetic performance and investigate the most appropriate compartmental models in 10 healthy subjects (6 HAB or 4 MAB). This work has been published in JNM in 2016 (Fan *et al.*, 2016), and permission has been granted by JNM to reproduce this article in the current PhD thesis (Appendix 1. Permission Table).

Study 2 was designed to evaluate the [^{18}F]GE180 PET in specific disease condition using 13 AD patients and 8 healthy controls (all HABs). Previously, by assessing the longitudinal data of 789 subjects with high-affinity, mix-affinity and low-affinity binders in ADNI database, I have published that clinical results gathered from a TSPO subgroup (HAB or MAB) can be translated to the entire AD and MCI population (Fan *et al.*, 2015a). Given the high cost of PET and the limited scan allowance, only HAB AD patients were included by genotyping at the time of recruitment for the preliminary [^{18}F]GE180 study to reach a maximal effective size between subjects.

III-2. METHODS

2.1. Subjects

The ethical approval was granted by the Riverside Research Ethics Committee, and administer radiotracers were approved by the Administration of Radioactive Substances Advisory Committee (ARSAC) UK. All participants were recruited from memory clinics, advertisements and the Join Dementia research website. Participants in this study were aged 50-85 years, underwent TSPO genotyping, detailed medical and

neurological assessments, and comprehensive evaluation and bloods tests at screening. Written informed consent was obtained from all participants.

In Study 1, ten cognitively normal healthy control subjects (6 HAB and 4 MAB) were included for the first [^{18}F]GE180 human trial (Fan *et al.*, 2016). In Study 2, thirteen patients with a diagnosis of probable AD (Recruited from Join Dementia Research) and eight age-matched control subjects were included (all HAB). AD cohort (MMSE = 21.38±4.01) showed significantly lower ($p<0.001$) MMSE score compared with healthy controls (MMSE = 29.25±1.16). The DSM-IV or NIA-AA criteria were met for AD diagnosis. Inclusion and exclusion criteria were demonstrated in Appendix 2. In addition, two stroke patients (age=67 and age=79), both female, were included to provide preliminary finding of feasibility of supervised cluster analysis for [^{18}F]GE180 PET. In the first stroke patient (Figure III-11), the T2 MRI demonstrated a clear visualized ischemic stroke in the putamen and part of the caudate nucleus head in the right hemisphere. The second stroke patient had scattered little ischemic infarcts throughout the brain.

2.2. Data Acquisition

2.2.1 MRI

Each participant had a T1/T2 MRI scan on a 3 Tesla Siemens 32-channel Verio scanner. MRI image was generated as MPRAGE format (repetition time = 2300 ms, echo time = 2.98 ms, time to inversion = 900 ms, matrix = 240 x 256) with anteroposterior phase encoding direction and a symmetric echo. T1-weighted images were used for PET image co-registration, and T2-weighted images were used to detect significant lesions or white matter microvascular disease.

2.2.2 [^{18}F]GE180 PET

[^{18}F]GE180 radioligand was manufactured by GE FASTlab (Wickstrøm *et al.*, 2014). PET scans were performed in the Imperial Clinical Imaging Facility at Hammersmith Hospital, using a Siemens Biograph 6 PET/CT scanner. The axial field-of-view is 15.5 cm with 63 transaxial image planes displayed as 2.46 mm per slice. All subjects had arterial cannula inserted into their radial artery, along with venous cannula in the opposite antecubital vein. Prior to the PET scan, a low dose CT scan was performed for head positioning, attenuation correction and scatter correction. An average bolus

intravenous injection of 182 ± 5.0 MBq (n=25) [^{18}F]GE180 was administrated immediately after start of the dynamic emission scan. Image reconstruction was performed through standard Siemens software. The scatter correction and attenuation correction was based on 3D ordinary Poisson ordered-subset expectation maximization (OP-OSEM) algorithm. Filtered back projection was carried out during the reconstruction (Bailey, 2005).

In Study 1, subjects underwent two sessions of 90 min PET scan with a rest period of 30 mins in between (in total 210 mins). Two 90 min scans were acquired in list mode separately. Two dynamic PET scans were then re-binned as 24 time frames (6x15 s, 3x60 s, 5x120 s, 5x300 s, and 5x600 s) and 9 time frames (9x600 s) in order to minimise the noise and maximise the information in the scan. In Study 2, 90min dynamic PET data were collected for AD and healthy controls. The 90 min dynamic PET was acquired in list mode and re-binned as 24 time frames during reconstruction (6x15 s, 3x60 s, 5x120 s, 5x300 s, and 5x600 s).

2.2.3 Blood acquisition

The continuous blood sampling was done for the first 15 mins after the scan start using an automated blood sampling system (Allogg ABSS, Mariefred, Sweden). The discrete blood samples were collected throughout the PET scan at 5, 10, 15, 30, 60, 90, 120, 150, 180 and 210 min for Study 1, and 5, 10, 15, 30, 50, 70 and 90 min for Study 2. These discrete blood samples were then used to measure the tracer activity concentration in whole blood and plasma ($kBq \cdot ml^{-1}$) using a well-counter. The parent fraction was measured by high-performance liquid chromatography (HPLC) (Passchier, 2009). All radioactivity concentration was decay corrected to the scan start time.

2.3. Kinetic Modelling

2.3.1 Time activity curve

Frame-by-frame realignment was performed to correct for head motion during scanning using SPM8. The brain atlas was generated in the native PET space for each subject (CHAPTER II.3.1). The regional TAC (time activity curve) was generated by sampling the dynamic PET data based on the individualised atlas in MATLAB 2014a. In this study, ROIs for the following cortical regions were sampled: frontal, temporal, parietal, occipital lobes and whole brain. Additional subcortical regions of posterior cingulate,

thalamus, brainstem, medial temporal lobe, hippocampus, and cerebellum were calculated.

2.3.2 Compartment modelling

As the first human trial for [^{18}F]GE180, five compartmental models (Figure II-1) were evaluated for [^{18}F]GE180 tissue uptake for microglial activation. The reversible one-tissue compartment model (1TCM2k), the reversible two-tissue compartment model (2TCM4k) and the irreversible two-tissue compartment model (1TCM3k) were evaluated, where k implies the rate constant for tracer travelling between different compartments. Considering the lipophilic feature of TSPO tracer, the impact of the tracer binding to the endothelial cells on blood-brain barrier (BBB) is noticed (Rizzo *et al.*, 2014). Therefore, one-tissue (1TCM2k-1k) and two-tissue with extra vascular component models (2TCM4k-1k) were also investigated, where the vascular component describes the irreversible trapping of the TSPO tracer in the endothelial cells of blood vessels. In order to select the best model, visual assessment and Akaike Information Criterion (AIC) (Bozdogan, 1987; Akaike, 1973) were conducted for each model fitting (Equation 2). AIC applies the maximised log-likelihood to estimate Kullback-Leibler distance between the candidate model and the true data, Therefore, the model with the lowest value of AIC demonstrated the closest signal. Wald-Wolfowitz test was applied to assess the randomness of the data distribution around the candidate model. Coefficient of variation (CV) was measured to evaluate the dispersion and precision of parameter estimations. Additionally, the frequency of AIC preferences for each model across all subjects was calculated to evaluate the fraction of the model preference (AIC fraction).

2.3.3 Scan length

In Study 1, the optimum scan length for [^{18}F]GE180 was evaluated using dynamic PET data at 60 min, 75 min, 90 min, 150 min, 180 min and 210 min. V_T (Equation 3), rate constant k values and the BP_{ND} (Equation 4) were estimated to investigate the most appropriate scanning time for [^{18}F]GE180 PET in human trial.

2.4. Parametric Mapping

2.4.1 Spectral analysis

Spectral analysis was applied to produce impulse response function (IRF) parametric maps by convolving the parent plasma input function and the dynamic PET data. Spectral analysis uses basis function and separates the tissue response into the early, blood flow dependent signal component and the later signal component indicative tracer targets (CHAPTER II.2.1). In this study, 1 min, 30 min, 45 min, 60 min, 75 min and 90 min IRF parametric maps were generated for [^{18}F]GE180. Based on the estimated set of n spectral peaks in the spectrum (peak position β_i, peak height α_i), the IRF(t) parametric maps were generated (Equation 6). Apart from the blood volume component, the sum of all other components in the spectrum was applied to generate the IRF curves. For the [^{18}F]GE180 IRF(t), 50-1000 basis function curves (50, 100, 500, 1000) were set to logarithmically space between βmin=0.00010532 s^{-1} (decay constant of the 18F) and βmax=0.1 s^{-1}. Visual assessment of the optimal candidate interpolation model was performed for different sets of parameters in MATLAB. The coefficient of variance (COV) was calculated for each IRF(t) to assess the best parametric map for [^{18}F]GE180 quantification.

Voxel-level evaluation of the IRF(t) parametric maps was interrogated using single-subject analysis, which compares each individual patient to the healthy control cohort using one-way ANOVA. The cluster-level significant p values were corrected with FWE for multiple comparisons. The total volume of the significant VOI clusters was calculated in MATLAB 2014a for each AD patient.

2.4.2 Graphic analysis

Graphic analysis transforms the measurements of plasma input function and tissue dynamic data of [^{18}F]GE180 into a linear plot, where the slope indicates the amount of the available [^{18}F]GE180 at that time-point. Depending on the reversibility of [^{18}F]GE180, V_T can be estimated by the slope of the linear section of the Logan plot, while K_I can be estimated from the Patlak plot (CHAPTER II.2.2). Based on the kinetic modelling result, [^{18}F]GE180 showed a reversible nature. Therefore, Logan plot was applied to generate Logan V_T parametric map. The optimal t* was evaluated on the Logan linear fitting of the model to the real data points against the time.

2.4.3 SUV and SUVR

To investigate the feasibility of a non-invasive quantification of [^{18}F]GE180 without arterial line, a previous study has suggested that cerebellum could be used as a pseudo reference region for TSPO tracers (Lyoo *et al.*, 2015). In this study, the standardised uptake value (SUV) was generated for summed dynamic PET at 40-60 min frames and 60-90 min frames, which were used to evaluate whether simplified methods for [^{18}F]GE180 quantification would perform as well as arterial input methods (Equation 10). SUV images demonstrated the [^{18}F]GE180 distribution for each individual by normalising the tracer administration activity and body weight. ROI analysis was performed for SUV images. For SUVR (Standardized uptake value ratio), the grey matter of the cerebellum was used as the pseudo reference region for TSPO binding. The SUVR was calculated by dividing regional SUV with their cerebellar SUV value using MATLAB 2014a.

2.4.4 Supervised cluster analysis

A typical tracer-free reference region is not available for TSPO tracers, cluster analysis is another alternative approach to generate a BP parametric image of [^{18}F]GE180 without arterial input (Koon-Pong Wong *et al.*, 2002). To develop supervised cluster analysis for [^{18}F]GE180, the scaling coefficient of four predefined TAC kinetic classes are required to be estimated in a specific pathological condition. Since neuroinflammation in AD appears to be heterogeneous and complex, in the present investigation, the [^{18}F]GE180 PET was also evaluated in stroke patients in order to derive a supervised algorithm for multiple kinetic classes (supervised cluster analysis). [^{18}F]GE180 scan for stroke patients was performed without invasive arterial blood. T1 and T2 MRI were used to localize the ischemic stroke. Regional maps for ischemic stroke, contralateral region to the stroke, white matter and blood of each kinetic classes were drawn manually using ITK-SNAP (Yushkevich *et al.*, 2006). After manually drawing the ROI object map for ischemic stroke, the opposite side of the stroke (putamen and caudate nucleus on the left hemisphere), white matter and blood, the atlas was applied to the dynamic [^{18}F]GE180 PET to generate the time activity curves. The time activity curve was calculated on the dynamic sequence of [^{18}F]GE180 PET data of 90 mins.

2.5. Extraction of Vascular Signal from Brain Tissue

Due to the high lipophilic feature of the TSPO ligands, a significant proportion of [^{18}F]GE180 signals was found in the vascular component, where those signals may very much represent the non-specific binding of the lipids and cause some signal dispersion into the brain tissue. Thus, one challenge for quantifying [^{18}F]GE180 tissue binding is to separate the vascular signal and signal dispersion from tissue binding.

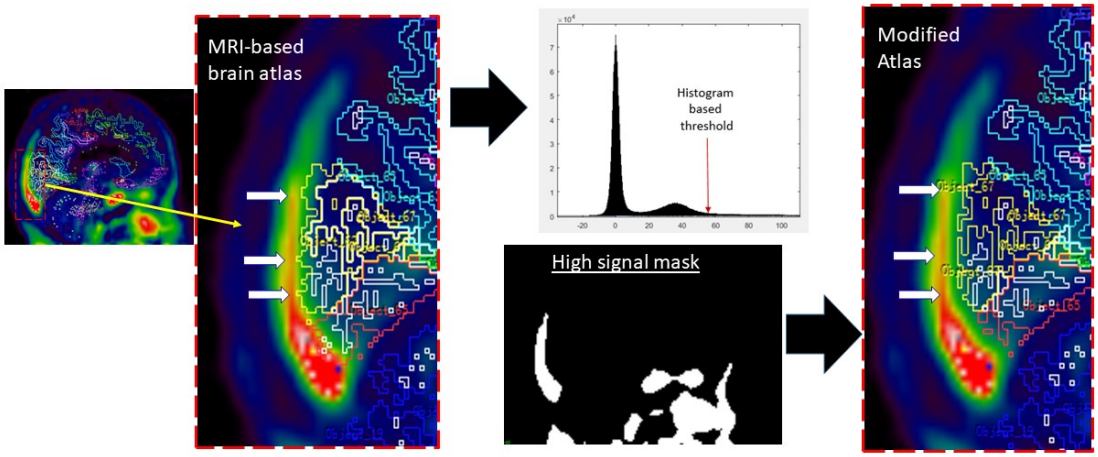


Figure III-1. Extraction of vascular signal and signal dispersion from brain tissue.

The histogram of all [^{18}F]GE180 PET scans showed a consistent pattern: a noise peak (around 0) and a normal distributed signals. In this case, a histogram-based high signal exclusion mask was generated by separating signals from a 30 – 90 min summed PET image into 200 intervals. The peak and width of each interval were measured, and then used to generate and select an optimal binary high signal mask. Visual assessment on the high signal mask was performed to ensure signals located inside the brain tissue were intact. Lastly, the high signal mask was multiplied to the original atlas to exclude the vascular signal dispersion.

As part of my PhD, I designed an atlas modulation approach that extracts the high tracer signal dispersion from venous sinuses and endothelial cells of the BBB (Figure III-1). By reviewing the histogram of [^{18}F]GE180 signal, apart from the noise peak (around 0), the tracer activity followed a typical normal distribution pattern in all [^{18}F]GE180 scans. In order to improve quality of TAC sampling, an additional PET histogram-based exclusion mask was multiplied to the individual MRI-based brain atlas to remove the high dispersed signal from vascular component. In details, the 30 - 90 min PET summed image was firstly separated into 200 intervals. After that, the peak and the width of each interval were measured. Based on the histogram, threshold was selected using the histogram bin edge to generate an individualized vascular signal mask. Furthermore, a

visual assessment throughout the histogram-based mask was performed to ensure signals located inside the brain tissue were intact. In the end, the PET histogram-based exclusion mask was applied to the MRI-based atlas to generate a modified atlas for [^{18}F]GE180 TAC sampling.

III-3. RESULTS

3.1. Study 1: Quantification of [^{18}F]GE180 PET in Healthy Control

3.1.1 Blood modelling

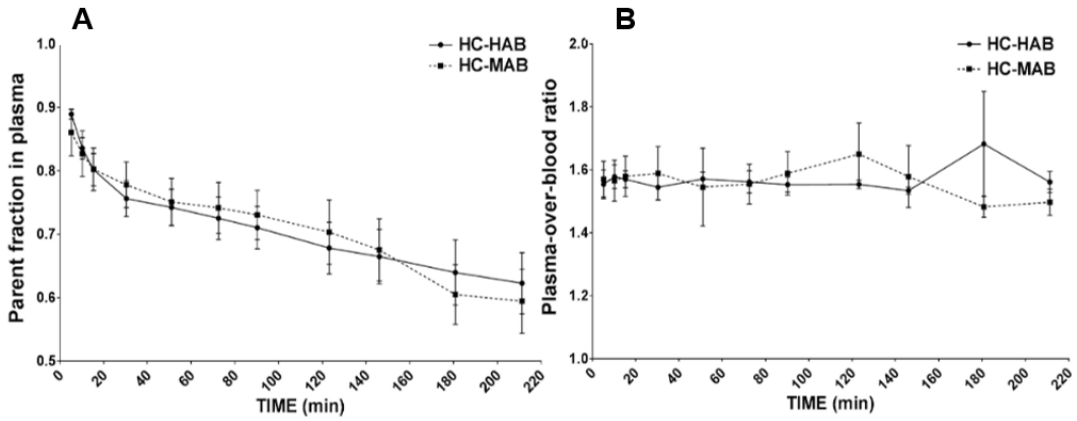


Figure III-2. [^{18}F]GE180 blood modelling for parent fraction and POB (plasma over blood) ratio.

(A) [^{18}F]GE180 parent fraction was fitted with a sigmoid model and (B) plasma over blood was fitted with a constant model. The dashed line with error bar represents the mean and the standard deviation of the high affinity binding group; and the dotted line with error bar represents the mean and the standard deviation of the mix affinity binding group in healthy controls.

Three identifiable radiolabelled metabolites of [^{18}F]GE180 were detected, which is consistent with the preclinical finding (Boutin *et al.*, 2014). The parent fraction of [^{18}F]GE180 gradually reduced from 90% to 70% over 90 mins, and then kept reducing to 60% towards to the end of the scan. The parent fraction can be modelled by an exponential curve. The ratio of activity concentration in plasma and blood followed a constant model, where [^{18}F]GE180 concentration in plasma was 1.6 times higher than in whole blood. (Figure III-2)

3.1.2 Time activity curve

The time activity curves (TAC) of dynamic [^{18}F]GE180 image were corrected with the injected dose and individual weight for each time frame (corrected TAC). Based on the course of TAC, the [^{18}F]GE180 activity concentration in the brain peaked at 125 seconds. Then it quickly washed out and reached a relatively steady level around 40 min, which lasts to the end of the scan. The highest [^{18}F]GE180 activity concentration was found consistently in the venous sinuses during the whole scan. Compared to binding in the white matter, grey matter demonstrated around 30% higher SUV.

3.1.3 Model selection

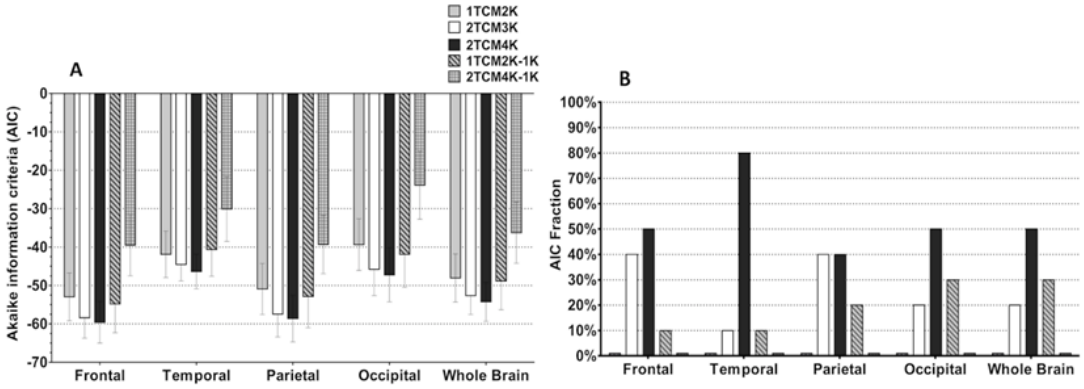


Figure III-3. Results of mean AIC and AIC fraction.

(A) AIC values for five models in frontal lobe, temporal lobe, parietal lobe, occipital lobe and whole brain. (B) AIC fraction reveals the frequency of AIC preferences for each model across all subjects.

The compartmental modelling analysis was carried out for [^{18}F]GE180 with five candidate models. As a result, the reversible two-tissue compartment model (2TCM4k) revealed the lowest AIC values (-54.7±4.8) suggesting the closest estimation to the true [^{18}F]GE180 uptake (Figure III-3). This is in agreement with the visual assessment of fitted TAC. While the 2TCM3k model also demonstrated a low AIC values (less than 10% difference to 2TCM4k model), it showed poor parameter estimation accuracy with a high COV (104±85%) of Ki. In contrast, the V_T derived from 2TCM4k model showed a better precision with an average CV of 21±13% in large cortices. Additionally, 2TCM4k model demonstrated the most frequent model preference (AIC fraction) among different subjects. The 2TCM4k model for [18]GE180 was further supported by the equal number of residuals that distributed around the model curve using Wald-

Wolfowitz test, suggesting a true randomness of distribution. In summary, 2TCM4k model was selected as the most appropriate kinetic model to describe the kinetic behaviour of [^{18}F]GE180.

3.1.4 HAB vs. MAB

ROI	All Subjects (n=10)		HAB (n=6)		MAB (n=4)		HAB vs. MAB	
	Mean	SD	Mean	SD	Mean	SD	t test	Increase
FL	0.15	0.06	0.17	0.06	0.12	0.05	0.11	39%
TL	0.16	0.07	0.18	0.07	0.13	0.05	0.09	45%
PL	0.15	0.05	0.17	0.05	0.12	0.05	0.12	36%
OL	0.17	0.06	0.2	0.06	0.14	0.05	0.06	45%
WB	0.15	0.06	0.17	0.07	0.12	0.05	0.11	40%
Thalamus	0.2	0.09	0.24	0.09	0.14	0.06	0.04*	73%
Striatum	0.15	0.06	0.17	0.05	0.1	0.05	0.07	64%
MTL	0.17	0.06	0.19	0.07	0.13	0.05	0.06	50%
Hippo	0.17	0.08	0.2	0.08	0.13	0.06	0.09	51%
CB	0.15	0.07	0.18	0.07	0.11	0.05	0.05*	63%

Table III-1. Regional V_T (mL·cm^{-3}) for [^{18}F]GE180 applied 2TCM4k model in all healthy controls, HABs and MABs.

**p<0.05; FL = Frontal Lobe; TL = Temporal Lobe; PL = Parietal Lobe; OL = Occipital Lobe; WB = Whole Brain; MTL = Medial Temporal Lobe; Hippo = Hippocampus; and CB = Cerebellum.*

Relatively low [^{18}F]GE180 brain uptake of 0.15 ± 0.06 mL·cm^{-3} was observed in all healthy controls. This could due to a low BBB permeability and the significant amount of signal presented in the plasma (fraction=97.3%), which led to a low availability of the [^{18}F]GE180 in the tissue. The model estimated blood volume contribution was around 6.4%. While the mean V_T was generally low, evidence of heterogeneity was found across different ROI regions, where higher V_T was found in temporal-occipital lobe, medial temporal lobe and hippocampus (Table III-1), which was in line with

neuroinflammation aging studies (Niraula, Sheridan & Godbout, 2017; Mosher & Wyss-Coray, 2014). Group-wise higher binding was found in HAB in thalamus ($p=0.04$ $mL \cdot cm^{-3}$) and cerebellum ($p=0.05$ $mL \cdot cm^{-3}$) compared with MABs. To note, a relatively high variability between subjects was observed within each genetic subgroup, where HAB healthy control showed a COV of 41.2% while MAB healthy controls showed a COV of 41.7%. No significant V_T difference was found between HAB and MAB subjects in large cortical regions.

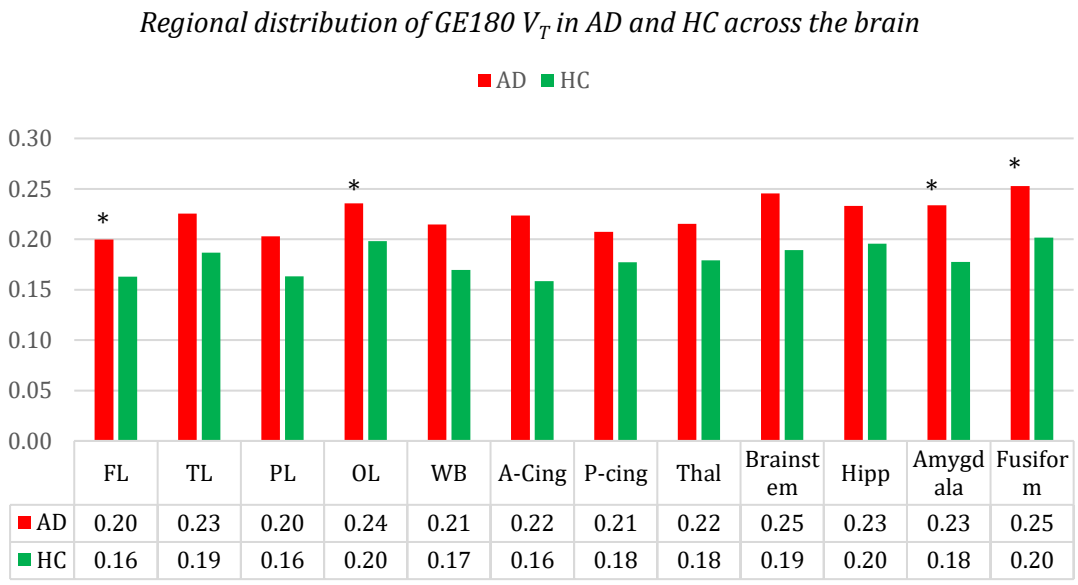
3.1.5 Scan length

Due to the high variance towards to the end of the [^{18}F]GE180 PET scans (e.g. head motion), 180-210 min data was discarded from the calculation. Repeated ANOVA was applied to V_T values using data from different predefined scan length, and no difference was found. The k values and BP_{ND} (k_3/k_4) were then estimated to assess the data consistency of each duration. As a result, the BP_{ND} and k values stayed the same when scan length was reduced from 180 min to 90 min ($p>0.2$). However, compared to BP_{ND} derived from 90 min data, the BP_{ND} estimation of 75 min and 60 min data showed a reduction of 14% ($p<0.04$) and 51% ($p<0.01$), respectively. This finding suggested that 90 min might be the minimal scan length for [^{18}F]GE180 scanning.

3.2. Study 2. Quantification of [^{18}F]GE180 in Neurodegenerative Disease

3.2.1 Compartmental modelling

As shown previously (Fan *et al.*, 2016; Feeney *et al.*, 2016; Zanotti-Fregonara *et al.*, 2018), two-tissue reversible model also gave a good fit to [^{18}F]GE180 data in patients with Alzheimer's disease. AD patients showed similar blood volume estimation of 5-6%, which was consistent with Study 1. The heterogeneous regional distribution of [^{18}F]GE180 uptake was found in the patients and healthy controls (Figure III-4). Within AD cohort, higher tracer distribution was found in temporal lobe, occipital lobe, brainstem, hippocampus, amygdala and fusiform throughout the brain, which was distinct from the distribution pattern in healthy controls.



	FL	TL	PL	OL	WB	A-Cing	P-cing	Thal	Brainstem	Hipp	Amygdala	Fusiform
AD	0.20	0.23	0.20	0.24	0.21	0.22	0.21	0.22	0.25	0.23	0.23	0.25
HC	0.16	0.19	0.16	0.20	0.17	0.16	0.18	0.18	0.19	0.20	0.18	0.20

Figure III-4. Heterogeneity of [^{18}F]GE180 Volume of distribution (mL·cm^{-3}) in AD (n=13) and HC (n=8) throughout the brain. The V_T estimations were derived from a reversible two-tissue compartmental model with arterial input function.

*FL = Frontal Lobe; TL = Temporal Lobe; PL = Parietal Lobe; OL = Occipital Lobe; WB = whole brain; A-cing = Anterior Cingulate; P-cing = Posterior Cingulate; Thal = Thalamus; and Hippo = Hippocampus. *p<0.05.*

The AD cohort demonstrated an average brain V_T of 0.24 mL·cm^{-3} (SD = 0.08), while healthy controls showed an average brain V_T of 0.18 mL·cm^{-3} (SD = 0.05). As a group-level comparison, AD patients showed a statistically significant increase in mean V_T in frontal (38%, p=0.04), occipital (37%, p = 0.05), amygdala (42%, p = 0.04) and fusiform (70%, p = 0.02) compared with healthy controls (Figure III-5). V_T in cerebellum revealed no statistical difference between AD and HC (32%, p=0.08). The average brain BP_{ND} was 0.43 in AD, while healthy controls showed an average brain BP_{ND} of 0.23, but only striatum reached significant difference at group level (p=0.04).

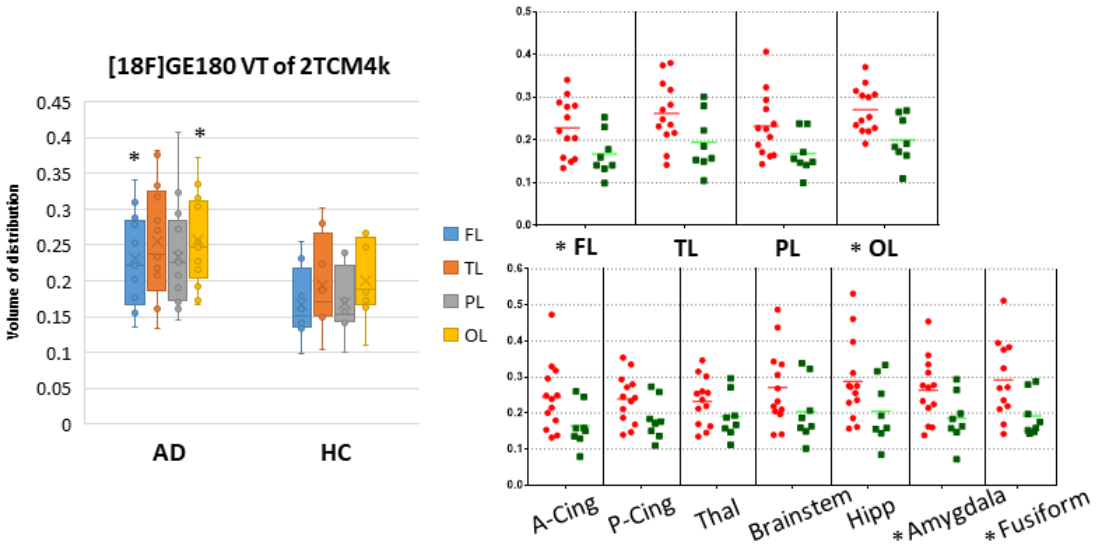


Figure III-5 Volume of distribution in AD and healthy controls in whole brain (left) and cortical regions (right top) and subcortical regions (right bottom).

**p<0.05; FL = Frontal Lobe; TL = Temporal Lobe; PL = Parietal Lobe; OL = Occipital Lobe; P-cing = Posterior Cingulate; Thal = Thalamus; and Hippo = Hippocampus.*

3.2.2 Spectral analysis

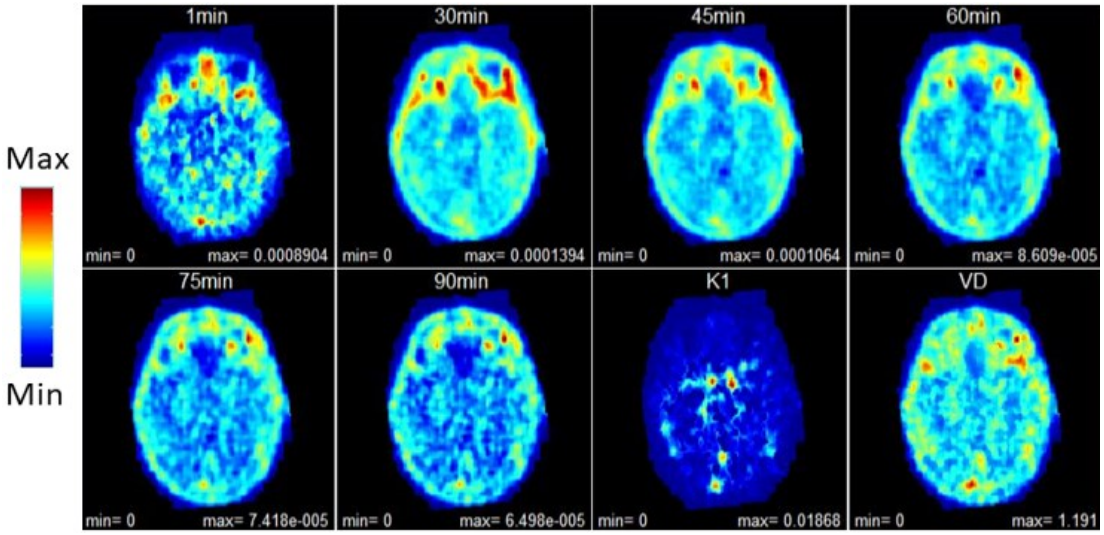


Figure III-6. Illustration of IRF parametric images for [^{18}F]GE180.

Parametric maps illustrated for [^{18}F]GE180 using spectral analysis via different set of observation time for IRF (IRF-1, IRF-30, IRF45, IRF-60, IRF-75, and IRF-90), K_1 and total volume of distribution images

In [^{18}F]GE180 spectrum, apart from the high frequency blood volume peak (5-6%), two intermediate spectral components were found, which may reflect the free and bound

[^{18}F]GE180 compartment in brain tissue. Interestingly, some subjects demonstrated a third low frequency peak, indicating a possible irreversible trapping of the tracer. Depending on the model fitting, 100 basis functions logarithmically spaced between βmin=0.00010532 s^{-1} and βmax=0.1 s^{-1} was used, which reached a preference fraction of 76% across all subjects. Based on different sets of observation time, IRF(t) parametric images and total volume of distribution image of [^{18}F]GE180 were generated in MATLAB 2016a (CHAPTER II.2.1). Depending on the noise level and the dynamic course of IRF curve, 90 mins (COV=18%) was selected as the best observation time for IRF of [^{18}F]GE180. (Figure III-6)

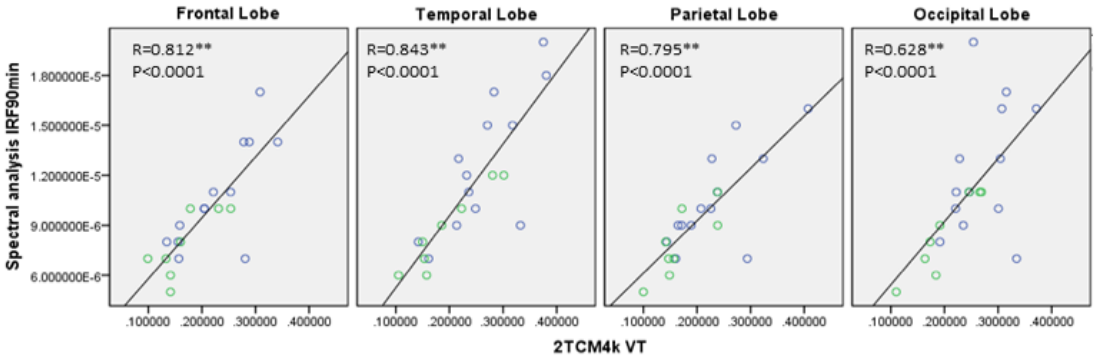


Figure III-7. Pearson correlation between 2TCM4k and IRF-90 in frontal lobe, temporal lobe, parietal lobe and occipital lobe. The [^{18}F]GE180 V_T derived from the 2TCM4k were significantly correlated with the tissue response function derived from IRF-90 in all four regions.

***p<0.0001; AD subjects = blue circle and HC subjects = green circle.*

Good correlation was found between [^{18}F]GE180 V_T derived from two-tissue compartmental model and the IRF-90 parametric maps (Figure III-7). Similar to the compartmental modelling, the AD patients demonstrated a similar heterogeneous distribution of the binding across the brain using IRF-90. Compared with healthy controls using IRF-90 parametric maps, group-wise significant increase in [^{18}F]GE180 uptake was found in AD patients at frontal lobe (33%, p=0.03), temporal lobe (40%, p=0.03), parietal lobe (35%, p=0.02), occipital lobe (43%, p=0.02), anterior cingulate (52%, p=0.02), posterior cingulate (39%, p=0.02), amygdala (46%, p=0.05) and fusiform (46%, p=0.04). (Figure III-8) Additionally, no significant difference were found between AD and HC in cerebellum IRF-90 values.

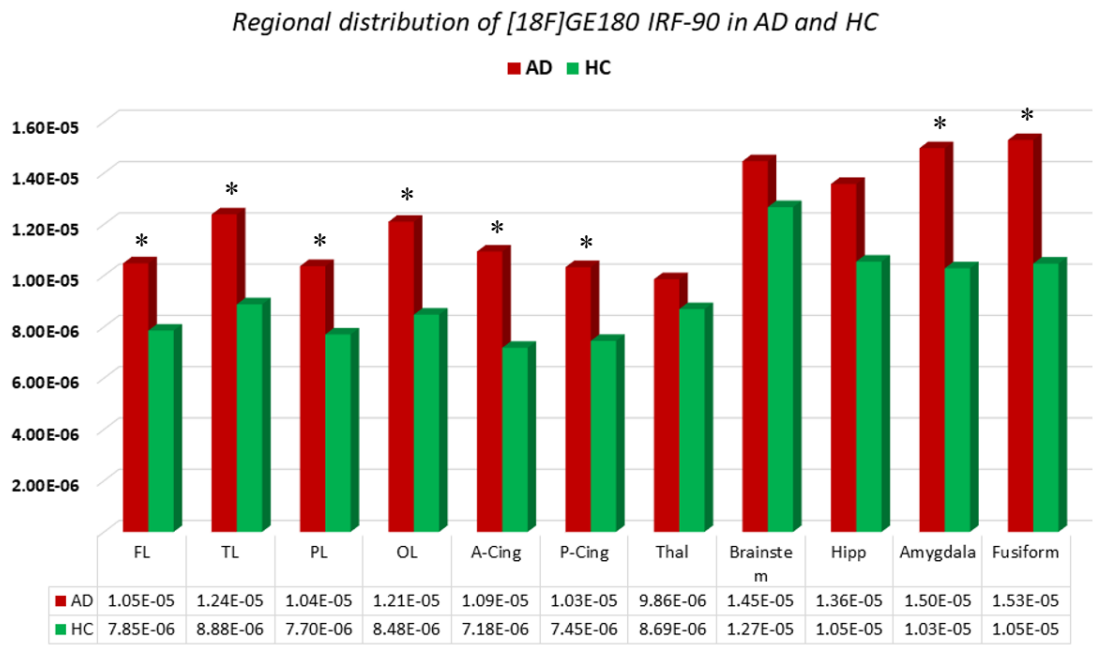


Figure III-8. ROI regional results of [^{18}F]GE180 IRF-90 parametric maps in 13 AD and 8 HC subjects. Significantly increased [^{18}F]GE180 IRF were found in AD patients compared with healthy controls in frontal lobe, temporal lobe, parietal lobe, occipital lobe, anterior cingulate, posterior cingulate, amygdala and fusiform.

**p<0.05; FL = Frontal Lobe; TL = Temporal Lobe; PL = Parietal Lobe; OL = Occipital Lobe; A-cing = Anterior Cingulate; P-cing = Posterior Cingulate; Thal = Thalamus; and Hippo = Hippocampus.*

Compared to 2TCM4k model, IRF-90 demonstrated a higher sensitivity in differentiating the AD patients' [^{18}F]GE180 uptake from the healthy controls (Figure III-5 and Figure III-8). Moreover, IRF-90 parametric maps allowed voxel-level comparison of the [^{18}F]GE180 uptake between AD patients and healthy controls. On the individual level, 11/13 patients had clusters of significantly increased [^{18}F]GE180 uptake compared with the healthy control cohort with a cluster threshold of $p<0.05$ and minimal voxels of 50 (Figure III-9). The total volume of the localized individual significant clusters ranged from 68,025mm^3 to 643,885mm^3.

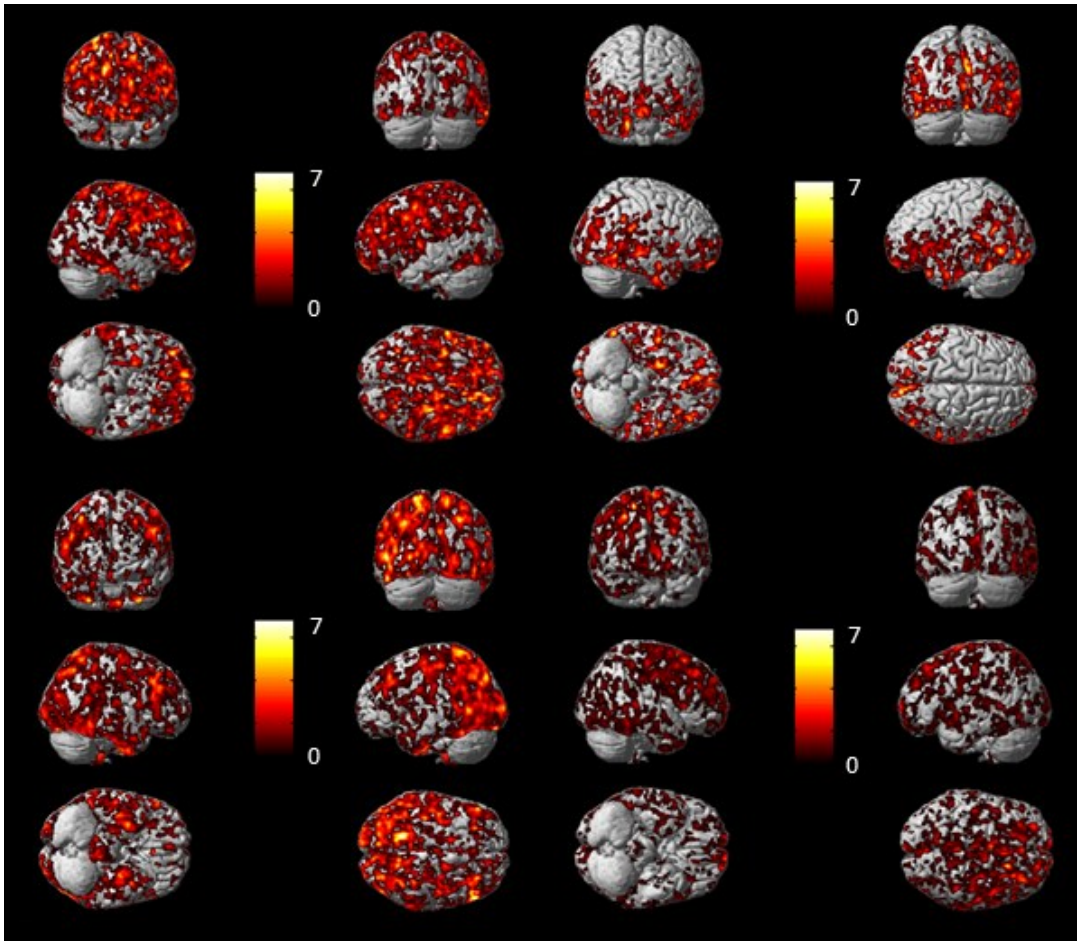


Figure III-9. Single subject SPM analysis of [^{18}F]GE180 IRF-90 when compared each patient to the healthy controls.

The colour map reveals the Z-scores for significant clusters of increased [^{18}F]GE180 uptake.

3.2.3 Graphic analysis

[^{18}F]GE180 has a reversible feature, therefore Logan graphical analysis (Logan, 2000) was selected for [^{18}F]GE180. Based on linear fit of the whole brain with appropriate weighting for different frame time points (based on the frame length), data from 20 min to 90 min (8 data points) was selected to generate Logan parametric map (slope=0.147±0.06 and intercept=-1623±387 in whole brain). The Logan V_T values were correlated well with 2TCM4k V_T values using Pearson correlation (Figure III-10). In the ROI group analysis, AD subjects demonstrated a trend of 13-28% higher average Logan V_T values compared with controls. However, no group-level statistical significance was reached in any ROI (p=0.17) between AD and healthy controls.

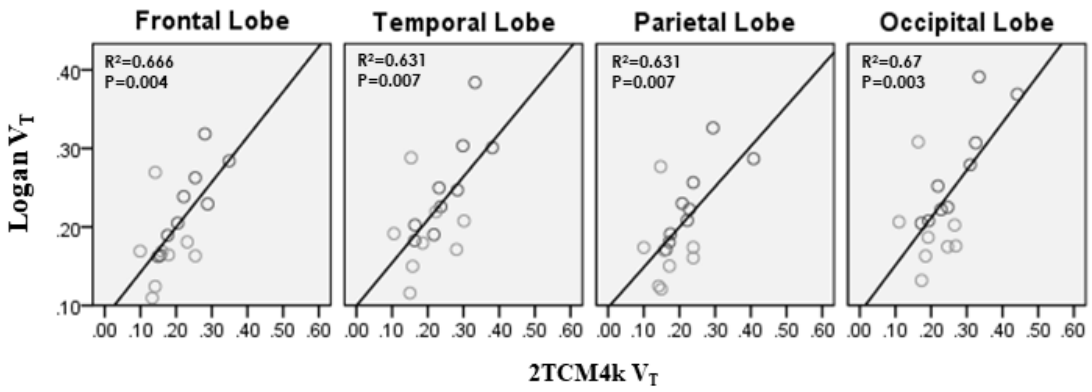


Figure III-10. Good correlation were found between Logan V_T and 2TCM4k V_T in frontal lobe, temporal lobe, parietal lobe and occipital lobe.

3.2.4 SUV and SUVR

Among four cortices, 40-60 min SUV showed around 19-26% higher average value in AD than controls, while 60-90 min SUV showed 24-31% higher average value in AD compared with controls. However, no group-wise significance was reached for either 40-60 min (p=0.19) or 60-90 min (p=0.18) SUV image. Cerebellum demonstrated around 19% (p=0.53) and 24% (p=0.4) higher trend in AD subjects compared with HC, using 40-60 min and 60-90 min SUV, respectively, but none of them were significant. When cerebellum grey matter was applied as a pseudo reference region for [^{18}F]GE180 signal, the whole brain SUVR failed to reveal any difference between AD and HC using 40-60 min SUVR (-4%, p=0.38) or 60-90 min SUVR (0%, p=0.40) in any ROIs. Both SUV and SUVR images failed to show any significant correlation to the V_T derived from the two-tissue reversible model in any predefined ROI regions.

3.2.5 Cluster analysis

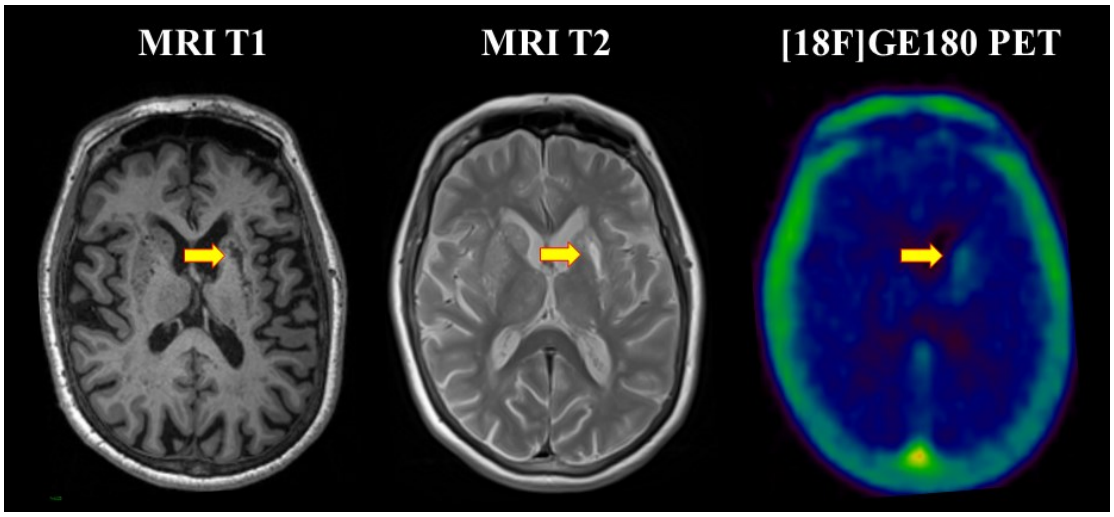


Figure III-11. MRI T1, MRI T2 and [^{18}F]GE180 PET of an ischemic stroke patient.

In cluster analysis, the 60-90 min SUV image of [^{18}F]GE180 PET was generated and revealed increased activity at the putamen area in the right hemisphere, which was consistent with the MRI T2 image (Figure III-11). Based on the manual drawing atlas, the tracer concentration in the blood vessel peaked at around 1 min, and then gradually washed out during the rest of the scan, which was similar to the arterial input function. Compared to the contralateral region of the stroke (grey matter), the stroke region demonstrated 25% (p=0.026) higher activity during the 90 min data, 54% (p=0.000005) higher during 20-90 min, and 62% (p=0.001) higher during 60-90 min. Compared to the white matter, the stroke region showed 49% (p=0.00001) higher activity during the 90 min scan, 58% (p=7.4E-07) higher during the 20-90 min, and 62% (p=0.003) higher during the 60-90 min. The TAC in white matter showed a similar dynamic course to the contralateral stroke region (p=0.7). (Figure III-12)

For the other stroke patient, the T2 MRI showed scattered little ischemic infarcts throughout the brain, which was challenging to generate reliable ROI atlas for those infarcts. During the visual assessment, 60-90 min SUV image of [^{18}F]GE180 failed to reveal any clear signal increasing around those scattered ischemic infarcts.

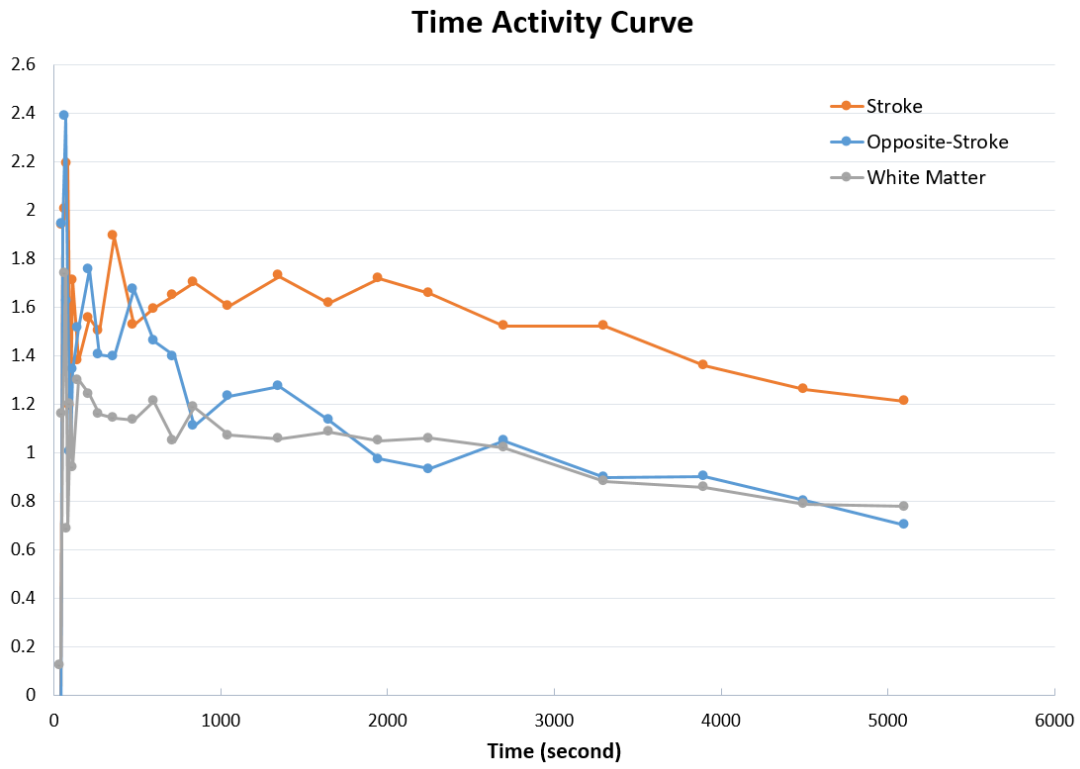


Figure III-12. Time activity curve for stroke (orange), opposite-stroke (blue) and white matter (grey).

III-4. DISCUSSION

4.1. Consensus in [^{18}F]GE180 studies

Since the first in human study of [^{18}F]GE180 published in 2016 (Fan *et al.*, 2016), a number of [^{18}F]GE180 studies in healthy controls and disease conditions came out (Feeney *et al.*, 2016; Zanotti-Fregonara *et al.*, 2018; Vomacka *et al.*, 2017; Albert *et al.*, 2017). Similarities and discrepancies were revealed across different labs. The general consensus for [^{18}F]GE180 was that compared with other TSPO PET tracers, the brain uptake was relatively low. This could be due to the low [^{18}F]GE180 penetration of blood brain barrier, or fast clearance by efflux pumps at the blood brain barrier (e.g. P-glycoprotein), or disproportional higher plasma protein binding in human brain (Feeney *et al.*, 2016; Zanotti-Fregonara *et al.*, 2011; Schinkel, 1999; Fan *et al.*, 2016). In contrast, preclinical studies in rodents demonstrated promising results of [^{18}F]GE180 (Deussing *et al.*, 2018; Boutin *et al.*, 2014; James *et al.*, 2017; Sridharan *et al.*, 2016). The specificity of [^{18}F]GE180 binding was confirmed in a rodent blocking study

(Deussing *et al.*, 2018). In an ischemic stroke model, [^{18}F]GE180 demonstrated higher signal-to-noise ratio than using the [^{11}C]PK11195 PET (Boutin *et al.*, 2014). [^{18}F]GE180 radioligand showed good sensitivity in differentiating neuroinflammation in acute model of neuroinflammation, LPS-induced model and AD model (James *et al.*, 2017; Boutin *et al.*, 2014; Sridharan *et al.*, 2016). In preclinical studies, [^{18}F]GE180 penetrated the blood brain barrier readily in animal models (Boutin *et al.*, 2014). While difference between species was widely accepted, the discrepancy of the results found in human trials and animal models could be due to penetration of the brain and high vascular binding in human.

4.2. Kinetic Modelling

Various compartmental model candidates for [^{18}F]GE180 were investigated in different labs, a consensus was reached that two-tissue compartment model without considering the vascular component provides the best model fit for [^{18}F]GE180 quantification (Zanotti-Fregonara *et al.*, 2018; Feeney *et al.*, 2016; Fan *et al.*, 2016). Similar to other PET tracers, there were different opinions on whether to estimate or fix the blood volume contribution for [^{18}F]GE180. In 2016, Feeney et al. indicated a fit problem in the early section of the model and selected to fix the blood volume (V_B) for [^{18}F]GE180 quantification. While similar fit problem in the early part of the curve was noticed in our cohort as well, the model with estimated V_B still performed better in estimating [^{18}F]GE180 uptake than fixed V_B model. Additionally, it provided a reasonable V_B estimation around 5-6% (Fan *et al.*, 2016; Turkheimer *et al.*, 2015). This finding was supported by Zanotti-Fregonara et al. who demonstrated that [^{18}F]GE180 fitting was improved when using the estimated V_B model (Zanotti-Fregonara *et al.*, 2018).

Plasma free fraction (f_p) reflects the percentage of free tracer in the plasma that are available to travel into the tissue. Due to the facility limitations, our radiochemist was not able to measure an accurate and reliable f_p for [^{18}F]GE180 *in vivo*. A recent study has managed to measure the f_p of [^{18}F]GE180 *in vivo* (Zanotti-Fregonara *et al.*, 2018). As expected, consistent with the *in vitro* experiments (f_p=2-3%), they found a low f_p around 3-4% of [^{18}F]GE180 in the parent plasma activity *in vivo*, indicating the low brain uptake for [^{18}F]GE180 may result from the low availability of the free tracer in the plasma. Indeed, the f_p of [^{18}F]GE180 showed slightly better than [11C](R)PK11195 (f_p=1-5%), and comparable to [^{11}C]PBR28 (4%). On the contrary, due to the slow

metabolite rate of [^{18}F]GE180, Zanotti-Fregonara et al. implied while [^{18}F]GE180 has 3-fold higher effective exposure of the brain compared to [^{11}C]PBR28, [^{18}F]GE180 still showed a much lower V_T than [^{11}C]PBR28. Thus, they suggested that rather than the low level of free tracer, the low brain uptake of [^{18}F]GE180 may be driven by the difficulty in penetration of the blood-brain barrier.

4.3. HAB vs. MAB

In 2011, Owen et al. showed that apart from [^{11}C](R)PK11195, all newly developed TSPO PET ligands were affected by the TSPO genotypes: HAB, MAB and LAB (Owen *et al.*, 2011b). They found as much as 50-fold (e.g. [^{11}C]PBR28) and as low as 4-fold (e.g. DAA1106, DPA713 and PBR111) of difference in binding potential between HAB and LAB cohort, while most MAB appears to possess only one class of binding sites with an affinity approximately equal to the mean of HABs and LABs. In case of [^{18}F]GE180, an unpublished *in vitro* work from Owen's group demonstrated the binding affinity difference between HAB and LAB was 15-fold with cold GE180 displacing [^{3}H]PK11195 (Feeney *et al.*, 2016). This seems appeared to be consistent with our finding, which demonstrated a marginal difference between HAB and MAB in thalamus ($p=0.04$) and cerebellum ($p=0.05$) in healthy controls (Fan *et al.*, 2016), however the difference would be expected much more pronounced. Feeney's group demonstrated they expected MAB to have around 50% of the binding in HAB cohort, but they failed to observe any differences *in vivo,* and they suggested it may be a consequence of the low TSPO level in their cohort (Feeney *et al.*, 2016). Indeed, compared to our subjects (50-85 years), they had a much younger group (28-56 years old) who may have less TSPO expression (Niraula, Sheridan & Godbout, 2017; Schuitemaker *et al.*, 2012). To note, this finding was conducted with a small sample group ($n=10$) in healthy controls with a marginal group-level difference and only observed in small subcortical regions (e.g. thalamus and cerebellum). Additionally, considering the high variation (COV=41%) observed in each genetic group, more data between HAB and MAB was certainly needed to further establish the TSPO genetic impacts on [^{18}F]GE180 in human brain. However, as a pilot study in human trial, this study provided the evidence that [^{18}F]GE180 can be effectively modelled by 2TCM4k model with 90 min PET scan, which allows quantification of the TSPO binding in the healthy human brain. Moreover,

the high plasma binding and low brain uptake of this tracer in human brain were reported for the first time (Fan *et al.*, 2016).

4.4. [^{18}F]GE180 in Disease

4.4.1 Volume of distribution in AD

In the study 2, [^{18}F]GE180 was applied in patients who were diagnosed with Alzheimer's disease. In the disease cohort, heterogeneous distribution of [^{18}F]GE180 V_T was found throughout the brain, and higher regional uptake was presented throughout the temporal lobe, occipital lobe, and subcortical regions, such as hippocampus, amygdala and fusiform, which was in line with previous neuroinflammation findings (Heneka *et al.*, 2015). Compared with age-matched healthy controls, the V_T of [^{18}F]GE180 PET demonstrated group-level higher values in frontal and occipital lobes for the AD cohort. This finding was consistent with postmortem study, where interleukin-1β-positive microglia was observed in the brain section of frontal cortex in an AD brain (Heneka *et al.*, 2015). Interestingly, similar regional distribution of microglial activation in AD brain was observed in my previous longitudinal study of microglial activation using [^{11}C](R)PK11195 PET (Fan *et al.*, 2015b). In the subcortical regions, amygdala and fusiform were observed with significantly higher V_T in AD subjects. It is was previously reported that amygdala was significantly affected by amyloid deposition in AD brain (Unger *et al.*, 1991), thus the increased microglial activation in amygdala suggesting upregulated activated microglia may follow the spreading of amyloid accumulation in AD brain. A previous fMRI study in AD patients showed an impairment in connection at medial temporal lobe, lingual and fusiform regions, resulted in a graded deficit in explicit memory encoding (Golby *et al.*, 2005), suggesting the upregulated neuroinflammation may relate to the impairment of memory. Additionally, [^{18}F]GE180 BP_{ND} demonstrated significant elevation in striatum in AD patients compared with healthy controls. The anatomical connectivity of striatum was shown to be associated with the level of amyloid deposition during AD development (Ishibashi *et al.*, 2014), our data illustrated again the neuroinflammation may closely relate to the regional distribution of the amyloid deposition.

Regarding the micro-parameters in 2TCM4k model, AD subjects in general showed a trend of 30% higher K_1 and 15% lower k_2 compared to healthy controls in large ROIs,

suggesting that more tracer flashed into the tissue from the plasma (K_1), but less was washed out from the brain tissue (k_2) in AD brain. Although k_3 and k_4 showed heterogeneous changes throughout different brain regions, AD demonstrated 58% higher in K_1/k_2 ratio and 25% higher in k_3/k_4 ratio than age-matched healthy controls. While no statistical significance was found in K_1 ($mL.min^{-1}mL^{-1}$) between AD and healthy controls, those micro-parameters indicated that AD subjects may have a higher [^{18}F]GE180 availability in target tissue compared to healthy controls, suggesting a possible alteration on cerebral blood flow in AD subjects. To note, as the [^{18}F]GE180 tissue uptake is very low, therefore, more subject data and blood flow analysis are suggested to further investigate the reliability of those micro-parameters estimates and to conclude whether the difference between AD and controls were due to the higher tracer availability.

4.4.2 Parametric mapping

Spectral analysis was applied for [^{18}F]GE180 PET. IRF-90 was selected as the optimal parametric map to quantify the [^{18}F]GE180 binding via spectral analysis. It demonstrated a good correlation with V_T derived from the compartmental modelling. Compared with kinetic modelling, IRF-90 revealed more ROI regions with significantly higher [^{18}F]GE180 uptake in AD patients than healthy controls in major cortices, anterior cingulate, posterior cingulate, amygdala and fusiform. This finding indicated that IRF-90 parametric map of [^{18}F]GE180 may have a higher sensitivity in differentiating the pathological binding in AD brains due to the high sensitivity of signal interpolation. Additionally, the 3-D parametric map allowed the voxel-level comparisons between subjects, where 11/13 patients showed clusters of significantly elevated [^{18}F]GE180 IRF-90 values. While Logan V_T also showed a good correlation with compartmental modelling, it failed to differentiate the AD subjects from the age-matched controls. This was perhaps due to the inherent bias in Logan graphical analysis, where the linear interpolation generally underestimates the true dynamic signals. In summary, although [^{18}F]GE180 uptake was relatively low in the brain compared to other TSPO tracers, the result in AD patients has demonstrated that both kinetic compartmental modeling and spectral analysis may be suitable in quantifying the [^{18}F]GE180 signal which was sensitive enough to differentiate pathological binding in AD from the healthy controls.

4.4.3 Reference region

The searching for a proper reference region is always popular due to the simplicity of the modelling and the non-invasive procedure without arterial blood sampling. The assumption of reference model requires a predefined reference region to be free of specific radioligand binding or pathological binding. There were studies applying a pseudo reference region SUVR approach for [^{18}F]GE180 without arterial input function, which showed a good contrast of the lesions in multiple sclerosis patients and tumour in glioma patients (Vomacka *et al.*, 2017; Albert *et al.*, 2017). Different pseudo reference regions were applied: frontal cortex was selected for multiple sclerosis, while background activity that derived from the healthy contralateral hemisphere was used for glioma, respectively. This again reiterated the fact that there is no general anatomical reference region for [^{18}F]GE180, the possible pseudo region with non-pathological TSPO binding is disease specific. In AD, a previous TSPO study has applied cerebellum grey matter as the pseudo reference region using another TSPO tracer, [^{11}C]PBR28 (Lyoo *et al.*, 2015). In this case, cerebellum grey matter was tested as the pseudo reference region for [^{18}F]GE180. In this study, both V_T (2TCM4k) and IRF-90 values in cerebellum showed no significant difference between AD and HC. However, when applied the semi-quantitative SUVR method with cerebellum as the reference region, it has failed to replicate the group-level change in [18F]GE180 uptake in AD cohort, which was found in the arterial input function models (e.g. 2TCM4k and spectral analysis). This suggested that a simplified reference region method of [^{18}F]GE180 may not perform as well as the arterial input methods in AD.

4.4.4 Cluster analysis

Given the low brain uptake of [^{18}F]GE180 and the diffuse feature of neuroinflammation in Alzheimer's disease, it is in fact difficult to determine any anatomic reference region. Therefore, another non-invasive method to be evaluated is the cluster analysis. In this study, for developing the non-invasive supervised cluster analysis for [^{18}F]GE180, predefined kinetic classes of [^{18}F]GE180 were evaluated in stroke patients. One stroke patient who had an ischemic stroke in the putamen area in the right hemisphere demonstrated a significant higher [^{18}F]GE180 activity in the stroke area compared to contralateral brain regions. Interestingly, it demonstrated around 50-60% increase in microglial activation in the stroke area comparing to contralateral grey matter or white

matter. This was consistent with a [^{18}F]GE180 tumour study, where patients with untreated or pretreated glioblastoma had a remarkable contrast between the tumour and background activity, which was even better than the MRI contrast (Albert *et al.*, 2017). Albert et al. suggested that the tracer uptake in the tumour was independent of the integrity of the blood-brain barrier, as they found the peripheral regions of the glioma lesions was only observed in the [^{18}F]GE180 PET but not in MRI, where MRI revealed a significantly smaller tumour mass than the [^{18}F]GE180 PET (Albert *et al.*, 2017). However, due to lack of the validation of biopsies and histopathological assessments, the high contrast of [^{18}F]GE180 uptake in the glioma reported in this tumour study was questioned with the possibility of disruption of blood-brain barrier by the other group (Zanotti-Fregonara *et al.*, 2018). While it is recommended to include histologic analysis for the BBB integrity, this stroke patient showed 50-60% increased [^{18}F]GE180 signal specifically at the area of ischemic stroke, suggesting the signal elevation may reflect the specific binding rather than a simply influx of tracer due to BBB disruption.

4.5. Blood-Brain Barrier

The major criticism of [^{18}F]GE180 radioligand was the low brain uptake observed in human brain, which is in contrast to the [^{18}F]GE180 findings in preclinical animal models in rodents (Deussing *et al.*, 2018; James *et al.*, 2017; Sridharan *et al.*, 2016). One of the suspicions was focused on the tracer's capability of penetrating the blood brain barrier in human brain. However, the logD assessment of [^{18}F]GE180 demonstrated an optimal range for the passive transportation *in vivo* to cross the blood brain barrier (Feeney *et al.*, 2016), indicating a high permeability and high lipophilic feature of the tracer. Another hypothesis was based on the possibility of a fast washout of [^{18}F]GE180 tracers by efflux proteins on the blood-brain barrier. This hypothesis was rejected by Zanotti-Fregonara's group, who argued that [^{18}F]GE180 had a parent-to-whole blood ratio higher than one, which is in agreement with our finding, suggesting the tracer even has a difficulty to penetrate the red cell walls. Therefore they proposed that [^{18}F]GE180 tracers were likely to be blocked by the blood-brain barrier from entering the brain in the first place (Zanotti-Fregonara *et al.*, 2018). In this study, a disproportional high plasma protein binding in the blood vessels was observed in both healthy controls and AD brains, suggesting the [^{18}F]GE180 tracers might be trapped in blood vessels before becoming available to be transported into the brain. Recent study

reported that they had successfully measured the plasma free fraction *in vivo*, and demonstrated a plasma free fraction of 3.5% for [^{18}F]GE180 in healthy controls (Zanotti-Fregonara *et al.*, 2018). Compared to other TSPO tracers (Sridharan *et al.*, 2016), the low plasma free fraction of the [^{18}F]GE180 supported our hypothesis that the low [^{18}F]GE180 brain uptake may be caused by the high level of plasma protein binding and the low level of the free tracer available for entering the brain. Indeed, there is possibility that blood-brain barrier could be altered or disrupted in AD brain. Given the difficulty of brain penetration of this tracer, for the future studies, it is therefore suggested to perform a histologic analysis for the blood-brain barrier integrity, in order to prove that the increased signal was due to pathological changes, rather than an influx of tracers due to the disruption of blood-brain barrier.

4.6. Conclusion

In this chapter, I investigated the [^{18}F]GE180 PET tracer in human brain by applying the novel TSPO tracer 1) in the HAB and MAB healthy controls, and 2) in AD patients. As a result, it has demonstrated that two-tissue compartmental model provided the best fit in quantifying 18F-GE180 PET. The low brain uptake of [^{18}F]GE180 made the quantification modelling very challenging, which requires a highly sensitive model to interpolate the signal, such as spectral analysis. In regional analysis, due to the high binding presented in the blood vessel and low brain uptake, the peripheral area of the brain atlas was eroded by vascular extraction mask and visual assessment to reduce the signal dispersion from the blood vessels and bones. The preliminary results in disease condition demonstrated that both V_T derived from two-tissue compartmental model and spectral analysis were able to differentiate the microglial activation in Alzheimer's disease. IRF-90 parametric map of [^{18}F]GE180 demonstrated 11/13 AD patients who had significantly increased clusters of microglial activation at voxel-level. Interestingly, those 2/13 AD patients without increased microglial activation revealed relatively high MMSE score (MMSE=28 and MMSE=26) compared to the AD group mean (MMSE=21.38±4.01), suggesting less microglial activation was associated with less cognitive impairment.

As a preliminary study of [^{18}F]GE180 in Alzheimer's disease, I noticed that several improvements were necessary to be involved in future prospective [^{18}F]GE180 studies. While V_T difference was found between HAB and MAB in our healthy control cohort,

compared to other second generation TSPO tracers, the binding difference was minimal and observed only in a few subcortical regions. Thus, larger sample size was needed to examine the genetic influence of [^{18}F]GE180 binding. In the current AD investigation, in order to account for the possible TSPO genetic influence, the comparison between patients and HC were conducted in HABs. Regardless whether there is genetic influence on [18F]GE180 binding, MAB AD patients should be evaluated in the future study to validate the finding in AD. A stroke patient demonstrated a high contrast of neuroinflammation between ischemic stroke area and contralateral regions using [^{18}F]GE180 PET, but more cases and longitudinal analysis were needed to be studied.

In conclusion, this chapter showed a preliminary finding of [^{18}F]GE180 quantification in human and demonstrated a signal-to-noise ratio of [^{18}F]GE180 which was large enough to differentiate the neuroinflammation in disease condition (AD and ischemic stroke). However, considering the fast evolution of TSPO tracer development, in my opinion, the low brain uptake and difficulty in modelling is unlikely to improve the competitiveness of the [^{18}F]GE180 ligand versus other new generation of TSPO tracers. The research of the best TSPO tracer for neuroinflammation in human brain remains to be explored. Taking a future perspective, due to the nature of TSPO distribution and the divergent presentation between patients, larger patient cohort in different inflammation conditions are recommended to be investigated along with the histologic validation of blood-brain barrier integrity for [^{18}F]GE180, or for any other novel TSPO tracers.

CHAPTER IV. QUANTIFICATION OF MICROGLIAL ATIVATION USING [^{11}C]PBR28 PET

IV-1. INTRODUCTION

In the previous chapter, the novel TSPO tracer [^{18}F]GE180 was evaluated for the first time in human trial, which demonstrated high vascular bindings and low tracer penetration of the blood brain barrier in both healthy controls and patients with Alzheimer's disease. In this Chapter, I evaluated the spatial distribution of microglial activation in patients with MCI using another TSPO tracer, [^{11}C]PBR28. Amnestic MCI is a transitional stage between preclinical AD and dementia (CHAPTER I). Microglial activation plays a significant role in AD along with amyloid and tau deposition (Calsolaro & Edison, 2016; Heneka *et al.*, 2015; Higuchi *et al.*, 2016). Recent PET imaging studies suggested that microglial activation correlates closely with the severity of dementia (Calsolaro & Edison, 2016; Edison *et al.*, 2013; Kreisl *et al.*, 2016).

[^{11}C]PBR28 is a second generation TSPO tracer which was designed for quantifying microglial activation in neurodegenerative disease in the last couple of years. However, discordant results were found in recent [^{11}C]PBR28 studies (Kreisl *et al.*, 2016, 2013; Schuitemaker *et al.*, 2013; Nair *et al.*, 2016). Different labs applied different quantification models and approaches for [^{11}C]PBR28, such as reversible two-tissue compartmental model, two-tissue compartmental model with extra vascular component, plasma free fraction corrected binding, Logan graphic analysis and SUVR with cerebellum as the pseudo-reference region (Lyoo *et al.*, 2015). The variation of quantification approaches applied across different labs can result in varying results for [^{11}C]PBR28 PET. Spectral analysis is a powerful kinetic approach and makes no assumptions about kinetic compartments, instead identifies heterogeneous components based on their kinetics, which separate the parenchymal TSPO binding from the high frequency, vascular binding (Veronese *et al.*, 2016; Cunningham & Jones, 1993).

1.1. Objective

The objective for this chapter is to seek the most appropriate approach to quantify the microglial activation using [^{11}C]PBR28 PET in neurodegenerative diseases.

1) The IRF parametric mapping of [^{11}C]PBR28 was compared to the V_T in compartmental models, and the parametric mapping using Logan graphic analysis.
2) Microglial activation between two cohorts (MCI vs. HC) was evaluated using [^{11}C]PBR28 IRF parametric maps, compartment model's V_T and Logan V_T map.

The results described in this Chapter have been published in EJNMMI, which was titled as 'Parametric mapping using spectral analysis for 11C-PBR28 PET reveals neuroinflammation in MCI subjects' (Fan *et al.*, 2018). This article is distributed under the terms of the Creative Commons Attribution 4.0 International License that permits unrestricted use, distribution, and reproduction in any medium. (Appendix 1. Permission Table)

IV-2. METHODS

2.1. Demographics

This study was approved by the local and regional regulatory ethics committee (London Riverside Research Ethics Committee - National Health Research Services, Health Research Authority, UK). The approval for administration of radioactivity was given by ARSAC. Subjects were recruited from local memory clinics, a national dementia recruitment website and advertisements in local media. Written informed consent was obtained from all participants. 13 Patients with MCI and 9 age-matched healthy controls were evaluated in this study (all TSPO HABs). MAB were excluded due to the small sample size. The Petersen criteria (2004) were used for the diagnosis of MCI subjects, while NIA-AA (National Institute of Ageing and Alzheimer's Association) or NINCDS-ADRDA (National Institute of Neurological and Communicative Disorders and Stroke-AD and Related Disorders Association criteria were used for the diagnosis of Alzheimer's disease.

2.2. Data Acquisition

2.2.1 MRI acquisition

All subjects underwent MRI and [^{11}C]PBR28 PET scans. The MRIs were performed with a 3 Tesla SIEMENS 32-channel Verio scanner. The MRI data was acquired with MPRAGE format, time repetition of 2400ms, time echo of 3.06 ms, inversion time of

900 ms and matrix of 256 x 246. MRI T1 and T2 images were used for co-registration of the PET image and detection of white matter microvascular disease, respectively.

2.2.2 [^{11}C]PBR28 PET Acquisition

[^{11}C]PBR28 PET images were acquired with a SIEMENS Biograph True Point PET/CT scanner with axial field of 21.8cm, transaxial planes of 111, and spatial resolution of 2.056mm x 2.056mm x 2mm in Invicro, London. A bolus around 300 ± 7.0 MBq (n=22) of [^{11}C]PBR28 was injected intravenously right after a low dose CT scan (for attenuation and scatter correction). A 90 min dynamic scan was acquired in list mode, and reconstructed as 26 time frames with attenuation correction, scatter correction, random correction and decay correction.

2.2.3 Blood acquisition

During the 90 min [^{11}C]PBR28 scan, continuous online blood sampling was acquired for the first 15 mins right after the scan started to assess the radioactivity concentration in the whole blood. Twelve discrete blood samples were taken at 5, 10, 15, 20, 25, 30, 40, 50, 60, 70, 80 and 90 min to measure the tracer activity concentration in whole blood and plasma. Based on the discrete blood samples, the [^{11}C]PBR28 activity in POB was fitted with a linear model. The POB model was then applied to the first 15 mins' online blood sampling to estimate the [^{11}C]PBR28 tracer activity concentration in plasma for the first 15 mins. Parent fraction was measured by HPLC using discrete blood samples and fitted with a sigmoid model. Lastly, the parent plasma input function was generated by multiplying the total plasma tracer concentration with the parent fraction curve.

2.3. Spectral Analysis of [^{11}C]PBR28

Spectral analysis constrains a general linear model to fit the tissue kinetics with a large matrix of exponential functions with the parent plasma input function (CHAPTER II.2.1). In this study, the decay constant of the carbon 11 (0.00056629 s^{-1}) was used for the beta-min, and 100 basis function was applied in spectral analysis of [^{11}C]PBR28. The IRF parametric maps of [^{11}C]PBR28 were generated with observation time of 30, 45, 60, 75 and 90 min (Equation 6). The coefficient of variation of ^{11}C-PBR28 IRF estimates in major cortices and thalamus were calculated to determine the optimal

observation time for [^{11}C]PBR28 IRF(t). The lower CV, the higher the robustness of the IRF estimates.

2.4. Compartmental Modelling of [^{11}C]PBR28

[^{11}C]PBR28 dynamic data was fitted with five different kinetic models, one-tissue and two-tissue reversible model, two-tissue irreversible model along with one-tissue and two-tissue model reversible model with an extra vascular component, which accounts for tracer trapping in vascular binding (Rizzo *et al.*, 2014; Guo *et al.*, 2012) (Figure II-1). The AIC and visual assessment were evaluated to assess the performance of different compartmental models (Akaike, 1973). In the present study, total volume of distribution V_T was the output measurements derived from the candidate kinetic models. (CHAPTER II.1.1)

2.5. Graphic Analysis of [^{11}C]PBR28

Logan graphic analysis was applied to generate a parametric map of [^{11}C]PBR28 PET. Graphic analysis doesn't require any assumptions of specific model of the [^{11}C]PBR28 kinetics in the brain as long as the activity reaches the equilibrium within the scan time. Logan plot was selected for [^{11}C]PBR28 PET based on the reversible feature of the tracer. Depending on fitting of the dynamic data, an optimal threshold time (t*) was selected to define the linear section, and generate the Logan V_T parametric map by estimating the slope of the linear section (Logan, 2000). In the current study, the signal variation in different Logan V_T maps was assessed by CV analysis in four cortices and thalamus (CHAPTER II.2.2).

2.6. SUVR of [^{11}C]PBR28

Cerebellum grey matter was used as a pseudo reference region for SUVR of [^{11}C]PBR28, by dividing the regional 60-90 min [^{11}C]PBR28 summed image by the concentration of radioactivity from the cerebellum (grey matter).

2.7. Amyloid Deposition

The clinical presentation in MCI cohort could be heterogeneous; therefore, 12 MCI patients and 9 healthy controls underwent [^{18}F]Flutemetamol PET scans for assessing the amyloid deposition with the Siemens Biograph 6 PET/CT scanner. A bolus dose of

182 (±2.5) MBq [^{18}F]Flutemetamol was injected intravenously. After 90 min of the injection, the PET data were acquired for 30 mins (90 – 120 min from the injection time) to generate a static [^{18}F]Flutemetamol PET image. The cerebellum (grey matter) was used as the reference region for generating the [^{18}F]Flutemetamol RATIO image (Landau *et al.*, 2014). In the present study, amyloid-positive subject was classified as presence of increased amyloid in at least one of the large cortices or in two separate cortical regions in ROI analysis, and at least one cluster of significant increased amyloid in individual voxel-wise analysis. (CHAPTER II.2.3.3)

2.8. Imaging Analysis

ROI analysis was performed for [^{11}C]PBR28 IRF parametric maps, Logan V_T and compartmental model V_T based on 83-region Hammersmith atlas via SPM8 and Analyze 11.0 (CHAPTER II.3.1). The ROI regions were selected for the following regions: posterior cingulate, frontal, temporal, parietal and occipital lobes. Additionally, ROI analysis was also performed for medial temporal lobe, hippocampus and thalamus. SPSS23 (SPSS, Chicago, Illinois, USA) was used for calculation of the group mean and standard deviation in ROI analysis. The correlation analysis between two groups of variables were conducted using Pearson correlation coefficient in SPSS23, where $p<0.05$ was regarded as a significant correlation.

Voxel-wise comparisons between patients and healthy controls were performed for IRF and Logan V_T [^{11}C]PBR28 parametric maps using SPM8 (CHAPTER II.2.2). For the individual SPM analysis, patient data was compared against a group of healthy controls using Onaway-ANOVA, and the total volume of significant clusters was extracted and calculated in mm^3 using Analyze 11.0.

IV-3. RESULTS

3.1. Demographics and Amyloid Status

Diagnosis group	Total number (Female)	Amyloid Positive	Age (SD)	Age range	MMSE (SD)
MCI	13 (8)	7	70.9 (8.1)	57 - 79	26.8 (2.9)*
HC	9 (5)	0	65.4 (7.5)	54 - 75	29.4 (1.0)

Table IV-1. Demographics for [^{11}C]PBR28 study
*p<0.05

In the Table IV-1, MCI cohort (n=13) revealed significantly lower MMSE score compared with the age-matched healthy controls. The amyloid deposition was evaluated in twelve MCIs and nine controls using [^{18}F]Flutemetamol PET, as a result, seven MCI subjects were classified as amyloid-positive patients based on the criterion illustrated in methods CHAPTER IV.2.7.

3.2. Spectral Analysis

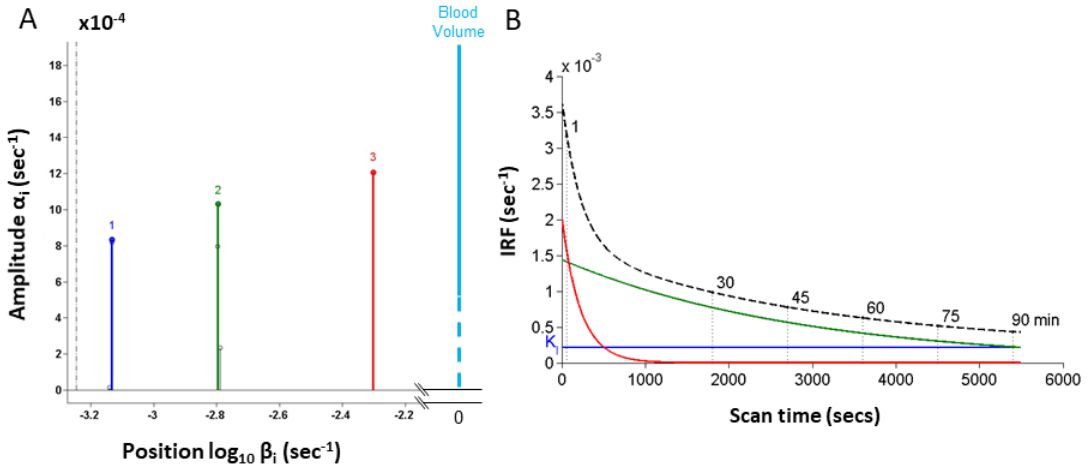


Figure IV-1. Kinetic spectrum and dynamic IRF curve of [^{11}C]PBR28 PET.

A) Kinetic spectrum revealed three spectral components (blue, green, and red) along with a fractional blood volume component (cyan). B) IRF (impulse response function) for [^{11}C]PBR28 activity (dashed line) estimated by the sum of three individual components of the spectrum. The blue component shown as an irreversible peak hence the horizontal line with K_1 in panel B indicating an infinite area under the impulse response function.

Two to three spectral peaks were found in the individuals' [^{11}C]PBR28 kinetic spectrum along with an average blood volume of 6.5%. In Figure IV-1, the two kinetic spectral components with intermediate frequency (green and red) reflected the two tissue components in the brain, while the additional peak (blue), which shows a constant impulse response function, may indicate an additional irreversible component.

Comparing the IRF(t) images with different observation times, IRF at 90 min (IRF-90) demonstrated the global (grey matter) IRF values with the lowest coefficient of variation mean of 18% (±4%), and therefore been selected as the optimal time duration. The IRF-90 of [11C]PBR28 allows voxel-wise quantification of the tracer binding for each patient. In contrast to healthy controls, seven MCI patients revealed voxel-wise significantly increased [11C]PBR28 in frontal gyrus, temporal lobe, parietal gyrus, anterior cingulate gyrus, occipital lobe and thalamus (Figure IV-2). Among these seven MCI patients, five of them were amyloid-positive MCI patients. The total volume of interest (VOI) with significantly increased [11C]PBR28 was calculated in Analyze11.0, where the volumes ranged from 114,982 to 714,801 mm^3 (Table IV-2). As a group, ROI analysis revealed significantly higher [11C]PBR28 binding in amyloid positive MCI subjects compared to healthy controls in multiple cortical regions, particularly in the temporal lobe (Table IV-3). Individually, six MCI patients (four amyloid-positive MCIs) revealed higher regional binding of [^{11}C]PBR28 than the healthy control cohort (mean+2SD).

Subject	Increased volume (mm^3)	^{11}C-PBR28
	IRF	Logan
MCI 1	191073	\
MCI 2	714801	423979
MCI 3	114982	\
MCI 4	260442	165193
MCI 5	177119	\
MCI 6	360328	289142
MCI 7	373282	108237

Table IV-2. The total volume of significantly increased binding in individual MCIs compared to healthy controls at voxel-level, using [^{11}C]PBR28 parametric mapping of IRF-90 and Logan V_T

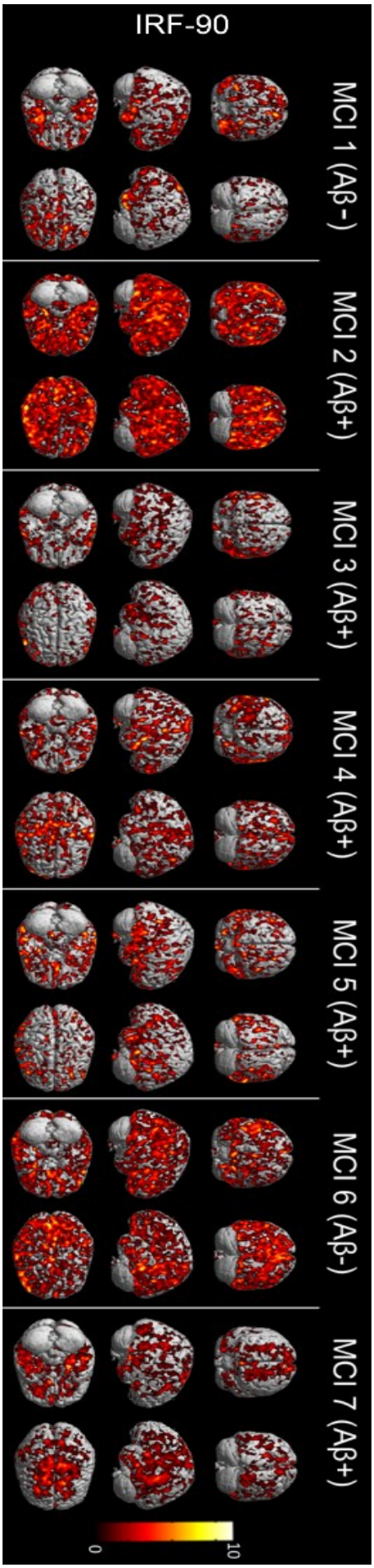


Figure IV-2. Voxel-wise individual SPM analysis of IRF-90 of [11C]PBR28.

Compared to healthy controls, the colour map reveals the clusters of significant increased [11C]PBR28 in individual MCI patient. Aβ+ = amyloid-positive MCI and Aβ- = amyloid-negative MCI.

	Healthy control		Amyloid positive MCIs			
	Mean	SD	Mean	SD	P value	%
Frontal Lobe	3.7E-04	8.0E-05	4.5E-04	8.0E-05	0.074	19%
Temporal Lobe	3.9E-04	6.0E-05	4.8E-04	8.0E-05	0.010*	25%
Parietal Lobe	3.5E-04	6.0E-05	4.1E-04	1.0E-04	0.115	16%
Occipital Lobe	3.6E-04	5.0E-05	4.1E-04	1.1E-04	0.136	14%
Post-Cingulate	3.7E-04	8.0E-05	4.8E-04	1.1E-04	0.025*	31%
Thalamus	4.5E-04	7.0E-05	5.7E-04	1.4E-04	0.024*	29%
MTL	4.2E-04	5.0E-05	5.3E-04	8.0E-05	0.005*	27%
Hippocampus	4.4E-04	5.0E-05	5.4E-04	1.0E-04	0.019*	22%
Amygdala	4.4E-04	6.0E-05	5.7E-04	8.0E-05	0.003*	29%
Cerebellum	3.7E-04	7.0E-05	4.7E-04	1.0E-04	0.023*	27%
Whole brain	3.7E-04	6.0E-05	4.5E-04	9.0E-05	0.049*	20%

Table IV-3. ROI analysis of IRF-90 mean (s^{-1}) and SD (standard deviation) in amyloid-positive MCI and healthy controls. The percentage changes of the means and p values (parametric test) were reported for the group-level comparison.

**P<0.05; MTL = Medial temporal Lobe; SD = Standard deviation.*

3.3. Compartmental Modelling

Depending on the mean of AIC and model preference fraction in different subjects, both two-tissue (2TCM4k) and two-tissue with vascular component models (2TCM4k-1K) have outperformed other models (Figure IV-3). In agreement with previous studies (Rizzo *et al.*, 2014; Bloomfield *et al.*, 2016), the two-tissue model with vascular component (AIC = -84) demonstrated a marginally better fit for the [^{11}C]PBR28 activity than the two-tissue model (AIC = -76).

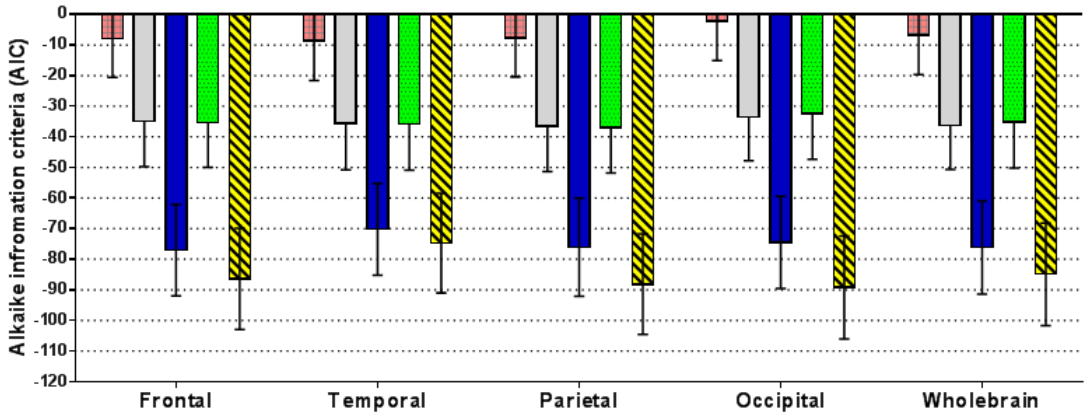


Figure IV-3. AIC (Akaike Information Criteria) values were estimated for [^{11}C]PBR28 PET using 1TCM4k (red), 2TCM3k (grey), 2TCM4k (blue), 1TCM2k-1K (green) and 2TCM4k-1K (yellow) compartmental model. The bar chart showed that the lower AIC values were found in both 2TCM4k and 2TCM4k-1K models in frontal lobe, temporal lobe, occipital lobe and whole brain.

In compartmental modelling, the amyloid-positive MCIs demonstrated a group-wise significantly higher [^{11}C]PBR28 V_T in thalamus (31%, $p<0.04$) and left MTL (32%, $p<0.05$) compared with the control cohort. On the individual basis, five MCI patients (four amyloid-positive MCIs) demonstrated higher V_T compared to healthy controls. Additionally, the [^{11}C]PBR28 IRF-90 parametric map was found highly correlated with V_T that were derived from 2TCM4k-1K and 2TCM4k model (Figure IV-4). No difference was found between amyloid-positive patients and HC in cerebellum V_T (grey matter). No correlation between age and [^{11}C]PBR28 V_T in any given ROI regions.

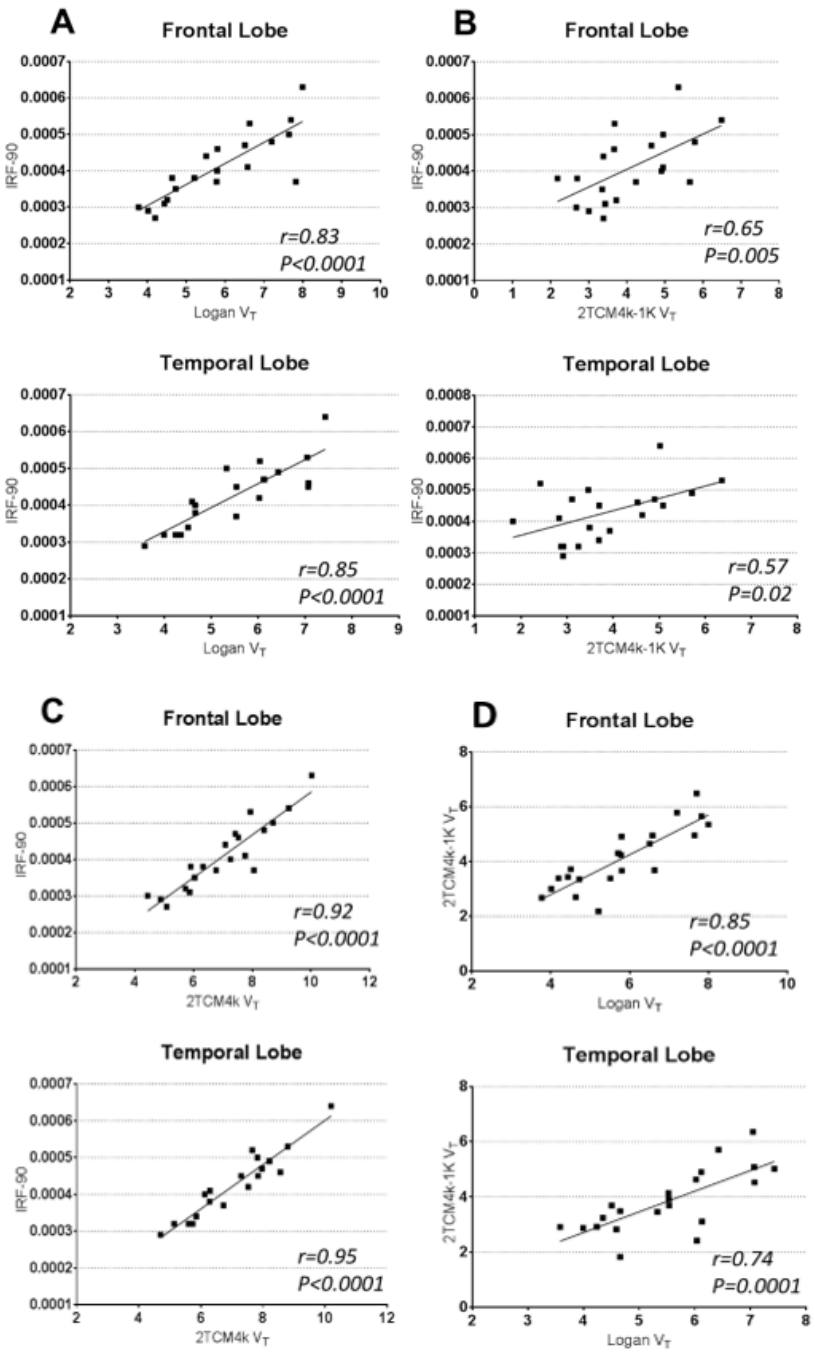


Figure IV-4. The Pearson correlation between [^{11}C]PBR28 binding potentials derived from different modelling methods in frontal lobe and temporal lobe.

A) [^{11}C]PBR28 IRF-90 and Logan V_T; B) [^{11}C]PBR28 IRF-90 and 2TCM4k-1K V_T; C) [^{11}C]PBR28 IRF-90 and 2TCM4k V_T and D) 2TCM4k-1K V_T and 2TCM4k V_T.

3.4. Logan Graphic Analysis

Based on the data fitting, the linear fit of six dynamic data points (from 2000 to 5400 seconds) from the Logan plot were selected to generate the Logan V_T parametric map

of [^{11}C]PBR28 PET, with cohort average slope of 3.8±0.09 and intercept of -3033±214 (mean ± SD).

Logan V_T parametric map showed a good global correlation with the IRF-90 parametric map. Slightly higher global CV was observed in Logan V_T parametric maps (Table IV-4). Unlike kinetic modelling (2TCM4k-1K) and spectral analysis (IRF-90), Logan V_T parametric maps failed to reveal any group-wise difference in microglial activation for the amyloid-positive MCIs versus healthy controls. Individually, ROI analysis of Logan V_T showed higher [^{11}C]PBR28 binding in three MCI patients (two amyloid-positive MCIs). At voxel basis, SPM analysis (VOI) localised clusters of significantly increased [^{11}C]PBR28 in four MCI patients (three amyloid-positive), where the volume ranged from 108,237 to 423,979 mm^3 (Table IV-2).

	CV of IRF		CV of Logan	
	MEAN	SD	MEAN	SD
Frontal Lobe	20%	5%	21%	3%
Temporal Lobe	18%	5%	22%	4%
Parietal Lobe	18%	4%	20%	3%
Occipital Lobe	16%	5%	19%	2%
Posterior Cingulate	15%	4%	16%	5%
Thalamus	22%	4%	27%	5%
Striatum	26%	4%	33%	5%
Hippocampus	13%	3%	22%	4%
Cerebellum	20%	4%	22%	4%

Table IV-4. Coefficient of variation (CV) for IRF-90 and Logan parametric maps of [^{11}C]PBR28 across all subjects. The mean and standard deviation (SD) of CV were reported for both IRF-90 and Logan analysis.

3.5. SUVR

In this study, the SUVR image which normalized to the cerebellum tracer uptake using 60 - 90 summed image has failed to correlate with the [^{11}C]PBR28 V_T derived from compartmental modelling (R= -0.43, p=0.15). And no group-level difference (p=0.47) was found between patients (whole brain SUVR=1.01) and HC (whole brain SUVR=0.99) using the [^{11}C]PBR28 SUVR.

IV-4. DISCUSSION

4.1. Quantification of [^{11}C]PBR28 PET

Quantification of TSPO tracers is challenging due to the genetic TSPO binding affinities and the heterogeneous TSPO cellular distribution in endothelial cells (CHAPTER I.4.4). Compared to the previous TSPO tracers, [^{11}C]PBR28 radioligand demonstrated 80-fold higher binding affinity for TSPO than [^{11}C](R)PK11195; however, discrepancy were found in previous [^{11}C]PBR28 studies (Kreisl *et al.*, 2016; Yoder *et al.*, 2013; Guo *et al.*, 2014; Rizzo *et al.*, 2017; Lyoo *et al.*, 2015; Rizzo *et al.*, 2014). While [^{11}C]PBR28 tracer has been widely used for the last couple of years (Owen *et al.*, 2011a; Brown *et al.*, 2007), a wide variety of methods were applied for quantifying the [^{11}C]PBR28 binding, which could lead to heterogeneous results (Owen *et al.*, 2011a; Brown *et al.*, 2007; Owen *et al.*, 2014; Guo *et al.*, 2014; Yoder *et al.*, 2015; Rizzo *et al.*, 2014; Yoder *et al.*, 2013; Lyoo *et al.*, 2015). Therefore, the objective for the present chapter was to seek the most appropriate approach to quantify the microglial activation using [^{11}C]PBR28 PET in neurodegenerative diseases. I proposed to quantify [^{11}C]PBR28 binding using the spectral analysis for the first time (Fan *et al.*, 2018), which provided a high consistency with compartmental modelling V_T, and allowed further voxel-level comparison of microglial activation in patients with cognitive impairment.

4.2. IRF-90 [^{11}C]PBR28 PET

In order to allow the voxel-level assessment of radiotracer binding to TSPO in individual subjects using [^{11}C]PBR28, the feasibility of generating a [^{11}C]PBR28 parametric map using spectral analysis was evaluated (Veronese *et al.*, 2016; Turkheimer *et al.*, 1994). Spectral analysis separates kinetic components for individual subject and exhibits the spectral components on a spectrum with an amplitude (α) and a frequency (β). The time-course of total changes in [^{11}C]PBR28, which reflected the brain tissue's response to the injected [^{11}C]PBR28 radioligand per second, is called impulse response function (IRF). The dynamic course of the IRF can be estimated by the sum of low and intermediate frequency components in the spectrum. An IRF(t) parametric map of [^{11}C]PBR28 can be generated at different observation time t*. By evaluating the coefficient of variation in different IRF(t) parametric maps, it has

demonstrated that IRF at 90 min created the optimal parametric map of [^{11}C]PBR28 (IRF-90).

Compare to other parametric approaches (e.g. Logan), spectral analysis is very sensitive to the signals, thus it is crucial to demonstrate that spectral analysis did not overestimate the binding by fitting to the noise. Therefore, the outcome measurements derived from spectral analysis, compartmental modelling and Logan graphic analysis were compared. In this study, IRF-90 parametric mapping correlated well with V_T generated by compartmental models (both 2TCM4k and 2TCM4k-1K) and Logan V_T parametric maps, suggesting there is consistency in quantifying [^{11}C]PBR28 binding using spectral analysis and other approaches. Therefore, the IRF-90 parametric mapping generated by spectral analysis was able to produce reliable results without overestimating the signal.

4.3. IRF-90 [^{11}C]PBR28 vs. Other Methods

The heterogeneous distribution of TSPO in the brain has been widely recognized, where TSPO is not only found in the microglial cells, but also expresses in endothelial, smooth muscle, and parenchymal components, and probably in reactive astrocytes. The expression of TSPO in different components also exhibits different kinetic behaviour. Although compartmental modelling is the golden standard of quantification, an on-going debate on the [^{11}C]PBR28 model selection: whether to include an additional irreversible vascular component to represent TSPO tracers that trapped in the vascular endothelium (2TCM4k-1K vs. 2TCM4k) (Rizzo *et al.*, 2014; Kreisl *et al.*, 2016). In our cohort, the vascular model (2TCM4k-1K) demonstrated slightly higher preference than the 2TCM4k model, which is similar to a recent study that evaluate another TSPO tracer [^{18}F]DPA714 (Wimberley *et al.*, 2018).

Previous study have demonstrated that the SUV method without arterial input function could produce variable results in [^{11}C]PBR28 PET based on the multiple physiological factors (Yoder *et al.*, 2013). Therefore, the arterial input function may be necessary for quantifying the [^{11}C]PBR28. Some studies have used the cerebellum as a pseudo reference region for [^{11}C]PBR28, by dividing the regional 60-90 min [^{11}C]PBR28 summed image by the concentration of radioactivity from the cerebellum (Kreisl *et al.*, 2016; Lyoo *et al.*, 2015). However, many studies have demonstrated a reference region is unavailable for [^{11}C]PBR28 which may due to the complexity of the tissue composite and the existence of the non-displayable binding in cerebellum (Hinz & Boellaard,

2015; Guo *et al.*, 2014; Rizzo *et al.*, 2017; Owen *et al.*, 2011a). This is in line with our cohort, where the ratio of the cerebellum tracer uptake failed to correlate with the [^{11}C]PBR28 V_T, and no cohort difference was found between SUVR in patients and HC, indicating the cerebellum may not be served as an ideal reference region for [^{11}C]PBR28.

On the contrary, spectral analysis requires no priory assumptions of kinetic models or assumptions on the reversible nature of a tracer (which graphic analysis requires). Instead, spectral analysis identified heterogeneous spectral components based on the [^{11}C]PBR28 kinetics, and separated components for tracer delivery, vascular binding, and later parenchymal tracer binding by basis function (Cunningham & Jones, 1993; Veronese *et al.*, 2016). As mentioned previously, one of the challenge in quantifying parenchymal binding using any TSPO tracers is to avoid the high vascular binding interference (Rizzo *et al.*, 2017). Spectral analysis accounts for the vascular binding, and is capable to differentiate the high frequency component in spectrum, which represents the blood volume contribution (Rizzo *et al.*, 2014; Cunningham & Jones, 1993). Interestingly, in addition to two tissue spectral components, most subjects demonstrated a third low frequency peak, indicating a possible irreversible trapping component to [^{11}C]PBR28 kinetics. This is consistent with the spectral analysis of the first generation TSPO tracer, [^{11}C](R)PK11195 (Turkheimer *et al.*, 2007).

In contrast to compartmental modelling, the [^{11}C]PBR28 IRF-90 parametric maps differentiate heterogeneous components based on the tracer kinetics for each subject, which requires no prior model selection. Compared to kinetic modelling, both spectral analysis and Logan graphic analysis were able to generate a static parametric map, which enables voxel-level comparison of microglial activation between subjects or between regions. Logan graphic analysis produced a Logan V_T parametric map with a linear interpolation of the dynamic data, whereas spectral analysis generated IRF-90 parametric maps by convoluting multiple kinetic components. The analysis demonstrated that IRF-90 parametric map had a lower noise level (lower CV estimation) in both healthy controls and patients than Logan V_T. Additionally, spectral analysis was able to separate the high frequency component for [^{11}C]PBR28 vascular binding, which established the advantage of quantifying TSPO tracers.

4.4. IRF-90 [^{11}C]PBR28 Reveals Neuroinflammation In MCI Subjects

In 2018, NIA-AA published a research framework suggesting AD should be defined based on the biological construct, such as presentation of amyloid deposition, neurofibrillary tangles (tau) and neurodegeneration (Jack *et al.*, 2018a). In this study, the amyloid deposition was assessed using [^{18}F]Flutemetamol, and seven individuals were classified as amyloid-positive MCI patients. Numerous studies have shown evidences that microglial activation was found being surrounded with amyloid deposition in AD and MCI patients(Fan *et al.*, 2014; Cai, Hussain & Yan, 2014; Okello *et al.*, 2009). In previous study, significantly higher level of microglial activation was observed in MCI patients who had amyloid deposition (Okello *et al.*, 2009).

The results have demonstrated that quantification of [^{11}C]PBR28 using IRF parametric mapping was sensitive enough to differentiate the neuroinflammation in amyloid-positive MCI subjects from healthy controls. In the ROI analysis of IRF-90 parametric maps, amyloid-positive MCIs showed 19-27% group-wise significant increases in microglial activation across temporal lobe and multiple cortical regions. In contrast to other quantification approaches, compartmental modelling V_T only revealed a group-level increased neuroinflammation in thalamus, while Logan failed to reach any group-level significance when compared amyloid-positive MCIs with healthy controls.

As the intermediate phase between healthy controls and Alzheimer's disease, a highly heterogeneous neuropathological presentation was observed in MCI cohort. Therefore, it is crucial to evaluate not only the group-wise results, but also the neuroinflammation in individual MCI patients. Consistent with the neuropathological findings (Joshi *et al.*, 2014; Lucin *et al.*, 2013), IRF-90 of [^{11}C]PBR28 localized a larger volume of voxel-level increased microglial activation in patients who had significant amyloid deposition. IRF-90 revealed more MCI patients and larger individual VOI of voxel-wise significantly increased [^{11}C]PBR28 binding than using Logan V_T. This finding reiterated that IRF-90 of [^{11}C]PBR28 demonstrated a better sensitivity than Logan V_T in detecting the voxel-level changes in microglial activation in MCI patients. Interestingly, one amyloid-positive MCI patient demonstrated significant elevation of microglial activation at voxel-level using both IRF-90 and Logan V_T parametric map, but failed to reveal any increase in regional ROI analysis, indicating the importance of having a static [^{11}C]PBR28 parametric map to allow researchers to interrogate microglial activation at voxel-level.

4.5. Conclusion

In conclusion, the present study has demonstrated for the first time that spectral analysis can be used to quantify the [^{11}C]PBR28 PET and provided reliable results of microglial activation in prodromal AD (Fan *et al.*, 2018). Depending on the tracer kinetics, the spectrum identified a high frequency blood volume with three other spectral components, suggesting a possible low frequency component of vascular trapping along with the two-tissue reversible model for [^{11}C]PBR28. IRF-90 parametric map generated by spectral analysis had a signal-to-noise ratio large enough to reveal voxel-level neuroinflammation in MCI patients on the individual basis, especially those with amyloid deposition. While it was previously shown that results from a TSPO HAB or MAB subgroup can be translated to the entire AD and MCI population (Fan *et al.*, 2015a), more data from different TSPO subgroups and more patients with different cognitive stages were needed to further establish the relevance of spectral analysis of [^{11}C]PBR28. However, this preliminary study has demonstrated a new strategy to quantify [^{11}C]PBR28 PET using spectral analysis, and provided powerful evidences of better sensitivity in differentiating the microglial activation in MCI patients, especially who had amyloid presentation at both group and individual level.

CHAPTER V. QUANTIFICATION OF [^{11}C]BU99008 PET IN PATIENTS WITH ALZHEIMER'S DISEASE

V-1. INTRODUCTION

In CHAPTER III and CHAPTER IV, two novel TSPO tracers for microglial activation were evaluated in human trial. Apart from microglial activation, astrocytes are a major type of glial cells in the CNS which regulate homeostasis, regeneration, and defence function in the brain. The receptors and intracellular signalling cascades in astrocytes allow them to quickly detect and become activated to any alteration in brain milieu to maintain homeostasis (Sofroniew, 2015, 2014). Abnormal serum proteins, aggregated proteins, cytokines, chemokine and purines can trigger astrocyte reactivity; additionally, the absence of specific signals, such as growth factors or neurotransmitters from neighbouring cells can also lead to astrocyte reactivity (Burda & Sofroniew, 2014; Sofroniew, 2015). Astrocytes always act in an active surveillance state, like microglial cells. As discussed previously, apart from amyloid and tau tangles, neuroinflammation and synaptic dysfunction in AD play a significant role and culminate in severe neuronal loss. For the last decade, microglial activation has been the main focus of the glial mediated neuroinflammation in AD research. However, recent studies have suggested that astrocyte alterations could play a fundamental role in many neurodegenerative diseases (Gomez-Arboledas *et al.*, 2018; Lynch *et al.*, 2010; Hallmann *et al.*, 2017; Radford *et al.*, 2015; Tyacke *et al.*, 2012). Neuroimaging studies have demonstrated that astrocyte reactivity was detected in the human brain prior to the onset of AD symptoms (Carter *et al.*, 2012). It is shown that in AD mouse models, activated astrocytes preceded amyloid deposition (Heneka *et al.*, 2005). At molecular level, astrocyte reactivity can be detected by monitoring the increased expression of the intermediate filament protein, glial fibrillary acidic protein (GFAP). Studies in both animal models and post-mortem brain have revealed the presence of reactive astrocytes in the surroundings of amyloid plaques. GFAP levels were closely associated with the Braak's stage, again emphasising the likely role of astrocyte reactivity in disease progression. (Carter, Meng & Thompson, 2012; Olabarria *et al.*, 2010; Simpson *et al.*, 2010) An *in vitro* study has demonstrated that isolated human astrocytes from the adult cerebral cortex can be induced by exogenous Aβ and collaborate with neurons to spread

and produce neurotoxic tau and Aβ42 oligomers (Dal Prà *et al.*, 2015). Oksanen et al. (2017) have demonstrated a direct association between astrocytes and the pathogenesis of AD using an induced pluripotent stem cell disease model. They found that astrocytes under AD conditions generated significantly more beta-amyloid, cytokines and reactive oxygen species than the astrocytes in healthy controls (Oksanen *et al.*, 2017). However, recent studies shared a different view, suggesting a protective theory of reactive astrocyte (Masgrau *et al.*, 2017; Sofroniew, 2015). Kraft et al. found reactive astrocytes in AD mice showing a protective role by preventing further accumulation of amyloid plaques by phagocytising and degrading amyloid beta (Kraft *et al.*, 2013). This protective theory of astrocyte was in agreement with the *in vitro* astrocyte studies (Xiao & Hu, 2014).

When astrocytes become active, there is an overexpression of I_2BS on the mitochondrial membrane (Tyacke *et al.*, 2012). Therefore, a radioligand was developed to target I_2BS for evaluating the astroglial activation *in vivo*. [^{11}C]BU99008 PET ligand showed a high binding affinity for the I_2BS *in vitro* (Tyacke *et al.*, 2012), with good blood-brain barrier penetration and a clear differentiation between the ligand in regions with known expression of I_2BS and the reference region (Kealey *et al.*, 2013; Parker *et al.*, 2014). A previous study demonstrated that the reversible two tissue compartmental model showed the best fitting of the [^{11}C]BU99008 data in healthy controls and found a heterogeneous [^{11}C]BU99008 distribution in the brain (Tyacke *et al.*, 2018). In this study, the [^{11}C]BU99008 was used to evaluate the astrocyte reactivity in AD and MCI patients. In order to further evaluate the influence of astrocyte reactivity on other biomarkers in AD, [^{18}F]FDG and [^{18}F]Florbetaben PET were performed to assess the individual's cerebral glucose metabolism and amyloid deposition, respectively.

1.1. Objectives

1- To evaluate the optimal quantification method for [^{11}C]BU99008 PET in AD subjects, and generate appropriate parametric mapping for astrocyte reactivity

2- To evaluate relationship between astrocyte activation, amyloid deposition and glucose metabolism in AD and MCI subjects using [^{11}C]BU99008, [^{18}F]FDG and [^{18}F]Florbetaben PET images

We hypothesized that astrocyte activation could be detected in AD using novel astrocyte marker [^{11}C]BU99008 PET, and this positively correlates with the amyloid deposition and reduction of glucose metabolism.

V-2. METHODS

2.1. Demographics

	Number	Age (yrs.) Mean (SD)	Age (yrs.) range	MMSE Mean (SD)	MMSE range
Patients	11	73.6 (4.6)	66-82	22.2 (4.0)*	17-29
Healthy controls	10	70.2 (5.5)	59-78	28.8 (1.0)	26-30

Table V-1. Demographics of patients and control subjects.

**p<0.05. MMSE = Mini Mental State Examination score (full score 30); SD = Standard deviation; and yrs. = years. There was no significant difference between patients and healthy controls in age. The patient group showed statistically significant lower MMSE score compared with healthy controls.*

Subjects were recruited from memory clinics, advertisements and research registries. Ethical approval for this study was granted by the local and regional research ethics committee (West London & GTAC Research Ethics Committee), and approval to administer radiotracers by the Administration of Radioactive Substances Advisory Committee (ARSAC) UK. Written informed consent was obtained from all participants. All the subjects met the NIA-AA (McKhann et al., 2011) or Petersen criteria (Petersen and Knopman, 2006). Twenty-one subjects were recruited in this study, including 11 patients (MMSE=22.2±4.0) with AD or MCI (Appendix 3), and ten age-matched healthy controls (MMSE=28.8±1.0) (Table V-1). Each subject underwent T1 and T2 weighted MRI scan for anatomical structural information and volumetric analysis.

2.2. Blood Data Analysis of [^{11}C]BU99008 PET

For [^{11}C]BU99008 PET, 15 mins of continuous blood sampling was performed to monitor the arterial tracer activity in the whole blood. Twelve discrete arterial blood samples were taken at 5, 10, 15, 20, 25, 30, 40, 50, 60, 70, 80, and 100 min during the PET scan. The tracer activity in the whole blood and plasma samples were estimated in

the well-counter. The parent fraction of the [^{11}C]BU99008 was measured by HPLC analysis using discrete blood samples.

The parent fraction of [^{11}C]BU99008 and the POB data were both fitted with a sigmoidal fitting. The total plasma activity from the first 15 mins was calculated by applying the POB model to the 15 mins' total blood activity measurement. The parent fraction curve was applied to total plasma to generate the parent plasma input function.

2.3. Acquisition of [^{11}C]BU99008 PET

All PET scans were performed at Invicro Centre for Imaging Sciences, London, UK using the Biograph TruePoint 6 PET/CT scanner. The spatial resolution of the scanner is 2.056mm x 2.056mm x 2mm (voxel size). An initial CT was acquired for the attenuation correction. After injection of 256 (±24) MBq, the dynamic emission images were acquired over 120 mins and reconstructed as 29 time frames: 8x15s, 3x60s, 5x120s, 5x300s, and 8x600s. The Fourier re-binning using 2D filtered discrete inverse Fourier transform algorithm, with 5mm isotropic Gaussian filter was used for reconstruction. The correction was applied for attenuation, random, and scatter based on the 3-dimensional ordinary Poisson ordered-subset expectation maximization algorithm. Additional non-attenuation corrected dynamic [^{11}C]BU99008 PET images were also generated for motion correction in MIAKAT^{TM} software (www.miakat.org). The motion of the PET data was corrected using a frame-to-frame rigid registration algorithm by selecting one frame as the reference. The frame-by-frame registration was performed on the non-attenuated corrected dynamic PET data, which often provides more accurate movement parameters than the attenuation corrected data.

2.4. Quantification of [^{11}C]BU99008 PET

2.4.1 Quantification of [^{11}C]BU99008 PET using compartmental modelling

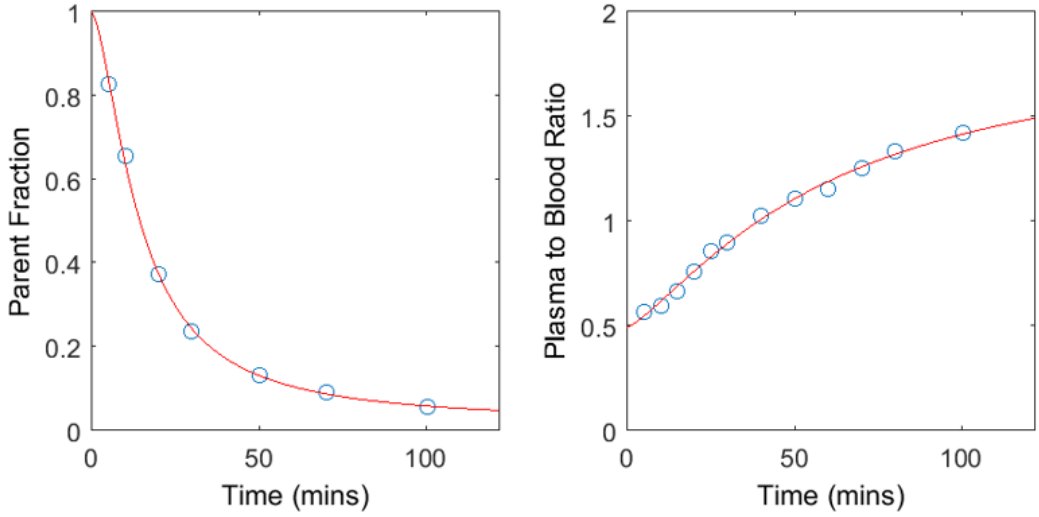


Figure V-1. Parent fraction was fitted with a (decreasing) sigmoid model and plasma over blood ratio was fitted with an (increasing) sigmoid model in an AD patient.

MIAKAT^{TM} software, which is developed by Invicro (A Konica Minolta Company) on the MATLAB 2017 and SPM12 function, was used to generate the arterial parent plasma input function and kinetic compartmental modelling for the [^{11}C]BU99008 PET. Parent fraction and plasma to blood ratio were modelled by sigmoid curve (Figure V-1). The parent fraction curve showed a fast metabolism. Interestingly, the first POB ratio measured at 5 min was lower than 1, indicating the tracer rapidly transported into red blood cells and might also bind to other proteins on platelets. The POB ratio was then gradually increased, suggesting the metabolites may not enter red blood cells or some radioactive metabolites may persist in the plasma. By using the non-attenuation corrected PET, a frame-to-frame realignment was applied to the dynamic [^{11}C]BU99008 PET to correct for motion. The individual brain ROI (region of interest) atlas was generated using the corresponding MRI image and a modified CIC atlas version 2.0 (Fonov *et al.*, 2011; Tziortzi *et al.*, 2014) via segmentation and registration. After that, the TAC for each ROI region was calculated by sampling the tracer activity for motion-corrected registered dynamic PET. The parent plasma input function and TACs were used to model the underlying biological system for [^{11}C]BU99008 tracer.

To further verify the model preference in aged healthy controls and patients with AD / MCI, I have performed one-tissue compartmental model (1TCM2k) and multilinear analysis (MA1) for patients and age-matched controls, where Akaike Information Criterion (AIC) for each model was calculated to select the best model to describe the [^{11}C]BU99008 uptake in brain. (CHAPTER II.1.2)

2.4.2 Quantification of [^{11}C]BU99008 PET using spectral analysis

Spectral analysis was applied to the [^{11}C]BU99008 and separated the tracer activity into heterogeneous spectral peaks for component of tracer delivery, vascular binding, and later tissue binding (Cunningham & Jones, 1993; Veronese *et al.*, 2016). The [^{11}C]BU99008 IRF parametric maps were generated with a decay constant λ of 0.00056629 s^{-1}. Different times (1 min, 30 min, 45 min, 60 min, 75 min, 90 min, 105 min and 120 min) were used to create the spectral analysis IRF(t) parametric maps of [^{11}C]BU99008 PET using MICKPM (Modelling, Input functions Compartmental Kinetics, and Parametric Map) (Fan *et al.*, 2018; McGinnity *et al.*, 2017). To determine the best IRF(t), repeated ANOVA and the F-ratio were estimated (Equation 8). Tracer differentiation among healthy controls, patients, and subgroup of seven amyloid positive patients were evaluated for different IRF(t) to help determine the most robust IRF(t) for [^{11}C]BU99008. Their correlation with 2TCM4k compartmental model was also assessed.

2.4.3 Quantification of [^{11}C]BU99008 PET using graphic analysis

Previous biological studies and compartmental modelling of [^{11}C]BU99008 suggested that [^{11}C]BU99008 is reversible, which gave the preference to the Logan graphic analysis (Logan, 2000). Based on the quality of graphic linear fitting, the optimal threshold time (t*) for [^{11}C]BU99008 Logan analysis was selected. MIAKAT was used to generate the [^{11}C]BU99008 Logan V_T parametric maps using the parent plasma input function.

2.4.4 Quantification of [^{11}C]BU99008 PET using SUV

To investigate whether simplified quantification method is able to perform as well as arterial input for this novel astrocyte tracer, SUV was generated for the [^{11}C]BU99008 PET (CHAPTER II.2.4). To calculate the [^{11}C]BU99008 SUV, based on the TAC and

tracer washout rate for 120 mins, image frames of 60-120 min and 30-120 min were summed, and their SUV (Equation 10):

2.5. Quantification of [^{18}F]Florbetaben PET Using Reference Input Approach

In this study, the brain amyloid status for each subject was measured by the cerebellum RATIO images of [^{18}F]Florbetaben, which were generated by normalizing the [^{18}F]Florbetaben 60-90 min (after scan start) summed image to the regional mean uptake of cerebellum (CHAPTER II.2.3.3).

2.6. Quantification of [^{18}F]FDG PET Using Reference Input Approach

The glucose metabolism was calculated by the normalizing the static [^{18}F]FDG image to the pons. Image calculator in Analyze 11.0 was used to generate the RATIO images for [^{18}F]FDG PET. (CHAPTER II.2.3)

2.7. Imaging Processing

2.7.1 Region of Interest (ROI) analysis

In regional ROI analysis, the SMP12 in MATLAB 2017 were used to perform (CHAPTER II.3.1) based on the requirement of MIAKAT. The regional activity of [^{11}C]BU99008 was sampled at the following cortical regions: frontal lobe, temporal lobe, parietal lobe, occipital lobe, whole brain, hippocampus and medial temporal lobe. Group mean and standard deviation were calculated in SPSS23 (Chicago, IL, USA) for patient and healthy control cohort. The amyloid positivity was described in CHAPTER II.2.3.3.

2.7.2 SPM voxel-wise image analysis

The voxel-wise group comparison between patients and healthy controls were performed using the two-tailed t test in SPM12. Compared to healthy controls, the significant clusters of increased astrocyte activation and amyloid deposition in the patient group were interrogated at voxel-level using a minimal cluster threshold at $p<0.01$ with an extent threshold of 50 voxels. The clusters of significantly decreased glucose metabolism in the patient group compared with healthy controls were detected at a voxel-level using the same cluster threshold ($p<0.01$ and 50 voxels).

Apart from the group-wise result, the individual levels of astrocyte reactivity, glucose metabolism and amyloid deposition were evaluated. In this study, the individualized SPM t-map was generated by comparing each patient against a group of healthy controls using SPM8 one-way ANOVA analysis (Fan *et al.*, 2015b), which reflected the level of biomarker changes in each individual in relation to the control cohort. (CHAPTER II.3.2)

2.7.3 BPM voxel-wise correlation analysis

In order to evaluate the relationship between different pathologies, the Z-score map (Zmap) of each PET modality was created to present the individual level of astrocyte reactivity, glucose metabolism and amyloid deposition in relation to the healthy controls' mean and variance (standard deviation). The Z-score maps of [^{11}C]BU99008, [^{18}F]FDG and [^{18}F]Florbetaben PET tracers were generated (Equation 11).

The Zmap of each patient demonstrates the individual level of astrocyte reactivity, glucose metabolism, and amyloid deposition different from the control cohort. The voxel-level correlation between astrocyte reactivity, glucose metabolism and amyloid deposition were estimated via BPM toolbox. The correlation in all patients, and subgroups of amyloid-positive and amyloid-negative patients were evaluated separately.

V-3. RESULTS

3.1. Brain Amyloid Status

As a group, both ROI and SPM analysis have demonstrated a significant elevation of amyloid deposition in patients compared with healthy controls (Table V-2). Individually, seven out of eleven patients were classified as brain amyloid positive (CHAPTER II.2.3.3).

	FL	TL	PL	OL	P-Cing	MTL	Brain
Patients (n=11)							
MEAN	1.60	1.49	1.58	1.49	1.73	1.27	1.55
SD	0.35	0.30	0.34	0.26	0.40	0.21	0.32
P value	0.011	0.010	0.005	0.015	0.007	0.099	0.008
% Increase	24%*	21%*	25%*	17%*	27%*	10%	23%*
HC (n=10)							
MEAN	1.29	1.23	1.26	1.27	1.36	1.16	1.27
SD	0.14	0.10	0.11	0.09	0.14	0.08	0.11

Table V-2. ROI (grey matter) results for amyloid deposition in patients and healthy controls using [^{18}F]Florbetaben RATIO PET.

*Patients showed group-level significantly increased amyloid deposition in frontal lobe, temporal lobe, parietal lobe, occipital lobe, posterior cingulate and whole brain compared with healthy controls. *p <0.05; SD = Standard deviation; HC = Healthy Control; FL = Frontal lobe, TL = Temporal lobe, PL = Parietal lobe; OL = Occipital lobe; P-Cing = Posterior cingulate; MTL = medial temporal lobe.*

3.2. Results of [^{11}C]BU99008 Quantification

3.2.1 Results of [^{11}C]BU99008 PET using compartmental modelling

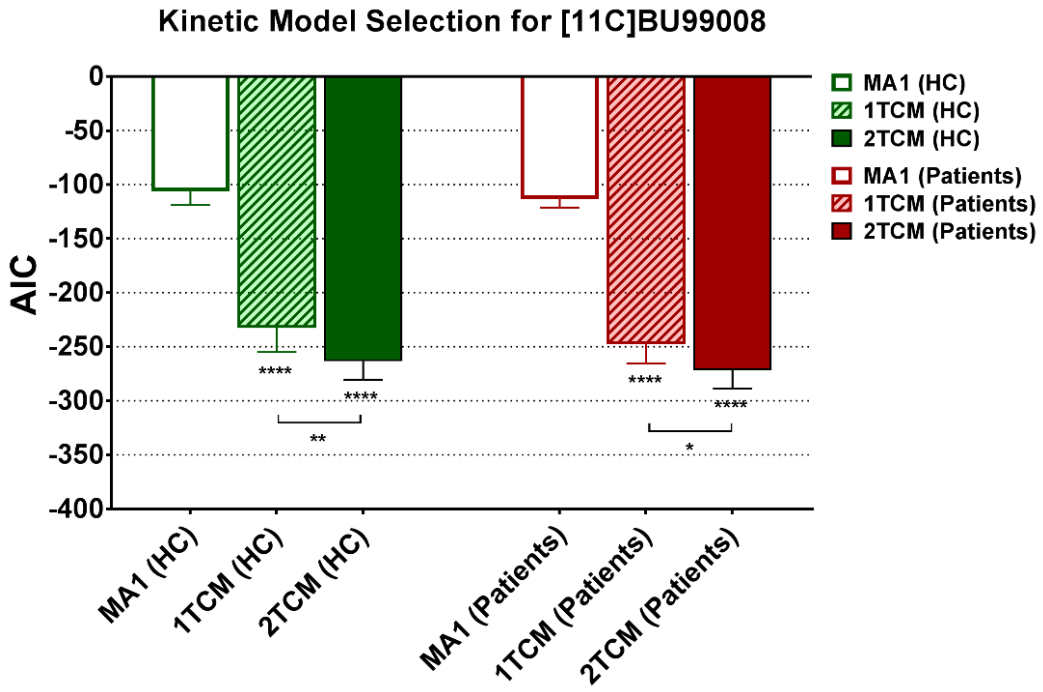


Figure V-2. Kinetic model selection of [^{11}C]BU99008 PET in healthy controls and patients with AD and MCI.

*Bar chart showing MA1 (clear bar), 1TCM (striped bar) and 2TCM (filled bar) models' mean and standard deviation of whole brain AIC. The bars for healthy controls are in green colour and the bars for patients are in red. One-way ANONVA and Turkey's multiple comparisons test were performed in healthy control and patient's cohort, where *p<0.05, **p<0.01, and ****p<0.0001.*

Previous study showed that two-tissue compartmental model had the lowest Akaike Information Criterion and the greatest reliability in test-retest analysis in healthy controls (Tyacke *et al.*, 2018). In the current study, AIC was applied to one-tissue, two-tissue and MA1 kinetic models in both healthy controls and patients with AD or MCI, where two-tissue compartmental model (2TCM4k) provided the best fitting of the [^{11}C]BU99008 tracer distribution. Additionally, 2TCM4k model demonstrated significantly lower AIC values compared with MA1 and 1TCM2k in both healthy controls and patients (Figure V-2).

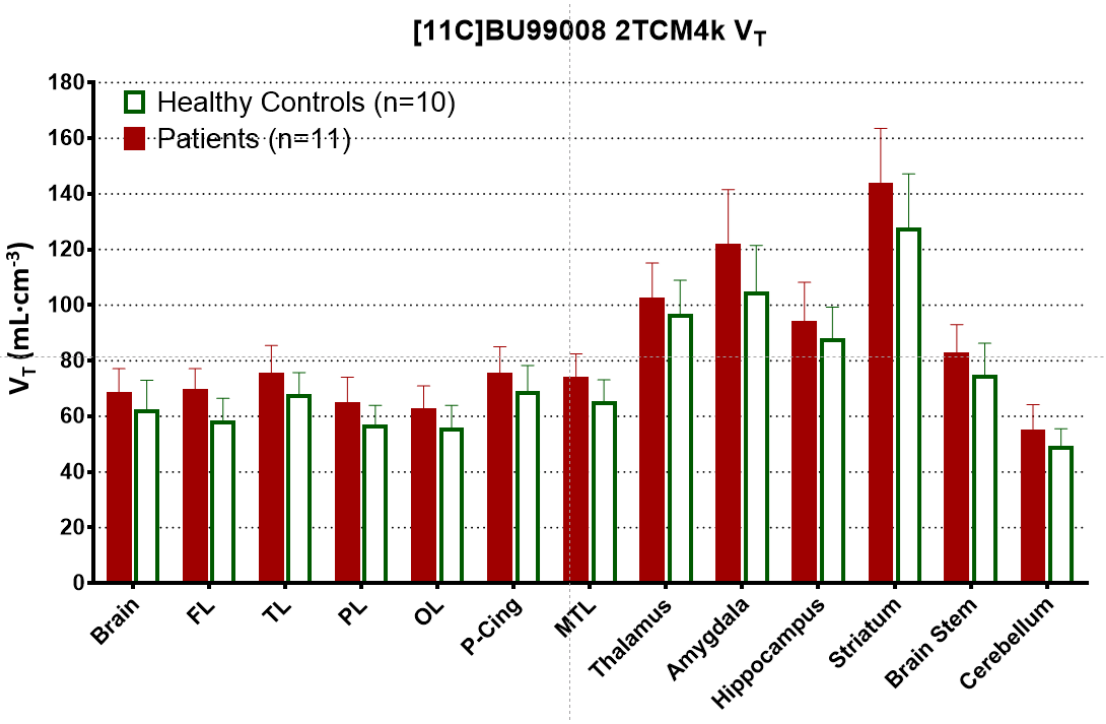


Figure V-3. Bar chart revealing regional [^{11}C]BU99008 distribution (V_T) in 11 patients (red) and 10 healthy controls (clear).

Bars shows mean and the standard deviation (SD) of 11 patients and 10 healthy controls in 13 ROI regions. FL=Frontal lobe, TL=Temporal lobe, PL=Parietal lobe; OL=Occipital lobe; P-Cing=Posterior cingulate; MTL = medial temporal lobe.

The [^{11}C]BU99008 V_T estimation using 2TCM4k model has revealed a heterogeneous brain uptake (Figure V-3). Temporal lobe demonstrated a slightly higher uptake than other brain cortices. In the subcortical regions, striatum, amygdala, thalamus and hippocampus revealed a relatively high tracer uptake, whereas cerebellum has showed a consistently lower uptake among both patients and healthy controls. [^{11}C]BU99008 distribution in striatum (HC=125 mL·cm^{-3}; Patients=144 mL·cm^{-3}) has demonstrated 1.5 and 1.6 times higher than that in the cerebellum (HC=49 mL·cm^{-3}; Patients=55 mL·cm^{-3}) in healthy and patient cohort, respectively ($p<0.0001$).

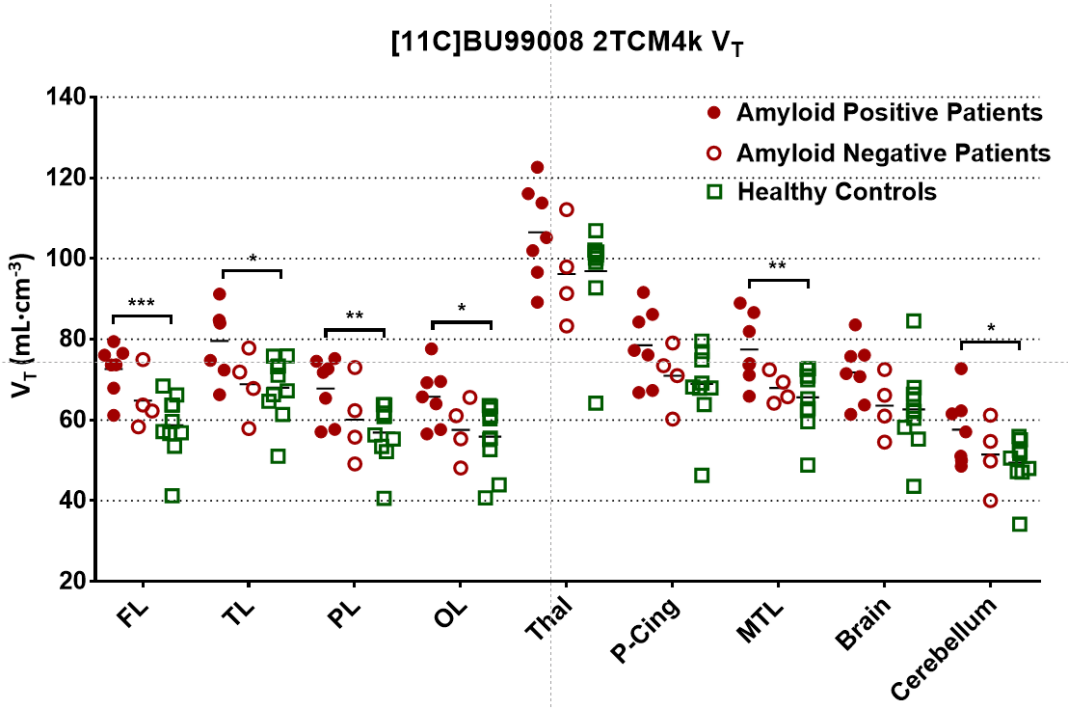


Figure V-4. Scatter plot demonstrating the regional [^{11}C]BU99008 V_T using 2TCM4k model.

*Scatter plot demonstrated [^{11}C]BU99008 V_T in seven amyloid positive patients (red filled circle), four amyloid negative patients (red unfilled circle) and ten healthy controls (green square). * p<0.05, ** p<0.01, ***p<0.005. FL=Frontal lobe, TL=Temporal lobe, PL=Parietal lobe; OL=Occipital lobe; P-Cing=Posterior cingulate; MTL = medial temporal lobe.*

Astrocyte activation was found significantly increased at frontal lobe, parietal lobe and medial temporal lobe in patients group compared with healthy controls. Based on the amyloid status, seven patients were classified as amyloid positive patient (CHAPTER II.2.3.3). In amyloid positive patients, [^{11}C]BU99008 V_T demonstrated a group-wise significant increase at frontal lobe (24%), temporal lobe (17%), parietal lobe (19%), occipital lobe (18%), medial temporal lobe (18%), amygdala (29%), striatum (19%) and cerebellum (17%) compared with healthy controls. Conversely, amyloid negative patients failed to reveal any group-wise increase in astrocyte activation (Figure V-4). Comparing the amyloid positive and amyloid negative patients, astrocyte activation in amygdala was found to be significantly higher in amyloid positive patients.

3.2.2 Results of [^{11}C]BU99008 PET using spectral analysis

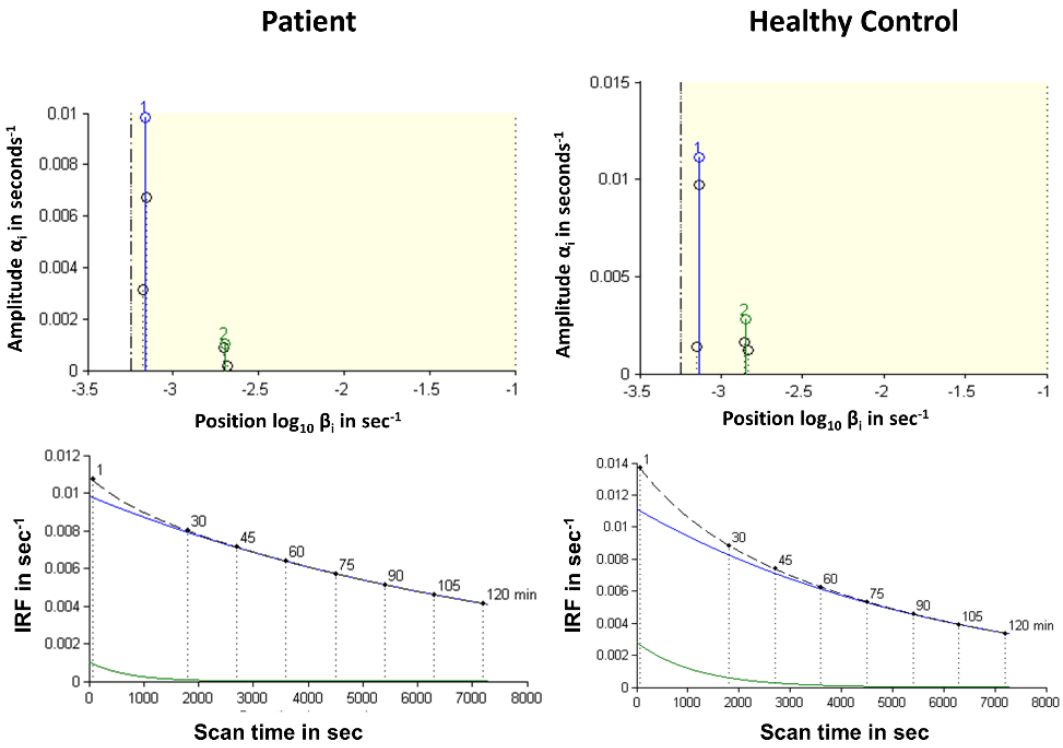


Figure V-5. Kinetic spectrum and IRF plots of [^{11}C]BU99008 PET of whole brain.

Upper panel showing the spectrum revealed two different spectral components in both patient (at position βi of 6.89e-04 s^{-1} and 3.25e-03 s^{-1} with amplitude αi of 9.97e-3 s^{-1} and 1.43e-3 s^{-1}) and healthy control (at position βi of 7.32e-04 s^{-1} and 1.43e-03 s^{-1} with amplitude αi of 1.11e-2 s^{-1} and 2.83e-3 s^{-1}). Lower panel demonstrated the predicated curves (dashed black line) using spectral analysis IRF (impulse response function) for [^{11}C]BU99008, which calculated by the sum of the two components.

In spectral analysis of [^{11}C]BU99008, two distinct spectral components were revealed in both patients and healthy control subjects (Figure V-5). Those two equilibrating components in spectrum demonstrated a possible two-tissue compartmental model, which was consistent with our kinetic model selection.

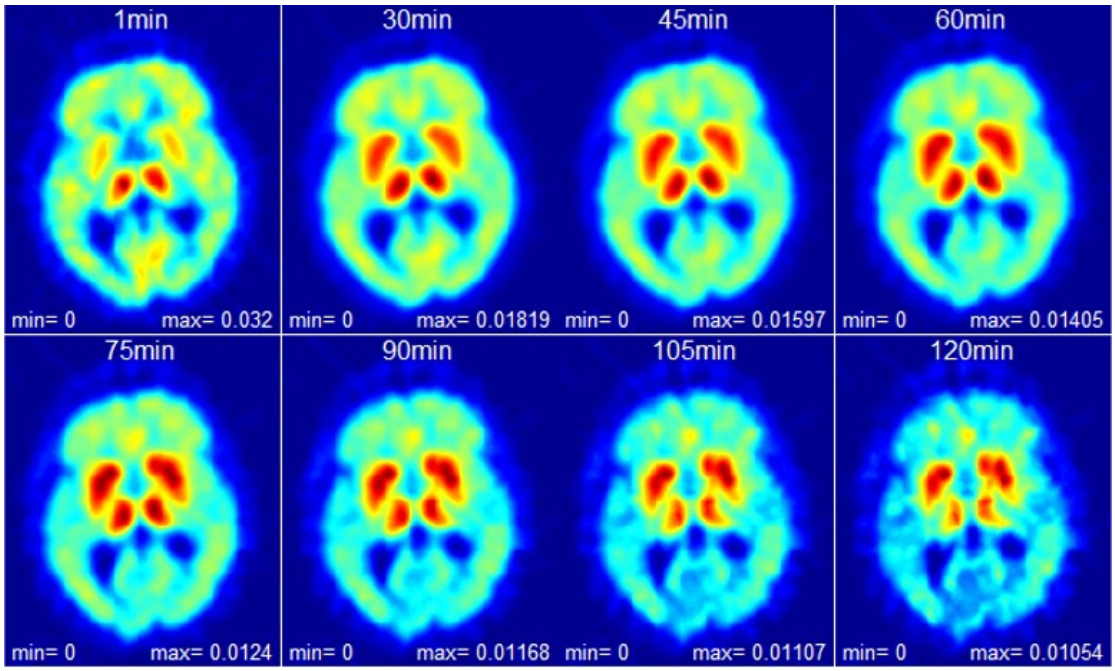


Figure V-6. Impulse Response function (IRF) parametric maps generated for [^{11}C]BU99008 PET.

Generating spectral analysis IRF parametric images for [^{11}C]BU99008 using different set of observation time (IRF-1, IRF-30, IRF45, IRF-60, IRF-75, IRF-90, IRF-105, and IRF-120)

Different IRF parametric maps were generated based on different observation time (Figure V-6). Repeated ANOVA has revealed a significant effect of the observation time used in different IRF parametric map generation on the total tracer activity in the brain, F-statistic = 496.49 (degree of freedom for time = 1, degree of freedom for error = 25), with a Greenhouse-Geisser corrected p value = 1.8E-18. [^{11}C]BU99008 IRF parametric maps generated with observation time of 120 min (IRF-120) demonstrated a good sensitivity in differentiating AD patients from healthy controls. When reduced the observation time to 105 min or 90 min, the pathological difference in patient group remained but with less significance (Figure V-7). When the observation times were shorter than 75 min, IRF parametric maps (IRF-75, IRF-60, IRF-45, IRF-30 and IRF-1) were unable to differentiate the astrocyte reactivity in patients from the healthy controls. Coefficient of variation in whole brain demonstrated a global mean CV of 15.6% in IRF-120, CV of 16.4% in IRF-105 and CV of 17.7% in IRF-90 parametric maps. Good correlation was found between V_Ts derived from IRF-120 and two-tissue compartmental model in cortical lobes (Figure V-8). Additionally, good correlation was

found in both high uptake (striatum=0.77, p<0.002) and low uptake regions (cerebellum=0.91, p<0.001).

.

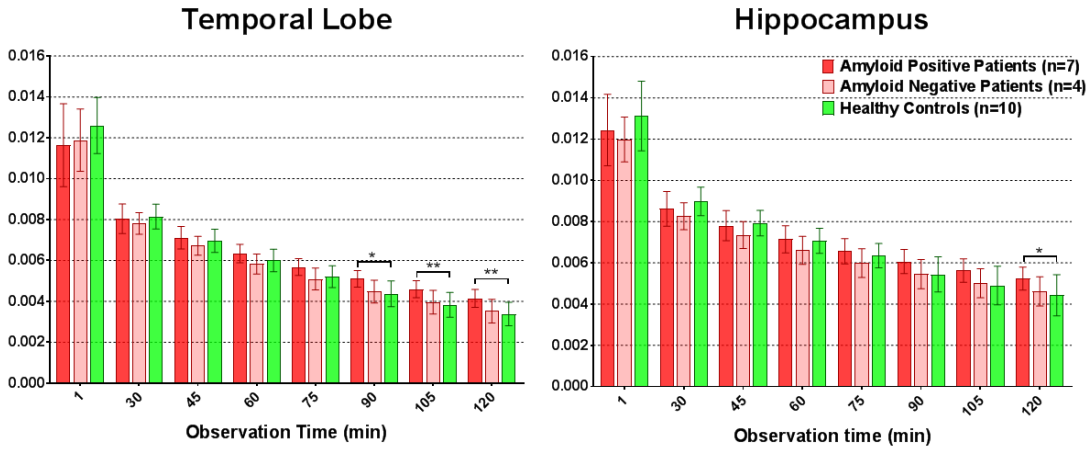


Figure V-7. [^{11}C]BU99008 IRF (s^{-1}) in amyloid positive patients, amyloid negative patients and healthy controls at temporal lobe (Left) and hippocampus (Right) using 8 different IRF parametric images.

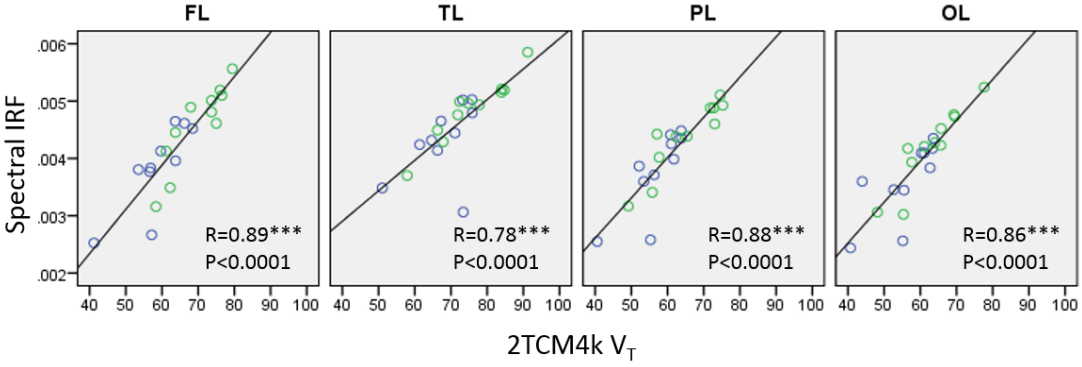


Figure V-8. Correlation between [^{11}C]BU99008 Spectral IRF-120 parametric maps and 2TCM4k V_T in frontal lobe (FL), temporal lobe (TL), parietal lobe (parietal lobe) and occipital lobe (OL). Blue circle=healthy control; green circle= patient.

Regional ROI analysis of [^{11}C]BU99008 IRF-120 has demonstrated a group-wise significant increase in patients at whole brain, frontal, temporal, parietal, occipital lobe, and poster-cingulate compared with healthy controls. In the subgroup of amyloid positive patients, significantly increased astrocyte reactivity was found in the same area, with additional ROI regions at anterior cingulate, thalamus, striatum, brainstem, hippocampus, precuneus and amygdala. In the frontal lobe and thalamus, the astrocyte

reactivity was significantly higher in amyloid positive patients than the amyloid negative patients. (Figure V-9)

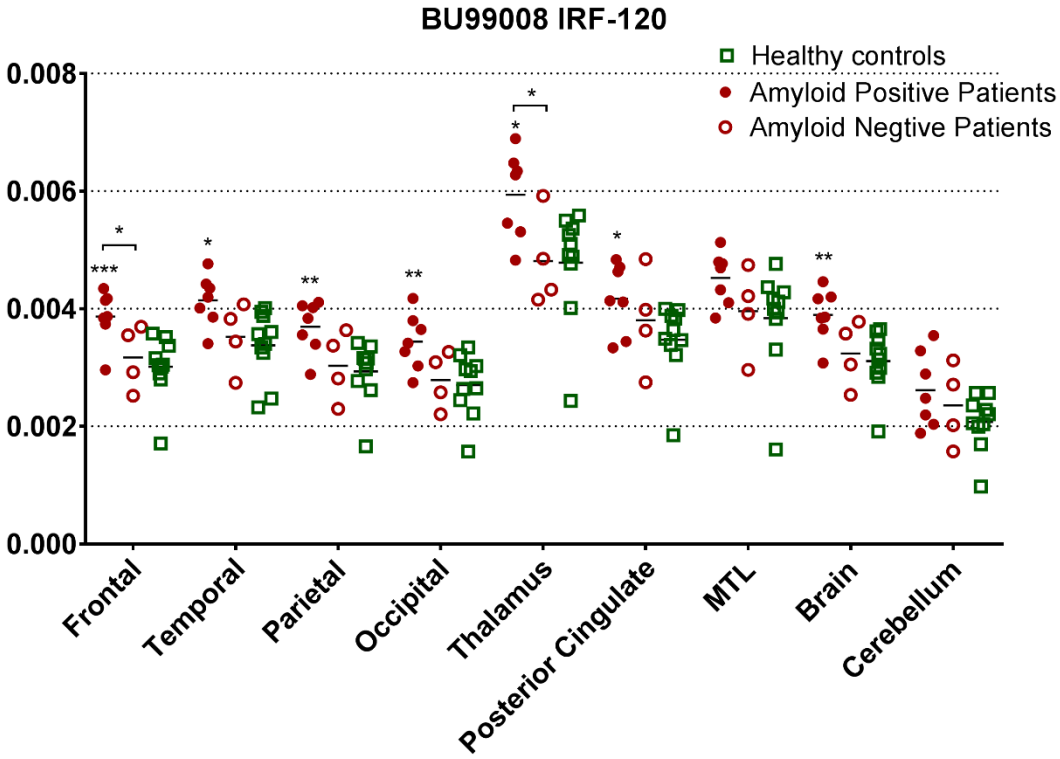


Figure V-9. Scatter plot demonstrating the regional [^{11}C]BU99008 IRF-120 (s^{-1}) in amyloid positive patients (red filled circle), amyloid negative patients (red unfilled circle) and healthy controls (green square).

*Amyloid positive patients showed significant higher astrocyte reactivity in frontal lobe, temporal lobe, parietal lobe, occipital lobe, thalamus, posterior cingulate, striatum, and whole brain. In the frontal lobe and thalamus, the astrocyte reactivity was significantly higher in amyloid positive patients compared with the amyloid negative patients. *p<0.05; ** p<0.01; ***p<0.005; MTL = medial temporal lobe.*

3.2.3 Results of [^{11}C]BU99008 PET using Logan graphic analysis

The graphic linear fitting of the whole brain [^{11}C]BU99008 activity has showed that the dynamic data from 2000 to 7200 seconds (ten data points) provided the optimal of the data with fitness visual assessment. Logan linear plot (whole brain slope = 79.9 ± 8.34 intercept = -94.5 ± 9.9) can be used to generate the Logan V_T parametric map of [^{11}C]BU99008 PET.

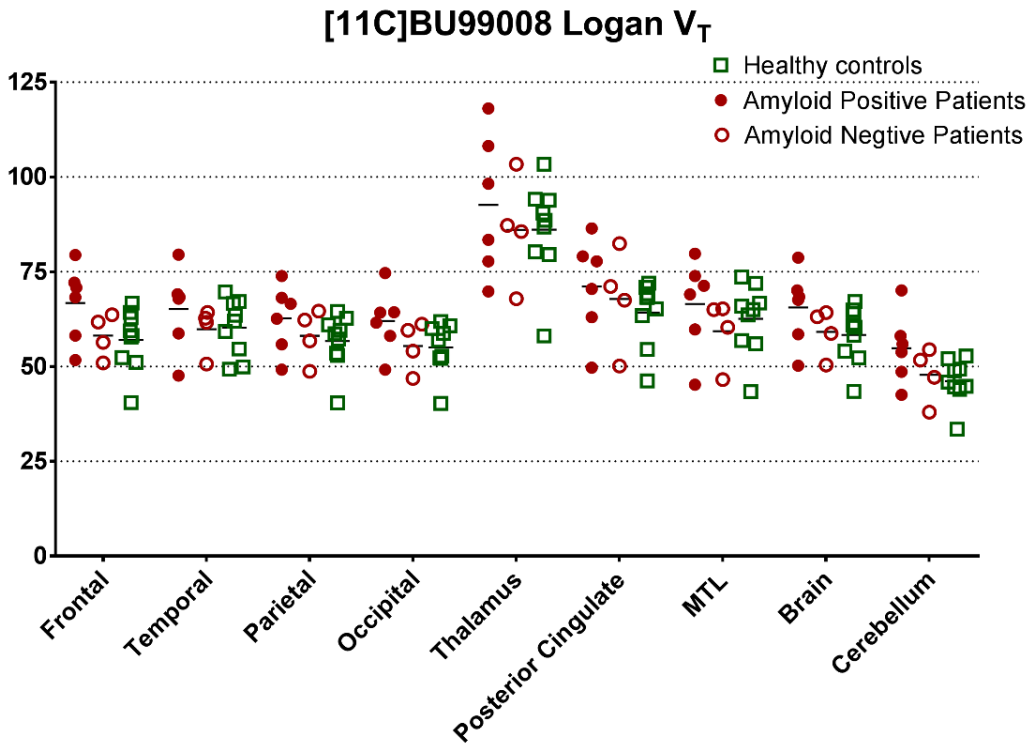


Figure V-10. Scatter plot demonstrating the regional [^{11}C]BU99008 Logan V_T in amyloid positive patients (red filled circle), amyloid negative patients (red unfilled circle) and healthy controls (green square).

There were no statistical significances found between any groups using V_T derived from Logan analysis. FL=Frontal lobe, TL=Temporal lobe, PL=Parietal lobe; OL=Occipital lobe; P-Cing=Posterior cingulate; MTL = medial temporal lobe.

Among amyloid positive patients, amyloid negative patients and healthy controls, Logan V_T did not differentiate any differences of astrocyte reactivity in the patient groups from healthy controls. (Figure V-10) Good correlation was observed between the [^{11}C]BU99008 V_T estimated from Logan analysis and 2TCM4k model in frontal lobe, temporal lobe, parietal lobe and occipital lobe (Figure V-11). The [^{11}C]BU99008 Logan V_T parametric maps showed a global CV mean of 27% (SD=3%), which is slightly higher than SA IRF parametric maps.

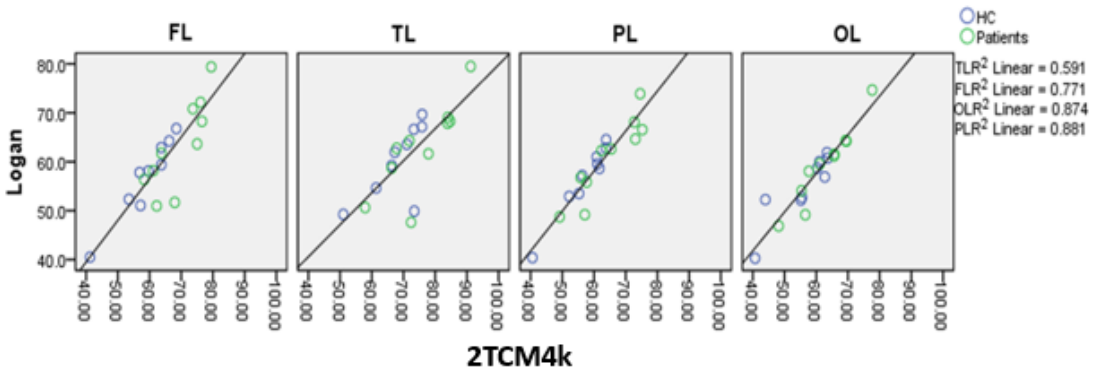


Figure V-11. Pearson correlation between [^{11}C]BU99008 Logan V_T parametric maps and 2TCM4k V_T in frontal lobe (FL), temporal lobe (TL), parietal lobe (parietal lobe) and occipital lobe (OL). The blue circles represent the healthy controls (HC) and the green circles represent the patients. The R square for each ROI region was estimated.

3.2.4 Results of [^{11}C]BU99008 PET using SUV

Both SUV images generated with 30-120 min (p=0.3) and 60-120 min [^{11}C]BU99008 summed images (p=0.6) failed to show any correlation with the V_T using two-tissue compartmental model. Unlike the arterial blood input function model, SUV images failed to reproduce any group-level significant increase [^{11}C]BU99008 in the patients. Additionally, hippocampus (-14% p=0.04) and medial temporal lobe (-12% p=0.05) in SUV 60-120 min summed images revealed an even lower uptake of [^{11}C]BU99008 in patients than in healthy controls.

3.3. Astrocyte Reactivity in Patients

In ROI analysis, the seven amyloid positive patients revealed group-level significant higher astrocyte activation compared with healthy controls (Figure V-9), which was consistent at SPM group analysis at voxel-level (Figure V-12). Individually, among the seven amyloid positive patients, six of them revealed clusters of significant higher astrocyte reactivity.

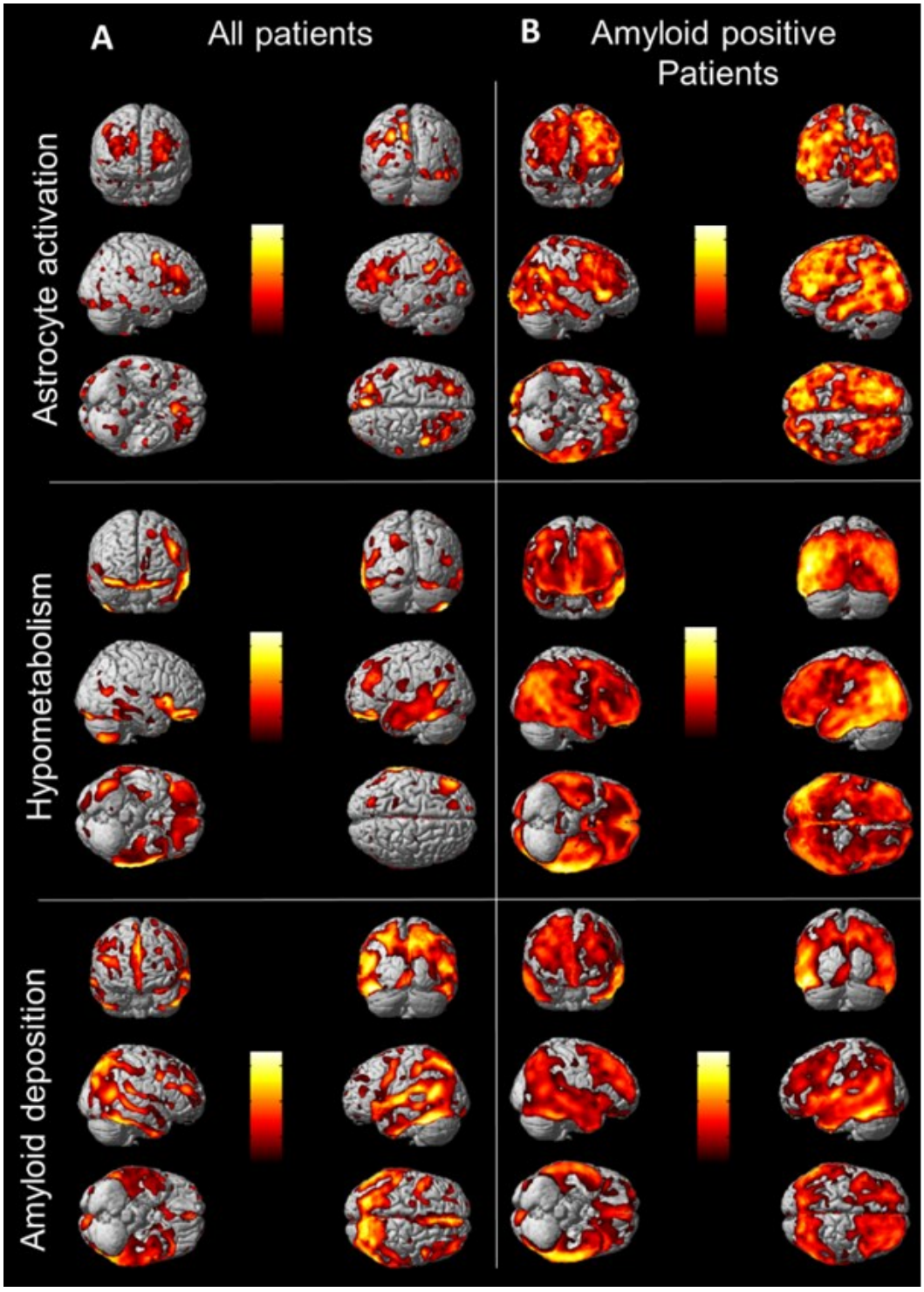


Figure V-12. SPM group analysis of astrocyte reactivity, glucose metabolism and amyloid deposition.

SPM analysis of significant increased astrocyte reactivity, reduced glucose metabolism and increased amyloid deposition in all patients (A) or subgroup of amyloid positive patients (B) compared with healthy controls. Except the amyloid in amyloid positive patients ($p<0.0005$ with extend of 200 voxels), the significant cluster was threshold at $p<0.01$ with extend of 50voxels.

3.4. Glucose Metabolism in Patients

As a group, the ROI analysis revealed group-level significant reduced glucose metabolism in temporal lobe (11%, p=0.05), thalamus (15%, p=0.008), striatum (11%, p=0.01) and MTL (10%, p=0.05) in patients compared with controls. This finding was supported at voxel-level, where SPM analysis demonstrated clusters with significant reduction of glucose metabolism at temporal lobe, thalamus, striatum, posterior cingulate and MTL (Figure V-12). The voxel-level single subject analysis demonstrated eight patients with significant reduction in glucose metabolism, who had a lower average cognitive scores (MMSE=21) compared with other patients (MMSE=24). In the amyloid positive patients, the RATIO images of [^{18}F]FDG demonstrated a group-level whole brain reduction in glucose metabolism compared with healthy controls. Individually, all seven amyloid positive patients showed clusters with significantly lower glucose metabolism than healthy controls at voxel-level.

3.5. Correlation between Astrocyte Reactivity, Glucose Metabolism and Amyloid Deposition

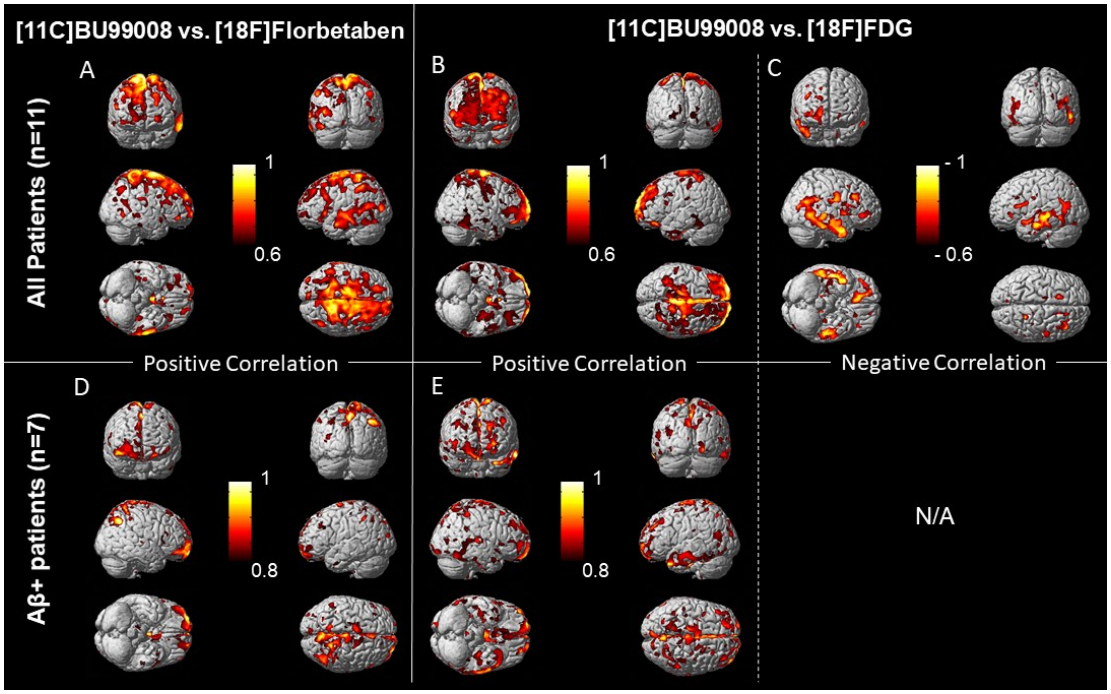


Figure V-13. Biological parametric mapping correlation between levels of astrocyte reactivity, amyloid and glucose metabolism.

Biological parametric mapping correlation was performed on the Z-maps of each biomarker image. In all patients, the level of astrocyte reactivity, amyloid and glucose metabolism was demonstrated on the upper panel. Positive correlated clusters were found between [^{11}C]BU99008 and [^{18}F]Florbetaben. Both positive correlated clusters and negative correlated clusters were found between [^{11}C]BU99008 and [^{18}F]FDG. The subgroup of amyloid positive patients were presented in the lower panel. Positive correlated clusters were found between [^{11}C]BU99008 and [^{18}F]Florbetaben Z-maps, and positive correlated clusters were found between [^{11}C]BU99008 and [^{18}F]FDG. The clusters were considered as significant with a threshold of $p<0.05$ with an extent of 50 voxels.

The BPM correlation results have demonstrated a positive correlation between astrocyte reactivity and amyloid in eleven patients, as well as the subgroup of seven amyloid positive patients at voxel level (Figure V-13A and D).

The correlation between astrocyte reactivity and [^{18}F]FDG signal was interesting, where some clusters were found to be positively correlated, while others which located in a distinct area of the brain have revealed inverse correlation. For instance, in the patient cohort, increased [^{11}C]BU99008 was found to inversely correlated with [^{18}F]FDG at voxel-level in temporal lobe, inferolateral parietal lobe, thalamus, putamen

and insula (Figure V-13C), indicating a higher level of astrocyte activation was associated with lower glucose metabolism. However, in frontal gyrus, orbital gyrus, and posterior temporal lobe, the [^{11}C]BU99008 was positively correlated with [^{18}F]FDG, suggesting those regions with higher level of astrocyte activation was associated with higher glucose metabolism (Figure V-13B). In the subgroup of amyloid positive patients, we found only a positive correlation between [^{11}C]BU99008 and [^{18}F]FDG in frontal gyrus, posterior temporal lobe, superior parietal gyrus, and left lateral occipital lobe (Figure V-13E). Amyloid negative patients (n=4) failed to reveal any significant correlation among astrocyte activation, glucose metabolism and amyloid deposition.

V-4. DISCUSSION

4.1. Quantification of [^{11}C]BU99008 PET

In this study, it has demonstrated that the two-tissue compartmental reversible model (2TCM4k) also provided the best fit to the [^{11}C]BU99008 data in AD cohort. This is consistent with previous study on young adults (Tyacke *et al.*, 2018). Heterogeneous tracer distribution was observed in both disease and age-matched controls. In general, the cerebellum showed the lowest level of [^{11}C]BU99008 uptake, while hippocampus, thalamus, striatum and amygdala demonstrated a relatively higher [^{11}C]BU99008 uptake. Although cerebellum had a low [^{11}C]BU99008 uptake, it was found significantly increased in amyloid positive patients (Figure V-4), suggesting that astrocyte reactivity may occur in the cerebellum at a later stage. Again, this is in line with the previous findings (Tyacke *et al.*, 2018) which suggested there is no suitable reference brain region for [^{11}C]BU99008 PET. As a result, arterial blood sampling may be necessary for [^{11}C]BU99008 quantification.

Parametric mapping methods are used to convert the dynamic PET data into three-dimensional images, which provides the opportunity to assess the pathological alterations at voxel-level. Spectral analysis is a powerful kinetic approach to generate parametric images (CHAPTER II.2.1). With the [^{11}C]BU99008 parent plasma input function and dynamic PET data, the spectrum revealed two tissue components with a fixed blood volume peak (0.05) at equilibrium. The low frequency component showed a higher amplitude and the high frequency component showed a lower amplitude,

suggesting that the two-tissue compartmental model was reversible in the brain for [^{11}C]BU99008 tracer, which supported our kinetic modelling.

The [^{11}C]BU99008 IRF parametric maps were generated using different sets of observation time. As a result, the parametric maps of IRF-90, IRF-105 and IRF-120 showed relatively low noise level (CV ranged from 16% to 18%) and more importantly, they were sensitive enough to differentiate the patients' astrocyte reactivity from the healthy controls. The contrast between patients and healthy controls were enhanced when longer observation time was applied, for instance, only IRF-120 revealed statistically significant elevation of astrocyte reactivity in amyloid positive patients versus controls at hippocampus, while IRF-90 and IRF105 failed to demonstrate any difference in hippocampus. Interestingly, given the fact that [^{11}C]BU99008 V_T estimated from compartmental modelling was relatively high (69±8 mL/cm^3), it has indicated that [^{11}C]BU99008 tracer had a very slow washout rate, thus a longer observation time (IRF-120) may be more appropriate. While it is possible that observation time beyond 120 min may provide a better quantification of the tracer, carbon 11 has a relatively short half-life. Therefore, IRF-120 could be the optimal time with a good balance between the slow washout rate and the short half-life of [^{11}C]BU99008 tracer. In this study, strong correlations were found between IRF-120 and 2TCM4k model, suggesting that IRF-120 parametric maps can reliably be used in quantifying the [^{11}C]BU99008 PET for astrocyte reactivity in aged healthy controls and patients with MCI or Alzheimer's disease.

Graphic analysis is another popular approach for creating PET parametric maps through the convolution of the blood input function and dynamic PET. Based on linear fit of the dynamic [^{11}C]BU99008 PET data, data from 2000 to 7200 seconds were selected to generate Logan V_T images. It demonstrated a good correlation with the two-tissue compartmental model in all cortices, with a reasonable low global mean CV of 27%. However, when compared with healthy controls, Logan parametric maps failed to localise any group-level changes, which may be due to the underestimation of the signal when using a Logan linear model.

A simplified SUV approach was applied to [^{11}C]BU99008 PET add images (30-120 min and 60-120 min) to verify whether the acquisition of arterial blood is necessary. As a result, SUV images failed to correlate with kinetic modelling V_T; and the regional mean SUV failed to show any group-wise differences between patients and healthy

controls. This suggested that the arterial input function is crucial in quantifying and interrogating the specific binding of [^{11}C]BU99008 PET tracer, especially in Alzheimer's disease.

In summary, IRF-120 [^{11}C]BU99008 parametric maps generated by spectral analysis provided high quality three-dimensional images, which correlated with [^{11}C]BU99008 V_T derived from two-tissue compartmental modelling, and was able to differentiate the astrocyte reactivity alterations in patients versus age-matched controls at voxel-level.

4.2. Astrocyte Reactivity in AD Subjects and age-matched Controls

A recent study (Tyacke *et al.*, 2018) reported the [^{11}C]BU99008 V_T for eight young healthy controls (age 52±8 years) and it found a heterogeneous tracer distribution in the brain with an average [^{11}C]BU99008 V_T of 48.8 mL/cm^3, where higher V_T was found in striatum (105.7±21 mL/cm^3), amygdala (94.6±20 mL/cm^3), and thalamus (80.0±14 mL/cm^3), while lowest V_T in cerebellum (41.9±7 mL/cm^3). Compared with younger healthy controls (48.8 mL/cm^3), we observed an average [^{11}C]BU99008 V_T of 62.6±10 mL/cm^3 in normal aged brain (aged 70±5 years), and average of 68.8±8 mL/cm^3 in patients. In human post-mortem studies (Fabricius, Jacobsen & Pakkenberg, 2013), the total number of astroglial cell counts do not show any significant changes with aging, however, the age-associated increases in GFAP immunoreactivity and/or GFAP mRNA for reactivity of astrocyte were reported in selective brain regions in both aged animal models and human brains (Hayakawa, Kato & Araki, 2007; Lynch *et al.*, 2010; Sheng *et al.*, n.d.; Unger, 1998). Interestingly, the age-related astrocyte activation in selective brain regions was reported dramatically up-regulated after 65 years of age (David *et al.*, 1997), which is also known as the age when the prevalence of AD starts rising substantially (Isik, 2010). Although the mechanism underlying the age-related changes in astrocyte reactivity is inconclusive, there is now a consensus that changes in astrocyte activation in aged brains are not homogeneous distributed throughout the brain, but highly heterogeneous and region-specific (Lynch *et al.*, 2010). This is supported in our study when comparing the V_T in healthy aged brains versus results reported for a cohort of young adult brains using the same tracer (Tyacke *et al.*, 2018), where higher level of [^{11}C]BU99008 signals were found in parietal (31%), occipital lobe (31%), cingulate (11%) and cerebellum (18%). (Figure V-3)

Compared with age-matched healthy controls, the present study demonstrated statistically significant increased astrocyte activation in the patient cohort, especially for those patients who had amyloid plaques. It has also revealed a heterogeneous regional distribution of astroglial activation in patients with cognitive impairment. These findings suggest that in selective brain regions which are more vulnerable to neuronal loss (e.g. hippocampus), a possible compensatory increase in astroglial reaction may occur to support the local glucose demand from neurons (Forsyth *et al.*, 1996), which is in agreement with neuroplasticity studies that showed the existence of the adaptive mechanism in the human brain (Coleman & Flood, 1987).

4.3. Relationship between Astrocyte Reactivity and Amyloid in AD

In this study, we found a voxel-level positive correlation between astrocyte reactivity and amyloid in patients with cognitive impairment. This was supported by previous studies which demonstrated activated astrocytes were found in close vicinity to amyloid plaques and contributed to the clearance of extracellular Aβ peptides via internalization and phagocytosis (Funato *et al.*, 1998; Nagele *et al.*, 2003). ApoE is one of the astrocytes membrane receptors which binds to Aβ peptides and extrudes across the blood brain barrier (Bu, 2009), suggesting a possible astrocyte clearance mechanism of Aβ peptides at the molecular level via ApoE. It was shown that amyloid-degrading enzymes, such as neprilysin, insulin-degrading enzyme (IDE) and matrix metalloproteinase 2 and 9 (MMP), were overexpressed in reactive astrocytes, and were found closely located with amyloid plaques in AD brain (Dorfman *et al.*, 2010). However, the astrocyte reactivity appears to serve a mixture (toxic or protective) role as the disease progresses. While astrocyte reactivity was found correlated with amyloid, there was no difference in astrocyte reactivity between AD and MCI patients, suggesting a lack of linear progression in astrocyte reactivity during the disease progression. This could be due to the fact that clinical presentation in dementia population is highly divergent (Jack *et al.*, 2018a). On the other hand, unlike a linear progression biomarker (e.g. tau), activated astrocytes may change their functionality as the disease progress, and result in different influence towards one's cognitive function. Consistent with functional experiments *in vitro,* it demonstrated that only when astrocytes were isolated from healthy brain, astrocytes can participate in degrading Aβ peptides; if astrocytes were transferred from APP transgenic AD mice, such scavenger

function was compromised (Wyss-Coray *et al.*, 2003). It again suggests that astrocytes may serve in different roles based on the environment. BACE1 (β-secretase) is a β-site APP cleaving enzyme and a main endoprotease for generating Aβ peptides. In a healthy brain, the expression of BACE1 is extremely low. In patients and several mouse model of AD, activated astrocytes that surrounded by amyloid plaques were observed with an overexpression of BACE1, which therefore promoted the production of Aβ peptides (Heneka *et al.*, 2005; Rossner *et al.*, 2005). In summary, studies have shown evidences of the protective character of reactive astrocytes in the brain, but in the AD condition where various insults were presented (e.g. abundance amyloid plaques), the functionality of activated astrocytes may eventually affected and turned into toxic Aβ producers by overexpressing BACE1 (Rossner *et al.*, 2005; Verkhratsky *et al.*, 2010).

4.4. Relationship between Astrocyte Reactivity and Glucose Metabolism in AD

This study revealed a group-level increase in astrocyte reactivity and reduction of glucose metabolism in patients, especially for patients who had higher level of amyloid plaques. In a normal brain, glucose is regarded as the major energy source for neuronal and glial activities. Apart from maintaining the homeostasis in the brain, astrocytes are vital in regulating the local energy metabolism. The astrocyte-to-neuron glucose lactate shuttle hypothesis suggests that when there is an increase in neuronal activity, the glucose is taken up by astrocytes, then undergoes the glycolysis and lactate synthesis; and finally produces lactate which is subsequently redistributed to neurons with specific transporters (Pellerin & Magistretti, 1994). It is well-known that cerebral glucose metabolism is impaired in most neurodegenerative diseases, where the glucose metabolism is significantly reduced (Edison *et al.*, 2013; Fan *et al.*, 2015b; Gallivanone, Della Rosa & Castiglioni, 2016), however little is known about the mechanism alterations of neuronal and astroglial metabolism in a disease brain.

In this study, [^{11}C]BU99008 was found positively correlated with [^{18}F]FDG in frontal gyrus, orbital gyrus, and posterior temporal lobe. This suggested that when there was an increase in astrocyte reactivity in patients' brains, glucose metabolism was enhanced, suggesting a compensational mechanism by the accumulative reactive astrocytes, which continue to consume the glucose to provide metabolic support in response to the excessive energy demands from the impaired neurons. In a mouse model of

Huntington's disease (Boussicault *et al.*, 2014), researchers found that expression of mHtt (mutant huntingtin) protein in astrocyte affected the glucose usage *in vivo* by impairing the glucose uptake in neurons specifically, but the glucose can still be taken up by astrocytes, suggesting that in the disease condition, astrocyte may still consume glucose as normal, and regulate local energy metabolism via astrocyte-to-neuron glucose lactate shuttle in the brain. However, those generated lactate may not able to be consumed by neurons due to the disease condition. As discussed previously, rather than homogeneously distributed throughout the brain, astrocyte reactivity appears in a highly regional specific manner. In the AD cohort, we also observed an inverse correlation between reactive astrocytes and glucose metabolism mainly in temporal lobe, inferolateral parietal lobe thalamus, putamen and insula, suggesting increased astrocyte reactivity in those regions was associated with reduction of glucose metabolism. This finding indicates activated astrocyte in some regions may fail to enhance the glucose metabolism, or even become detrimental by accelerating the reduction of glucose metabolism. Interestingly, the amyloid deposition and synapse loss in AD are predominately observed in temporal lobe (Wong *et al.*, 2010; Scheff & Price, 1993), suggesting astrocytes may have a higher risk in compromising their function due to the higher stress of local amyloid burden. This is supported by the preclinical findings where the astrocyte reactivity in AD rat model was found impairing the glutamate-glutamine cycle, and further decreasing the glucose metabolism (Nilsen, Witter & Sonnewald, 2014; Sancheti *et al.*, 2014). In AD brain preparations, both elevation and reduction of metabolic enzyme activity in AD brain model were reported for glucose metabolism related enzymes (Liang *et al.*, 2008; Soucek *et al.*, 2003). This fluctuation of metabolic enzyme activity observed during disease progression may due to the functional shifting in astrocytes reactivity at different stages.

Furthermore, evaluation of the relationship between astrocyte reactivity, glucose metabolism and amyloid was also performed in a subgroup of patients who had high amyloid load. A positive correlation between astrocyte reactivity and glucose metabolism were identified, indicating a possible compensatory mechanism where increased astrocyte reactivity. By comparing correlated regions between astrocyte reactivity and glucose usage, against the correlated regions between astrocyte reactivity and amyloid, most of those correlated regions were found in distinct brain regions. This finding indicated that astrocyte reactivity which was positively enhanced the glucose

metabolism, was found in the absence of amyloid load. This is consistent with previous studies, which suggested Aβ aggregation could profoundly change reactive astrocytes' metabolic phenotype by up-regulating the 3-kinase (PI3-kinase) pathway, and lead to significant reduction of glucose utilization and neuronal survival rate (Allaman *et al.*, 2010).

4.5. [^{11}C]BU99008 vs. other astrocyte PET tracers

Apart from I_2BS, Mononamine oxidase-B (MAO-B) is another popular molecular target for astrocyte imaging. MAO-B is an enzyme residing on the outer mitochondrial membrane and catalyses the oxidation of neurotransmitters. [^{11}C]-L-deprenyl, [^{11}C]SL25.1188, and [^{11}C]-L-deprenyl-D2 were PET radiotracers developed for targeting cellular expression of MAO-B. In an autoradiographic study, AD patients demonstrated significant higher [^{11}C]-L-deprenyl binding in temporal lobe and white matter compared with healthy controls (Gulyás *et al.*, 2011). Additionally, they found negatively correlation between Braak's stage and the tracer binding in hippocampus, temporal lobe and white matter in AD patients. In this [^{11}C]BU99008 work, amyloid positive AD patients showed significantly increased astrocyte reactivity compared with healthy controls in several cortical regions, including temporal lobe, occipital lobe and medial temporal lobe. Those regional increased [^{11}C]BU99008 signals were consistency with the GFAP immunohistochemistry results, where increased number of astrocytes were found in the similar area (García-Sevilla *et al.*, 1998). However, MAO-B is not selectively expressed in astrocytes, and most MAO-B PET tracers (e.g. [^{11}C]-L-deprenyl) showed an irreversible binding kinetics in the brain, which may limit the quality of PET signal quantification due to the perfusion/delivery of the tracer. In this study, the kinetics of [^{11}C]BU99008 radiotracer in both healthy controls and AD disease brains showed a reversible feature and the tissue signal and were well described by the two-tissue compartmental model, which provides more reliable V_T estimations than the irreversible trapping rates (K_I).

In vitro, [^{11}C]BU99008 PET ligand demonstrated high affinity and specificity for I_2BS in preclinical species (Parker *et al.*, 2014). To date, compared with other potential I_2BS PET tracers, [^{11}C]FTIMD showed relatively lower specific signals in preclinical studies (Kawamura *et al.*, 2012) and [^{11}C]benazoline hasn't been investigated in vivo (Roeda, Hinnen & Dollé, 2003). A distribution and heterologous competition of [^{11}C]BU99008

binding *in vivo* in human was performed in a recent study using Idazoxan (high affinity for I_2BS) and Isocarboxazid (blocks both isoforms of MAO-A and MAO-B) (Tyacke *et al.*, 2018). A dose-dependent [^{11}C]BU99008 signal reduction was observed in the subjects who had pre-treatment of Idazoxan (60% reduction at the highest dose), while no reduction was found in subjects who had Isocarboxazid. The result showed that [^{11}C]BU99008 has a high affinity to I_2BS (dose sensitive) and significantly lower affinity to MAO-B, suggesting a good tracer binding specificity and selectivity *in vivo* in human brain. Therefore, [^{11}C]BU99008 imaging has a great potential to provide an in-depth clinical imaging tool to investigate the specific role of I_2BS in human brain.

4.6. Conclusion

In conclusion, this study has shown that [^{11}C]BU99008 PET was able to differentiate the higher astrocyte reactivity in patients versus age-matched controls using 2TCM4k compartmental modelling. I have also found that spectral analysis was able to generate high quality IRF-120 parametric maps to quantify [^{11}C]BU99008 PET, which not only revealed strong correlation with V_T estimated from kinetic modelling, but also provided parametric images with a signal-to-noise ratio large enough to differentiate the astroglial reactivity in patients compared with age-matched controls.

In this study, both voxel-level positive and negative correlations were revealed between astrocyte activation and cerebral glucose metabolism in patients with cognitive impairment. Along with previous studies, it suggested that astrocyte activation may have heterogeneous effects on neuronal function in different brain regions, which was associated with the presence of amyloid deposition. More data is needed to further establish the relevance of this finding, however this preliminary study has demonstrated the best PET methods to quantify the astrocyte reactivity in Alzheimer's trajectory using the novel [^{11}C]BU99008 PET tracer. Moreover, it provided some insight into the possible influence of astrocyte reactivity on glucose metabolism and amyloid deposition in patients with AD and MCI.

CHAPTER VI. NOVEL TECHNIQUES: INTERACTIVE VOLUME OF INTEREST (VOI) PREDICTION TOOL, INDIVIDUAL CORRELATION MAP (ICM), AND AUTOMATED QUALITY CONTROL

VI-1. BACKGROUND

Neuroimaging has been widely applied in the evaluation of the trajectory of neurodegenerative diseases *in vivo*. In Alzheimer's disease, amyloid-β deposition, neurofibrillary tangles, neuroinflammation, glucose metabolism, synaptic dysfunction, cortical and subcortical atrophy can readily be measured *in vivo* using different PET tracers. In the last chapter, the influence of astrocyte activation was evaluated along with the amyloid deposition and glucose metabolism using multiple PET images, which provided interesting results on the astrocyte interaction with other AD pathological biomarkers. Recently NIA-AA (National Institute on Aging-Alzheimer's Association) research framework acknowledged the diversity of AD patients, the multifactorial nature of dementia and complexity of clinical staging; therefore they proposed a biological related definition and characterised AD patient should be presented with both amyloid plaques and tau-based neurofibrillary tangles, irrespective of the clinical state of the person (Silverberg *et al.*, 2018). This again reiterates the importance of evaluate multiple biomarkers on an individual basis (but independent of clinical continua) can provide a pure biological-based evidence of interactive pathology, which is able to facilitate a better understanding in diverse dementia populations. Benefitting from the fast development of medical imaging, it has demonstrated that often the presentation of multiple biomarkers in neurodegenerative disease along with genetic and environmental factors lead on to progressive neurodegeneration (Parbo *et al.*, 2017; Reiman *et al.*, 2009; Kantarci *et al.*, 2012; Ittner *et al.*, 2010; Nelson, Gard & Tabet, 2014). Therefore, evaluation of multiple pathological imaging biomarkers in the same individual with neurodegenerative disease has become increasingly popular in the research field, supported by emerging evidence indicating the importance of the pathological interaction in causing disease progression (Latta, Brothers & Wilcock, 2015; Heneka *et al.*, 2015).

Neuropathological studies have demonstrated that different pathological processes (e.g. tau and amyloid) may follow a sequential stereotypical pattern of disease progression (Braak & Braak, 1991; Mori *et al.*, 2008). These findings introduced the concept of staging systems for different neurodegenerative diseases. In 1991, for the first time, Braak published a pioneering study which established the stereotypical pathological staging of AD based on the distribution pattern of amyloid deposits and neurofibrillary tangles in eighty-three brains at autopsy. They suggested that amyloid deposition was not sensitive enough to differentiate the neuropathological stages in AD; however, the distribution of neurofibrillary tangles was capable of classifying Alzheimer-related changes into six disease stages. In stage I-II, neurofibrillary tangles were firstly observed in the locus coeruleus (LC) of the pontine tegmentum and then were found in the trans-entorhinal layer of the anterior part of medial temporal lobe. Subsequently, neurofibrillary tangles were found spreading to other parts of the temporal lobe, including layer Pre-alpha in trans-entorhinal region, entorhinal cortex and hippocampal regions, which were regarded as stage III-IV. The final two stages (V-VI) were characterized by the presence of neurofibrillary tangles in the basal temporal lobe and the insular cortex, and eventually extended to the neocortex with virtually all isocortical associated regions (Braak & Braak, 1991; Braak *et al.*, 2006; Mori *et al.*, 2008).

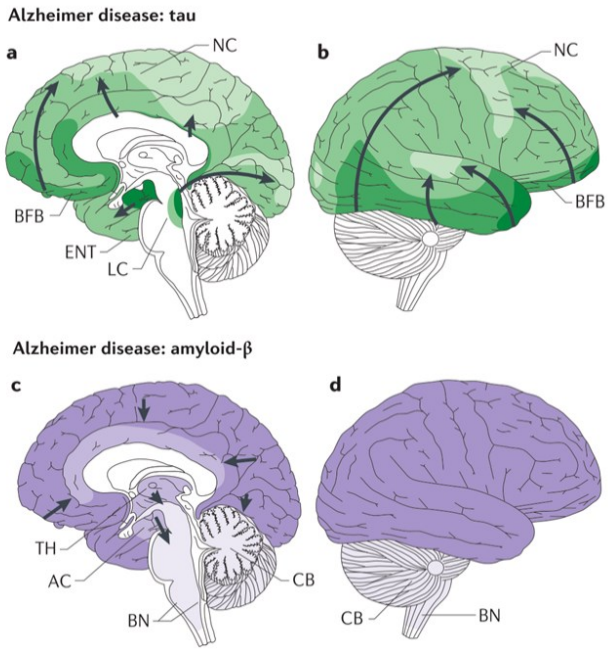


Figure VI-1. Stereotypical patterns of tau (a-b) and amyloid (c-d) in Alzheimer's disease. The sequential pattern of amyloid deposition follows an opposite direction in contrast to the neurofibrillary tangles in AD

AC = allocortex; BFB = basal forebrain; BN = brainstem nuclei; ENT = entorhinal cortex; TH = thalamus; LC = locus coeruleus; NC = neocortex and CB = cerebellum. J. Brettschneider, 2015 Nature Reviews Neuroscience (Brettschneider et al., 2015) (Appendix 1. Permission Table)

Interestingly, the sequential pattern of amyloid deposition seems to follow an opposite direction in contrast to the neurofibrillary tangles in AD (Brettschneider *et al.*, 2015). (Figure VI-1) Firstly, the formation of amyloid plaques in AD is found exclusively in the neocortex, and then they build up in allocortical brain regions. Then amyloid deposits are detected in diencephalic nuclei, the striatum and the basal ganglia structures. Eventually, Aβ deposition spreads to the brainstem and in late stages, the cerebellum with high burden of Aβ across the brain (Thal *et al.*, 2000, 2002). The divergent patterns of tau and amyloid could indicate separate mechanisms; however, observations in both *in vitro* and *in vivo* studies have suggested that tau is capable of mediating further accumulation of Aβ, while the Aβ may enhance the aggregation of neurofibrillary tangles in AD (Chételat, 2013; De Felice *et al.*, 2008; Ittner *et al.*, 2010; Roberson *et al.*, 2007). Therefore, evaluation of pathological interactions and co-localization may shed a light in interpreting the sequential pathological staging patterns in AD.

Neuroinflammation has been increasingly recognized as a key event in accelerating cognitive deficiency in dementia and shows high variability across patients. However, the complex mechanisms that underlie neuroinflammation in neurodegenerative diseases remain elusive; it may play a detrimental role to the human brain by degenerating neurons, or it may also be neuroprotective, such as clearance of amyloid plaques under certain conditions or during specific stage of the disease progression (Hickman, Allison & El Khoury, 2008). In the hTauCx3cr1$^{-/-}$ mouse model of tauopathy (Maphis *et al.*, 2015), microglial activation was found to be correlated with the spatial memory deficit and the spread tau in the hippocampus. Additionally, the microglia which derived from the hTauCx3cr1$^{-/-}$ mice (deficiency of microglia-specific fractalkine receptor) were able to promote the hyperphosphorylation and aggregation of tau in the normal mice brain, and the induced tau aggregation could be suppressed by interleukin 1 receptor antagonist through attenuating the microglial reactivity (Maphis *et al.*, 2015). This finding suggested that microglial reactivity is associated with the aggregation of tau, and maybe sufficient to drive the further spreading of pathological tau.

1.1. Objectives

Given the complex interaction between AD pathologies (e.g. tau, amyloid and neuroinflammation), this chapter is aiming to develop novel tools to explore:

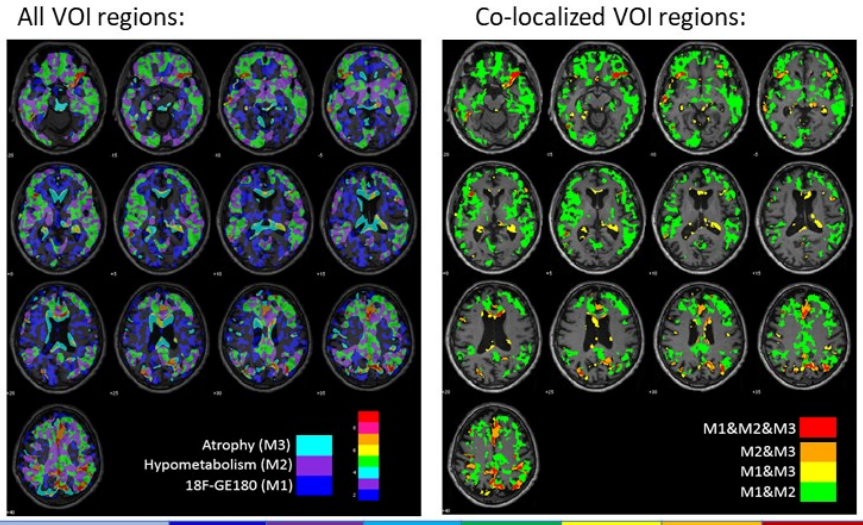
1- VOI Prediction Tool is designed to evaluate the temporal relationship of co-localized biomarker volume of interests on the individual cognitive function
2- Individual Correlation Mapping is developed to investigate the local biomarker significant correlation in individual patient
3- Automated QC method is introduced to aim for performing effective quality control of the imaging spatial transformation

In this chapter, I start with two novel imaging approaches to integrate the co-localized pathologies, to assess and predict cognitive performance. The methods are designed on an individual basis: 1) VOI Prediction Tool (VPT) and 2) Individual Correlation Mapping (ICM). Then I introduce an automated spatial transformation quality control (QC) approach for detecting the imaging spatial transformation, which was mainly designed for big dataset analysis, such as imaging data collected from open sources in Alzheimer's Disease Neuroimaging Initiative (ADNI: http://adni.loni.usc.edu/),

Australian Imaging, Biomarker & Lifestyle Study of Ageing (AIBL: https://ida.loni.usc.edu/) and Dominantly Inherited Alzheimer Network (DIAN: https://dian.wustl.edu/). For each novel technique, I start with the aim and principle for the novel approach, including aim of design, imaging modality inputs and approach framework. Subsequently, the new technique is applied to a clinical application. Finally, discussions about possible implementations of each technique and future development. Additionally, the correlation between microglial activation *in vivo* with both tau and amyloid in AD at group-wise were found using BPM analysis, which was published in Brain in July 2018 with myself as a co-author (Dani *et al.*, 2018). For this study, I used the similar subject cohort to further evaluate the clinical influence of the correlation between microglial activation and other pathologies at individual level using novel techniques (VPT and ICM).

VI-2. TECHNIQUE I. VOI PREDICTION TOOL

2.1. Principle of VPT



Region Category	M1	M2	M3	M1&M2	M1&M3	M2&M3	M1&M2&M3
Volume(mm3)	643,885	743,366	152,793	310,226	24,364	30,159	20,251
Percentage of brain	36%	42%	9%	17%	1%	2%	1%

Figure VI-2. A partition VOI map generated for an AD patient.

In this illustration, Modality biomarker 1 represents the microglial activation using [^{18}F]GE180 PET, Modality biomarker 2 represents the hypometabolism using [^{18}F]FDG, and Modality 3 represents the atrophy using MRI image. Blue (M_1), purple (M_2) and cyan (M_3) demonstrated the VOI region which showed significant changes only in one modality (devoid with other changes); Green ($M_{1\&2}$), yellow ($M_{1\&3}$) and orange ($M_{2\&3}$) showed the VOI regions which showed co-localization of any two modalities, and colour red (M_{123}) represented the VOI regions which revealed significant changes in all three modalities.

The disease progression in neurodegenerative disease is characterized by an increase in the size of affected regions/lesions and an increase in the number of cells with pathological alterations. For instance, the different sequential patterns of amyloid deposition and neurofibrillary tangles in AD; and the different volume of affected regions with single or co-existent pathologies in a patient's brain (Figure VI-2). These results could provide information about disease progression. The interaction of each pathological process on cognitive performance is also important to provide compensational information for designing future clinical trials. In this case, rather than assessing a singular pathology, the new VOI partition model allows me to analyse how multiple pathologies influence cognitive performance at individual level.

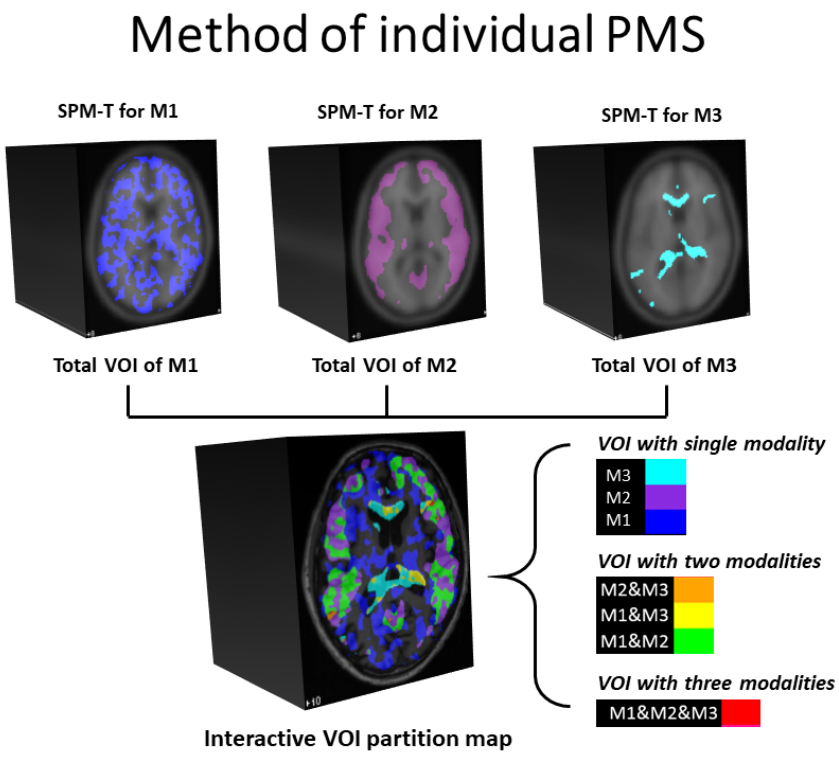


Figure VI-3. The algorithm of generating Interactive VOI partition map.

M1, M2 and M3 were SPM-T maps which were generated from SPM8 by comparing an individual's PET image against a group of healthy control data. Thus each M1, M2 and M3 represented clusters of statistically significant changes from the healthy controls. By analysing three biomarker images with their significantly changed clusters, the novel VOI partition tool segmented the clusters into three major classes 1) VOI with single modality (M_1, M_2, M_3), 2) VOI with two modalities (M_{12}, M_{13}, M_{23}), and 3) VOI with three modalities (M_{123}).

The individual VOI Prediction Tool was aim to firstly separate the VOI of a specific pathology into different VOI categories to account for the volume of pathological co-localization. In a 3D VOI partition map of an individual subject, three VOI categories were expected, 1) VOI that is significant in only one modality, 2) spatial overlaying VOI that co-localized every two modalities, and 3) VOI which revealed positive in all three modalities (Figure VI-2 and Figure VI-3). The VOI partition map was displayed with different colour-coded VOIs in three anatomical orientations: transverse plane, sagittal plane and coronal plane. This display function stemmed from the SPM toolbox *Slover* (Penny *et al.*, 2011). In addition to the VOI partition maps, the volume of each VOI category was measured for each image modality in 3D space (Figure VI-2).

In order to run the VPT, the imaging input must be three-dimensional volumetric images, such as Impulse Response Function parametric maps, Logan V_T images,

summed images, SUVR images and Binding Potential images. Those images were also expected to be spatially transformed into the same space (e.g. native space or common space). To compare different pathological maps at a voxel level, T-scored maps were generated for each modality for each patient by comparing to control cohort. Thus, it reflected the pathological changes of the biomarker in each patient relative to the normal mean and variance in age-matched healthy controls. (Figure VI-4)

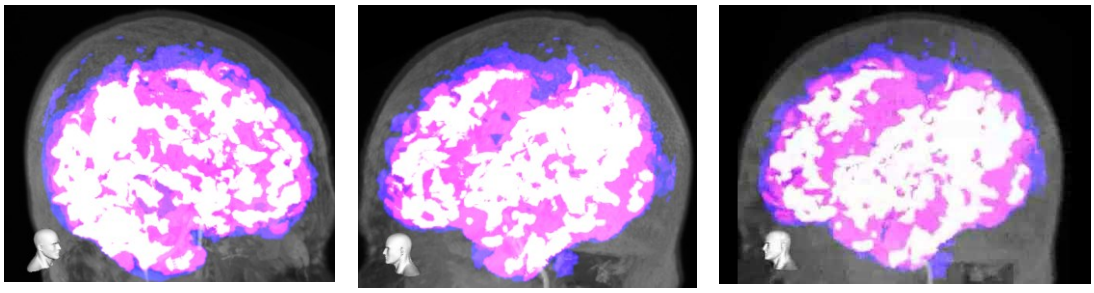


Figure VI-4. Demonstration of VOI partition map with different colour lumps, which represented different VOI categories.

The image inputs were T-scored maps for tau, amyloid and microglial activation. Figure on the right is a video demonstration of VOI partition map viewing in 3D space (Ctrl + click to watch).

Subsequently, the volume of each VOI partition regions shown on the partition map was inputted into the VOI cognitive prediction model. In the following clinical application to use VPT, I would like to investigate 1) whether the VOI volumes could be a prediction index for the annual cognitive function decline rate; and 2) whether the interactive VOI volumes of multiple pathologies correlated better with cognitive function than individual pathology. Linear model fitting was applied for the prediction of the cognitive decline against either total VOI pathological volume or multiple volume of VOI partitions at baseline using MATLAB 2017. The R-squared and p value were estimated to describe the goodness of the model fitting. Adjusted R-squared was calculated to account for the number of predictors, which increases only if the new predictor improves the model fitting more than expected by chance. Depending on the contribution of each VOI volume (term) to the prediction model, the stepwise linear regression selects certain terms to be used in the prediction model. For instance, at each step, based on the statistical significance (p value of an F-statistic) in a regression model, a new term would be added or subtracted from the cohort of predictors (Field, 2013).

2.2. Clinical Application of VPT

2.2.1 VPT methods

The data used for evaluating the new techniques VPT were from the [^{11}C]PBR28 study. The ethical approval was granted by the Riverside Research Ethics Committee, and administer radiotracers was approved by the Administration of Radioactive Substances Advisory Committee UK. Written informed consent was obtained from all participants. A total of 18 patients (15 MCI and 3 AD) and 19 age-matched healthy controls were involved. All participants had MRI scan, 80-100 min summed RATIO image (reference to cerebellum) of [^{18}F]AV1451 PET for tau plaques, 90-120 min summed RATIO image (reference to cerebellum) of [^{18}F]Flutemetamol PET for amyloid deposition and [^{11}C]PBR28 IRF-90 for microglial activation (Dani *et al.*, 2018; Fan *et al.*, 2018). The cognitive performances were assessed at baseline and then followed up after 13 ± 6 months with Mini-Mental State Examination (MMSE) for all patients. The annual cognitive decline rate for MMSE was calculated using the formula below:

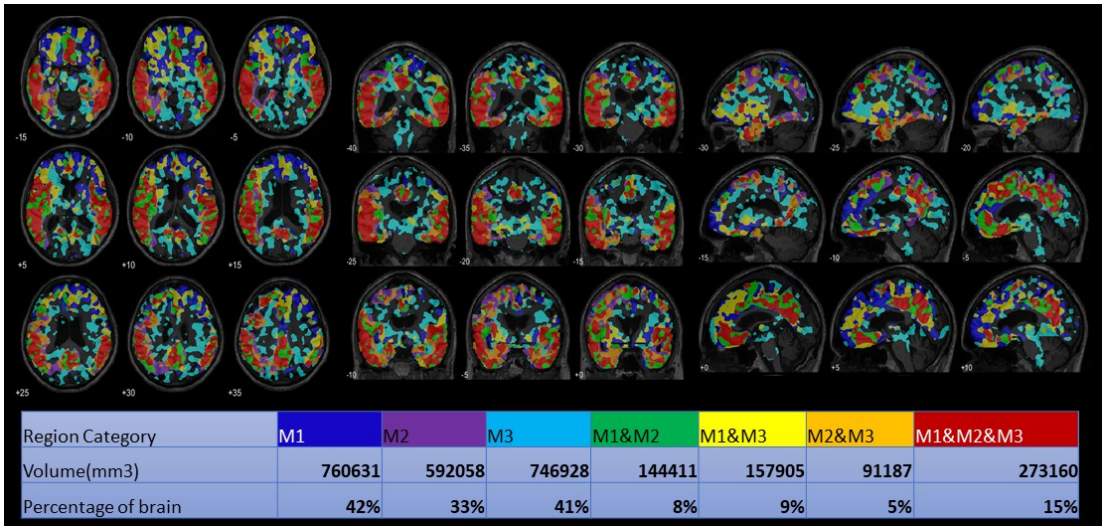
Equation 12. MMSE annual decline rate

$$MMSE\ anual\ decline\ rate = \frac{(Baseline\ Score - Followup\ Score)}{Followup\ Score * t} \times 12 \times 100\%,$$

where t denotes the month duration between the baseline and follow-up tests.

In order to assess statistical pathological changes, the T-scored image was generated for each patient to represent the regions with statistically changes in relative to the age-matched control mean and standard deviation using One-way ANOVA. The p values were corrected for multiple comparison with FEW (Family-wise error) at cluster level. In this case, apart from considering the affected region with one biomarker as one volume (VOI), the affected region was classified as different VOI partitions. For instance, the volume of amyloid deposition was separated into 1) VOI of amyloid deposition where the amyloid was present alone (e.g. M_i), 2) VOI of amyloid that co-existed with neurofibrillary tangles, 3) VOI of amyloid that was found co-localized with activated microglia (e.g. M_{ij}), and 4) VOI of amyloid which was surrounded by both neurofibrillary tangles and activated microglia (e.g. M_{ijk}). In this clinical application, the novel method classified the volume of three pathologies into seven separated VOI partitions (M_1, M_2, M_3, M_{12}, M_{13}, M_{23} and M_{123}). The volume of each VOI categories was calculated at voxel-level in 3D dimension. An automatic display of the VOI partition brain colour maps in transverse, coronal and sagittal view with multiple slices

was incorporated, based on the SPM toolbox Solver function, providing a visualization of the co-localizing pathology at individual basis. (Figure VI-5) The co-localizing VOIs of amyloid deposition, tau plaques and microglial activation at baseline were correlated with the cognitive performance decline rate to evaluate whether the volume of specific VOIs could serve as a predict index for cognitive performance. The adjusted R-squared in the linear model was estimated to account for the effect due to different number (e.g. n=7 VOIs) of predictors.



Region Category	M1	M2	M3	M1&M2	M1&M3	M2&M3	M1&M2&M3
Volume(mm3)	760631	592058	746928	144411	157905	91187	273160
Percentage of brain	42%	33%	41%	8%	9%	5%	15%

Figure VI-5. An illustration of volumes of VOI partitions in an AD patient using three SPM-T imaging modalities: tau PET (M1), amyloid PET (M2) and TSPO PET (M3). Each modality represents the significant increased biomarkers in an individual compared with controls using one-way ANOVA.

The regional VOI with a single increased modality (M1, M2, M3), 2) the regional VOI with two increased modalities (M12, M13, M23), and 3) the VOI with three modalities (M123). The volume of each region category can be measured, and the percentage of the volume out of the whole brain volume can be calculated.

2.2.2 VPT results and discussion

When applying a multilinear model to the total volume of a single pathology VOI (M_A=amyloid deposition, M_B=neurofibrillary tangles and M_C=microglial activation), I found a significant multilinear regression between the three variables (M_A, M_B and M_C) and the annual decline rate of cognition (y=response data) (Figure VI-6 A). The 3-variable multilinear model can be expressed as following:

Equation 13. Multilinear regression of three variables

$$y = \beta_0 + \beta_1 \times M_A + \beta_2 \times M_B + \beta_3 \times M_C + \epsilon \,,$$

Where n denotes the number of variables, β denotes the coefficients for each input variable and ϵ presents a constant. With three coefficient estimates, the model demonstrated an adjusted R-squared of 0.422 (p=0.013), suggesting there is a statistically significant relationship between the three variables (M_1, M_2 and M_3) and the response data (rate of cognition); and this model could explain 42.2% of the variability of the response data fall to the linear regression. This correlation was good, but not impressive.

In the new VPT method, seven different VOI variables were segmented based on the interaction of these three pathologies (n=7 VOIs). Thus the model can be improved and expressed with the following equation:

Equation 14. The multilinear model of VOI prediction tool

$$y = \sum_{i=0}^{n=7} \beta_i \times M_i + \epsilon$$
$$= \beta_0 + \beta_1 \times M_1 + \beta_2 \times M_2 + \beta_3 \times M_3 + \beta_{12} \times M_{12} + \beta_{13} \times M_{13} + \beta_{23} \times M_{23} + \beta_{123} \times M_{123} + \epsilon$$

To note, each M_A, M_B and M_C in the previous 3-variable multilinear model presented the total volume of an individual biomarker (e.g. M_A = total volume of increased amyloid). In the novel 7-variable model, based on the biomarker co-localization, each of the partition presented only partial of the total volume of increase. For instance, the volume of M_A equals to the sum of M_1, M_{12} and M_{13} and M_{123}, namely the total volume of increased amyloid (M_A) was composited by regions of amyloid increased alone (M_1), regions of amyloid increased with tau (M_{12}), regions of amyloid increased with microglial activation (M_{13}), and regions of amyloid increased with both tau and microglial activation (M_{123}).

As a result, I found a statistically significant multilinear regression model with improved adjusted R-squared of 85.9% and statistical p value of 0.00011 (Figure VI-6 B). The improvement of adjusted R-squared (85.9%) in the 7-varaiable model demonstrated that the VOI partition truly improves the model prediction rather than a reflection of a higher number of inputs (i.e. n=3 vs. n=7 VOIs). Compared with the 3-variables model, the 7-varibale multilinear model improved the prediction of the cognitive decline with higher probability (p value from 0.013 to 0.000114), and higher percentage (adjusted R-square from 42.2% to 85.9%) of the response data variability that can be explained by the model.

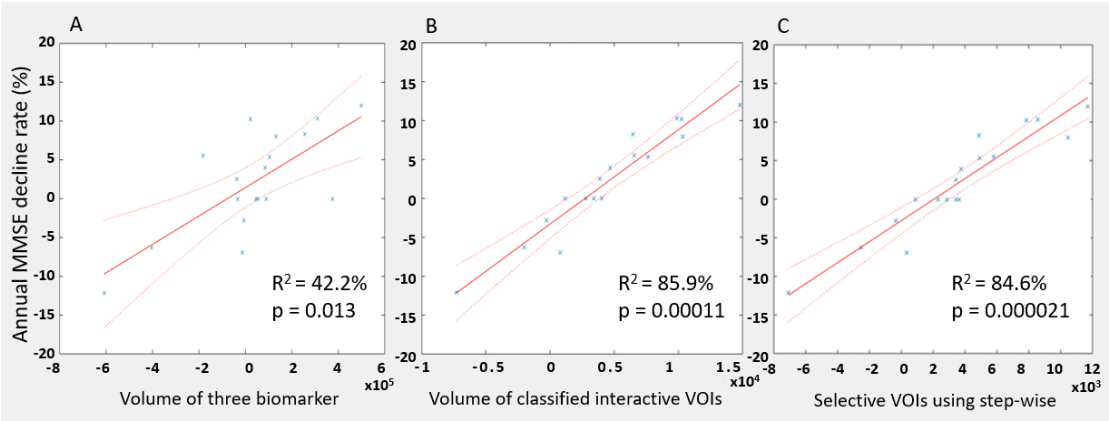


Figure VI-6. Multilinear regression model between different sets of VOI variables (amyloid, tau and microglial activation) and the annual cognitive decline rate (MMSE).

A) Multilinear model based on three VOI variables: the total volume of VOI using three individual biomarkers (M_A, M_B and M_C). B) Multilinear model based on seven VOI variables which were created by segmentation of the significant clusters based on the biomarker interaction (M_1, M_2, M_3, M_{12} and M_{13} and M_{123}) using the VPT tool. C) Step-wise multilinear regression model performed for seven VOI variable. The adjusted R-squared and p value estimation were presented for each plot.

Interestingly, rather than forcing the multilinear model to account for all seven VOI variables, I have applied a step-wise procedure to allow the model to automatically determine which VOI variables are able to improve the model fitting (Figure VI-6 C). Namely, the model would make a decision in adding and removing redundant predictors to the final prediction model purely based on the contribution of each variable input. In this case, the step-wise linear model fitting has removed the VOI-M_2 (volume of amyloid alone) and VOI-M_{12} (volume of amyloid and tau) from the prediction model, which estimated an adjusted R-squared of 84.6% and p value of 0.000021. With this modulation, the new model improved the significant p value with 10 folds, and presented similar R-squared, suggesting the affected volume of amyloid deposition alone may not improve the sensitivity of predicting the cognitive data. Instead, the volume of amyloid which localized along with microglial activation (VOI-M_{13}, p=0.00037) and presented with both microglial activation and tauopathy (VOI-M_{123}, p=7.26e-05) showed significant improvement of predicting the cognitive decline in Alzheimer's patients. Thus, from this preliminary application of the VPT method with a small-size patient data, it demonstrated that the volume of amyloid which co-localised

with activated microglia and tauopathy may influence the cognitive performance more than the amyloid presented alone.

2.3. Possible Usage in VPT

The VOI partition map provides 3D dimensional visualization of the 3D spatial anatomical overlay among multiple pathological modalities at voxel level. With the VOI prediction tool, it provides an effective way to evaluate data about multiple pathological processes and cognitive performance on individual basis. In the current clinical application, I found that different VOI partitions might serve as a predictive index for predicting the annual cognitive decline. In the current patient cohort, it demonstrated that the volume of amyloid deposition that co-localized with activated microglia and tau plaques showed a stronger association with cognitive performance than the volume where amyloid presented alone.

The development of VPT is on-going. In baseline studies, I have been working on applying the VPT in tau, amyloid and FDG PET using the ADNI dataset with a much larger patient cohort, to evaluate standalone pathology and co-localized pathologies' relevance to individuals' cognitive performance. In the longitudinal imaging studies, by measuring the longitudinal changes in volumes of different pathological VOIs, VPT model may discover compensational associations underlie the pathology of the AD brain and individuals' cognitive performance. After establishing a trained VPT model in big dataset, theoretically, clinicians and researchers could use the model to estimate the possible clinical outcome for individual patient by applying relevant VOI partitions.

VI-3. TECHNIQUE II. INDIVIDUAL CORRELATION MAPPING (ICM)

3.1. Principle of ICM

3.1.1 General concept of ROI-Correlation

The second approach is called Individual Correlation Map (ICM). Compared with the previous technique, rather than the spatial co-localization of the mixed pathologies, the ICM is designed to evaluate the statistically meaningful correlation between two image modalities on an individual basis. Thus, this method provides quantitative measurements of the biomarker interaction, such as the R squares and statistical

significance (p value) of the correlation at voxel-level. Furthermore, it generates an individualized three-dimensional map of ROI-Corr (Region of Interest – Correlation) to present the pathological interaction in a 3-D space, which offers a direct visualization of the pathological relationship in the brain. ICM is a voxel-level comparison framework developed in MATLAB 2017, which assesses the statistical correlation between different biomarkers in individuals. As a multi-parametric imaging approach, ICM provides a novel way to generate individual ROI-Corr maps (Figure VI-8 and Figure VI-9), which improves the comprehensive understanding of the dynamic pathological alterations in AD.

The ICM framework requires the input images to be in the same space. Therefore, initially all image modalities need to be coregistered or normalized to a common space. In this case, I generated the single subject SPM-T map to demonstrate the pathological alterations in each patient by comparing individual PET against the corresponding healthy control cohort using one-way ANOVA in MATLAB. In order to investigate the pathological correlation on an individual basis, a cluster-unit correlation concept is introduced. The idea is to transform the brain matrix into multiple cluster units, which enables us to run the statistical correlation on each cluster in 3D. Subsequently, the ICM runs the correlation for different clusters throughout the brain, and generates a new correlation image (ROI-Corr) that contains only significant clusters which pass the pre-defined significance threshold. For instance, the desirable size of the cluster unit (e.g. 5 x 5 x 5 mm^3), probability threshold (p-value and cluster-size threshold), correlation coefficient (r), background noise threshold, Bonferroni Correction, and brain masks can all be customized. All clusters are designed to be spatially independent, as allowing overlapping clusters may overestimate the signal and pick up false-positive correlations. Depending on the hypothesis and specific pathological changes, it is crucial to be customized those options accordingly before ICM carries out the single-subject correlation analysis.

3.1.2 Correlation framework

Figure VI-7 reveals the procedure of the ICM correlation framework. Within each spatial corresponded cluster-unit at voxel-level, the T-score values are collected for the correlation analysis. Shapiro-Wilk test was applied to assess the normality of the data distribution. Only when both clusters demonstrated a normal distribution, the Pearson

correlations were performed with additional Bonferroni correction for multiple comparisons. When the p value passes the requested threshold configured by the user, the correlation coefficient (r) of such cluster is transferred to the ROI-Corr map, otherwise the cluster is discarded. After completion of the cluster correlation throughout the brain, both the r value and spatial location for the significant correlated clusters are stored in the newly generated ROI-Corr image. It presents the significantly correlated regions between two input image modalities. As default, an individualized brain mask is applied to the ROI-Corr maps. ICM then estimates the total volume for positively or negatively correlated brain clusters. Additionally, ICM samples the mean tracer activity of each modality in the interactive region.

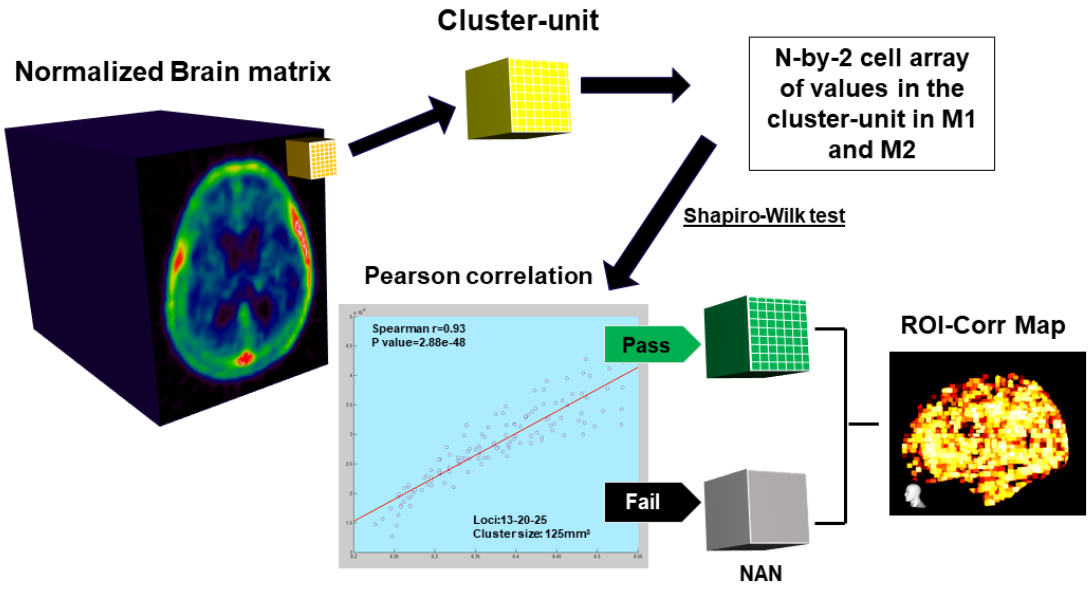


Figure VI-7. The procedure of ICM and generation of ROI-Corr Map.

Each image modality was normalized or co-registered into the same space. The cluster unit was predefined by the user (e.g. 5x5x5 mm³). In each cluster-unit, the corresponded T-score values at voxel-level (N-by-2) were collected for the correlation analysis. Shapiro-Wilk test was applied to exclude data which were not normal distributed. The Pearson correlations were performed with Bonferroni correction. When the p value passed the predefined threshold, the correlation coefficient (r) of such cluster would transferred to generate the ROI-Corr map, otherwise the cluster would be discarded. The newly generated ROI-Corr image presented the significantly correlated regions between two input image modalities (M1=Image Modality 1 and M2=Image Modality 2).

A further segmentation of ROI-Corr is implanted in the ICM functionality, which allows further segmentation using the individualized grey-matter brain atlas (CHAPTER

II.3.1). By applying individual brain atlas, it allows further evaluation in specific region of interest. As default, the volume of interactive region in frontal lobe, temporal lobe, parietal lobe and occipital lobe are estimated, which provides additional information of pathological interaction in the specific brain regions. Segmentation results for other ROI regions are available on the demand of the user. This segmentation function of ROI-Corr maps can be used in evaluating the diseases with established vulnerable regions, such as putamen/caudate in Parkinson's disease and hippocampus in Alzheimer's disease.

3.2. Clinical Application of ICM

3.2.1 ICM method

The data used for evaluating the new techniques ICM were from the [^{11}C]PBR28 project. The ethical approval was granted by the Riverside Research Ethics Committee, and administer radiotracers was approved by the Administration of Radioactive Substances Advisory Committee UK. Written informed consent was obtained from all participants. In the current ICM investigation, 34 patients (12 AD and 22 MCI) had [^{11}C]PBR28 and [^{18}F]AV1451 scans, while 49 patients (14 AD and 35 MCI) had [^{11}C]PBR28 and [^{18}F]Flutemetamol scans. Among the 34 patients, 6 AD and 17 MCI subjects have been followed up with neuropsychometric testing. Among 49 patients, the cognitive performance of 8 AD and 16 MCI patients were followed up after 12.4 ± 5.4 months. In HC, 21 had [^{18}F]Flutemetamol, 8 had [^{18}F]AV1451, 18 (11 HAB and 7 MAB) had [^{11}C]PBR28 PET. In order to run the ICM correlation analysis, IRF-90 [^{11}C]PBR28 parametric maps were generated using spectral analysis with arterial blood input function (CHAPTER IV), while [^{18}F]AV1451 and [^{18}F]Flutemetamol RATIO image were generated using the cerebellum as the reference region. Subsequently, the individual T-scored map was generated by comparing individual patient's [^{11}C]PBR28, [^{18}F]AV1451, and [^{18}F]Flutemetamol PET against the corresponded healthy controls using one-way ANOVA. All T-scored maps were threshold at $p<0.05$ with an extent of 50 voxels. In this application, the ICM cluster unit was set to 5 x 5 x 5 mm^3, correlation threshold as $p<0.01$ (with Bonferroni correction), and R-square was $r>0.5$. For each patient, the pathological correlation map (ROI-Corr) were generated either between microglial activation and tau, or between microglial activation and amyloid by ICM. Further segmentation analysis of the ROI-Corr was performed to assess the interaction

in different brain cortices. The total volume and average tracer uptake were estimated for ROI-Corr. Those estimations were then correlated with cognitive performance in AD and MCI using SPSS24.

Each subject enrolled had up to 2 hours detailed neuropsychological tests. Including Mini-Mental State Examination (MMSE), Rey-Osterrieth complex figure (Rey), Wechsler Logical Memory (WLM), Hopkins Verbal Learning Test (Hopkins), Verbal fluency test, Digit Span, Letter-Number Sequencing (LNS), Trail making test (Trail A and Trail B), anxiety and depression test, which were used to assess the visuospatial memory, learning, naming, verbal learning, executive functions, language and recall function for each subject at baseline. Wechsler Logical Memory test requires participant listens to a brief narrative story from the assessor, then retells the narrative once immediately and again after 30 min delay (Lehr *et al.*, 2012). The Trail Making Test (TMT) A and B are popular neuropsychological tests, TMT-A requires the subject to draw lines to sequentially connect 25 numbers which randomly distributed on a paper, while TMT-B requires the subject to draw lines to connect between number and letters (Tombaugh, 2004). The scores of TMT-A and TMT-B denote the amount of time an individual requires to complete the task, which evaluates an individual's visual search, scanning, motor speed of processing, cognitive flexibility and executive function (Arbuthnott & Frank, 2000; Bowie & Harvey, 2006). In order to generalize the score system for multiple neuropsychometric tests, in this case, a subject with a higher score represents a better score, while a subject with a lower score represents cognitive impairment. For trail A and trail B, lower times indicate better performance.

More than half of the participants were followed up for their cognitive performance. 6/12 ADs and 16/22 MCIs with both [^{11}C]PBR28 and [^{18}F]AV1451 scans were followed up for 12.7 ± 5.7 months, while 6/14 AD and 24/35 MCI with [^{11}C]PBR28 and [^{18}F]AV1451 scans were followed up for 12.4 ± 5.4 months. The annual cognitive decline rate was calculated using the formula below:

$$Cognitive\ decline\ rate = \frac{(Baseline\ Score - Followup\ Score)}{Followup\ Score * t} \times 12 \times 100\%$$

Where t denotes the months of time duration at follow up. In this application, the ROI-Corr estimations at baseline were evaluated against the cognitive decline rate to see whether the correlated pathologies can predict the cognitive decline.

3.2.2 ICM results of tau and microglial activation

As a result, there was a significant larger volume of interaction between microglial activation and tau in AD subjects compared with MCI subjects (177%, p=0.039), suggesting an expanding of the correlated region between microglial activation and tau plaques at the later stage of the disease. Moreover, segmentation results demonstrated that the correlated volume was predominantly found in temporal lobe (156%, p=0.01) and occipital lobe (203%, p=0.03) in AD subjects, indicating the interactive microglial activation and tau was spreading significantly in temporal and occipital lobe as the disease evolving. On the individual basis, 58% AD (n=7/12) and 32% MCI (n=7/22) patients showed positive correlation between tau and neuroinflammation, suggesting heterogeneity of the pathological interaction existing on individual basis (
Table VI-1).

	ROI-Corr volume (cv)	Fraction of patients	range (min-max)	% brain volume
AD	125,060 (0.93)	42% (5/12)	216,490 -- 283,647	12-16%
		16% (2/12)	60,266 -- 87,866	4-5%
		42% (5/12)	n/a	n/a
MCI	45,157 (1.18)	5% (1/22)	214,858	12%
		27% (6/22)	66,755 -- 122,706	3%-7%
		68% (12/22)	n/a	n/a
DIF	177% (p=0.039)			

Table VI-1. ICM individual results between tau and microglial activation.

DIF=Group difference between AD and MCI cohort (two sample t test), VOL=Volume, CV=Coefficient of variation, % Brain Volume = Percentage of ROI-Corr over total brain volume, and volume unit is mm³. n/a not applicable. In this case, 5/12 AD and 12/22 MCI subjects failed to locate any correlated clusters between increased tau and increased microglial activation.

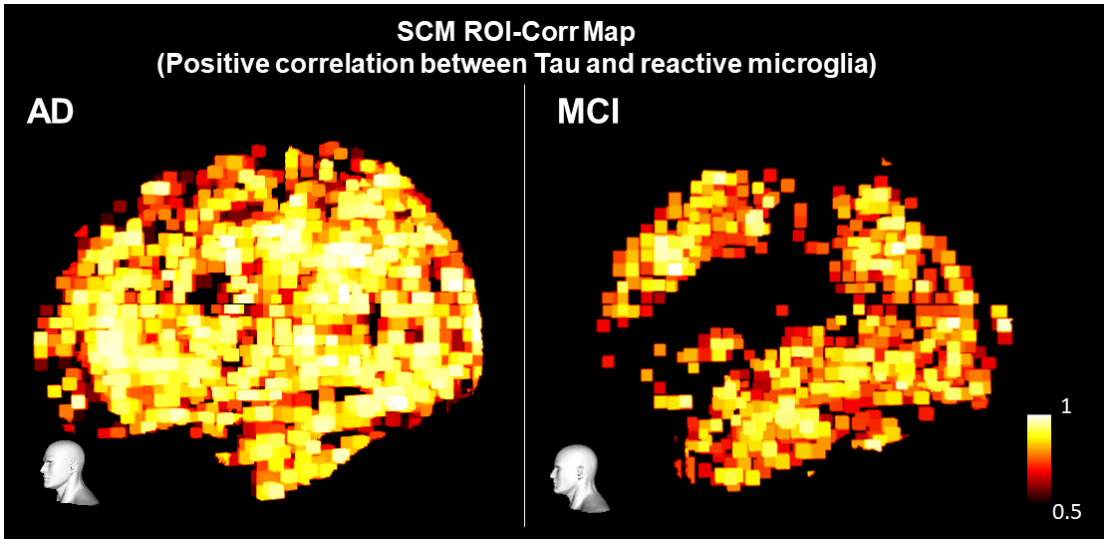


Figure VI-8. ICM ROI-Corr maps demonstrated the positive correlated clusters in three dimensional between tau and reactive microglia in an AD patient and an MCI patient.

The colour coded map represents the R-square value (range from 0.5 to 1) for each significant correlated cluster unit.

Of those patients who demonstrated significant correlation between tau and neuroinflammation (Figure VI-8), 5/7 AD subjects revealed correlated region occupied more than 10% of the brain volume, while only 1/7 MCI patient with significant correlation reached similar ROI-Corr volume. This finding reiterates the heterogeneity of the interaction between tau and neuroinflammation and demonstrates interactions between tau and microglial activation were expanded spatially in patients with advanced stage.

In AD patients, the longitudinal decline rate of Wechsler Logical Memory test (delayed recall) (R=0.89, p=0.039) and worsening of the Trail-A test (R=0.94, p=0.017) was found closely associated with baseline volume of correlated region between tau and microglial activation. The correlation with Wechsler Logical Memory test indicates that a higher volume of correlation between tau and microglial reactivity at baseline may contribute to a faster impairment of the retrieval function of logical memory after a brief delay. The association with TMT-A results suggests that the higher volume of correlated tau and reactive microglia in AD patients may lead to a faster decline in the visual search and motor speed measures.

In MCI subjects, the correlation between tau and microglial reactivity in the temporal lobe was found associated with annual decline of the Trail B performance (R=0.62,

p=0.009) and the MMSE score (R=0.59, p=0.017). Additionally, the volume of ROI-Corr in frontal and parietal lobe were found positively correlated with the annual decline of Digit Span (R=0.60, p=0.012) in MCIs. Thus, MCI patients who suffered from a higher volume of interaction between tau and reactive microglia might result in further deterioration in their visual search, ability to mentally maintain two simultaneous sequences, cognitive alternation measures, attention, and working memory functions.

3.2.3 ICM results of amyloid and microglial activation

The ICM analysis revealed positively correlated regions of amyloid and microglial activation in both AD and MCI patients. Similar to the interaction with tau, microglial activation demonstrated a heterogeneous interaction with amyloid at individual level, which reiterates the importance to evaluate the individual influence of each pathological process on the cognitive impairment (

Table VI-2). Compared to the number of AD and MCI patients who had significant correlation between microglial activation and amyloid, AD subjects showed higher volume of correlation (ROI-Corr) than that of MCI patients. (Figure VI-9)

	ROI-Corr VOL (CV)	Fraction of patients	Vol range (MIN-MAX)	% brain VOL
AD	111,806	21% (3/14)	177,568 -- 234,167	10-13%
	(0.67)	36% (5/14)	100,318 -- 156,613	6-9%
		43% (6/14)	n/a	n/a
MCI	59,029	9% (3/35)	186,594 -- 201,068	11%
	(1.00)	28% (10/35)	74,357 -- 138,958	4%-8%
		63% (22/35)	n/a	n/a
DIF	89% (p=0.035)			

Table VI-2. ICM individual results between amyloid and microglial activation.

DIF=Group difference between AD and MCI cohort (two sample t test), VOL=Volume, CV=Coefficient of variation, % Brain Volume = Percentage of ROI-Corr over total brain volume, and volume unit is mm³. n/a not applicable. In this case, 6/14 AD and 22/35 MCI subjects failed to locate any correlated clusters between increased amyloid and increased microglial activation.

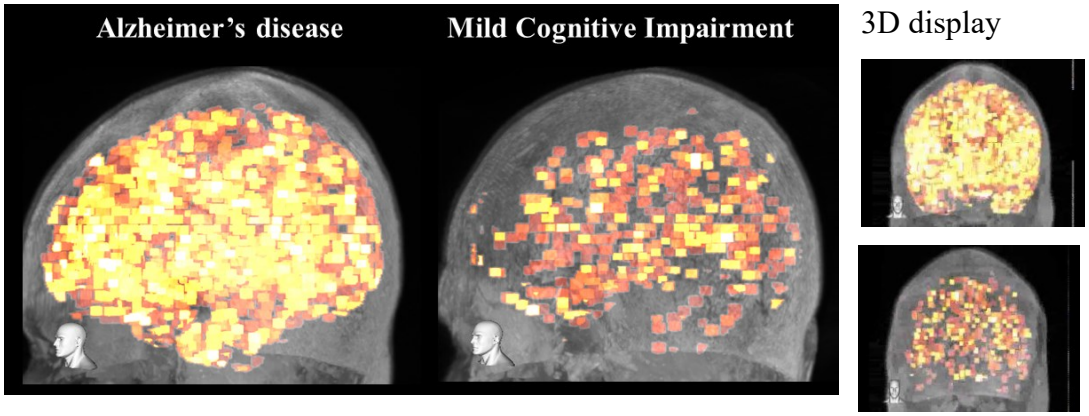


Figure VI-9. ROI-Corr maps demonstrated the positive correlated clusters between amyloid and microglial activation in an AD patient and an MCI patient.

The colour coded map represents the R-square value for each significant correlated cluster unit. 3D display is available on the right-hand panel.

At baseline, the volume of ROI-Corr between amyloid deposition and microglial activation in AD subjects was found correlated with the MMSE scores (R= -0.57, p=0.032). By further segmenting the brain, MMSE was found closely associated with the ROI-Corr in frontal lobe (R= -0.62, p= 0.019) and parietal lobe (R= -0.57, p= 0.032) in AD subjects. Additionally, the total ROI-Corr volume was correlated with Hopkins Verbal Learning Test (R= -0.60, p=0.038) in AD subjects at baseline. In MCI subjects, the total volume of ROI-Corr (amyloid and microglial activation) was found associated with both Rey-Osterrieth complex figure immediate (R= -0.35, p=0.039) and delayed recall (R= -0.39, P=0.02). By further segmenting the ROI-Corr, the cognitive function was closely associated with the ROI-Corr in frontal lobe (R= -0.40, p=0.016). Similar to AD subjects, Hopkins Verbal Learning Test in MCI subjects was associated with the amyloid and neuroinflammation interaction ROI-Corr in the frontal lobe (R=-0.38, p=0.044). Interestingly, when applying the volume of [^{11}C]PBR28 or [^{18}F]Flutemetamol PET separately, no correlation was found with any neuropsychological tests. Once again, the finding reiterated the fact that rather than investigation on a single pathology, the evaluation of the interactive pathologies for individual patient could be critical in interpreting the cognitive performance.

The total volume of ROI-Corr (amyloid and reactive microglia) in MCI patients at baseline was positively correlated with the annual worsening rate of Trail B test (R=0.511, p<0.013). On the contrary, the annual decline rate of immediate recall

performance of Hopkins Verbal Learning test in MCI patients was found inversely correlated with the ROI-Corr in the temporal ($R=0.45$, $p<0.031$) and occipital lobe ($R=-0.44$, $p<0.036$). Additionally, the total volume of amyloid deposition in AD subjects was associated with longitudinal decline rate of the Wechsler Logical Memory ($R=0.83$, $p<0.041$) and verbal fluency ($R=0.84$, $p<0.035$). In the current study, AD subjects demonstrated an inverse correlation between the total volume of interacted amyloid and activated microglia, and the MMSE score, suggesting the spreading of interaction between amyloid and inflammation in AD patients resulted in AD-related cognitive deficits. In particular, the volume of interactive pathologies occurred in frontal lobe and parietal lobe showed stronger connection to the cognitive function impairment.

3.2.4 ICM revealed correlation patterns in microglial activation with tau and amyloid in AD

Benefit from a group of 9 AD individuals who had scans with all three different tracers, further investigation on their correlation pattern in microglial activation with both tau and amyloid was evaluated in those AD brain. In order to better visualize the pattern of the individual correlation maps, I used a displaying technique, called 3-D intensity T-map, which I firstly introduced and published in 2015 in Brain (Fan *et al.*, 2015b). The idea behind the intensity T-maps is similar to the SPM render image, where superposed a summed image (slices on different orientation) as a surface plots in a three-dimension. The colour map represents the ICM correlation intensity of R-square on the corresponding cluster in the brain. Compared to the spatial demonstration of the ICM (e.g. Figure VI-9), the intensity T-maps provides a clear visualization of the distribution of significantly correlated clusters in each patient (Figure VI-10).

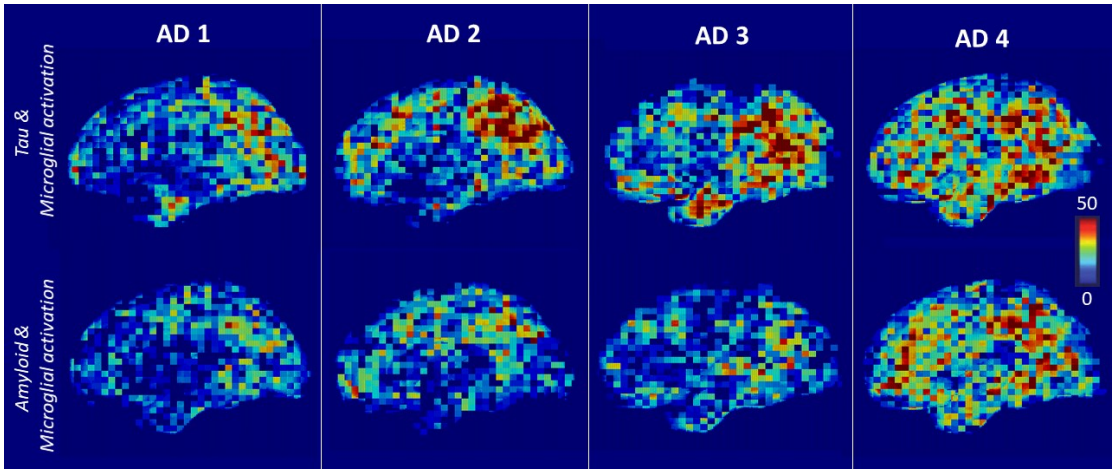


Figure VI-10. ICM plot shows the correlation pattern between tau and microglial activation (upper panel) and correlation pattern between amyloid and microglial activation (lower panel) in four AD subjects.

The viewing angle for the intensity T-maps were exhibited at horizontal rotation and vertical elevation at [-90, 90].

Microglial activation in AD subjects who had relatively higher correlation with tau plaques comparing to MCI patients, also demonstrated a higher association with amyloid in the similar brain regions, suggesting neuroinflammation may contribute in linking between tau pathology and amyloid deposition (Boon *et al.*, n.d.; Hoozemans *et al.*, 2011; Heneka *et al.*, 2015). The interaction between tau and reactive microglia in AD patients revealed a clear pattern of elevation that dominantly distributed in temporal, parietal lobe, and further spread into the frontal lobe in some individuals. The ICM correlation supported previous human studies which demonstrated that microglial activation was found paralleled with tau distribution, and was associated closely with the Braak's stage of tau pathology (Hoozemans *et al.*, 2011; Sheffield, Marquis & Berman, 2000), such as temporal lobe where tau based NFT was significant accumulated (Braak & Braak, 1991). Consistent with the preclinical studies, microglial activation was found associated with the aggregation of tau in the brain (Maphis *et al.*, 2015; Lee *et al.*, 2010a). Interestingly, the TSPO (microglial activation) in occipital cortex was weakly correlated with tau and amyloid. This is supported by a TSPO population study for pseudo reference region, which suggested occipital cortex may be free of pathological binding of activated microglia (Albrecht *et al.*, 2018).

Interestingly, the correlation between neuroinflammation and amyloid deposition in AD individuals was less robust than their correlation with tau (Figure VI-10). Longitudinal studies demonstrated that tau based NFT and neuroinflammation were found

progressing linearly throughout the AD disease courses, on the contrary, amyloid deposition quickly reached a plateau phase shortly after the symptom onset (Jack *et al.*, 2018b; Seppälä *et al.*, 2011; Fan *et al.*, 2015b). Additionally, post-mortem study demonstrated glial response was found positively related with tau tangles, but not associated with amyloid load (Serrano-Pozo *et al.*, 2011). These findings suggested that neuroinflammation may interact more closely with tau plaques, which leads to further synaptic loss and cognitive impairment.

3.2.5 ICM signal validation

Last but not least, the individual correlation mapping has conducted a powerful voxel-basis correlation at individual level, it is therefore necessary to ensure that those correlations which detected by ICM were not arising from random null data of negative individuals. For instance, noise/null signal observed in a healthy control or negative patient. In order to address the reliability of ICM correlation and validate those correlations were not false positives, individuals who revealed more than 10% brain volume of correlation in ICM were analysed as a group for their positivity for each tracer compared with healthy control.

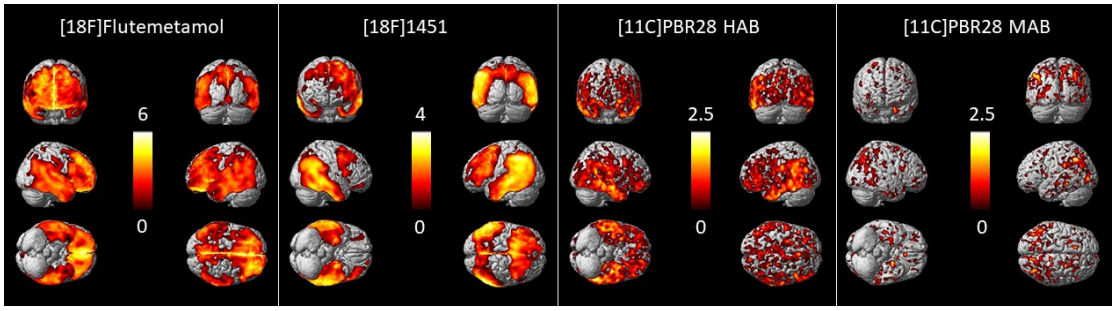


Figure VI-11. SPM group analysis for ICM positive subjects.

[^{18}F]Flutemetamol for amyloid deposition (threshold at p<0.005 and 200 voxels), [^{18}F]AV1451 for tau plaques (threshold at p<0.005 and 200 voxels), [^{11}C]PBR28 HAB and [^{11}C]PBR28 MAB for microglial activation (threshold at p<0.05 and 50 voxels).

In this case, six patients (5AD and 1 MCI) who revealed correlation between tau and microglial activation (

Table VI-1) and six patients (3AD and 3MCI) who showed correlation between amyloid and microglial activation (

Table VI-2) were investigated. Group SPM analysis between ICM positive patients and healthy controls were performed for [^{18}F]AV1451 for tau plaques, [^{18}F]Flutemetamol

for amyloid deposition, [^{11}C]PBR28 HAB and [^{11}C]PBR28 MAB for microglial activation. As expected, all four groups demonstrated group-level significant higher tracer uptake in amyloid deposition, tau plaques, and microglial activation at voxel-level compared with healthy controls, therefore ICM positive patients were proved to be positive in binding of all tracers compared with healthy controls (Figure VI-11), suggesting the ICM correlation were not arising from 'random noise' in tracer negative individuals.

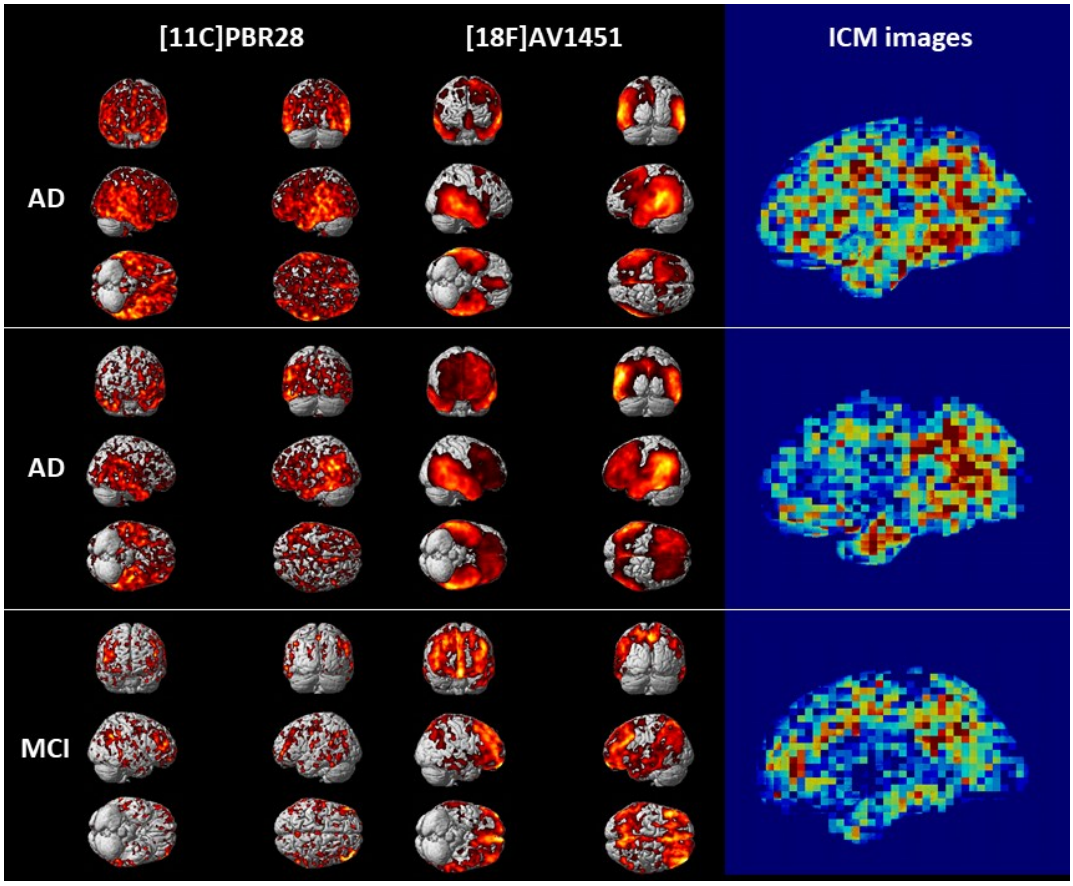


Figure VI-12. Spatial pattern between individual correlation maps (ICM) and individual SPM-T maps which showed the distribution of [^{11}C]PBR28 and [^{18}F]AV1451. Two AD subjects (1st and 2nd panel) and one MCI subject (3rd panel) were presented.

To further extend the strength of the validation, the spatial pattern derived from the individual correlation map (ICM) between [^{11}C]PBR28 and [^{18}F]AV1451 was compared to their individual distribution of each tracers in AD and MCI subjects. As demonstrated in Figure VI-12, in the two AD subjects, the correlation between tau and microglial activation was observed predominately in the frontal, temporal and parietal lobes, which was consistent with the distribution that revealed in the [^{11}C]PBR28 and

[^{18}F]AV1451 PET. As [^{11}C]PBR28 and [^{18}F]AV1451 PET demonstrated less uptake in the MCI subject, ICM image also localized a smaller volume of ROI-Corr, which was closely related to the regional distribution of individual microglial activation and tau deposition. The ICM positive patients were not only found to be positive in all three biomarkers, but also demonstrated a similar regional distribution of ROI-Corr on individual basis, indicating that correlation which produced by ICM analysis are reliable. Interestingly, the volume of individual ROI-Corr was smaller than the volume of anatomical co-localization of two biomarkers, suggesting, ICM is able to reveal the actual correlation and interaction between different biomarkers rather than regional co-localization.

3.3. Possible Use of ICM

Individual Correlation Map provides a novel tool to assess the pathological interaction on an individual basis, and enables a powerful voxel-level approach in detecting the influence of specific pathological interactions in the brain on individuals' cognitive and behaviour status. Regarding the potential false positive correlation, rather than using the raw PET as input, I applied the t-scored maps to demonstrate the significant changes relative to the healthy controls. Different mathematical correction was implanted, such as Bonferroni correction to correct for multiple comparisons. Additionally, the correlation maps were supported by the biomarker distribution, suggesting the ICM is not arising from random noise. Lastly, the individual correlation pattern of three biomarkers showed consistency with the pathological findings in AD patients. Although the improvement work is continuing, the voxel-wise ICM framework shows potential to assess the complex interaction between neuropathological substrates in neurodegenerative disease, and allows the scientists and doctors to evaluate a specific pathological condition in each patient (Latta, Brothers & Wilcock, 2015). ICM has the potential to be used in clinical diagnostic work and provides compensational pathological results.

VI-4. TECHNIQUE III. AUTOMATED SPATIAL TRANSFORMATION QC

4.1. Principle of Automated Spatial Transformation QC

Finally, I present an automated spatial transformation quality control approach for imaging analysis. This approach is designed to auto-detect the possible failure of spatial transformation and provide statistics to users. Due to the high cost of the image acquisition, data sharing has become popular in imaging research field. Subsequently, open sources of ADNI (http://adni.loni.usc.edu/), AIBL (http://adni.loni.usc.edu/) and DIAN (https://dian.wustl.edu/) database were established. The massive number of collective images data gathered from all over the world has led to a new era of imaging research, where researchers are able to make more convincing statistical arguments benefiting from a large database. However, due to the massive amount of data, it almost made it impossible for manually checking the quality of spatial transformation. Therefore, automated QC of imaging analysis is necessary to be developed which assists researchers and maintains the data integrity. In this section, I present the automated spatial transformation QC technique that I developed to help scientists who need to conduct imaging analysis with a big dataset.

Spatial transformation is a fundamental part of imaging analysis, which enables the coregistration, normalization and atlas fitting. Spatial transformation between 3D images requires a significant amount of mathematical calculations and interpolation methods. Fortunately, software such as SPM (http://www.fil.ion.ucl.ac.uk/spm/), FSL (https://www.fmrib.ox.ac.uk/fsl), FreeSurfer (https://surfer.nmr.mgh.harvard.edu/) and PMOD (http://www.pmod.com) are capable to handle most complicated calculations (Dale, Fischl & Sereno, 1999; Friston, 2007; Woolrich *et al.*, 2009). However, failures of image spatial transformation are often encountered due to manual or system errors.

Automated Spatial Transformation QC application is based on a 3D spatial overlapping percentage estimation system at voxel level. Firstly, for the reference image and coregistered image, two independent binary thresholds are estimated using the image 2-D binary function, a build-in function in the MATLAB image analysis toolbox. The binary function uses the global threshold at 2-D level, the binary function is therefore applied slice by slice to create the binary images. The summed original images (all slices) are shown next to their binary version for user to QC the binary procedure. After

binary images are generated for all subjects, subsequently the overlapping three-dimensional image is created to present the region of overlapping, region of reference image and region of coregistered image. After that, the overlapping percentage is calculated using the volume of overlapping region divided by the volume of the total three regions in each brain slice.

For each subject, the overlapping percentage is calculated slice by slice and produces a result table in an excel sheet. In the MRI, it has shown that the slice outside the brain tissue (e.g. bone) may provide highly variated estimation. In order to minimize the manual effort in the QC process, in the current investigation, 30 pairs of well-reregistered images and 30 pairs of non-registered images were used to evaluate a standard final measurement to differentiate the quality of spatial transformation with the minimal variation. The overlapping percentage for each image slice was reported and the middle slice of overlapping figure was generated for further visualization assessment.

4.2. Clinical application of Auto Spatial Transformation QC

In this clinical application, image data were collected from the ADNI website (http://adni.loni.usc.edu/). A total of 351 subjects who had AV45 PET and corresponding T1 MRI were randomly selected from year 2016 to 2018. The PET images were coregistered into MRI space using SPM12 with 7^{th} Degree B-Spline Interpolation, which applies the most neighbour values when conducting the spatial transformation (CHAPTER II.3.2). All procedures were done in MATLAB 2017.

After performing the automated spatial transformation QC application in MATLAB 2017, an overlapping image and QC statistical report were generated for each subject. In this QC application, three major tests were compared between reference image (MRI) and spatial transformed image (i.e. PET co-registration): 1) Comparison of spatial dimensions, 2) Comparison of image origin and voxel size (accurate to four decimal points), 3) overlapping 3D image is created for each QC and 4) finally a statistical report of overlapping percentage on multiple slices are generated for further evaluation.

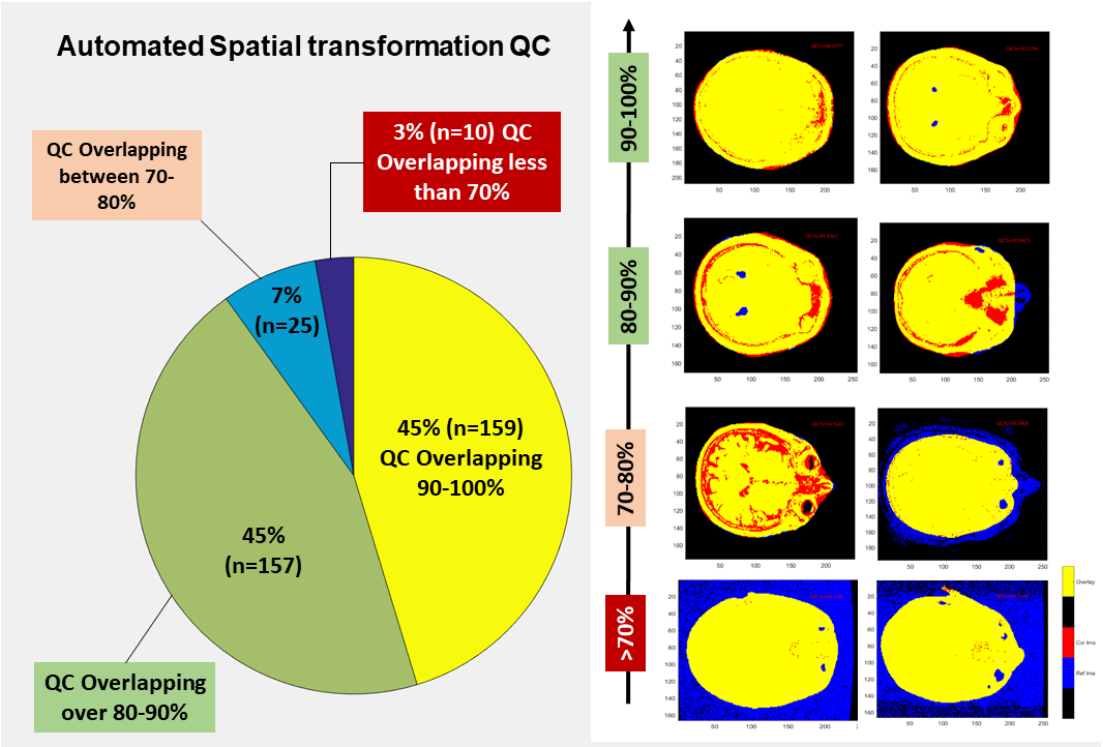


Figure VI-13. Automated Spatial transformation QC results summary.

On the left, the percentage pie chart has demonstrated an overall performance of the spatial transformation QC. On the right hand, one illustration of each category (90-100%, 80-90%, 70-80% and <70%) has been shown. The yellow colour encoded area where the reference image and co-registered image overlaid; the blue colour represented the reference image, and red colour represented co-registered image.

As a result, five subjects failed in dimension tests suggesting the process need to be repeated for those subjects. Based on the QC overlapping report, 90% subjects (n=316) showed more than 80% overlapping percentage between reference images and co-reregistered images, suggesting a successful spatial transformation. After manually reviewed the 316 images with over 80% overlapping, all subjects were reregistered correctly, suggesting a high accuracy with a low false positive rate in this subgroup. For 25 subjects (7%) who demonstrated an overlapping QC estimation between 70-80%, after manually inspections, 16/25 subjects failed the spatial transformation and the process need to be rerun. In this subgroup, the false positive rate become 64%, suggesting more than half of those images with 70-80% overlay requires reran or investigation. Lastly, 10 subjects demonstrated less than 70% in overlapping QC estimation indicating a failure of spatial transformation. As a result, the original MRIs of those 10 subjects that were not in a good quality, such as high noise or dimensional

distorted. In summary, when overlapping estimation exceeds 80%, the spatial transformation can be regarded as successful; when overlapping estimation falls between 70-80%, further manually visual inspection is required; lastly, if overlapping estimation falls below 70%, rerun of such subjects are highly recommended as the spatial transformation may well be failed. In this small clinical application, we observed a reasonably high successful rate (90%) in spatial transformation, however it also demonstrates the importance of having a QC step in place on each image spatial transformation process. The automated spatial QC application I developed provides a simple and effective framework to help researchers and clinicians to guard the data integrity. (Figure VI-13)

4.3. Possible Usage of Auto Spatial Transformation QC

Quality control in imaging analysis is essential, especially for spatial transformation which ensures the basic level of data integrity and quality of imaging sampling. This automated QC provides an automatic system which quickly detects images that are not transformed correctly. Compared to other existing QC methods, the presented auto Spatial Transformation QC method is independent of the resolution of input images (Alfaro-Almagro *et al.*, 2018), and do not require prior machine learning (Li & Fan, 2018). According to the clinical application, subjects which receive more than 80% in the 3-dimentional overlapping test can be classified as successful; any subjects which have overlapping results ranged around 70% to 80% are suggested to perform further visual assessment; while subjects which have overlapping scores below 70% are classified as failed co-registration. The automated spatial transformation QC is an independent tool which can be easily incorporated into any analysis pipeline, especially for a large database to provide objective and effective statistical tests to assess the performance of spatial transformation at voxel-level.

CHAPTER VII. SUMMARY AND CONCLUSIONS

VII-1. SUMMARY OF THIS WORK

1.1. GLIAL ACTIVATION IN PET

Positron Emission Tomography, a nuclear medicine neuroimaging technology, provides *in vivo* absolute quantification of the concentration and distribution of the radioligands, which are designed for specific biological target using a natural molecule labelled with positron emitters (e.g. 18F, 11C and 15O). AD is a neurodegenerative disease and accounts for 50-60% of the cause of dementia (Alzheimer & Association, 2018). Emerging evidence from immune genetic studies have suggested that there is a strong connection between the immunological mechanism and the AD pathogenesis; therefore, numerous disease-modifying therapies have increasing interests in targeting neuroinflammation in the pathogenesis of AD. Due to the complexity of inflammatory mechanisms and incomplete understanding of pathophysiology in brains, quantifying the clinical neuroinflammation *in vivo* is vital for pathogenesis studies and anti-inflammatory drug developments for AD. Hence there is an urgent need to develop novel PET tracers for glial activation and evaluate methods for quantifying the pharmacological meaningful signals.

In this work, I have evaluated the novel TSPO tracer [^{18}F]GE180 (CHAPTER III) and [^{11}C]PBR28 (CHAPTER IV) for regional distribution of microglial activation in AD and MCI patients; and novel I_2BS tracer (CHAPTER V) for astrocyte activation. As a result, IRF parametric maps generated by spectral analysis of all three glial activation tracers have shown a good consistency with V_T derived from the kinetic compartmental modelling, and demonstrated a high sensitivity in differentiating the glial activation changes in AD patients from the age-matched controls. Thus spectral analysis using basis function appears to be able to reliably quantify TSPO and I_2BS signals for glial activation, and provides parametric maps for statistical comparison between image cohorts at voxel-level. In general, higher glial activation of microglia and astrocyte were observed in both AD and MCI patients compared with age-matched healthy controls, especially for those who had amyloid deposition, suggesting sustained exposure of amyloid deposition in disease brain may play a role in elevating the glial activation. To

note, [^{18}F]GE180 demonstrated a disproportional high plasma binding and low brain uptake in human brain, suggesting possible difficulty in [^{18}F]GE180's penetration ability to cross the BBB. In my opinion, the utilization of [^{18}F]GE180 tracer for microglial activation remains inclusive until the histologic validation of blood-brain barrier integrity was performed in parallel with the [^{18}F]GE180 PET. Although higher [^{18}F]GE180 signals were observed in AD patients compared with healthy controls, the evaluation of BBB integrity is necessary to support and validate the hypothesis that higher signals observed in patients' brain are more pharmacologically meaningful rather than a reflection of BBB leakage in AD patients' brain. Additionally, due to the high level of TSPO binding presented in the blood vessel, as part of my PhD, I designed a vascular extraction procedure for TSPO tracers by eroding the peripheral area of the brain atlas to reduce the high signal disperse from the blood vessels and bones. This is suggested to be included in future analysis for novel TSPO tracer quantification based on the nature of TSPO tracer.

1.2. IMAGING BIOMARKER CORRELATION

In my opinion, there are several challenges in the AD research: 1) the diverse clinical presentation in dementia population, 2) the multifactorial nature of dementia and 3) the complexity of clinical staging along with genetic and environmental factors. Benefiting from the fast development in PET molecular imaging, it allows investigation on multiple pathological imaging biomarkers *in vivo* and offers the opportunity to fill the gaps in the understanding of pathogenesis in AD. Hence multiple imaging biomarkers' interaction in each patient's brain could be an interesting exploratory target to extend our knowledge on the disease progression.

In CHAPTER V, a voxel-level positive correlation was observed between astrocyte reactivity and amyloid, which again supports the close association between glial activation and amyloid in disease brain. However, similar to amyloid (BRAAK & BRAAK, 1991), level of astrocyte reactivity appears to be not associated with the cognition, suggesting astrocytes may influence the cognitive function differently during the course of AD development. The hypothesis of functionality shifting in reactive astrocytes in AD was further supported by the observation of different regional-specific correlations that were revealed between astrocyte reactivity and glucose metabolism at

voxel-level, which may be due to the level of local insults (e.g. amyloid burden and synapse loss).

In CHAPTER VI, two novel imaging strategies 1) the VOI Prediction Tool (biomarker co-localization) and 2) Individual Correlation Mapping (biomarker correlation) were developed to assess biomarker interactions in individual AD and MCI patient. In the clinical application (15MCI and 3AD) of VPT, I found the co-localized VOIs that derived from individuals' microglial activation, tauopathy and amyloid deposition were correlated closely with individuals' annual cognitive decline rate (R^2=85.9%, p=0.00011). This positive correlation suggested that a higher level of co-localization of imaging biomarkers (microglial activation, amyloid and tau) may result in a higher chance of cognitive decline. Individual Correlation Mapping focused on the statistically meaningful correlation between biomarkers, thus providing a quantitative measurement of biomarker correlation at voxel-level. Two separate clinical applications were applied for the ICM method, the *in vivo* correlation between microglial activation and tauopathy (12 AD and 22 MCI), as well as correlation between microglial activation and amyloid deposition (14 AD and 35 MCI). As a result, the volume of ICM estimated in both clinical applications showed a good sensitivity in differentiating the AD patients from the MCI patients, suggesting the individual ICM correlation (microglial activation vs. tauopathy or amyloid) could be a potential surrogate maker for disease staging. Moreover, the severity of clinical performance was found associated with the higher level of correlated volumes. In summary, the novel imaging techniques provide a new way to evaluate the influence of biomarker interaction in neurodegenerative disease. The clinical applications of correlation between glial activation (e.g. microglial and astrocyte activation) and other AD pathologies (e.g. amyloid, tau and glucose metabolism) have illustrated the critical role of pathological interactions on individual cognitive performance.

VII-2. LIMITATIONS AND FUTURE DIRECTION

In this work, the highly heterogeneous TSPO binding between subjects were observed. This variation is shared among most TSPO PET tracers in AD studies, which may be due to the nature of TSPO brain distribution or the divergent presentation of neuroinflammation in AD brain, suggesting larger subject cohort or more specific CNS inflammation disease should be evaluated to address the utilization of novel TSPO

tracers. Given the difficulty of [^{18}F]GE180 brain penetration in human, it is therefore suggested to perform a histologic analysis for the blood-brain barrier integrity in future analysis for the [^{18}F]GE180 ligand to rule out possibility of BBB leakage. Like most 2nd generation TSPO tracers, [^{11}C]PBR28 was found significantly influenced by the TSPO binding affinity (Owen *et al.*, 2011b). This limitation causes 15% of the population that have LAB are not available for scanning, hence for the future development of novel TSPO tracers, one should always consider the genetic influences and try to develop a TSPO tracer which is independent of genetic influences (e.g. [^{11}C](R)PK11195). Moreover, both microglial and astroglial activation appear to be highly associated with amyloid deposition; therefore, future imaging analysis for glial activation in AD is suggested to include amyloid imaging. Rather than depending on the diverse clinical presentation in dementia population, amyloid imaging provides additional biological-based results to better interpret the changes of glial activation in AD patients.

The novel methods developed for evaluation of biomarker correlation has provided a powerful voxel-basis correlation for individual patient. While statistical corrections and signal validation analysis were presented, it is still necessary to involve larger study cohort to ensure the relevance of those clinical findings. Future applications should be designed to verify those interactions located by the novel techniques are truly biological linked. Therefore, testing the methods in animal model and verifying the biological findings would be useful. Additionally, it would be interesting to test the method by correlating biomarkers which are biologically unrelated.

VII-3. CONLCUSION

There is an unmet need for brain glial activation measurements in human brain. In this thesis, three independent studies were conducted to explore the optimal PET methods and potential use of novel TSPO PET ligands ([^{18}F]GE180 and [^{11}C]PBR28) and novel I2BS ligand ([^{11}C]BU99008), for assessing glial activation in the trajectory of neurodegenerative diseases. Apart from [^{11}C]PBR28 which showed slightly higher preference to the vascular model, two-tissue compartmental model works the best with most glial activation PET tracers. Furthermore, spectral analysis has been proved to be a good candidate for generating reliable parametric maps for glial activation tracers.

Clinically, elevation of glial activation was observed in patients with neurodegenerative disease compared to age-matched controls using all three PET tracers, which is in line with concepts shown in previous reports that neuroinflammation is a common phenomenon and plays a critical role in neurodegenerative disease. Interestingly, I found patients who had higher amyloid burden have demonstrated a higher level of microglial and astroglial activation, indicating a close relationship between microglial cells and the amyloid deposition. However, results should be further evaluated with histologic validation and other CSF inflammation disease conditions to confirm that those are truly biological meaningful elevations. Additionally, with the enormous effort spending on PET tracer development for neuroinflammation, such as [^{18}F]DPA714, [^{18}F]FUIIS1009B, and [^{18}F]PBR06 (Tang *et al.*, 2012, 2017; Wimberley *et al.*, 2018; Simmons *et al.*, 2018), I consider that the search for the optimal glial tracer in human remains inconclusive.

In the past, imaging biomarker correlation analysis *in vivo* has been highly limited due to the high cost of the image acquisition. However, due to the urgent need to find a cure for the devastating disease, data sharing from all over the world has become popular and led to a new era of imaging research (e.g. ADNI, AIBL, and DIAN). Therefore, I believe developing techniques for *in vivo* imaging biomarker interaction and quality control may contribute not only in neurodegenerative disease field, but also to provide tools for *in vivo* imaging research in general. In this work, I have developed new imaging techniques (e.g. VOI Prediction Tool and Individual Correlation Mapping) to reveal the biomarker interaction (e.g. glial activation and tauopathy) at voxel level in individual patient, and demonstrated a good association between the level of pathological interaction and the severity of the cognitive deficiency. In my opinion, given the diverse clinical presentation in dementia population, the novel correlation methods have a great potential in providing future individualized patient management, by assessing the specific pathological interaction in each patient and developing more effective individual-based treatment.

REFERENCES

Akaike, H. (1973) Maximum Likelihood Identification of Gaussian Autoregressive Moving Average Models. *Biometrika*. 60 (2), 255.

Akama, K.T. & Van Eldik, L.J. (2000) Beta-amyloid stimulation of inducible nitric-oxide synthase in astrocytes is interleukin-1beta- and tumor necrosis factor-alpha (TNFalpha)-dependent, and involves a TNFalpha receptor-associated factor- and NFkappaB-inducing kinase-dependent signaling mech. *The Journal of biological chemistry*. 275 (11), 7918–7924.

Alam, M.M., Lee, J. & Lee, S.-Y. (2017) Recent Progress in the Development of TSPO PET Ligands for Neuroinflammation Imaging in Neurological Diseases. *Nuclear Medicine and Molecular Imaging*. 51 (4), 283–296.

Albert, N.L., Unterrainer, M., Fleischmann, D.F., Lindner, S., et al. (2017) TSPO PET for glioma imaging using the novel ligand 18F-GE-180: first results in patients with glioblastoma. *European Journal of Nuclear Medicine and Molecular Imaging*. 44 (13), 2230–2238.

Albrecht, D.S., Normandin, M.D., Shcherbinin, S., Wooten, D.W., et al. (2018) Pseudoreference Regions for Glial Imaging with ^{11}C-PBR28: Investigation in 2 Clinical Cohorts. *Journal of Nuclear Medicine*. 59 (1), 107–114.

Alfaro-Almagro, F., Jenkinson, M., Bangerter, N.K., Andersson, J.L.R., et al. (2018) Image processing and Quality Control for the first 10,000 brain imaging datasets from UK Biobank. *NeuroImage*. 166, 400–424.

Allaman, I., Gavillet, M., Belanger, M., Laroche, T., et al. (2010) Amyloid- Aggregates Cause Alterations of Astrocytic Metabolic Phenotype: Impact on Neuronal Viability. *Journal of Neuroscience*.

Alzheimer & Association (2018) 2018 Alzheimer's disease facts and figures. *Alzheimer's & Dementia*. 14, 367–429.

Amor, S., Puentes, F., Baker, D. & van der Valk, P. (2010) Inflammation in neurodegenerative diseases. *Immunology*. 129 (2), 154–169.

Arbuthnott, K. & Frank, J. (2000) Trail Making Test, Part B as a Measure of Executive Control: Validation Using a Set-Switching Paradigm. *Journal of Clinical and Experimental Neuropsychology (Neuropsychology, Development and Cognition: Section A)*. 22 (4), 518–528.

Assaf, Y. & Pasternak, O. (2008) Diffusion Tensor Imaging (DTI)-based White Matter Mapping in Brain Research: A Review. *Journal of Molecular Neuroscience*. 34 (1), 51–61.

Association, A. (2017) 2017 Alzheimer's disease facts and figures. *Alzheimer's and Dementia*. 13 (4), 325–373.

Bailey, D.L. (2005) *Positron emission tomography : basic sciences*. Springer.

Bailey, D.L. (1998) Transmission scanning in emission tomography. *European journal of nuclear medicine*. 25 (7), 774–787.

Bailey, J.A., Maloney, B., Ge, Y.-W. & Lahiri, D.K. (2011) Functional activity of the novel Alzheimer's amyloid β-peptide interacting domain (AβID) in the APP and BACE1 promoter sequences and implications in activating apoptotic genes and in amyloidogenesis. *Gene*. 488 (1–2), 13–22.

Beauquis, J., Pavía, P., Pomilio, C., Vinuesa, A., et al. (2013) Environmental enrichment prevents astroglial pathological changes in the hippocampus of APP transgenic mice, model of Alzheimer's disease. *Experimental Neurology*. 239, 28–37.

Benjamin, A.M. & Quastel, J.H. (1972) Locations of amino acids in brain slices from the rat. Tetrodotoxin-sensitive release of amino acids. *The Biochemical journal*. 128 (3), 631–646.

Biscaro, B., Lindvall, O., Tesco, G., Ekdahl, C.T., et al. (2012) Inhibition of Microglial Activation Protects Hippocampal Neurogenesis and Improves Cognitive Deficits in a Transgenic Mouse Model for Alzheimer's Disease. *Neurodegenerative Diseases*. 9 (4), 187–198.

Blomqvist, G. (1984) *Journal of Cerebral Blood Flow and Metahol i sm 4:629-632 On the Construction of Functional Maps in Positron Emission Tomography*.

Bloomfield, P.S., Selvaraj, S., Veronese, M., Rizzo, G., et al. (2016) Microglial Activity in People at Ultra High Risk of Psychosis and in Schizophrenia: An [(11)C]PBR28 PET Brain Imaging Study. *The American journal of psychiatry*. 173 (1), 44–52.

Boellaard, R., Turkheimer, F.E., Hinz, R., Schuitemaker, A., et al. (2008) Performance of a modified supervised cluster algorithm for extracting reference region input functions from (R)-[11C]PKll195 brain PET studies. *IEEE Nuclear Science Symposium Conference Record*. 5400–5402.

Boon, B.D.C., Hoozemans, J.J.M., Lopuhaä, B., Eigenhuis, K.N., et al. (n.d.) *Neuroinflammation is increased in the parietal cortex of atypical Alzheimer's*

disease.

Borlikova, G.G., Trejo, M., Mably, A.J., Mc Donald, J.M., et al. (2013) Alzheimer brain-derived amyloid β-protein impairs synaptic remodeling and memory consolidation. *Neurobiology of Aging*. 34 (5), 1315–1327.

Boussicault, L., Hérard, A.-S., Calingasan, N., Petit, F., et al. (2014) Impaired Brain Energy Metabolism in the BACHD Mouse Model of Huntington's Disease: Critical Role of Astrocyte–Neuron Interactions. *Journal of Cerebral Blood Flow & Metabolism*. 34 (9), 1500–1510.

Boutin, H., Murray, K., Pradillo, J., Maroy, R., et al. (2014) 18F-GE-180: a novel TSPO radiotracer compared to 11C-R-PK11195 in a preclinical model of stroke. *European Journal of Nuclear Medicine and Molecular Imaging*. 42 (3), 503–511.

Bowie, C.R. & Harvey, P.D. (2006) Administration and interpretation of the Trail Making Test. *Nature Protocols*. 1 (5), 2277–2281.

Boyle, P.A., Yang, J., Yu, L., Leurgans, S.E., et al. (2017) Varied effects of age-related neuropathologies on the trajectory of late life cognitive decline. *Brain*. 140 (3), aww341.

Bozdogan, H. (1987) Model selection and Akaike's Information Criterion (AIC): The general theory and its analytical extensions. *Psychometrika*. 52 (3), 345–370.

Braak, H., Alafuzoff, I., Arzberger, T., Kretzschmar, H., et al. (2006) Staging of Alzheimer disease-associated neurofibrillary pathology using paraffin sections and immunocytochemistry. *Acta Neuropathologica*. 112 (4), 389–404.

Braak, H. & Braak, E. (1991) Neuropathological stageing of Alzheimer-related changes. *Acta Neuropathologica*. 82 (4), 239–259.

Brettschneider, J., Del Tredici, K., Lee, V.M.Y. & Trojanowski, J.Q. (2015) Spreading of pathology in neurodegenerative diseases: A focus on human studies. *Nature Reviews Neuroscience*. 16 (2), 109–120.

Brown, A.K., Fujita, M., Fujimura, Y., Liow, J.-S., et al. (2007) Radiation Dosimetry and Biodistribution in Monkey and Man of 11 C-PBR28: A PET Radioligand to Image Inflammation. *J Nucl Med*. 48, 2072–2079.

Bu, G. (2009) Apolipoprotein e and its receptors in Alzheimer's disease: Pathways, pathogenesis and therapy. *Nature Reviews Neuroscience*.

Buffo, A., Rolando, C. & Ceruti, S. (2010) Astrocytes in the damaged brain: Molecular and cellular insights into their reactive response and healing potential. *Biochemical*

Pharmacology. 79 (2), 77–89.

Bullich, S., Villemagne, V.L., Catafau, A.M., Jovalekic, A., et al. (2017) Optimal Reference Region to Measure Longitudinal Amyloid-β Change with ^{18}F-Florbetaben PET. *Journal of Nuclear Medicine*. 58 (8), 1300–1306.

Burda, J.E. & Sofroniew, M. V. (2014) Reactive gliosis and the multicellular response to CNS damage and disease. *Neuron*.

Cai, Z., Hussain, M.D. & Yan, L.-J. (2014) Microglia, neuroinflammation, and beta-amyloid protein in Alzheimer's disease. *International Journal of Neuroscience*. 124 (5), 307–321.

Calsolaro, V. & Edison, P. (2016) Neuroinflammation in Alzheimer's disease: Current evidence and future directions. *Alzheimers & Dementia*. 12 (6), 719–732.

Cappellano, G., Carecchio, M., Fleetwood, T., Magistrelli, L., et al. (2013) Immunity and inflammation in neurodegenerative diseases. *American journal of neurodegenerative disease*. 2 (2), 89–107.

Carter, B.S., Meng, F. & Thompson, R.C. (2012) Glucocorticoid treatment of astrocytes results in temporally dynamic transcriptome regulation and astrocyte-enriched mRNA changes in vitro. *Physiological Genomics*.

Carter, S.F., Scholl, M., Almkvist, O., Wall, A., et al. (2012) Evidence for Astrocytosis in Prodromal Alzheimer Disease Provided by 11C-Deuterium-L-Deprenyl: A Multitracer PET Paradigm Combining 11C-Pittsburgh Compound B and 18F-FDG. *Journal of Nuclear Medicine*. 53 (1), 37–46.

Casanova, R., Srikanth, R., Baer, A., Laurienti, P.J., et al. (2007) Biological parametric mapping: A statistical toolbox for multimodality brain image analysis. *NeuroImage*. 34 (1), 137–143.

Castillo-Carranza, D.L., Guerrero-Muñoz, M.J. & Kayed, R. (2014) Immunotherapy for the treatment of Alzheimer's disease: amyloid-β or tau, which is the right target? *ImmunoTargets and therapy*. 3, 19–28.

Catafau, A.M., Bullich, S., Seibyl, J., Barthel, H., et al. (2015) Do cerebellar plaques influence 18F-florbetaben amyloid PET scan quantification? *Alzheimer's & Dementia*. 11 (7), P286–P287.

Chakravarthy, B., Whitfield, J., Armato, U., Pacchiana, R., et al. (2008) Emerging concepts of how β-amyloid proteins and pro-inflammatory cytokines might collaborate to produce an 'Alzheimer brain' (Review). *Molecular Medicine*

Reports. 1 (2), 173–178.

Charbonneau, P., Syrota, A., Crouzel, C., Valois, J.M., et al. (1986) Peripheral-type benzodiazepine receptors in the living heart characterized by positron emission tomography. *Circulation*. 73 (3), 476–483.

Chauveau, F., Boutin, H., Van Camp, N., Dollé, F., et al. (2008) Nuclear imaging of neuroinflammation: a comprehensive review of [11C]PK11195 challengers. *European Journal of Nuclear Medicine and Molecular Imaging*. 35 (12), 2304–2319.

Chen J, Gunn S, Nixon M, Myers R, G.R. (2000) Medical image understanding and analysis MIUA 2000: proceedings of the fourth annual conference. In: *A supervised method for PET reference region extraction.* 2000 p.

Cherry, J.D., Tripodis, Y., Alvarez, V.E., Huber, B., et al. (2016) Microglial neuroinflammation contributes to tau accumulation in chronic traumatic encephalopathy. *Acta Neuropathologica Communications*. 4 (1), 112.

Chételat, G. (2013) Alzheimer disease: Aβ-independent processes-rethinking preclinical AD. *Nature Reviews Neurology*.9 (3) pp.123–124.

Chiu, I.M., Morimoto, E.T.A., Goodarzi, H., Liao, J.T., et al. (2013) A Neurodegeneration-Specific Gene-Expression Signature of Acutely Isolated Microglia from an Amyotrophic Lateral Sclerosis Mouse Model. *Cell Reports*. 4 (2), 385–401.

Coleman, P.D. & Flood, D.G. (1987) Neuron numbers and dendritic extent in normal aging and Alzheimer's disease. *Neurobiology of Aging*. 8 (6), 521–545.

Cunningham, V.J. & Jones, T. (1993) Spectral analysis of dynamic PET studies. *Journal of cerebral blood flow and metabolism : official journal of the International Society of Cerebral Blood Flow and Metabolism*. 13, 15–23.

Dal Prà, I., Chiarini, A., Gui, L., Chakravarthy, B., et al. (2015) Do astrocytes collaborate with neurons in spreading the 'infectious' Aβ and Tau drivers of Alzheimer's disease? *Neuroscientist*. 21 (1), 9–29.

Dale, A.M., Fischl, B. & Sereno, M.I. (1999) Cortical surface-based analysis: I. Segmentation and surface reconstruction. *NeuroImage*. 9 (2), 179–194.

Dale, B.M., Brown, M.A. & Semelka, R.C. (2015) *MRI Basic Principles and Applications*. Chichester, UK, John Wiley & Sons, Ltd.

Dani, M., Wood, M., Mizoguchi, R., Fan, Z., et al. (2018) Microglial activation

correlates in vivo with both tau and amyloid in Alzheimer's disease. *Brain*.

David, J.-P.P., Ghozali, F., Fallet-Bianco, C., Wattez, A., et al. (1997) Glial reaction in the hippocampal formation is highly correlated with aging in human brain. *Neuroscience Letters*. 235 (1–2), 53–56.

Deussing, M., Blume, T., Vomacka, L., Mahler, C., et al. (2018) Data on specificity of [18F]GE180 uptake for TSPO expression in rodent brain and myocardium. *Data in Brief*. 19, 331–336.

Dickens, A.M., Vainio, S., Marjamäki, P., Johansson, J., et al. (2014) Detection of Microglial Activation in an Acute Model of Neuroinflammation Using PET and Radiotracers 11C-(R)-PK11195 and 18F-GE-180. *Journal of nuclear medicine : official publication, Society of Nuclear Medicine*. 55 (3), 466–472.

Dorfman, V.B., Pasquini, L., Riudavets, M., López-Costa, J.J., et al. (2010) Differential cerebral deposition of IDE and NEP in sporadic and familial Alzheimer's disease. *Neurobiology of Aging*. 31 (10), 1743–1757.

Edison, P., Ahmed, I., Fan, Z., Hinz, R., et al. (2013) Microglia, Amyloid, and Glucose Metabolism in Parkinson's Disease with and without Dementia. *Neuropsychopharmacology*. 38 (6), 938–949.

Fabricius, K., Jacobsen, J.S. & Pakkenberg, B. (2013) Effect of age on neocortical brain cells in 90+ year old human females-a cell counting study. *Neurobiology of Aging*. 34 (1), 91–99.

Fagan, A.M. (2015) What does it mean to be 'amyloid-positive'? *Brain : a journal of neurology*. 138 (Pt 3), 514–516.

Fan, Z., Aman, Y., Ahmed, I., Chetelat, G., et al. (2014) Influence of microglial activation on neuronal function in Alzheimer's and Parkinson's disease dementia. *Alzheimer's & dementia : the journal of the Alzheimer's Association*. 11, 1–14.

Fan, Z., Brooks, D.J., Okello, A. & Edison, P. (2017) An early and late peak in microglial activation in Alzheimer's disease trajectory. *Brain*. aww349.

Fan, Z., Calsolaro, V., Atkinson, R.A., Femminella, G.D., et al. (2016) Flutriciclamide (18F-GE180) PET: first in human PET study of novel 3rd generation in vivo marker of human translator protein. *Journal of Nuclear Medicine*. 57 (11), 1753–1759.

Fan, Z., Dani, M., Femminella, G.D., Wood, M., et al. (2018) *Parametric mapping using spectral analysis for 11 C-PBR28 PET reveals neuroinflammation in mild*

cognitive impairment subjects. 1432–1441.

Fan, Z., Harold, D., Pasqualetti, G., Williams, J., et al. (2015a) Can Studies of Neuroinflammation in a TSPO Genetic Subgroup (HAB or MAB) Be Applied to the Entire AD Cohort? *J Nucl Med*. 56 (5), 707–713.

Fan, Z., Okello, A.A., Brooks, D.J. & Edison, P. (2015b) Longitudinal influence of microglial activation and amyloid on neuronal function in Alzheimer's disease. *Brain*. awv288.

Feeney, C., Scott, G., Raffel, J., Roberts, S., et al. (2016) Kinetic analysis of the translocator protein positron emission tomography ligand [18F]GE-180 in the human brain. *European Journal of Nuclear Medicine and Molecular Imaging*. 43 (12), 2201–2210.

De Felice, F.G., Wu, D., Lambert, M.P., Fernandez, S.J., et al. (2008) Alzheimer's disease-type neuronal tau hyperphosphorylation induced by Aβ oligomers. *Neurobiology of Aging*. 29 (9), 1334–1347.

Fiala, M., Zhang, L., Gan, X., Sherry, B., et al. (1998) Amyloid-beta induces chemokine secretion and monocyte migration across a human blood--brain barrier model. *Molecular medicine (Cambridge, Mass.)*. 4 (7), 480–489.

Field, A. (2013) *Discovering Statistics Using SPSS: IBM SPSS Statistics*.

Firouzian, A., Whittington, A., Searle, G.E., Koychev, I., et al. (2018) Imaging Aβ and tau in early stage Alzheimer's disease with [18F]AV45 and [18F]AV1451. *EJNMMI Research*. 8 (1), 19.

Fletcher, J.W. & Kinahan, P.E. (2010) PET/CT Standardized Uptake Values (SUVs) in Clinical Practice and Assessing Response to Therapy. *NIH Public Access*. 31 (6), 496–505.

Fonov, V., Evans, A.C., Botteron, K., Almli, C.R., et al. (2011) Unbiased average age-appropriate atlases for pediatric studies. *NeuroImage*. 54 (1), 313–327.

Forbes, R.M., COOPER, A.R. & MITCHELL, H.H. (1953) *The composition of the adult human body as determined by chemical analysis.* 203 (1), 359–366.

Forsyth, R., Fray, A., Boutelle, M., Fillenz, M., et al. (1996) A Role for Astrocytes in Glucose Delivery to Neurons? *Developmental Neuroscience*. 18 (5–6), 360–370.

Friston, K. (2007) Statistical Parametric Mapping. In: *Statistical Parametric Mapping: The Analysis of Functional Brain Images*. pp. 10–31.

Fuhrmann, M., Bittner, T., Jung, C.K.E., Burgold, S., et al. (2010) Microglial Cx3cr1

knockout prevents neuron loss in a mouse model of Alzheimer's disease. *Nature Neuroscience*. 13 (4), 411–413.

Funato, H., Yoshimura, M., Yamazaki, T., Saido, T.C., et al. (1998) Astrocytes containing amyloid beta-protein (Abeta)-positive granules are associated with Abeta40-positive diffuse plaques in the aged human brain. *The American journal of pathology*. 152 (4), 983–992.

Gallivanone, F., Della Rosa, P.A. & Castiglioni, I. (2016) Statistical Voxel-Based Methods and [18F]FDG PET Brain Imaging: Frontiers for the Diagnosis of AD. *Current Alzheimer research*. 13 (6), 682–694.

García-Sevilla, J.A., Escribá, P. V, Walzer, C., Bouras, C., et al. (1998) Imidazoline receptor proteins in brains of patients with Alzheimer's disease. *Neuroscience Letters*. 247 (2–3), 95–98.

Gatliff, J. & Campanella, M. (2016) TSPO: kaleidoscopic 18-kDa amid biochemical pharmacology, control and targeting of mitochondria. *Biochemical Journal*. 473 (2), 107–121.

Ghosh, S., Wu, M.D., Shaftel, S.S., Kyrkanides, S., et al. (2013) Sustained interleukin-1β overexpression exacerbates tau pathology despite reduced amyloid burden in an Alzheimer's mouse model. *The Journal of neuroscience : the official journal of the Society for Neuroscience*. 33 (11), 5053–5064.

Goerdt, S. & Orfanos, C.E. (1999) Other functions, other genes: alternative activation of antigen-presenting cells. *Immunity*. 10 (2), 137–142.

Golby, A., Silverberg, G., Race, E., Gabrieli, S., et al. (2005) Memory encoding in Alzheimer's disease: an fMRI study of explicit and implicit memory. *Brain*. 128 (4), 773–787.

Gomez-Arboledas, A., Davila, J.C., Sanchez-Mejias, E., Navarro, V., et al. (2018) Phagocytic clearance of presynaptic dystrophies by reactive astrocytes in Alzheimer's disease. *Glia*. 66 (3), 637–653.

Gulyás, B., Pavlova, E., Kása, P., Gulya, K., et al. (2011) Activated MAO-B in the brain of Alzheimer patients, demonstrated by [11C]-l-deprenyl using whole hemisphere autoradiography. *Neurochemistry International*. 58 (1), 60–68.

Gunn, R.N., Lammertsma, A.A., Hume, S.P. & Cunningham, V.J. (1997) Parametric Imaging of Ligand-Receptor Binding in PET Using a Simplified Reference Region Model. *NeuroImage*. 6 (4), 279–287.

Guo, Q., Owen, D.R., Rabiner, E. a., Turkheimer, F.E., et al. (2012) Identifying improved TSPO PET imaging probes through biomathematics: The impact of multiple TSPO binding sites in vivo. *NeuroImage*. 60 (2), 902–910.

Guo, Q., Owen, D.R., Rabiner, E. a, Turkheimer, F.E., et al. (2014) A graphical method to compare the in vivo binding potential of PET radioligands in the absence of a reference region: application to [(11)C]PBR28 and [(18)F]PBR111 for TSPO imaging. *Journal of cerebral blood flow and metabolism : official journal of the International Society of Cerebral Blood Flow and Metabolism*. (April), 1–7.

Haley, M.J., Brough, D., Quintin, J. & Allan, S.M. (2018) Microglial Priming as Trained Immunity in the Brain. *Neuroscience*.

Halle, A., Hornung, V., Petzold, G.C., Stewart, C.R., et al. (2008) The NALP3 inflammasome is involved in the innate immune response to amyloid-β. *Nature Immunology*. 9 (8), 857–865.

Hallmann, A.-L., Araúzo-Bravo, M.J., Mavrommatis, L., Ehrlich, M., et al. (2017) Astrocyte pathology in a human neural stem cell model of frontotemporal dementia caused by mutant TAU protein. *Scientific Reports*. 7 (January), 42991.

Hatashita, S. & Yamasaki, H. (2013) Diagnosed mild cognitive impairment due to Alzheimer's disease with PET biomarkers of beta amyloid and neuronal dysfunction. *PloS one*. 8 (6), e66877.

Hayakawa, N., Kato, H. & Araki, T. (2007) Age-related changes of astorocytes, oligodendrocytes and microglia in the mouse hippocampal CA1 sector. *Mechanisms of Ageing and Development*. 128 (4), 311–316.

Heneka, M.T., Carson, M.J., Khoury, J. El, Landreth, G.E., et al. (2015) Neuroinflammation in Alzheimer's disease. *The Lancet Neurology*. 14 (4), 388–405.

Heneka, M.T., Kummer, M.P. & Latz, E. (2014) Innate immune activation in neurodegenerative disease. *Nature Reviews Immunology*. 14 (7), 463–477.

Heneka, M.T., Kummer, M.P., Stutz, A., Delekate, A., et al. (2012) NLRP3 is activated in Alzheimer's disease and contributes to pathology in APP/PS1 mice. *Nature*. 493 (7434), 674–678.

Heneka, M.T., Sastre, M., Dumitrescu-Ozimek, L., Dewachter, I., et al. (2005) Focal glial activation coincides with increased BACE1 activation and precedes amyloid plaque deposition in APP[V717I] transgenic mice. *Journal of Neuroinflammation*.

2 (1), 22.

Hickman, S.E., Allison, E.K. & El Khoury, J. (2008) Microglial dysfunction and defective beta-amyloid clearance pathways in aging Alzheimer's disease mice. *The Journal of neuroscience : the official journal of the Society for Neuroscience*. 28 (33), 8354–8360.

Higuchi, M., Ji, B., Maeda, J., Sahara, N., et al. (2016) *Neuroimmunology*. 7, 139–144.

Hinz, R. & Boellaard, R. (2015) Challenges of quantification of TSPO in the human brain. *Clinical and Translational Imaging*. 3 (6), 403–416.

Hoozemans, J.J.M., Rozemuller, A.J.M., Haastert, E.S. Van, Eikelenboom, P., et al. (2011) *Neuroinflammation in Alzheimer ' s disease wanes with age*. 1–8.

Hwang, C.J., Park, M.H., Hwang, J.Y., Kim, J.H., et al. (2016) CCR5 deficiency accelerates lipopolysaccharide-induced astrogliosis, amyloid-beta deposit and impaired memory function. *Oncotarget*. 7 (11), 11984–11999.

Ichise, M., Toyama, H., Innis, R.B., Carson, R.E., et al. (2002) Strategies to Improve Neuroreceptor Parameter Estimation by Linear Regression Analysis. *Journal of Cerebral Blood Flow & Metabolism*. 22 (10), 1271–1281.

Innis, R.B., Cunningham, V.J., Delforge, J., Fujita, M., et al. (2007) Consensus nomenclature for in vivo imaging of reversibly binding radioligands. *Journal of cerebral blood flow and metabolism : official journal of the International Society of Cerebral Blood Flow and Metabolism*. 27 (9), 1533–1539.

Ishibashi, K., Ishiwata, K., Toyohara, J., Murayama, S., et al. (2014) Regional analysis of striatal and cortical amyloid deposition in patients with Alzheimer's disease. *European Journal of Neuroscience*. 40 (4), 2701–2706.

Ishizuka, K., Kimura, T., Igata-yi, R., Katsuragi, S., et al. (1997) Identification of monocyte chemoattractant protein-1 in senile plaques and reactive microglia of Alzheimer's disease. *Psychiatry and clinical neurosciences*. 51 (3), 135–138.

Isik, A.T. (2010) Late onset Alzheimer's disease in older people. *Clinical interventions in aging*. 5, 307–311.

Ittner, L.M. & Götz, J. (2011) Amyloid-β and tau — a toxic pas de deux in Alzheimer's disease. *Nature Reviews Neuroscience*. 12 (2), 67–72.

Ittner, L.M., Ke, Y.D., Delerue, F., Bi, M., et al. (2010) Dendritic function of tau mediates amyloid-beta toxicity in Alzheimer's disease mouse models. *Cell*. 142 (3), 387–397.

Jack, C.R., Bennett, D.A., Blennow, K., Carrillo, M.C., et al. (2018a) NIA-AA Research Framework: Toward a biological definition of Alzheimer's disease. *Alzheimer's and Dementia*. 14 (4), 535–562.

Jack, C.R., Wiste, H.J., Schwarz, C.G., Lowe, V.J., et al. (2018b) Longitudinal tau PET in ageing and Alzheimer's disease. *Brain*. 141 (5), 1517–1528.

James, M.L., Belichenko, N.P., Shuhendler, A.J., Hoehne, A., et al. (2017) [18F]GE-180 PET Detects Reduced Microglia Activation After LM11A-31 Therapy in a Mouse Model of Alzheimer's Disease. *Theranostics*. 7 (6), 1422–1436.

Johnson, K.A., Minoshima, S., Bohnen, N.I., Donohoe, K.J., et al. (2013) Appropriate use criteria for amyloid PET: a report of the Amyloid Imaging Task Force, the Society of Nuclear Medicine and Molecular Imaging, and the Alzheimer's Association. *Alzheimer's & dementia : the journal of the Alzheimer's Association*. 9 (1), e-1-16.

Joshi, P., Turola, E., Ruiz, A., Bergami, A., et al. (2014) Microglia convert aggregated amyloid-β into neurotoxic forms through the shedding of microvesicles. *Cell Death & Differentiation*. 21 (4), 582–593.

Kantarci, K., Lowe, V., Przybelski, S.A., Weigand, S.D., et al. (2012) APOE modifies the association between Aβ load and cognition in cognitively normal older adults. *Neurology*. 78 (4), 232–240.

Kawamura, K., Kimura, Y., Yui, J., Wakizaka, H., et al. (2012) PET study using [11C]FTIMD with ultra-high specific activity to evaluate I2-imidazoline receptors binding in rat brains. *Nuclear Medicine and Biology*. 39 (2), 199–206.

Kealey, S., Turner, E.M., Husbands, S.M., Salinas, C.A., et al. (2013) Imaging Imidazoline-I2 Binding Sites in Porcine Brain Using 11C-BU99008. *Journal of Nuclear Medicine*. 54 (1), 139–144.

Kiyota, T., Yamamoto, M., Xiong, H., Lambert, M.P., et al. (2009) CCL2 Accelerates Microglia-Mediated Aβ Oligomer Formation and Progression of Neurocognitive Dysfunction Ashley I. Bush (ed.). *PLoS ONE*. 4 (7), e6197.

Koenigsknecht-Talboo, J. & Landreth, G.E. (2005) Microglial Phagocytosis Induced by Fibrillar -Amyloid and IgGs Are Differentially Regulated by Proinflammatory Cytokines. *Journal of Neuroscience*. 25 (36), 8240–8249.

Koon-Pong Wong, Dagan Feng, Meikle, S.R. & Fulham, M.J. (2002) Segmentation of dynamic PET images using cluster analysis. *IEEE Transactions on Nuclear*

Science. 49 (1), 200–207.

Kraft, A.W., Hu, X., Yoon, H., Yan, P., et al. (2013) Attenuating astrocyte activation accelerates plaque pathogenesis in APP/PS1 mice. *The FASEB Journal*. 27 (1), 187–198.

Kreisl, W.C., Lyoo, C.H., Liow, J.-S., Wei, M., et al. (2016) 11C-PBR28 binding to translocator protein increases with progression of Alzheimer's disease. *Neurobiology of Aging*. 44, 53–61.

Kreisl, W.C., Lyoo, C.H., McGwier, M., Snow, J., et al. (2013) In vivo radioligand binding to translocator protein correlates with severity of Alzheimer's disease. *Brain*. 136 (7), 2228–2238.

Kulijewicz-Nawrot, M., Verkhratsky, A., Chvátal, A., Syková, E., et al. (2012) Astrocytic cytoskeletal atrophy in the medial prefrontal cortex of a triple transgenic mouse model of Alzheimer's disease. *Journal of anatomy*. 221 (3), 252–262.

Kumar, A., Singh, A. & Ekavali (2015) A review on Alzheimer's disease pathophysiology and its management: An update. *Pharmacological Reports*. 67 (2), 195–203.

Kummer, M.P., Hammerschmidt, T., Martinez, A., Terwel, D., et al. (2014) Ear2 deletion causes early memory and learning deficits in APP/PS1 mice. *The Journal of neuroscience : the official journal of the Society for Neuroscience*. 34 (26), 8845–8854.

Kurz, A. & Perneczky, R. (2011) Novel insights for the treatment of Alzheimer's disease. *Progress in Neuro-Psychopharmacology and Biological Psychiatry*. 35 (2), 373–379.

Lammertsma, A.A. & Hume, S.P. (1996) Simplified reference tissue model for PET receptor studies. *NeuroImage*. 4 (3 Pt 1), 153–158.

Landau, S., Thomas, B., Thurfjell, L., Schmidt, M., et al. (2014) *Amyloid PET imaging in Alzheimer's disease: A comparison of three radiotracers*. 41 (7), 1398–1407.

Laske, C., Stransky, E., Hoffmann, N., Maetzler, W., et al. (2010) Macrophage colony-stimulating factor (M-CSF) in plasma and CSF of patients with mild cognitive impairment and Alzheimer's disease. *Current Alzheimer research*. 7 (5), 409–414.

Latta, C.H., Brothers, H.M. & Wilcock, D.M. (2015) Neuroinflammation in Alzheimer's disease; A source of heterogeneity and target for personalized therapy.

Neuroscience. 302, 103–111.

Lawson, L.J., Perry, V.H. & Gordon, S. (1992) Turnover of resident microglia in the normal adult mouse brain. *Neuroscience*. 48 (2), 405–415.

Lee, D.C., Rizer, J., Selenica, M.-L.B., Reid, P., et al. (2010a) LPS- induced inflammation exacerbates phospho-tau pathology in rTg4510 mice. *Journal of neuroinflammation*. 7, 56.

Lee, S., Varvel, N.H., Konerth, M.E., Xu, G., et al. (2010b) CX3CR1 Deficiency Alters Microglial Activation and Reduces Beta-Amyloid Deposition in Two Alzheimer's Disease Mouse Models. *The American Journal of Pathology*. 177 (5), 2549–2562.

Lee, Y.K., Kwak, D.H., Oh, K.W., Nam, S.-Y., et al. (2009) CCR5 deficiency induces astrocyte activation, Aβ deposit and impaired memory function. *Neurobiology of Learning and Memory*. 92 (3), 356–363.

Lehr, M., Prud'hommeaux, E., Shafran, I. & Roark, B. (2012) Fully automated neuropsychological assessment for detecting Mild Cognitive Impairment. *Proceedings of Interspeech 2010*. 1–4.

Li, H. & Fan, Y. (2018) Non-rigid image registration using self-supervised fully convolutional networks without training data. In: *2018 IEEE 15th International Symposium on Biomedical Imaging (ISBI 2018)*. April 2018 IEEE. pp. 1075–1078.

Liang, W.S., Reiman, E.M., Valla, J., Dunckley, T., et al. (2008) Alzheimer's disease is associated with reduced expression of energy metabolism genes in posterior cingulate neurons. *Proceedings of the National Academy of Sciences*. 105 (11), 4441–4446.

Logan, J. (2000) Graphical analysis of PET data applied to reversible and irreversible tracers. *Nuclear medicine and biology*. 27, 661–670.

Lowe, V.J., Kemp, B.J., Jack, C.R., Senjem, M., et al. (2009) Comparison of 18F-FDG and PiB PET in cognitive impairment. *Journal of nuclear medicine : official publication, Society of Nuclear Medicine*. 50 (6), 878–886.

Lowe, V.J., Lundt, E., Knopman, D., Senjem, M.L., et al. (2017) Comparison of [18F]Flutemetamol and [11C]Pittsburgh Compound-B in cognitively normal young, cognitively normal elderly, and Alzheimer's disease dementia individuals. *NeuroImage. Clinical*. 16, 295–302.

Lucin, K.M., O'Brien, C.E., Bieri, G., Czirr, E., et al. (2013) Microglial Beclin 1 Regulates Retromer Trafficking and Phagocytosis and Is Impaired in Alzheimer's

Disease. *Neuron*. 79 (5), 873–886.

Lue, L.F., Rydel, R., Brigham, E.F., Yang, L.B., et al. (2001) Inflammatory repertoire of Alzheimer's disease and nondemented elderly microglia in vitro. *Glia*. 35 (1), 72–79.

Lue, L.F., Walker, D.G. & Rogers, J. (2001) Modeling microglial activation in Alzheimer's disease with human postmortem microglial cultures. *Neurobiology of aging*. 22 (6), 945–956.

Lynch, A.M., Murphy, K.J., Deighan, B.F., O'Reilly, J.-A., et al. (2010) The impact of glial activation in the aging brain. *Aging and disease*. 1 (3), 262–278.

Lyoo, C.H., Ikawa, M., Liow, J.-S.J.-S.S., Zoghbi, S.S., et al. (2015) Cerebellum Can Serve As a Pseudo-Reference Region in Alzheimer Disease to Detect Neuroinflammation Measured with PET Radioligand Binding to Translocator Protein. *Journal of Nuclear Medicine*. 56 (5), 701–706.

Maloney, B. & Lahiri, D.K. (2011) The Alzheimer's amyloid β-peptide (Aβ) binds a specific DNA Aβ-interacting domain (AβID) in the APP, BACE1, and APOE promoters in a sequence-specific manner: Characterizing a new regulatory motif. *Gene*. 488 (1–2), 1–12.

Mantovani, A., Sozzani, S., Locati, M., Allavena, P., et al. (2002) Macrophage polarization: tumor-associated macrophages as a paradigm for polarized M2 mononuclear phagocytes. *Trends in immunology*. 23 (11), 549–555.

Maphis, N., Xu, G.X., Kokiko-Cochran, O.N., Jiang, S., et al. (2015) Reactive microglia drive tau pathology and contribute to the spreading of pathological tau in the brain. *Brain*. 138 (6), 1738–1755.

Martinez, F.O. & Gordon, S. (2014) The M1 and M2 paradigm of macrophage activation: time for reassessment. *F1000Prime Reports*. 6 (March), 1–13.

Masgrau, R., Guaza, C., Ransohoff, R.M. & Galea, E. (2017) Should We Stop Saying 'Glia' and 'Neuroinflammation'? *Trends in Molecular Medicine*. 23 (6), 486–500.

McGinnity, C.J., Riaño Barros, D.A., Rosso, L., Veronese, M., et al. (2017) Test-retest reproducibility of quantitative binding measures of [11C]Ro15-4513, a PET ligand for GABAA receptors containing alpha5 subunits. *NeuroImage*. 152, 270–282.

Medeiros, R. & LaFerla, F.M. (2013) Astrocytes: Conductors of the Alzheimer disease neuroinflammatory symphony. *Experimental Neurology*. 239, 133–138.

Mori, F., Tanji, K., Zhang, H.-X.X., Nishihira, Y., et al. (2008) Maturation process of

TDP-43-positive neuronal cytoplasmic inclusions in amyotrophic lateral sclerosis with and without dementia. *Acta Neuropathologica*. 116 (2), 193–203.

Mosher, K.I. & Wyss-Coray, T. (2014) Microglial dysfunction in brain aging and Alzheimer's disease. *Biochemical Pharmacology*. 88, 594–604.

Nagele, R.G., D'Andrea, M.R., Lee, H., Venkataraman, V., et al. (2003) Astrocytes accumulate A beta 42 and give rise to astrocytic amyloid plaques in Alzheimer disease brains. *Brain research*. 971 (2), 197–209.

Nair, A., Veronese, M., Xu, X., Curtis, C., et al. (2016) Test-retest analysis of a non-invasive method of quantifying [(11)C]-PBR28 binding in Alzheimer's disease. *EJNMMI research*. 6 (1), 72.

Nelson, L., Gard, P. & Tabet, N. (2014) Hypertension and Inflammation in Alzheimer's Disease: Close Partners in Disease Development and Progression! *Journal of Alzheimer's Disease*. 41 (2), 331–343.

Nilsen, L.H., Witter, M.P. & Sonnewald, U. (2014) Neuronal and Astrocytic Metabolism in a Transgenic Rat Model of Alzheimer's Disease. *Journal of Cerebral Blood Flow & Metabolism*. 34 (5), 906–914.

Nimmerjahn, A., Kirchhoff, F. & Helmchen, F. (2005) Resting microglial cells are highly dynamic surveillants of brain parenchyma in vivo. *Neuroforum*. 11 (3), 95–96.

Niraula, A., Sheridan, J.F. & Godbout, J.P. (2017) Microglia Priming with Aging and Stress. *Neuropsychopharmacology*. 42 (1), 318–333.

Nunomura, A., Tamaoki, T., Tanaka, K., Motohashi, N., et al. (2010) Intraneuronal amyloid beta accumulation and oxidative damage to nucleic acids in Alzheimer disease. *Neurobiology of disease*. 37 (3), 731–737.

O'Sullivan, M.J. & Vann, S.D. (2016) Amyloid imaging and Alzheimer's disease: the unsolved cases. *Brain : a journal of neurology*. 139 (Pt 9), 2342–2344.

Okello, A., Edison, P., Archer, H.A., Turkheimer, F.E., et al. (2009) Microglial activation and amyloid deposition in mild cognitive impairment: A PET study. *Neurology*. 72 (1), 56–62.

Oksanen, M., Petersen, A.J., Naumenko, N., Puttonen, K., et al. (2017) PSEN1 Mutant iPSC-Derived Model Reveals Severe Astrocyte Pathology in Alzheimer's Disease. *Stem Cell Reports*. 9 (6), 1885–1897.

Olabarria, M., Noristani, H.N., Verkhratsky, A. & Rodríguez, J.J. (2011) Age-dependent

decrease in glutamine synthetase expression in the hippocampal astroglia of the triple transgenic Alzheimer's disease mouse model: mechanism for deficient glutamatergic transmission? *Molecular Neurodegeneration*. 6 (1), 55.

Olabarria, M., Noristani, H.N., Verkhratsky, A. & Rodríguez, J.J. (2010) Concomitant astroglial atrophy and astrogliosis in a triple transgenic animal model of Alzheimer's disease. *Glia*. 58 (7), NA-NA.

Ossenkoppele, R., Jansen, W.J., Rabinovici, G.D., Knol, D.L., et al. (2015) Prevalence of amyloid PET positivity in dementia syndromes: a meta-analysis. *JAMA*. 313 (19), 1939–1949.

Owen, D.R., Guo, Q., Kalk, N.J., Colasanti, A., et al. (2014) Determination of [^{11}C]PBR28 Binding Potential *in vivo:* A First Human TSPO Blocking Study. *Journal of Cerebral Blood Flow & Metabolism*. 34 (6), 989–994.

Owen, D.R., Yeo, A.J., Gunn, R.N., Song, K., et al. (2011a) *An 18-kDa Translocator Protein (TSPO) polymorphism explains differences in binding affinity of the PET radioligand PBR28*. 32 (1), 1–5.

Owen, D.R.J., Gunn, R.N., Rabiner, E.A., Bennacef, I., et al. (2011b) Mixed-Affinity Binding in Humans with 18-kDa Translocator Protein Ligands. *Journal of Nuclear Medicine*. 52 (1), 24–32.

Parbo, P., Ismail, R., Hansen, K. V., Amidi, A., et al. (2017) Brain inflammation accompanies amyloid in the majority of mild cognitive impairment cases due to Alzheimer's disease. *Brain*. 140 (7), 2002–2011.

Park, E., Gallezot, J.-D., Delgadillo, A., Liu, S., et al. (2015) 11C-PBR28 imaging in multiple sclerosis patients and healthy controls: test-retest reproducibility and focal visualization of active white matter areas. *European Journal of Nuclear Medicine and Molecular Imaging*. 42 (7), 1081–1092.

Parker, C.A., Nabulsi, N., Holden, D., Lin, S. -f., et al. (2014) Evaluation of 11C-BU99008, a PET Ligand for the Imidazoline2 Binding Sites in Rhesus Brain. *Journal of Nuclear Medicine*. 55 (5), 838–844.

Parkhurst, C.N., Yang, G., Ninan, I., Savas, J.N., et al. (2013) Microglia Promote Learning-Dependent Synapse Formation through Brain-Derived Neurotrophic Factor. *Cell*. 155 (7), 1596–1609.

Passchier, J. (2009) Fast high performance liquid chromatography in PET quality control and metabolite analysis. *The quarterly journal of nuclear medicine and*

molecular imaging : official publication of the Italian Association of Nuclear Medicine (AIMN) [and] the International Association of Radiopharmacology (IAR), [and] Section of the Society of... 53 (4), 411–416.

Patel, N.S., Paris, D., Mathura, V., Quadros, A.N., et al. (2005) Inflammatory cytokine levels correlate with amyloid load in transgenic mouse models of Alzheimer's disease. *Journal of Neuroinflammation*. 2 (1), 9.

Pellerin, L. & Magistretti, P.J. (1994) Glutamate uptake into astrocytes stimulates aerobic glycolysis: a mechanism coupling neuronal activity to glucose utilization. *Proceedings of the National Academy of Sciences of the United States of America*. 91 (22), 10625–10629.

Penny, W., Friston, K., Ashburner, J., Kiebel, S., et al. (2011) *Statistical parametric mapping: The analysis of functional brain images*.

Portet, F., Ousset, P.J., Visser, P.J., Frisoni, G.B., et al. (2006) Mild cognitive impairment (MCI) in medical practice: a critical review of the concept and new diagnostic procedure. Report of the MCI Working Group of the European Consortium on Alzheimer's Disease. *Journal of Neurology, Neurosurgery & Psychiatry*. 77 (6), 714–718.

Radford, R.A., Morsch, M., Rayner, S.L., Cole, N.J., et al. (2015) The established and emerging roles of astrocytes and microglia in amyotrophic lateral sclerosis and frontotemporal dementia. *Frontiers in cellular neuroscience*. 9 (October), 414.

Rahmim, A., Qi, J. & Sossi, V. (2013) Resolution modeling in PET imaging: Theory, practice, benefits, and pitfalls. *Medical Physics*. 40 (6Part1), 064301.

Reiman, E.M., Chen, K., Liu, X., Bandy, D., et al. (2009) Fibrillar amyloid-beta burden in cognitively normal people at 3 levels of genetic risk for Alzheimer's disease. *Proceedings of the National Academy of Sciences of the United States of America*. 106 (16), 6820–6825.

Rizzo, G., Veronese, M., Tonietto, M., Bodini, B., et al. (2017) Generalization of endothelial modelling of TSPO PET imaging: Considerations on tracer affinities. *Journal of cerebral blood flow and metabolism : official journal of the International Society of Cerebral Blood Flow and Metabolism*. 271678X17742004.

Rizzo, G., Veronese, M., Tonietto, M., Zanotti-Fregonara, P., et al. (2014) Kinetic modeling without accounting for the vascular component impairs the

quantification of [(11)C]PBR28 brain PET data. *Journal of cerebral blood flow and metabolism : official journal of the International Society of Cerebral Blood Flow and Metabolism*. 34 (6), 1060–1069.

Roberson, E.D., Scearce-Levie, K., Palop, J.J., Yan, F., et al. (2007) Reducing endogenous tau ameliorates amyloid beta-induced deficits in an Alzheimer's disease mouse model. *Science (New York, N.Y.)*. 316 (5825), 750–754.

Roeda, D., Hinnen, F. & Dollé, F. (2003) Radiosynthesis of a 2-substituted 4,5-dihydro-1H-[2- ^{11} C] imidazole: the I $_2$ imidazoline receptor ligand [^{11} C] benazoline. *Journal of Labelled Compounds and Radiopharmaceuticals*. 46 (12), 1141–1149.

Rohn, T.T., Kokoulina, P., Eaton, C.R. & Poon, W.W. (2009) Caspase activation in transgenic mice with Alzheimer-like pathology: results from a pilot study utilizing the caspase inhibitor, Q-VD-OPh. *International journal of clinical and experimental medicine*. 2 (4), 300–308.

Rossner, S., Lange-Dohna, C., Zeitschel, U. & Perez-Polo, J.R. (2005) Alzheimer's disease beta-secretase BACE1 is not a neuron-specific enzyme. *Journal of Neurochemistry*. 92 (2), 226–234.

Sancheti, H., Patil, I., Kanamori, K., Brinton, R.D., et al. (2014) Hypermetabolic State in the 7-Month-Old Triple Transgenic Mouse Model of Alzheimer'S Disease and the Effect of Lipoic Acid: A ^{13} C-NMR Study. *Journal of Cerebral Blood Flow & Metabolism*. 34 (11), 1749–1760.

Di Scala, C., Troadec, J.-D., Lelièvre, C., Garmy, N., et al. (2014) Mechanism of cholesterol-assisted oligomeric channel formation by a short Alzheimer β-amyloid peptide. *Journal of Neurochemistry*. 128 (1), 186–195.

Scheff, S.W. & Price, D.A. (1993) Synapse loss in the temporal lobe in Alzheimer's disease. *Annals of Neurology*. 33 (2), 190–199.

Schinkel, A.H. (1999) P-Glycoprotein, a gatekeeper in the blood–brain barrier. *Advanced Drug Delivery Reviews*. 36 (2–3), 179–194.

Schuitemaker, A., van Berckel, B.N.M., Kropholler, M.A., Veltman, D.J., et al. (2007) SPM analysis of parametric (R)-[11C]PK11195 binding images: Plasma input versus reference tissue parametric methods. *NeuroImage*. 35 (4), 1473–1479.

Schuitemaker, A., van der Doef, T.F., Boellaard, R., van der Flier, W.M., et al. (2012) Microglial activation in healthy aging. *Neurobiology of Aging*. 33 (6), 1067–1072.

Schuitemaker, A., Kropholler, M.A., Boellaard, R., van der Flier, W.M., et al. (2013)

Microglial activation in Alzheimer's disease: An (R)-[11C]PK11195 positron emission tomography study. *Neurobiology of Aging*. 34 (1), 128–136.

Selkoe, D.J. & Hardy, J. (2016) The amyloid hypothesis of Alzheimer's disease at 25 years. *EMBO Molecular Medicine*. 8 (6), 595–608.

Semple, B.D., Frugier, T. & Morganti-Kossmann, M.C. (2010) CCL2 modulates cytokine production in cultured mouse astrocytes. *Journal of Neuroinflammation*. 7 (1), 67.

Seppälä, T.T., Koivisto, A.M., Hartikainen, P., Helisalmi, S., et al. (2011) Longitudinal changes of CSF biomarkers in alzheimer's disease. *Journal of Alzheimer's Disease*. 25 (4), 583–594.

Serrano-Pozo, A., Mielke, M.L., Gómez-Isla, T., Betensky, R.A., et al. (2011) Reactive Glia not only Associates with Plaques but also Parallels Tangles in Alzheimer's Disease. *Am J Pathol*. 179, 1373–1384.

Shaftel, S.S., Carlson, T.J., Olschowka, J.A., Kyrkanides, S., et al. (2007) Chronic Interleukin-1 Expression in Mouse Brain Leads to Leukocyte Infiltration and Neutrophil-Independent Blood Brain Barrier Permeability without Overt Neurodegeneration. *Journal of Neuroscience*. 27 (35), 9301–9309.

Sheffield, L.G., Marquis, J.G. & Berman, N.E.. (2000) Regional distribution of cortical microglia parallels that of neurofibrillary tangles in Alzheimer's disease. *Neuroscience Letters*. 285 (3), 165–168.

Sheng, J.G., Mrak, R.E., Rovnaghi, C.R., Kozlowska, E., et al. (n.d.) Human brain S100 beta and S100 beta mRNA expression increases with age: pathogenic implications for Alzheimer's disease. *Neurobiology of aging*. 17 (3), 359–363.

Silverberg, N., Elliott, C., Ryan, L., Masliah, E., et al. (2018) NIA commentary on the NIA-AA Research Framework: Towards a biological definition of Alzheimer's disease. *Alzheimer's and Dementia*. 14 (4), 576–578.

Simmons, D.A., James, M.L., Belichenko, N.P., Semaan, S., et al. (2018) TSPO–PET imaging using [18F]PBR06 is a potential translatable biomarker for treatment response in Huntington's disease: preclinical evidence with the p75NTR ligand LM11A-31. *Human Molecular Genetics*. 27 (16), 2893–2912.

Simpson, J.E., Ince, P.G., Lace, G., Forster, G., et al. (2010) Astrocyte phenotype in relation to Alzheimer-type pathology in the ageing brain. *Neurobiology of Aging*. 31 (4), 578–590.

Singh, T.D., Josephs, K.A., Machulda, M.M., Drubach, D.A., et al. (2015) Clinical, FDG and amyloid PET imaging in posterior cortical atrophy. *Journal of neurology*. 262 (6), 1483–1492.

Smits, H.A., Rijsmus, A., van Loon, J.H., Wat, J.W.Y., et al. (2002) Amyloid-beta-induced chemokine production in primary human macrophages and astrocytes. *Journal of neuroimmunology*. 127 (1–2), 160–168.

Sofroniew, M. V. (2015) Astrocyte barriers to neurotoxic inflammation. *Nature Reviews Neuroscience*. 16 (5), 249–263.

Sofroniew, M. V. (2014) Multiple Roles for Astrocytes as Effectors of Cytokines and Inflammatory Mediators. *The Neuroscientist*. 20 (2), 160–172.

Soscia, S.J., Kirby, J.E., Washicosky, K.J., Tucker, S.M., et al. (2010) The Alzheimer's Disease-Associated Amyloid β-Protein Is an Antimicrobial Peptide Ashley I. Bush (ed.). *PLoS ONE*. 5 (3), e9505.

Soucek, T., Cumming, R., Dargusch, R., Maher, P., et al. (2003) The regulation of glucose metabolism by HIF-1 mediates a neuroprotective response to amyloid beta peptide. *Neuron*. 39 (1), 43–56.

Sridharan, S., Lepelletier, F.X., Trigg, W., Banister, S., et al. (2016) Comparative Evaluation of Three TSPO PET Radiotracers in a LPS-Induced Model of Mild Neuroinflammation in Rats. *Molecular Imaging and Biology*. 19 (August), 1–13.

Stefaniak, J. & O'Brien, J. (2015) Imaging of neuroinflammation in dementia: a review. *Journal of Neurology, Neurosurgery and Psychiatry*. 87 (1), 21–28.

Stein, M., Keshav, S., Harris, N. & Gordon, S. (1992) Interleukin 4 potently enhances murine macrophage mannose receptor activity: a marker of alternative immunologic macrophage activation. *The Journal of experimental medicine*. 176 (1), 287–292.

Su, Z., Herholz, K., Gerhard, A., Roncaroli, F., et al. (2013) [11C]-(R)PK11195 tracer kinetics in the brain of glioma patients and a comparison of two referencing approaches. *European Journal of Nuclear Medicine and Molecular Imaging*.

Tabaton, M., Zhu, X., Perry, G., Smith, M.A., et al. (2010) Signaling effect of amyloid-β42 on the processing of AβPP. *Experimental Neurology*. 221 (1), 18–25.

Takuma, H., Arawaka, S. & Mori, H. (2003) Isoforms changes of tau protein during development in various species. *Brain research. Developmental brain research*. 142 (2), 121–127.

Tang, D., Hight, M.R., McKinley, E.T., Fu, A., et al. (2012) Quantitative preclinical imaging of TSPO expression in glioma using N,N-diethyl-2-(2-(4-(2-18F-fluoroethoxy)phenyl)-5,7-dimethylpyrazolo[1,5-a]pyrimidin-3-yl)acetamide. *Journal of nuclear medicine : official publication, Society of Nuclear Medicine*. 53 (2), 287–294.

Tang, D., Li, J., Buck, J.R., Tantawy, M.N., et al. (2017) Evaluation of TSPO PET Ligands [18F]VUIIS1009A and [18F]VUIIS1009B: Tracers for Cancer Imaging. *Molecular imaging and biology : MIB : the official publication of the Academy of Molecular Imaging*. 19 (4), 578–588.

Tarkowski, E., Andreasen, N., Tarkowski, A. & Blennow, K. (2003) Intrathecal inflammation precedes development of Alzheimer's disease. *Journal of neurology, neurosurgery, and psychiatry*. 74 (9), 1200–1205.

Thal, D.R., Rüb, U., Orantes, M. & Braak, H. (2002) Phases of Aβ-deposition in the human brain and its relevance for the development of AD. *Neurology*. 58 (12), 1791–1800.

Thal, D.R., Rüb, U., Schultz, C., Sassin, I., et al. (2000) Sequence of Abeta -Protein Deposition in the Human Medial Temporal Lobe. *Journal of neuropathology and experimental neurology*. 59 (8), 733–748.

Tofts, P. & John Wiley & Sons, L. (2003) *Quantitative MRI of the brain : measuring changes caused by disease*. Wiley.

Tomasi, G., Edison, P., Bertoldo, A., Roncaroli, F., et al. (2008) Novel reference region model reveals increased microglial and reduced vascular binding of 11C-(R)-PK11195 in patients with Alzheimer's disease. *Journal of nuclear medicine : official publication, Society of Nuclear Medicine*. 49 (8), 1249–1256.

Tombaugh, T.N. (2004) Trail Making Test A and B: Normative data stratified by age and education. *Archives of Clinical Neuropsychology*. 19 (2), 203–214.

Townsend, D.W. (2008) Positron Emission Tomography/Computed Tomography. *Seminars in Nuclear Medicine*. 38 (3), 152–166.

Tremblay, M.-È. (2011) The role of microglia at synapses in the healthy CNS: novel insights from recent imaging studies. *Neuron glia biology*. 7 (1), 67–76.

Turkheimer, F., Moresco, M., Sokoloff, L., Fazio, F., et al. (1994) *The Use of Spectral Analysis to Determine Regional Cerebral Glucose Utilization with Positron Emission Tomography and eSP]Pluorodeoxyglucose: Theory, Implementation,*

and Optimization Procedures. 406–422.

Turkheimer, F.E., Edison, P., Pavese, N., Roncaroli, F., et al. (2007) Reference and target region modeling of [11C]-(R)-PK11195 brain studies. *Journal of nuclear medicine : official publication, Society of Nuclear Medicine*. 48 (1), 158–167.

Turkheimer, F.E., Hinz, R. & Cunningham, V.J. (2003) On the undecidability among kinetic models: from model selection to model averaging. *Journal of cerebral blood flow and metabolism : official journal of the International Society of Cerebral Blood Flow and Metabolism*. 23 (4), 490–498.

Turkheimer, F.E., Rizzo, G., Bloomfield, P.S., Howes, O., et al. (2015) The methodology of TSPO imaging with positron emission tomography. *Biochemical Society Transactions*. 43 (4), 586–592.

Tyacke, R.J., Fisher, A., Robinson, E.S.J., Grundt, P., et al. (2012) Evaluation and initial in vitro and ex vivo characterization of the potential positron emission tomography ligand, BU99008 (2-(4,5-Dihydro-1H-imidazol-2-yl)-1- methyl-1H-indole), for the imidazoline2 binding site. *Synapse*. 66 (6), 542–551.

Tyacke, R.J., Myers, J.F.M., Venkataraman, A., Mick, I., et al. (2018) Evaluation of 11 C-BU99008, a PET Ligand for the Imidazoline 2 Binding Site in Human Brain. *Journal of Nuclear Medicine*. 59 (10), 1597–1602.

Tziortzi, A.C., Haber, S.N., Searle, G.E., Tsoumpas, C., et al. (2014) Connectivity-Based Functional Analysis of Dopamine Release in the Striatum Using Diffusion-Weighted MRI and Positron Emission Tomography. *Cerebral Cortex*. 24 (5), 1165–1177.

Unger, J.W. (1998) Glial Reaction in Aging and Alzheimer ' s Disease. *Microscopy Research and Technique 43:24–28*. 28 (July), 24–28.

Unger, J.W., Lapham, L.W., Mcneill, T.H., Eskint, T.A., et al. (1991) The Amygdala in Alzheimer's Disease: Neuropathology and Alz 50 Immunoreactivity. *Neurobiology of Aging*.12.

van de Veerdonk, F.L., Netea, M.G., Dinarello, C.A. & Joosten, L.A.B. (2011) Inflammasome activation and IL-1β and IL-18 processing during infection. *Trends in Immunology*. 32 (3), 110–116.

Verkhratsky, A., Olabarria, M., Noristani, H.N., Yeh, C.Y., et al. (2010) Astrocytes in Alzheimer's Disease. *Neurotherapeutics*. 7 (4), 399–412.

Veronese, M., Rizzo, G., Bertoldo, A. & Turkheimer, F.E. (2016) Spectral Analysis of

dynamic PET studies : a review of 20 years of method developments and applications. *Computational and Mathematical Methods in Medicine*. 2016, 1–15.

Vivash, L. & OBrien, T.J. (2016) Imaging Microglial Activation with TSPO PET: Lighting Up Neurologic Diseases? *Journal of Nuclear Medicine*. 57 (2), 165–168.

Vomacka, L., Albert, N.L., Lindner, S., Unterrainer, M., et al. (2017) TSPO imaging using the novel PET ligand [18F]GE-180: quantification approaches in patients with multiple sclerosis. *EJNMMI Research*. 7 (1), 89.

Wadsworth, H., Jones, P. a., Chau, W.F., Durrant, C., et al. (2012) GE-180: A novel fluorine-18 labelled PET tracer for imaging Translocator protein 18 kDa (TSPO). *Bioorganic and Medicinal Chemistry Letters*. 22 (3), 1308–1313.

Wickstrøm, T., Clarke, A., Gausemel, I., Horn, E., et al. (2014) The development of an automated and GMP compliant FASTlab™ Synthesis of [18F]GE-180; A radiotracer for imaging translocator protein (TSPO). *Journal of Labelled Compounds and Radiopharmaceuticals*. 57 (1), 42–48.

Wimberley, C., Lavisse, S., Brulon, V., Peyronneau, M.-A., et al. (2018) Impact of Endothelial 18-kDa Translocator Protein on the Quantification of 18F-DPA-714. *Journal of Nuclear Medicine*. 59 (2), 307–314.

Wong, D.F., Rosenberg, P.B., Zhou, Y., Kumar, A., et al. (2010) In vivo imaging of amyloid deposition in Alzheimer disease using the radioligand 18F-AV-45 (florbetapir [corrected] F 18). *Journal of nuclear medicine : official publication, Society of Nuclear Medicine*. 51 (6), 913–920.

Woolrich, M.W., Jbabdi, S., Patenaude, B., Chappell, M., et al. (2009) Bayesian analysis of neuroimaging data in FSL. *NeuroImage*. 45 (1 Suppl).

Worsley, K.J., Marrett, S., Neelin, P., Vandal, A.C., et al. (1996) A unified statistical approach for determining significant signals in images of cerebral activation. *Human Brain Mapping*. 4 (1), 58–73.

Wyss-Coray, T., Loike, J.D., Brionne, T.C., Lu, E., et al. (2003) Adult mouse astrocytes degrade amyloid-β in vitro and in situ. *Nature Medicine*. 9 (4), 453–457.

Xia, M.Q., Qin, S.X., Wu, L.J., Mackay, C.R., et al. (1998) Immunohistochemical study of the beta-chemokine receptors CCR3 and CCR5 and their ligands in normal and Alzheimer's disease brains. *The American journal of pathology*. 153 (1), 31–37.

Xiao, M. & Hu, G. (2014) Involvement of Aquaporin 4 in Astrocyte Function and Neuropsychiatric Disorders. *CNS Neuroscience & Therapeutics*. 20 (5), 385–390.

Xue, J., Schmidt, S.V., Sander, J., Draffehn, A., et al. (2014) Transcriptome-Based Network Analysis Reveals a Spectrum Model of Human Macrophage Activation. *Immunity*. 40 (2), 274–288.

Yeh, C.-Y., Vadhwana, B., Verkhratsky, A. & Rodríguez, J.J. (2011) Early Astrocytic Atrophy in the Entorhinal Cortex of a Triple Transgenic Animal Model of Alzheimer's Disease. *ASN Neuro*. 3 (5), AN20110025.

Yoder, K.K., Nho, K., Risacher, S.L., Kim, S., et al. (2013) Influence of TSPO genotype on 11C-PBR28 standardized uptake values. *Journal of nuclear medicine : official publication, Society of Nuclear Medicine*. 54 (8), 1320–1322.

Yoder, K.K., Territo, P.R., Hutchins, G.D., Hannestad, J., et al. (2015) Comparison of standardized uptake values with volume of distribution for quantitation of [11C]PBR28 brain uptake. *Nuclear Medicine and Biology*. 42 (3), 305–308.

Yushkevich, P.A., Piven, J., Hazlett, H.C., Smith, R.G., et al. (2006) User-guided 3D active contour segmentation of anatomical structures: Significantly improved efficiency and reliability. *NeuroImage*. 31 (3), 1116–1128.

Zanotti-Fregonara, P., Liow, J.-S., Fujita, M., Dusch, E., et al. (2011) Image-derived input function for human brain using high resolution PET imaging with [C](R)-rolipram and [C]PBR28. *PloS one*. 6 (2), e17056.

Zanotti-Fregonara, P., Pascual, B., Rizzo, G., Yu, M., et al. (2018) Head-to-head comparison of ^{11}C-PBR28 and ^{18}F-GE180 for the quantification of TSPO in the human brain. *Journal of Nuclear Medicine*. 59 (8), jnumed.117.203109.

Zelcer, N., Khanlou, N., Clare, R., Jiang, Q., et al. (2007) Attenuation of neuroinflammation and Alzheimer's disease pathology by liver x receptors. *Proceedings of the National Academy of Sciences*. 104 (25), 10601–10606.

APPENDIX

Appendix 1. Permission Table

TYPE OF WORK:	Name of work	Source of work	Copyright holder	permission requested on	I have permission yes /no	Permission note
FIGURE	Figure I-2. Molecular and cellular processes presumed to participate in AD pathogenesis.	Erik D. Roberson, and Lennart Mucke Science 2007 (Roberson et al., 2007)	The American Association for the Advancement of Science	30.08.2018	YES	Permission granted (RightsLink License)
FIGURE	Figure I-3. Microglia are rapidly activated after local BBB (blood brain barrier) disruption.	Axel Nimmerjahn et al. Science 2005; 308:1314-1318 (Nimmerjahn, Kirchhoff & Helmchen, 2005)	The American Association for the Advancement of Science	30.08.2018	YES	Permission granted (RightsLink License)

FIGURE	Figure I-4. Relationship between microglial activation and neurofibrillary tangle formation in Alzheimer's disease.	Z Fan, 2015, Brain (Fan et al., 2015b)	Oxford University Press	30.08.2018	YES	Permission granted (RightsLink License)
FIGURE	Figure I-5. Changes in microglia and astrocyte in Alzheimer's disease.	M. Heneka, 2015, The Lancet Neurology (Heneka et al., 2015)	Elsevier	30.08.2018	YES	Permission granted (RightsLink License)
FIGURE	Figure I-6. NLRP3 gene deficiency increases microglial Aβ phagocytosis and shows protective effects in APP/PS1 mice on memory and behaviours.	M. Heneka Nature. 2012 Jan 31; 493(7434): 674–678 (Heneka et al., 2012)	Nature	30.08.2018	YES	Permission granted (RightsLink License)
FIGURE	Figure I-9. Schematic diagram of PET imaging.	*Townsend D, Seminars in Nuclear Medicine, 2008. (Townsend, 2008)*	Elsevier	30.08.2018	YES	Permission granted (RightsLink License)

FIGURE	Figure VI-1. Stereotypical patterns of tau (a-b) and amyloid (c-d) in Alzheimer's disease.	J. Brettschneider, 2015 Nature Reviews Neuroscience (Brettschneider et al., 2015)	Springer Nature	30.08.2018	YES	Permission granted (RightsLink License)
PUBLICATION	CHAPTER III (Study 1 for QUANTIFICATION OF MICROGLIAL ACTIVATION USING [^{18f}]GE180 PET)	Z. Fan, 2016, Journal of Nuclear Medicine (Fan et al., 2016)	JNM	25.07.2018	YES	Written permission (Email)
PUBLICATION	CHAPTER IV (QUANTIFICATION OF MICROGLIAL ATIVATION USING [^{11C}]PBR28 PET)	Z. Fan, 2018, EJNMMI (Fan et al., 2018)	EJNMMI	25.07.2018	YES	Creative Commons CC

Appendix 2. Recruitment Criteria.

Inclusion criteria were a diagnosis of AD defined by DSM-IV or NIA-AA criteria, or healthy control subjects, age range 55–85, ability to give informed consent, at least eight years of education, MMSE of 17–26 for AD, and normal cognition for the age-matched healthy controls. MCI were diagnosis based on the Petersen criteria (2004). Exclusion criteria were Depression, any significant disease or unstable medical condition that could influence neuro-psychological testing, Participants in whom magnetic resonance image (MRI) is contraindicated, History of schizophrenia, schizoaffective disorder, bipolar disorder or any history of ECT, Subjects with significant lesions or white matter microvascular disease on MRI will be excluded, Pregnant and breast-feeding women – all women who could potentially be pregnant will have a pregnancy test. TSPO low affinity binders were excluded. (Clinical team provided)

Appendix 3. Recruitment Criteria.

Subjects who meet the National Institute on Aging-Alzheimer's Association (NIA-AA) core clinical criteria for probable Alzheimer's disease dementia or meeting the NIA-AA criteria for MCI due to AD. Clinical Dementia Rating (CDR) score of 0.5 or 1.0 and memory box score of 0.5 or greater. Age 50 or above. Mini Mental State Examination (MMSE) score ≥17/30. Females must not be pregnant or lactating, and specified contraceptive precautions must be followed. Subjects on symptomatic (cholinesterase inhibitor or memantine) therapy for AD must be on a stable dose for at least 6 weeks prior to the baseline evaluation. Subjects must have partners/caregivers able to monitor for, and report, any adverse events to the study team throughout the course of study
Subjects must be able to provide and confirm informed consent. After obtaining the consent, all subjects underwent medical, neurological and detailed cognitive assessment, using the Repeatable Battery for the Assessment of Neuropsychological Status (RBANS). Subject presenting with memory concern or impairment but without diagnosis will undergo the screening, in view of the potential diagnosis of MCI due to AD. If subjects have not had MRI as diagnostic work up, the MRI scan will be used to make the decision about the diagnosis.